



Part 3 of 4

April 1993

Conference Proceeding

APPROVED FOR PUBLIC RELEASE; DISTRIBUTION IS UNLIMITED.



PHILLIPS LABORATORY
Directorate of Space and Missiles Technology
AIR FORCE MATERIEL COMMAND
KIRTLAND AIR FORCE BASE, NM 87117-5776

PL-CP--93-1001

This final report was prepared by the Phillips Laboratory, Kirtland Air Force Base, New Mexico, under Job Order 11050502. The Laboratory Project Officer-in-Charge was Marko M. Stoyanof (VTPT).

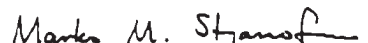
When Government drawings, specifications, or other data are used for any purpose other than in connection with a definitely Government-related procurement, the United States Government incurs no responsibility or any obligation whatsoever. The fact that the Government may have formulated or in any way supplied the said drawings, specifications, or other data, is not to be regarded by implication, or otherwise in any manner construed, as licensing the holder, or any other person or corporation; or as conveying any rights or permission to manufacture, use, or sell any patented invention that may in any way be related thereto.

This report has been authored by employees and contractors of the United States Government and Foreign Governments. Accordingly, the United States Government retains a nonexclusive royalty-free license to publish or reproduce the material contained herein, or allow others to do so, for the United States Government purposes.

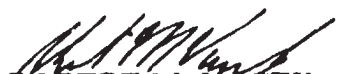
This report has been reviewed by the Public Affairs Office and is releasable to the National Technical Information Service (NTIS). At NTIS, it will be available to the general public, including foreign nationals.

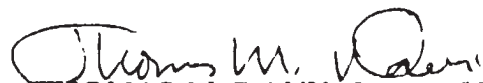
If your address has changed, or if your organization no longer employs the addressee, please notify PL/VTPT, Kirtland AFB, NM 87117-5776 to help maintain a current mailing list.

This conference proceeding has been reviewed and is approved for publication.


MARKO M. STOYANOF
Project Officer

FOR THE COMMANDER


ROBERT M. VACEK, GM-14, DAF
Chief, Thermal Management Br


THOMAS M. DAVIS, Lt Col, USAF
Acting Director of Space & Missile
Technology

DO NOT RETURN COPIES OF THIS REPORT UNLESS CONTRACTUAL OBLIGATIONS OR NOTICE ON A SPECIFIC DOCUMENT REQUIRES THAT IT BE RETURNED.

REPORT DOCUMENTATION PAGE

Form Approved
OMB No. 0704-0188

Public reporting burden for this collection of information is estimated to average 1 hour per response, including the time for reviewing instructions, searching existing data sources, gathering and maintaining the data needed, and completing and reviewing the collection of information. Send comments regarding this burden estimate or any other aspect of this collection of information, including suggestions for reducing this burden, to Washington Headquarters Services, Directorate for Information Operations and Reports, 1215 Jefferson Davis Highway, Suite 1204, Arlington, VA 22202-4302 and to the Office of Management and Budget, Paperwork Reduction Project (0704-0188), Washington, DC 20503.

1. AGENCY USE ONLY (Leave blank)	2. REPORT DATE April 1993	3. REPORT TYPE AND DATES COVERED 17-19 Nov 92, Conference Proceeding
----------------------------------	-------------------------------------	--

4. TITLE AND SUBTITLE 7th International Cryocooler Conference Part 1 of 4	5. FUNDING NUMBERS PE: 62601F PR: 1105 TA: 05 WU: 02
6. AUTHOR(S) Several authors	

7. PERFORMING ORGANIZATION NAME(S) AND ADDRESS(ES) Phillips Laboratory Kirtland AFB, NM 87117-5776	8. PERFORMING ORGANIZATION REPORT NUMBER PL-CP--93-1001
--	---

9. SPONSORING / MONITORING AGENCY NAME(S) AND ADDRESS(ES)	10. SPONSORING / MONITORING AGENCY REPORT NUMBER
---	--

11. SUPPLEMENTARY NOTES
Publication of this report does not constitute approval or disapproval of the ideas or findings. It is published in the interest of scientific and technical information exchange. The established procedures for editing reports were not followed for this report

12a. DISTRIBUTION / AVAILABILITY STATEMENT Approved for public release: distribution is unlimited.	12b. DISTRIBUTION CODE
--	------------------------

13. ABSTRACT (Maximum 200 words)

The 7th International Cryocooler Conference was held in Santa Fe, New Mexico, on 17-19 November, 1992. Jiri L. Ludwigsen of Nichols Research was the conference chairperson; Capt William Wyche and Marko Stoyanof of Phillips Laboratory served as the program committee chairmen.

The topics included Cryocooler Testing and Modeling, Space and Long Life Applications, Stirling Cryocoolers, Pulse Tube Refrigerators, Novel Concepts and Component Development, Low Temperature Regenerator Development, and J-T and Absorption Coolers.

14. SUBJECT TERMS Absorption, Cryocoolers, Cryogenic, Low Temperature Heat Exchanger, Pulse Tube Refrigerators, Regenerative, Recuperative, Stirling, Thermal Modeling	15. NUMBER OF PAGES 320
	16. PRICE CODE

17. SECURITY CLASSIFICATION OF REPORT Unclassified	18. SECURITY CLASSIFICATION OF THIS PAGE Unclassified	19. SECURITY CLASSIFICATION OF ABSTRACT Unclassified	20. LIMITATION OF ABSTRACT SAR
--	---	--	--

Chairman

Jill Ludwigsen
 Nichols Research Corporation
 2201 Buena Vista, S.E. #203
 Albuquerque, NM 87106
 (505) 843-7364

Program Committee

Capt. Bill Wyche, Co-Chairman
 Marko Stoyanof, Co-Chairman
 Air Force Phillips Laboratory
 Ronald White, WRDC/FIVE
 Dodd Stacy, Creare
 Ron Ross, Jet Propulsion Lab
 Al Johnson, Aerospace Corp.
 Peter Gifford, Cryomech

Local Arrangements

Peter Jones, Aerospace Corp.

Advisory Board

John Barclay University of Victoria	Joseph Smith MIT
Stephen Castles NASA/GSFC	Michael Superczynski DTRC
Ray Radebaugh NIST	Klaus Timmerhaus University of Colorado
Hiroshi Nagano Toyama University, Japan	Paul Sheihing DOE
Ralph Longsworth APD Cryogenics	Peter Kerney Janis Research
Martin Nisenoff NRL	George Robinson Nichols Research Corp.
Martin Nisenoff NRL	George Robinson Nichols Research Corp.

FOREWORD

This report contains the proceedings of the Seventh International Cryocooler Conference, held in Santa Fe, New Mexico, on 17-19 November, 1992. Jill L. Ludwigsen of Nichols Research was the conference chairperson; Capt William Wyche and Marko Stoyanof of Phillips Laboratory served as the program committee chairmen.

The first cryocooler conference held in 1980 was designed to stimulate interest and discussion in the scientific and engineering community about the latest developments and advances in refrigeration for cryogenic sensors and electronic systems. The conference is held every even numbered year and this year over 300 participants attended representing 11 countries.

The technical program consisted of over 100 unrestricted oral and poster presentations. The topics included Cryocooler Testing and Modeling, Space and Long Life Applications, Stirling Cryocoolers, Pulse Tube Refrigerators, Novel Concepts and Component Development, Low Temperature Regenerator Development, and J-T and Absorption Coolers. The proceedings show significant progress in the field of cryocooler technology.

ACKNOWLEDGEMENTS

The Seventh International Cryocooler Conference Board would like to thank the Air Force Phillips Laboratory for sponsoring the conference and publishing these proceedings. The generous supply of manpower and dedication contributed by Phillips Laboratory was key to the success of the 1992 conference.

The Conference Chairperson would like to express her appreciation to Nichols Research Corporation for providing the support, assets and time required for this effort.

CONTENTS

TUESDAY SESSION 1

SDIO AND AIR FORCE CRYOCOOLER TECHNOLOGY DEVELOPMENTS AT
USAF PHILLIPS LABORATORY
....P. J. Thomas 3

JPL CRYOCOOLER DEVELOPMENT AND TEST PROGRAM OVERVIEW
....R. G. Ross, Jr. 14

NASA/GSFC CRYOCOOLER DEVELOPMENT PROGRAM
....S. Castles, T. Cygnarowicz, R. Boyle, L. Sparr, R. Cory, F. Connors
....E. James, R. Fink, V. Arillo, J. Marketon, C. Lee, and D. Bugby 26

DEVELOPMENT AND DEMONSTRATION OF A DIAPHRAGM STIRLING 65 K
STANDARD SPACECRAFT CRYOCOOLER
....D. Stacy, J. McCormick, and J. Valenzuela 40

STIRLING SPACE COOLER
....C. K. Chan, M. Lopez, J. Raab, E. Tward, and G. Davey 50

THERMAL, VIBRATION, AND RELIABILITY TEST RESULTS FOR A
BALANCED 80 K CRYOCOOLER
....R. Boyle, L. Sparr, T. Cygnarowicz, S. Castles,
....R. G. Fink, and E. F. James 57

SPACECRAFT COOLER CHARACTERIZATION
....D. L. Johnson, G. R. Mon, and R. G. Ross, Jr. 73

PERFORMANCE OF A LONG LIFE REVERSE BRAYTON CRYOCOOLER
....W. Swift and H. Sixsmith 84

SDI CRYOCOOLER PRODUCIBILITY PROGRAM
....J. Bruning 98

MINIATURES PULSE TUBE COOLER
....C. K. Chan, C. B. Jaco, J. Raab, E. Tward, and M. Waterman 113

FLOW PATTERNS INTRINSIC TO THE PULSE TUBE REFRIGERATOR
....J. M. Lee, P. Kittel, K. D. Timmerhaus, and R. Radebaugh 125

EXPERIMENTAL PERFORMANCE OF MODIFIED PULSE TUBE
REFRIGERATOR BELOW 80 K DOWN 23 K
....Y. Ishizaki and E. Ishizaki 140

CONTENTS (Continued)

PULSE TUBE REFRIGERATOR RESEARCH
...Y. Zhou and Y. J. Han 147

DEVELOPMENT OF PULSE TUBE REFRIGERATOR WITH LINEAR-MOTOR DRIVE COMPRESSOR
...T. Kuriyama, H. Hatakeyama, Y. Ohtani, H. Nakagome, Y. Matsubara,
...H. Okuda, and H. Murakami 157

AN EXPERIMENTAL AND ANALYTICAL INVESTIGATION OF 4 K PULSE TUBE REFRIGERATOR
...Y. Matsubara, J. L. Gao, K. Tanida, Y. Hiresaki, M. Kaneko 166

A NEW CONFIGURATION FOR SMALL-CAPACITY, LIQUID-HELIUM-TEMPERATURE CRYOCOOLER
...J. A. Crunkleton 187

ANALYSIS OF A MINIATURE TWO-STAGE CRYOCOOLER
...E. B. Ratts, Dr J. L. Smith, Jr., and Dr Y. Iwasa 197

POWER, EFFICIENCY, AND OPTIMUM DESIGN OF ELECTROCHEMICAL REFRIGERATORS
...R. T. Ruggeri 213

LINEARIZED PULSE TUBE CRYOCOOLER THEORY
...H. Mirels 221

VIBROIMPACT RESONANCE APPLICATION FOR THE DISPLACER MOTION PASSIVE CONTROL IN THE SPLIT CRYOGENIC COOLER
...A. Veprik and N. Pundak 233

A HIGHLY RELIABLE, MINIATURE STIRLING-CYCLE CRYOCOOLER
...C. S. Keung and G. Esposito 247

PERFORMANCE TEST RESULTS ON A MINIATURE STIRLING CRYOCOOLER FOR USE IN INTEGRATED DEWAR DETECTOR ASSEMBLIES
...P. Ab-der-Halden 257

VALIDATION OF THE STIRLING REFRIGERATOR PERFORMANCE MODEL AGAINST THE PHILLIPS/NASA MAGNETIC BEARING REFRIGERATOR
...S. W. K. Yuan and I. E. Spradley 280

THE MS*2 STIRLING CYCLE CODE
...M. P. Mitchell 290

CONTENTS (Continued)

AN INTRODUCTION TO THE LUCAS AEROSPACE THERMODYNAMIC
COMPUTER MODEL CMOD
...C. S. Brice. 294

THERMOACOUSTIC THEORY FOR REGENERATIVE CRYOCOOLERS: A
CASE STUDY FOR A PULSE TUBE REFRIGERATOR
...J. H. Xiao 305

SOME PRELIMINARY EXPERIMENTAL RESULTS ON OSCILLATORY HEAT
TRANSFER IN A PERIODICALLY REVERSING PIPE FLOW
...X. Tang and P. Cheng 321

THERMOELECTRIC COOLERS FOR THE TWS, SFW, WAM AND SADARM
PROGRAMS, AND ASSOCIATED MANTECH PROGRAM OBJECTIVES
...W. L. Kolander, B. Morrison, J. Bierschenk,
...J. Fuhrer, and T. Kottak 332

CRYOGENIC ATTACHMENT FIXTURE WITH HIGH STRENGTH AND LOW
THERMAL CONDUCTION
...P. R. Roach 349

HELIUM LIQUID- AND GAS-GAP HEAT SWITCHES
...A. Kashani, B. P. M. Helvensteijn,
...F. J. McCormack, and A. L. Spivak 355

A RADIATIVE COOLING SYSTEM FOR THE EOS STRATOSPHERIC WIND
INFRARED LIMB SOUNDER
...D. J. Kuyper 371

NEW MAGNETIC REFRIGERANTS FOR THE LOW TEMPERATURES REGION
...M. D. Kuz'min, A. M. Tishin, and S. Y. Dan'kov 385

WEDNESDAY SESSION 387

EXPERIMENTAL INVESTIGATION OF THE REGENERATIVE MAGNETIC
REFRIGERATOR OPERATING BETWEEN 4.2 K AND 1.8 K
...S. Jeong, J. L. Smith, Jr., Y. Iwasa, and T. Numazawa 389

A 4 K GIFFORD-McMAHON REFRIGERATOR FOR RADIO ASTRONOMY
...R. Plambeck, N. Thatte, and P. Sykes 401

CONTENTS (Continued)

DYNAMIC CHARACTERISTICS OF REGENERATORS USED IN CRYOCOOLERS
B. J. Huang and C. W. Lu 416

REGENERATOR PERFORMANCE AND REFRIGERATION MECHANISM FOR 4 K GM REFRIGERATOR USING RARE EARTH COMPOUND REGENERATOR MATERIALS
T. Kuriyama, M. Takahashi, H. Nakagome, T. Hashimoto,
T. Eda, and M. Yabuki 429

A STIRLING CYCLE CRYOCOOLER FOR 4 K APPLICATIONS
D. Stacy, J. McCormick, and P. Wallis 444

SUPERFLUID STIRLING REFRIGERATOR WITH A COUNTERFLOW REGENERATOR
J. G. Brisson and G. W. Swift 460

GRADED AND NONGRADED REGENERATOR PERFORMANCE
W. Rawlins, K. D. Timmerhaus, R. Radebaugh,
J. Gary, and P. Bradley 471

SPECIFIC HEAT DESIGN AND PROPOSAL OF A NEW CUBIC TYPE MAGNETIC MATERIAL FOR A REGENERATOR MATRIX
Y. Tokai, A. Takahasi, M. Sahashi, and T. Hashimoto 484

A COMPACT 150 GHz SIS RECEIVER COOLED BY 4 K GM REFRIGERATOR
M. Takahasi, H. Hatakeyama, T. Kuriyama, H. Nakagome, R. Kawabe,
H. Iwashita, G. McCulloch, K. Shibata, and S. Ukita 495

DEVELOPMENT OF A PRECISION, SIX-AXIS LABORATORY DYNAMOMETER
P. J. Champagne, S. A. Cordova, M. S. Jacoby, and K. R. Lorell 508

DEVELOPMENT AND DEMONSTRATION OF AN ELECTRONIC CONTROLLER FOR A DOUBLE-ACTING DIAPHRAGM CRYOCOOLER
C. Konkell, T. Gibboney, L. Van Allen, K. Ha, and R. Boyle 526

MAGNETIC NOISE PRODUCED BY GM CRYOCOOLERS
S. Fujimoto, H. Ogata, and H. Kado 560

REGENERATOR TWO-PHASE "SINGLE-BLOW" FOR PERFORMANCE EVALUATION AT SMALL VELOCITIES: ORIENTATION INFLUENCE AT "1g"
K. V. Ravikumar, R. M. Carandang, T. H. K. Frederking,
R. Confair, W. Hong, F. Sherman, and C. Toribio 569

CONTENTS (Continued)

OPTIMIZATION ANALYSIS ON A TWO-STAGE AMR HYDROGEN LIQUEFIER
L. Zhang, A. J. DeGregoria, S. A. Sherif, and T. N. Veziroglu 586

SUBMILLIMETER SPACE ASTRONOMY WITHOUT LIQUID HELIUM?
C. Hagmann and P. L. Richards 595

RECENT PROGRESS ON APPLICATION OF HIGH ENTROPY MAGNETIC
 MATERIAL TO THE REGENERATOR IN HELIUM TEMPERATURE RANGE
T. Hashimoto, T. Eda, M. Yabuki, T. Kuriyama, and H. Nakagome 605

THE EFFECTS OF A LAYERED BED ON ACTIVE MAGNETIC REGENERATOR
 PERFORMANCE
S. R. Schuricht, A. J. DeGregoria, and C. B. Zimm 614

LONG LIFE STIRLING CYCLE COOLER DEVELOPMENTS FOR THE SPACE
 APPLICATION RANGE OF 20 K TO 80 K
B. G. Jones and R. C. Peddle 621

STIRLING CRYOCOOLER WITH DUAL OPPOSED DISPLACERS FOR SPACE
 APPLICATIONS
P. Arter, D. Berry, W. Gully, and C. Varner 644

DEVELOPMENT AND SPACE QUALIFICATION TESTING OF A RANGE OF
 MECHANICAL CRYOCOOLERS
C. Weir 656

NOVEL LINEAR FLEXURE BEARING
T. E. Wong, R. B. Pan, and A. L. Johnson 675

NASA/GSFC CRYOCOOLER TEST PROGRAM RESULTS
L. Sparr, R. Boyle, R. Cory, F. Connors, E. James,
R. Fink, V. Arillo, and J. Marketon 699

PERFORMANCE OF THE SIGNAAL USFA STIRLING COOLING ENGINES
D. Verbeek, H. Helmonds, and P. Roos 728

PRESENT LIFE-TESTING STATUS OF "OXFORD TYPE" CRYOCOOLERS FOR
 SPACE APPLICATIONS
C. Jewell, T. Bradshaw, A. Orłowska, and B. Jones 738

CONTENTS (Continued)

DESIGN AND TEST OF A COMPREHENSIVE FACILITY FOR LIFE-TESTING SPACE CRYOCOOLERS
R. G. Ross, Jr. and D. L. Johnson 748

SIMULATION PROGRAM FOR MULTIPLE EXPANSION STIRLING MACHINES
G. Walker, M. Weiss, R. Fauvel, G. Reader, and E. R. Bingham 759

COMPUTER MODELING OF STIRLING CYCLE COOLERS
T. W. Bradshaw, A. H. Orłowska, and J. Heatt 772

DESIGN EQUATIONS AND SCALING LAWS FOR LINEAR COMPRESSORS WITH FLEXURE SPRINGS
E. Marquardt, R. Radebaugh, and P. Kittel 783

NON-REAL TIME, FEED FORWARD VIBRATION CONTROL SYSTEM DEVELOPMENT AND TEST RESULTS
R. Boyle, F. Connors, J. Marketon, V. Arillo,
E. James, and R. Fink 805

DEMONSTRATION OF ACTIVE VIBRATION REDUCTION ON A STIRLING-CYCLE CRYOCOOLER TESTBED
B. G. Johnson, D. B. Eisenhaure, F. J. Flynn, M. S. Gaffney,
R. L. Hockney, D. L. Johnson, and R. G. Ross, Jr. 820

THURSDAY SESSION 829

EVOLUTION OF THE 10 K PERIODIC SORPTION REFRIGERATOR CONCEPT
A. L. Johnson and J. A. Jones 831

DEVELOPMENT OF A PERIODIC 10 K SORPTION CRYOCOOLER
S. Bard, T. Fujita, L. Wade, J. Rodriguez, and J. J. Wu 854

EVALUATION OF A PROTOTYPE HYDRIDE COMPRESSOR FOR PERIODIC HYDROGEN SORPTION CRYOCOOLERS
R. C. Bowman, Jr., B. D. Freeman, D. Labor, F. E. Lynch,
R. W. Marmaro, and L. A. Wade 867

ASSESSMENT OF A HYDROGEN JOULE-THOMSON EXPANDER AND VANADIUM HYDRIDE SORPTION BEDS FOR 20 K CRYOCOOLERS
E. L. Ryba, B. D. Freeman, R. C. Bowman, Jr., R. E. Spjut,
E. A. Liu, P. Budic, and C. Okado 880

CONTENTS (Continued)

DESIGN OF A METAL HYDRIDE SORPTION CRYOCOOLER SYSTEM
 ...H. J. Strumpf and R. H. Norman 898

LINEAR COMPRESSOR FOR JT CRYOCOOLER
 ...D. T. Kuo 921

PROGRESS REPORT ON THE DEVELOPMENT OF THE BALL J-T
 CRYOCOOLER
 ...R. Levenduski and R. Scarlotti 931

JT CRYOSTAT WITH LIQUID-SOLID CRYOGEN RESERVOIR
 ...R. C. Longworth 958

DESIGN AND OPERATION OF A 30 K TWO-STAGE NITROGEN-NEON J-T
 COOLER
 ...W. A. Little, R. Yaron, and C. Fuentes 971

DESIGN CONCEPTS FOR A 10 K SOLID HYDROGEN SORPTION
 REFRIGERATOR
 ...J. R. Phillips, B. D. Freeman, and R. C. Bowman, Jr. 978

EXPERIMENTAL VERIFICATION OF JOULE-THOMSON CRYOCOOLER
 COOLDOWN PERIOD SIMILARITY RATIOS
 ...B-Z. Maytal 996

BI-MATERIAL CONTROLLED DEMAND FLOW JOULE-THOMSON COOLERS
 ...G. E. Bonney 1003

CONTAMINATION CONTROL IN CLOSED CYCLE JOULE-THOMSON
 CRYOCOOLERS AND A NEW J-T VALVE
 ...J. Lester and S. Nieczkoski 1012

PHASE EQUILIBRIA IN CRYOGENIC MIXTURES
 ...L. B. Robinson 1025

INCORPORATING A MECHANICAL REFRIGERATOR WITH A REFREEZABLE
 CRYOGEN IN SPACE APPLICATIONS
 ...B. G. Williams and J. C. Batty 1043

APPLICATIONS AND PACKAGING OF SEMICONDUCTOR DEVICES FOR USE
 AT CRYOGENIC TEMPERATURES
 ...K. P. Hyde, J. R. McCoy, and C. S. Naiman 1064

CONTENTS (Concluded)

A METHOD TO ESTIMATE THE PULSE TUBE REFRIGERATOR PERFORMANCESM. David, J. Marechal, and Y. Simon	1078
CRYOCOOLER TIP MOTION SUPPRESSION USING ACTIVE CONTROL OF PIEZOELECTRIC ACTUATORSR. J. Glaser, R. G. Ross, Jr., and D. L. Johnson	1086
HIGH TEMPERATURE SUPERCONDUCTING SPACE EXPERIMENT CRYOGENIC SYSTEM OVERVIEWT. Kawecki	1098
10 K SORPTION CRYOCOOLER FLIGHT EXPERIMENT (BETSCE)S. Bard, P. Cowgill, J. Rodriguez, L. Wade, J. J. Wu,M. Gehrlein, and W. Von Der Ohe	1107
GAS ATOMIZED E_{13}Ni POWDER FOR CRYOCOOLER APPLICATIONSI. E. Anderson, M. G. Osborne, H. Takeya,and K. A. Gschneidner, Jr.	1120
MAGNETIC NANOCOMPOSITES AS MAGNETIC REFRIGERANTSR. D Shull, P. D. McMichael, J. J. Ritter,L. J. Swartzendruber, and L. H. Bennett	1133
ENTHALPY FLOW TRANSITION LOSSES IN REGENERATIVE CRYOCOOLERSP. Kittel	1145
NEODYMIUM REGENERATOR TEST RESULTS IN A STANDARD GIFFORD-McMAHON REFRIGERATORJ. Chuafe, G. Green, and R. C. Riedy	1157
SOLVAY REFRIGERATOR OPERATING AT HELIUM TEMPERATURESG. Chen, J. Zheng, F. Zhang, J. Yu, and T. Sun	1165

SUBMILLIMETER SPACE ASTRONOMY WITHOUT LIQUID HELIUM ?

C. Hagmann and P. L. Richards

*Department of Physics and Space Sciences Laboratory,
University of California, Berkeley CA 94720*

Abstract

In this paper we will discuss adiabatic demagnetization refrigerators (ADR's) with reservoir temperatures of 4 to 8 K, which can be used with mechanical cryocoolers. Very successful miniature ADR's have been previously developed for producing temperatures down to 100 mK starting from superfluid helium temperatures. These refrigerators are used for cooling bolometric infrared and x-ray detectors. An ADR can be made to operate satisfactorily from a 4 to 8 K reservoir if it uses two paramagnetic working substances with a single magnet. In a single refrigeration cycle, the ADR maintains a temperature of 100 mK for 10 to 80 hours. This time depends strongly on the magnetic field B and reservoir temperature T , but not on the volume of the working substance, as long as the heat leak is dominated by the suspension of the cold stage.

Introduction

Direct detectors used for broad band low background space astronomy require operating temperatures which depend on the wavelength. Stressed Ge:Ga photon detectors at a wavelength of 200 μm require a temperature of 1.5 K for best performance, while composite bolometers at millimeter

wavelengths require temperatures as low as 100 mK. By contrast niobium SIS quasiparticle heterodyne mixers to do narrowband molecular line spectroscopy can be operated at temperatures up to 4.5 K. It can be scientifically very important to have both kinds of detector on one space mission. It is generally assumed that the heterodyne mixers are compatible with mechanical cryocoolers, but that the direct detectors require superfluid liquid helium.

An ADR [1,2] operating at 100 mK has been developed to provide long wavelength bolometric bands for NASA's Space Infrared Telescope Facility (SIRTF) and is currently being used for a balloon measurement of the cosmic microwave background (MAX) [3]. A similar system [4] is under development for cooling x-ray micro-calorimeters on NASA's Advanced X-ray Astrophysics Facility (AXAF). Both ADR's require a superfluid ^4He bath in order to reduce the heat flow from the high temperature reservoir into the paramagnetic material to an acceptable level. The purpose of this paper is to describe a way in which space ADR technology can be extended so that it is compatible with higher reservoir temperatures. An ADR such as the one designed for SIRTF can be modified by adding an intermediate temperature stage using a second magnetic working substance to intercept the heat leak from the high temperature reservoir to the lowest temperature region. Thermal guards of this type, usually called guard salt pills, have occasionally been used in laboratory magnetic refrigerators for producing milliKelvin temperatures [5,6].

Construction

The basic building blocks of the 2-stage ADR are a superconducting magnet, a mechanical heat switch and two thermally isolated magnetic materials. The two stages are simultaneously magnetized while in contact with the high temperature reservoir and then adiabatically demagnetized until the second stage reaches $T=100$ mK. This refrigeration cycle which can last ≈ 0.5 hour is then followed by a feedback regulation mode lasting many hours in which the magnet current is slowly reduced in response to the external heat leak in order to maintain a temperature of 100 mK. A schematic

diagram of a particular compact version of the ADR is shown in Figure 1. Both stages are suspended in the magnet bore by Kevlar chords. Thermal intercepts from the guard stage are attached to the Kevlar chords midway between the 100 mK stage and the high temperature reservoir. The basic building blocks of this system are a straightforward extension of the single stage SIRTf design [1,2]. The heat leak into the 100 mK stage in regulation mode is dominated by the parasitic leak through the suspension. In the SIRTf ADR (see Table 1), the heat leak through the Kevlar suspension is about $0.25 \mu\text{W}$ with a reservoir temperature of 1.6 K. The resonance frequency of the ADR is proportional to $(AE/mL)^{1/2}$, where E is the elastic modulus of Kevlar, A and L its cross-sectional area and length respectively and m is the mass of the 100 mK stage. The hold time t of the ADR at its operating temperature is $t = \Delta Q/P$, where ΔQ is the heat which the ADR can pump and P is the heat leak. Since ΔQ is proportional to the mass of the paramagnetic material and P is proportional to A/L, the hold time is independent of ADR size for a fixed resonance frequency [7].

During magnetization, heat must be extracted from the paramagnetic material. Several types of heat switches are possible: a superconducting heat switch [8], a gas gap heat switch [9] or a mechanical heat switch [10]. Superconducting heat switches are generally used only below 1 K, because of the relatively large parasitic heat leak at higher temperatures. The gas gap heat switch has also a finite heat leak in the 'off' state and a failure mode associated with gas leakage. We have had very good success with a mechanical switch. It has no parasitic heat leak in the 'off' state and is very reliable. Figure 2 shows the switch which was developed for SIRTf, but with modified jaws to allow simultaneous thermal contact between the reservoir and both stages. The SIRTf switch has passed a room temperature shake test, where it was subjected to the vibration spectrum expected during a rocket launch. It has also been cycled more than 9000 times while held continuously at $T = 4 \text{ K}$ without loss in thermal conductance. The switch is activated by passing current through the superconducting coil. The yoke is pulled into the magnet and forces the two jaws together thus clamping the two cold fingers extending from the ADR. The thermal conductance of the SIRTf switch at $T = 4 \text{ K}$ is approximately 15 mW/K at 100 mA of current.

Paramagnetic Materials

We propose to use gadolinium-gallium-garnet ($\text{Gd}_3\text{Ga}_5\text{O}_{12}$) in the guard stage. GGG is an attractive magnetic coolant in the liquid helium temperature range. It is nearly magnetically isotropic with $g \approx 2$ [11] and angular momentum $J=7/2$ and has a Gd ion density of $1.27 \times 10^{22} \text{ cm}^{-3}$. It orders magnetically near $T = 1 \text{ K}$ resulting in the large zero field heat capacity (shown in Figure 3), which makes GGG an effective thermal buffer at this temperature. GGG has a density of 7.1 g cm^{-3} and a thermal conductivity of $\approx 0.1 \text{ W/cm-K}$ at 4 K [12], comparable to that of OFHC copper. This facilitates the extraction of heat during magnetization. Thermal contact to GGG can easily be made by gluing copper strips to the crystal surface. Garnets have the additional advantage of being chemically and thermally stable. Rod shaped single crystals of GGG are commercially available.

The material of the second stage is hydrated paramagnetic salt chrome-cesium-alum (CCA), which has the chemical formula $\text{CsCr}(\text{SO}_4)_2 \cdot 12 \text{ H}_2\text{O}$. CCA has a density of 2.1 g cm^{-3} and is magnetically similar to chrome-potassium-alum (CPA) but dehydrates at higher temperatures. Thermal stability at elevated temperatures is important for satellite applications. Obtaining a thermal vacuum in the cryostat typically requires baking at temperatures approaching 30°C for periods of up to 2 weeks [13]. The magnetic ions Cr^{3+} ($J=3/2$, $g=2$) in this salt have a density of $2.1 \times 10^{21} \text{ cm}^{-3}$. The quadruplet is split by the crystal electric field into two doublets separated by an energy of 0.19 K [14] and the remaining degeneracy is lifted due to magnetic dipole-dipole interactions at temperatures near 20 mK . The thermal conductivity of CCA is much lower than of GGG. Good contact is made in the SIRTAF ADR by growing the crystals directly on a skeleton of gold wires from an aqueous solution.

Performance

We have calculated the hold time of the ADR shown in Figure 1 as a function of magnetic field and reservoir temperature with the results shown

in Figure 3. The weight and suspension parameters were adopted from the SIRTf ADR and are listed in Table 1. The complete CCA salt pill including 0.1 moles of CCA, gold wires, copper rod and stainless steel can weighs 100 g and an additional 100 g is estimated for the weight of the bolometer stage. The mass of the GGG stage is assumed to be dominated by the garnet and fixed at 200 g corresponding to 0.2 moles of GGG. The entropy reduction in GGG during magnetization was calculated from published data [11,15]. For CCA, the entropy was calculated using the Brillouin function for an ideal paramagnet plus the lattice entropy [16]. Following demagnetization to 100 mK, the residual field is of order 100 mT and the entropy data from [11] are used to calculate the GGG temperature. The heat leak into the GGG is the combination of the flow through its own suspension and through the thermal intercepts on the CCA suspension. The attachment point of the intercepts is fixed to be midway between the CCA pill and the bath which is close to optimum for maximum hold time. The warm-up rate of the GGG is calculated using the zero field heat capacity data from Figure 4, which is justified for the small residual field strength. The heat leak P into the 100 mK stage is determined by the GGG temperature. The hold time at $T = 100$ mK is given by $t = 0.1 \Delta S / P$, where $\Delta S = S(B=0T, T=0.1K) - S(B, T_{\text{reservoir}})$ is the available entropy of the CCA pill at 100 mK. In an actual refrigerator, ΔS will be further reduced by the entropy lost in cooling the various parts of the 100 mK stage. For the assumptions given above this will reduce the available entropy by 10-20 % for $B/T \approx 1$ T/K. The zero field entropy was taken from the entropy curve for CPA [17]. As can be seen in Figure 4, hold times of 24 hours or longer with reservoir temperatures around 4 K are achievable for a modest field of 4 Tesla. It would be possible to increase the hold time at 100 mK by increasing the mass of GGG. This will asymptotically approach the limiting case when the heat flow into the GGG is entirely through its own suspension. An increase of order 50 % in hold time would be achievable by increasing the amount of GGG by a factor of 3. A limited amount of cooling at ~ 1 K is available directly from the GGG. This can be used, if appropriate, to cool stressed (or unstressed) Ge:Ga photoconductors. Assuming $G=15$ mW/K from the SIRTf heat switch, the time constant for isothermal magnetization is

limited by the heat capacity of GGG to $C/G \approx 15$ min. The duty cycle of the ADR at 100 mK for these parameters can thus be more than 95 %.

Because of the large heat capacity of GGG and the small thermal conductance of the Kevlar suspension, the time constant will be more than 10 days. Therefore, the small temperature fluctuations in the high temperature reservoir associated with mechanical coolers are not critical to the performance of the ADR. The thermal loading from the ADR on the high temperature reservoir will be dominated by the magnet leads. This can be much reduced by use of superconducting wire up to some intermediate temperature stage. Nb_3Sn wire can be used to $T \approx 12$ K and it is hoped that the new $YBa_2Cu_3O_7$ materials will be used up to $T \approx 50$ K.

Conclusion

The two-stage ADR presented here will be useful for producing temperatures near 100 mK in several situations. Future space astronomy missions employing mechanical coolers can use it for cooling submillimeter or x-ray detectors. It will also be useful for cooling submillimeter direct detectors at mountain top observatories where mechanical refrigerators are used. Finally it would permit a balloon launch of detectors at 100 mK without the need for pumped liquid helium during the launch.

Acknowledgements

This work was supported by NASA grants NAGW-2121 and NAGW-2864, and by the Center for Particle Astrophysics through NSF cooperative agreement AST 9120005.

References

- [1] P.T. Timbie, G.M. Bernstein, and P.L. Richards, *Cryogenics* 30, 271 (1990).
- [2] C. Hagmann *et al* (to be published).

- [3] M.L. Fischer, D.C. Alsop, E.S. Cheng, A.C. Clapp, D.A. Cottingham, J.O. Gundersen, T.C. Koch, E. Kreysa, P.R. Meinhold, A.E. Lange, P.M. Lubin, P.L. Richards, and G.F. Smoot, *Ap.J.* **388**, 242 (1992); D.C. Alsop, E.S. Cheng, A.C. Clapp, D.A. Cottingham, M.L. Fischer, J.O. Gundersen, E. Kreysa, A.E. Lange, P.M. Lubin, P.R. Meinhold, P.L. Richards and G.F. Smoot, *ibid.* **395**, 317 (1992).
- [4] A. Serlemitsos, B. Warner, S. Castles, S. Breon, M. SanSebastian and T. Hait, *Adv. Cryog. Eng.* **35**, 1431 (1990); A. Serlemitsos, M. SanSebastian and E. Kunes, *ibid.*, **37**, 899 (1992) A. Serlemitsos, M. SanSebastian and E. Kunes, *Cryogenics*, **32**, 117 (1992).
- [5] K.W. Mess, J. Lubbers, L. Nielsen and W.J. Huiskamp, *Physica* **41**, 260 (1969).
- [6] O.E. Vilches and J.C. Wheatley, *Rev. Sci. Instrum.* **37**, 819 (1966).
- [7] R.D. Britt and P.L. Richards, *Intl. J. IR and Millimeter Waves* **2**, 1083 (1981).
- [8] V.P. Peshkov and A. Parshin, *Sov. Phys. JETP* **21**, 258 (1965).
- [9] J.P. Torre and G. Chanin, *Rev. Sci. Instrum.* **55**, 213 (1984).
- [10] J.D. Siegwarth, *Cryogenics* **16**, 73 (1976).
- [11] R.A. Fisher, G.E. Brodale, E.W. Hornung and W.F. Giauque, *J. Chem. Phys.*, **59**, 4652 (1973); E.W. Hornung, R.A. Fisher, G.E. Brodale and W.F. Giauque, *J. Chem. Phys.*, **61**, 282 (1974); G.E. Brodale, E.W. Hornung, R.A. Fisher and W.F. Giauque, *J. Chem. Phys.*, **62**, 4041 (1975).
- [12] G.A. Slack and D.W. Oliver, *Phys. Rev.* **B4**, 592 (1971); B. Daudin, R. Lagnier and B. Salce, *J. Magn. Magn. Mat.* **27**, 315 (1982).
- [13] S.M. Volz and M.G. Ryschkewitsch, *Superfluid Helium Heat Transfer Vol 134* (Eds. J.P. Kelly and W.J. Schneider), 23 (Seattle 1990).
- [14] B. Bleaney, *Proc. Roy. Soc.* **A204**, 203 (1950).
- [15] J.A. Barclay and W.A. Steyert, *Cryogenics* **22**, 73 (1982).
- [16] D.G. Kapadnis, *Physica* **22**, 159 (1956).
- [17] O.E. Vilches and J.C. Wheatley, *Phys. Rev.* **148**, 509 (1966).

Table 1: Mass and suspension parameter of the SIRTf ADR.

CCA amount	0.1 moles
mass of 100 mK stage	200 g
resonance frequency	200 Hz
Kevlar cross section	10^{-3} cm^2
total A/L of suspension	$5 \times 10^{-3} \text{ cm}$
suspension heat leak	$0.25 \text{ } \mu\text{W}$
reservoir temperature	1.6 K

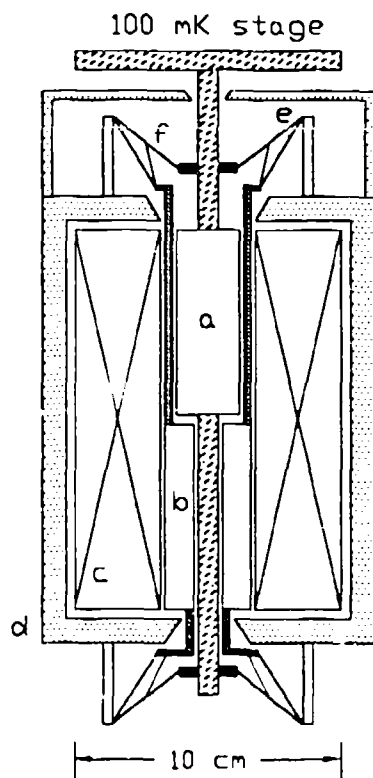


Fig. 1: Schematic diagram of 2-stage ADR with CCA salt pill (a), GGG crystal (b), superconducting magnet (c), magnetic shield (d), Kevlar suspension (e), and thermal intercepts (f).

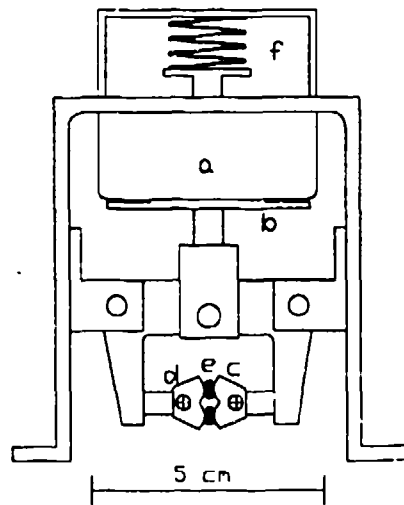


Fig.2: Mechanical heat switch with superconducting coil (a), ferromagnetic yoke (b), gold plated copper jaws (c), flex pivots (d), cold fingers (e) and restoring spring (f). The flex pivot corrects for small misalignments of the cold fingers extending from the two stages.

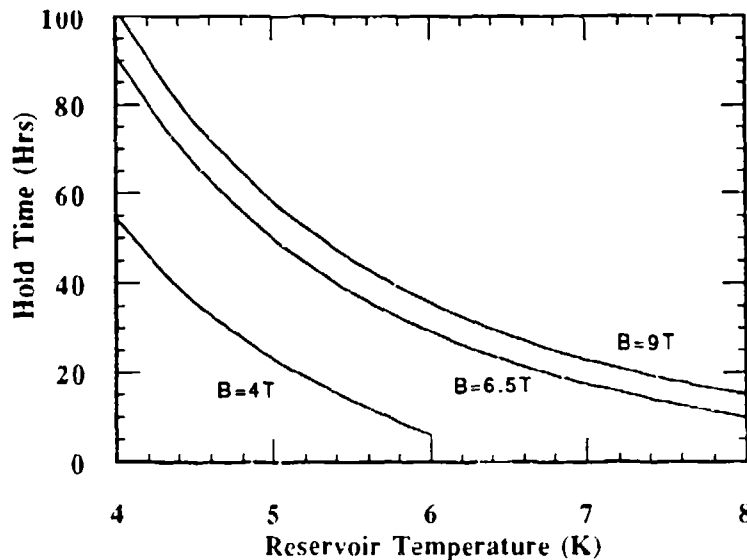


Fig.3: ADR hold time at $T=100$ mK as a function of magnetic field and reservoir temperature with 0.2 mole of GGG and 0.1 mole of CCA. The entropy lost in cooling the various components of the 100 mK stage is not included. The parasitic heat leak is assumed only due to the Kevlar suspensions. $A/L=0.005$ cm for both suspensions.

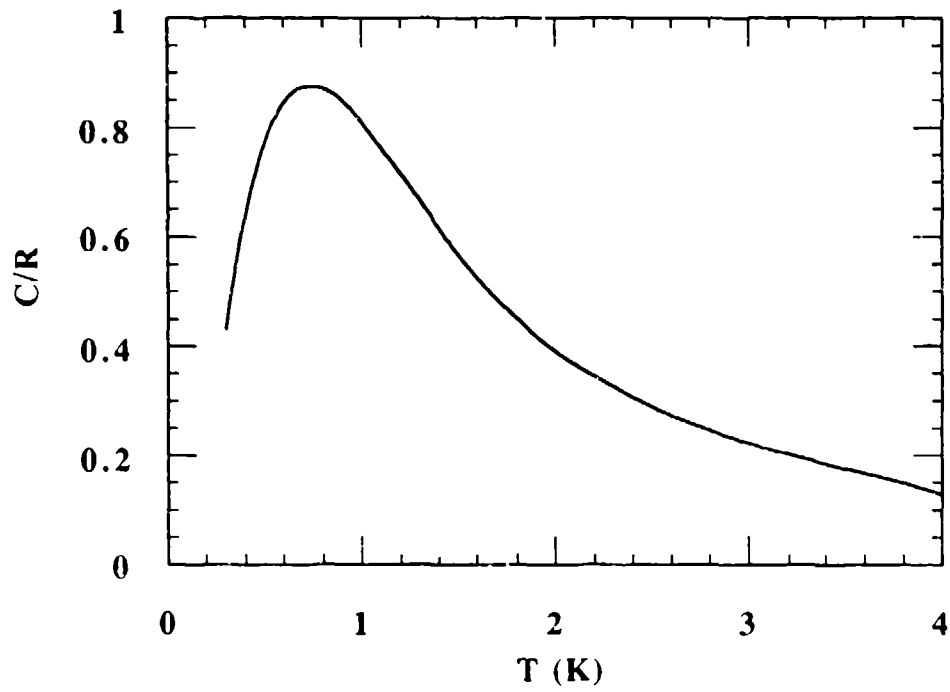


Fig.4: Specific heat of GGG per mole of Gd^{3+} in zero magnetic field. From [11].

Takasu Hashimoto, Tatsuji Eda, and Masanori Yabuki
Department of Applied Physics
Tokyo Institute of Technology
Oh-okayama, Meguro, Tokyo, Japan

Toru Kuriyama and Hideki Nakagome
Energy Science and Technology Laboratory
Toshiba Research and Development Center
Ukishima, Kawasaki, Japan

INTRODUCTION

Recently, application of the magnetic materials to the regenerator material in the small power regenerative refrigerators have attracted many cryocooler investigator's attentions, and several groups¹⁻¹⁷ in Japan have been able to reach to 3 K range and to obtain the refrigeration capacity of 0.5 Watt at 4.2 K using two stage GM refrigerator, in which the magnetic regenerator materials are applied.

Up to the present, in the most of commercial GM refrigerators Pb particles have been used as a regenerator material. However, the heat capacity of Pb decreases steeply below ~ 13 K in comparison with the He-gas and, as the result, Pb-particles can not play a role of a regenerator material in He temperature range. Therefore, as far as we use the Pb particles for regenerator, we can not reach 4.2 K using the GM refrigerator.

In this temperature range, only a peak of magnetic specific heat at the magnetic phase transition temperature T_m is comparable to the large specific heat of gaseous He. Therefore, the above groups³⁻¹⁷ have applied Er_3Ni particles for the regenerator and could reach below 4.2 K.

However, in the Er_3Ni compound, the peak of the magnetic

PL-CP--93-1001

specific heat at T_1 is not so large as shown in Fig. 1, because Er_3Ni has the large schottky specific heat at this temperature range. Therefore, as far as we use Er_3Ni , we will not be able to get so large refrigeration capacity more than ~ 500 mW.

Previously, as the magnetic regenerator to get the large refrigeration capacity, we proposed the layer structural regenerator^{1, 2}. The purpose in the present paper is to verify the above proposal. As the first step of this verification, we will compare the facility of the two kinds regenerators; One is the regenerator whose material is only Er_3Ni particle. Another is two layered regenerator whose regenerator materials are Er_3Ni (high temperature side) and $\text{Er}_{0.5}\text{Yb}_{0.5}\text{Ni}$ (low temperature side). The latter is the special model of the layer structural regenerator.

On the basis of the above results, we discuss again the developing way of the magnetic regenerator in future.

EXPERIMENTS AND RESULTS

In the present investigation we compared the refrigeration characteristy of three kinds of regenerators in which three kinds of regenerator materials, Pb, Er_3Ni and $\text{Er}_{0.5}\text{Yb}_{0.5}\text{Ni} + \text{Er}_3\text{Ni}$ are used, respectively. Specific heats of those materials are shown in Fig. 1. Up to the present, Pb has been used as regenerator material. Recently Er_3Ni is popularly used as the magnetic regenerator material and, however, refrigeration capacity is very small (300mW) at 4.2 K as far as using Er_3Ni . The reason for the small power suppose that specific heat of Er_3Ni below ~ 10 K is very small. Presently, we have found new magnetic material $\text{Er}_{0.5}\text{Yb}_{0.5}\text{Ni}$ ³ which has a large peak of specific heat at ~ 8 K. Therefore, in this chapter we compare the regenerative characters of Er_3Ni and $\text{Er}_{0.5}\text{Yb}_{0.5}\text{Ni} + \text{Er}_3\text{Ni}$.

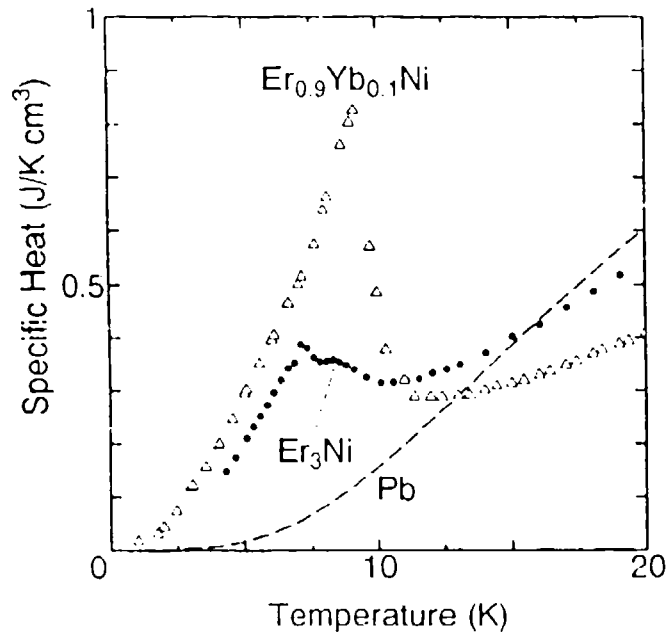


Figure 1 The specific heat of the several materials, $Er_{0.9}Yb_{0.1}Ni$, Er_3Ni and Pb , used as the regenerator materials in the present experiment.

(i) Computer simulation

The first experiment is computer simulation, and we estimate regenerator efficiencies of the three types of regenerators. In the numerical method, we used the following equations as a governing equations. These equations are come from the energy conservation law and equation of continuity.

$$\frac{\partial H_g}{\partial x} = \frac{hA_w L}{m} (T_s - T_g) \tag{1}$$

$$\frac{\partial H_s}{\partial t} = \frac{hA_w L \tau}{M_s} (T_g - T_s) \tag{2}$$

- T_g : temperature of gas
- T_s : temperature of regenerator matrix
- H_g : enthalpy of gas
- H_s : enthalpy of matrix

PL-CP--93-1001

- A_w : heat transfer area per unit length
- M_r : mass of regenerator matrix
- L : regenerator length
- m : mass flow rate of the gas
- τ : heat cycle period
- t : reduced time (t/τ)
- x : reduced length of the regenerator (x/L)

The regenerator efficiency is defined as enthalpy efficiency (η) as follows.

$$\eta = \frac{\Delta H_{\text{real}}}{\Delta H_{\text{ideal}}} \quad (3)$$

In the simulation we assumed the following three kinds of regenerators: The regenerator A is filled with only Pb particles. The B type regenerator is used only Er_3Ni particles and the C type regenerator is constructed to layered-type (Er_3Ni 50% (hot side) and $\text{Er}_{0.5}\text{Yb}_{0.5}\text{Ni}$ 50% (cold side)). The computer simulation result of the regenerator efficiencies in those three kinds of regenerator are shown in Fig. 2 (B). The layered-type regenerator (C type) has a higher regenerator efficiency at blow 10 K than the B type regenerator, used only Er_3Ni particle, as shown in Fig. 2 (C).

Table 1 The kind and weights of the regenerator materials in the three kind of experiments (I, II and III).

Experiment	Regenerator	Regenerator Material	Weight	Volume
I	A	Pb	644g	100%
II	B	Er_3Ni	542g	100%
III	C	Er_3Ni (high temp.)	256g	50%
		$\text{Er}_{0.5}\text{Yb}_{0.5}\text{Ni}$ (low temp.)	257g	50%

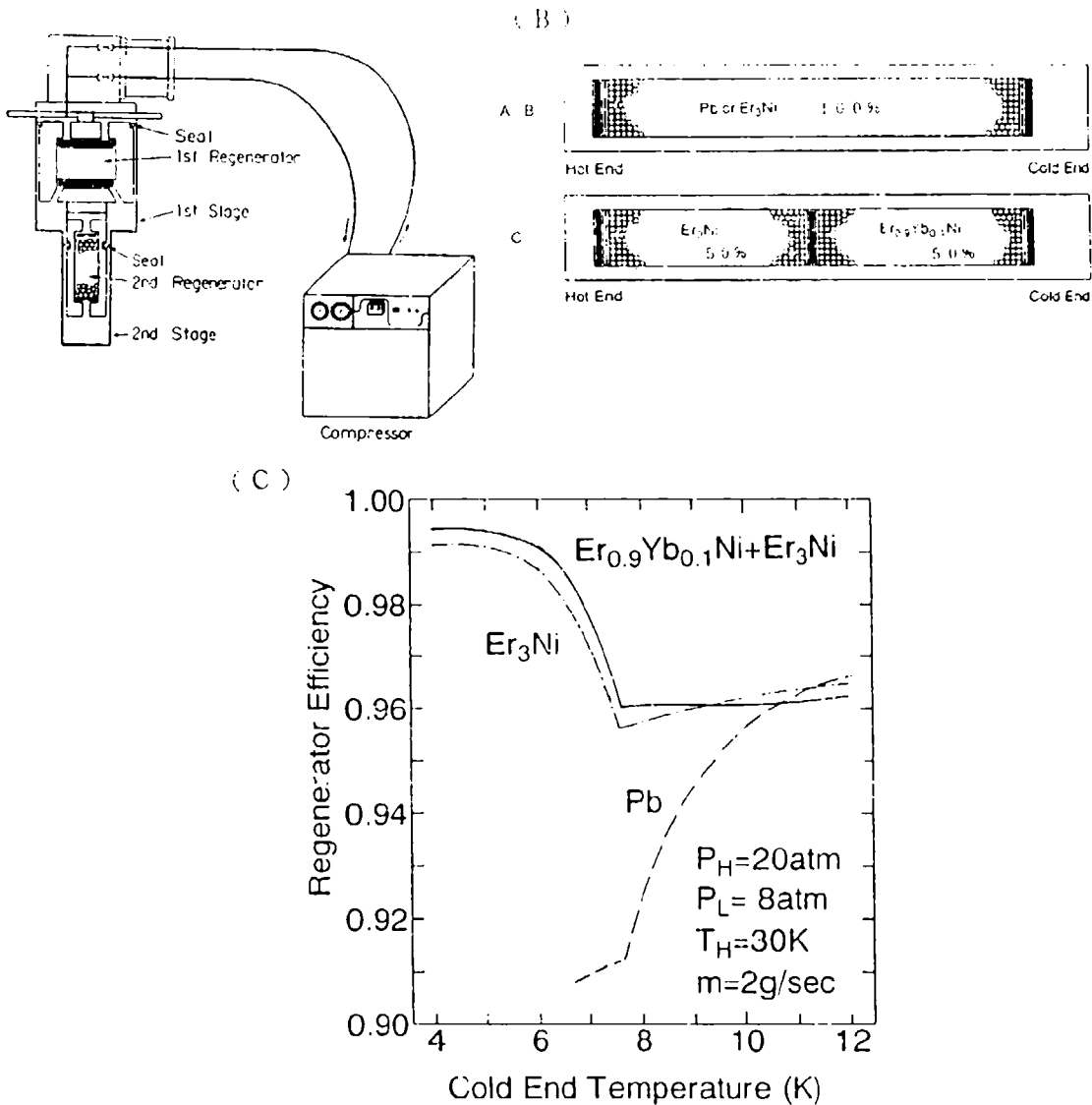


Figure 2 (A) Schematic figure of the first (high temperature side) and the second (low temperature side) regenerator in the GM (Gifford-McMahon) refrigerator.

(B) The usual type regenerator in which only the Pb (regenerator A) or the Er₃Ni particles (regenerator B) are housed.

The structure of the magnetic regenerator material in the regenerator C.

(C) Refrigeration efficiencies vs. cold end temperature in the regenerator A, B and C.

The refrigeration capacity against the refrigeration temperature is shown in Fig. 3, and we can find that the layered type (C type) regenerator has the largest refrigeration capacity.

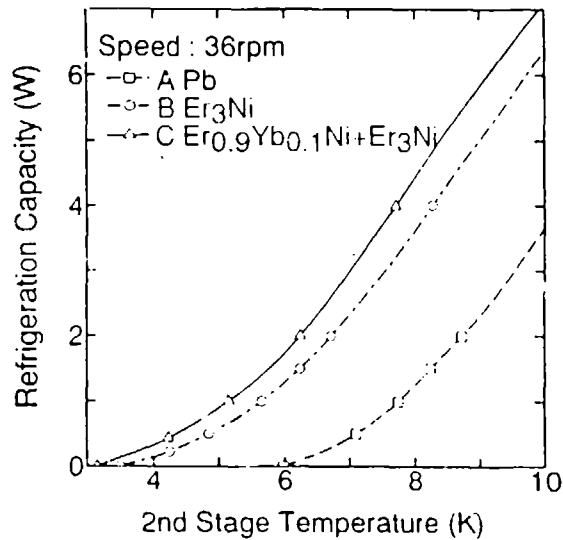


Figure 3 Refrigeration capacities vs. 2nd stage temperature in the regenerator A, B and C.

(ii) Experimental results

In order to confirm the results obtained from the computer simulation, we performed the experimental investigation of the refrigeration capacity. In the experiment, we have also used three kinds of regenerators similar to the models in the computer simulation.

In Fig. 4 the refrigeration capacity at 4.2 K are shown as the function of 1st stage temperature, and it is made clear that the layered type (C type) regenerator has a larger refrigeration capacity than that of the only Er₃Ni case (B type). The temperature span of the refrigeration cycle in the C-type (layered-type) regenerator is larger than that in the B-type similarly to the case of the refrigeration capacity.

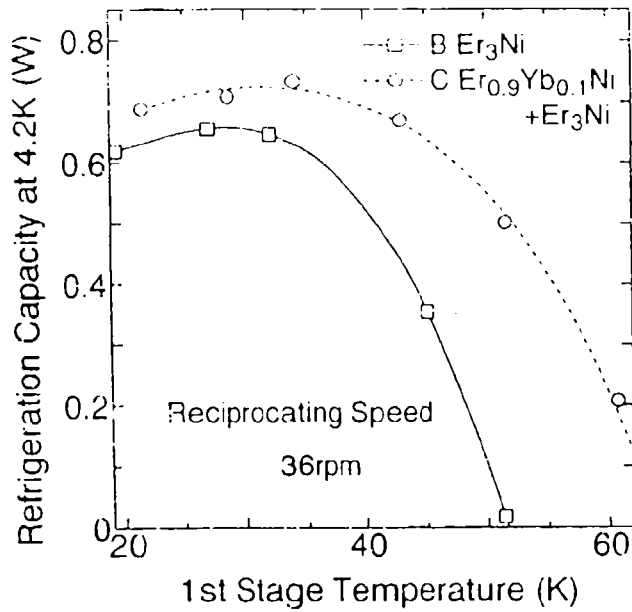


Figure 4 Refrigeration capacity of the regenerator B(Er₃Ni only) and C(layered type) as the function of 1st stage temperature.

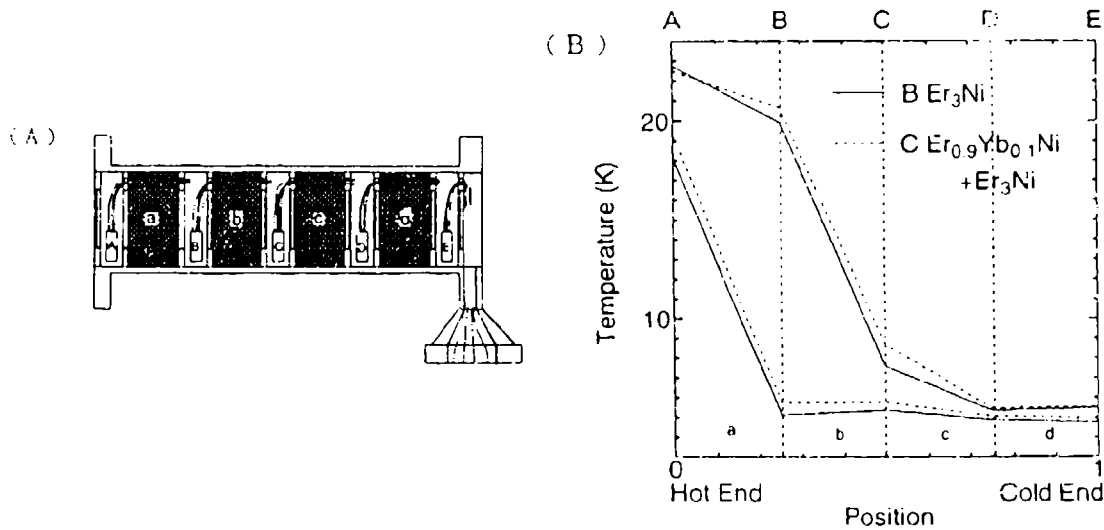


Figure 5 The temperature gradient measurement in the regenerator.
 (A) Schematic figure of the regenerator structure in the present experiments.
 (B) The experimental results of temperature gradient in the regenerator B(full line) and C (the dotted line).

In order to obtain the information for improvement of refrigeration capacity, we measured the inside temperature distribution in the regenerator shown in Fig.5(A). However, the experimental results of temperature gradient in the regenerator were obtained as shows in Fig.5(B), and we could not find conspicuous change between the Er_3Ni only and $Er_{0.9}Yb_{0.1}Ni + Er_3Ni$ case. Therefore, from this experiment we can not get any information for the improvement of the characteristics in the magnetic regenerator.

CONCLUSION

From the experimental results it has been made clear that the GM refrigerator equipped with the two-layered magnetic regenerator has the superior refrigeration capacities in comparison with that with the regenerator including in only one magnetic material, such as Er_3Ni . From comparison between the specific heats of those materials in the low temperature range, it may be concluded that the refrigeration character depends largely on the specific heat of regenerator materials in He temperature range. However, at present, the precise regenerative mechanism of the magnetic regenerator, such as the correlation between the regenerative characteristics and specific heat of regenerator materials, the correlation between the temperature gradient in the regenerator and the specific heat of the magnetic materials etc., has not been made clear qualitatively.

REFERENCES

1. T.Hashimoto, "Magnetic refrigeration and application of magnetic material to Cryogenics (in Japanese)", 1987, Kogyo-chosakai, Tokyo.
2. T.Hashimoto et al., Proc. of Intrn. Cryog. Matr. Conf. (ICMC), Vol.2, p.p.667, 1988, Shenyang (China).
T.Hashimoto, Proc. of Intrn. Conf. Cryog. Refri.,

- (1) Tokyo Institute of Technology and Toshiba Research and Development Center.
3. R. Li et al., Proc. Intern. Cryo Engr. Conf. (ICMC 12), P. P. 423, 1988. Buterworth.
 4. R. Li et al., Advances in Cryogenics Engineering 35, 1990, 1183.
 5. T. Kuriyama et al., Advances in Cryogenics Engineering 35, 1990, 1261.
 6. M. Sahashi et al., Advances in Cryogenics Engineering 35, 1990, 1175.
 7. R. Li, M. Ogawa and T. Hashimoto, Cryogenics 30, 1990, 521.
 8. T. Hashimoto et al., Cryogenics 30, 1990, 192.
 9. T. Kuriyama et al., Proc. Intrn. Cryocooler Conf., Vol. II, p. p. 3, 1990.
 10. H. Nakagome et al., Proc. Intrn. Cryocooler Conf., Vol. II, p. p. 15, 1990.
 11. M. Ogawa, R. Li, T. Hashimoto, Cryogenics 31, 1991, 405.
 12. H. Seshake et al., Advances in Cryogenics Engineering 37B, 1992, 995.
- (2) Mitubishi Electric Co.
13. H. Yoshimura et al., Rev. Sci. Intstr. 60, 1989, 3533.
 14. T. Inaguchi et al., Proc. Intrn. Cryocooler Conf., Vol. II, p. p. 25, 1990.
 15. M. Nagac et al., Advances in Cryogenics Engineering 35, 1990, 1251.
 16. T. Inaguchi et al., Advances in Cryogenics Engineering 35, 1990, 1271.
- (3) Tokyo Institute of Technology and Sumitomo Heavy Industrials.
17. T. Hashimoto et al., Advances in Cryogenics Engineering 37, 1992, 859.

THE EFFECTS OF A LAYERED BED ON ACTIVE
MAGNETIC REGENERATOR PERFORMANCE

S.R. Schuricht, A.J. DeGregoria, and C.B. Zimm
Astronautics Corporation of America
Astronautics Technology Center
Madison Wisconsin

Abstract

The effects of using multiple materials in an Active Magnetic Regenerator (AMR) to increase the operating temperature span are described. A model is described which will accept any number of materials in varying proportions. The results presented here are for a two material AMR bed, using material data obtained in house. For a fixed hot end temperature there is a large decrease in net cooling power when the low temperature of an AMR cycle is decreased. This is due to the magnetic material behavior deviating from that of an ideal magnetic material. The purpose of layering the bed is to minimize this effect and allow a single bed to operate over a greater temperature span. This could allow a single bed to replace a multiple stage device thereby reducing capital and operating costs. This paper compares the performance of a $GdNi_2$ bed with a layered bed, consisting of $GdNi_2$ and an erbium alloy operating between 30-77K and 25-77K. The results show that the layered bed will have a 5.6% increase in cooling power and a 7.8% increase in efficiency over the $GdNi_2$ bed for the 30-77K span and a 27% increase in cooling power and 34% increase in efficiency over the $GdNi_2$ bed for the 25-77K span.

Introduction

Based on the facts that an ideal magnetic material has a linear adiabatic temperature curve¹ and that an element of magnetic material in an AMR only operates over a narrow temperature span² the motivation of layering several materials together is to approach a linear temperature profile across the bed. The layering method is chosen because it is easier, less time consuming and potentially more effective than trying to alloy several materials together to produce a material with ideal behavior over the entire temperature range of interest.

Conventional single-material AMR beds work best when the hot temperature is close to the Curie temperature for the material. When the cold temperature is decreased conventional AMRs experience decreases in cooling power and efficiency. This is due to larger conduction losses, the lower adiabatic temperature change of the magnetic material, and deviations from ideal behavior of the material. As the cold temperature is decreased below 40 K, GdNi₂ shows substantial deviation from ideal behavior.

A layered bed can be employed to advantage in several ways. If the temperature span is to remain fixed then a layered bed will, with the right choice of materials, yield a higher cooling power and efficiency over a conventional bed. If the temperature span is changed by lowering the cold temperature, then a layered bed will help minimize the losses of the conventional AMR, though there will still be some reduction in performance. The final advantage is that a layered bed spanning a large temperature span might be able to replace two conventional beds operating over smaller temperature spans. This would result in a simpler and less expensive device.

Model

The computer program used for this study is based on the steady state program developed by DeGregoria² with modifications made to allow for the handling of multiple materials. The program will accept any number of materials in any proportions. This paper considers a two material layered bed with a fixed hot temperature and a varying cold temperature.

The bed model used is shown in figure 1. The AMR bed is filled with two materials, each in different proportions. In the current case a proprietary erbium alloy is material 1 and GdNi₂ is³ material 2. The material percentages are expressed by volume percent but the constant cross sectional area of the bed allows interpretation as percent of bed length. The adiabatic temperature profiles for the erbium alloy and GdNi₂ are shown in figure 2. From the profiles it is evident that the optimum material percentages will occur when the material interface is near the Curie point of the lower material, near 40K.

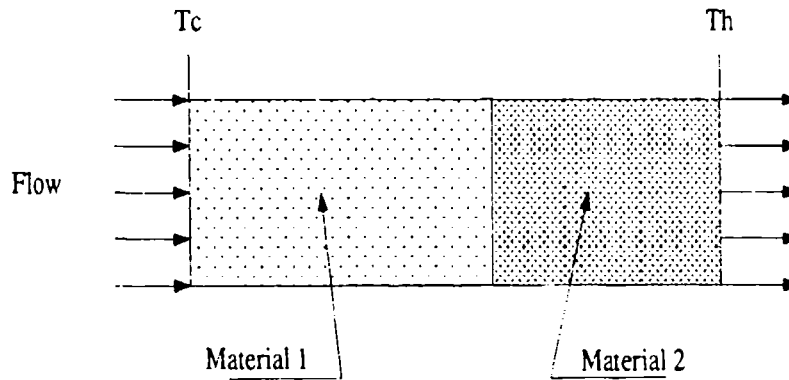


Figure 1. Model of a two material AMR bed

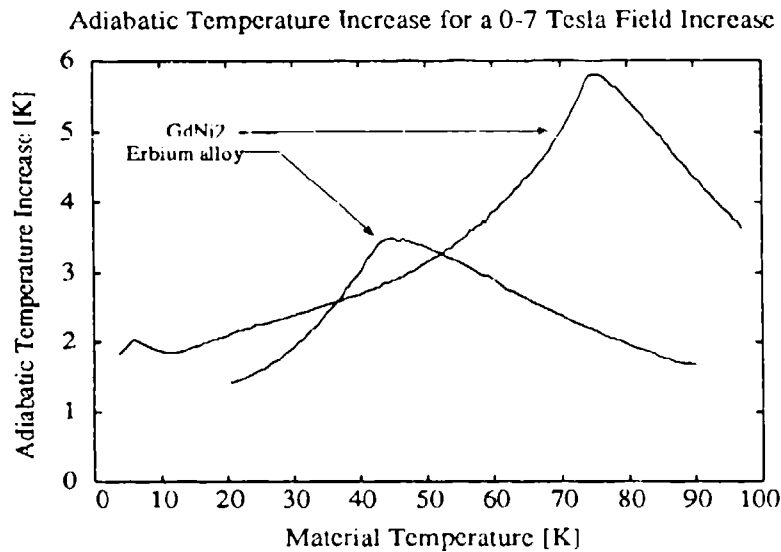


Figure 2. Adiabatic Temperature change for an erbium alloy and GdNi₂

Results

Figures 3 and 4 show the computed performance and bed temperature profiles for the steady state simulation. In this paper the helium gas flows are 37 g/s for the hot and cold periods, at an average pressure of 20 atm. The bed length is 5 cm and the cross section is 75 cm². The particle size is 0.015 cm and the field change is 7 T.

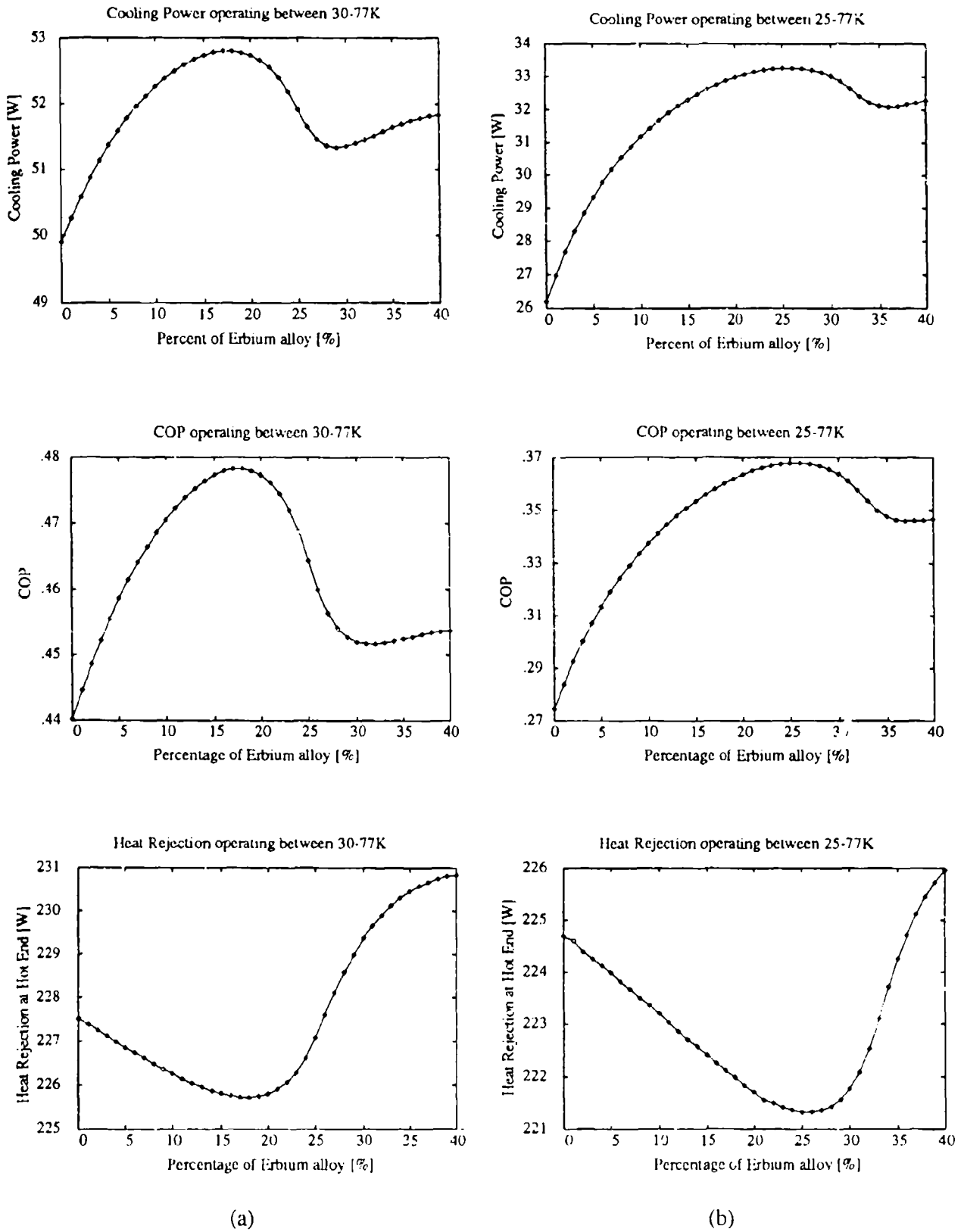


Figure 3. Performance plots of cooling power, efficiency and heat rejection for a (a) 30-77K temperature span and (b) 25-77K temperature span.

Figure 3 shows the performance results for a 30-77K temperature span and a 25-77K temperature span using a layered bed of the erbium alloy and GdNi_2 . The x-axis is the percentage of the erbium alloy in the bed starting at the cold end. The case of a conventional bed with one material (GdNi_2) corresponds to 0% of the erbium alloy. The COP is actually the bed efficiency, operating as a refrigerator, compared to the Carnot efficiency for the temperature span of interest.

Figure 3a shows the improvements in cooling power, efficiency and heat rejection for a temperature span of 30-77K. The optimum amounts of the materials is 18% erbium alloy and 82% GdNi_2 . This results in a 5.8% increase in cooling power and a 8.7% increase in efficiency over a single material AMR bed. The magnitude of the heat rejection decrease is negligible but the trend is as expected.

Figure 3b shows the results for a temperature span of 25-77K. The optimum amounts of the materials is 26% erbium alloy and 74% GdNi_2 . This results in a 27% increase in cooling power and a 34% increase in efficiency over a single material AMR bed. Again, the magnitude of the heat rejection decrease is negligible.

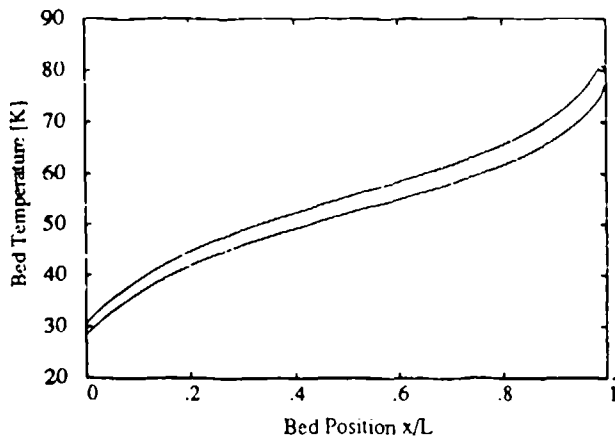
Figure 4 shows the temperature profiles across the AMR for the two temperature spans. From previous observations, as a magnetic material deviates from ideal behavior the bed temperature profiles change from linear to a concave downward profile. Therefore, the extent of downward curvature in the temperature profiles can be used as an indication to how close a material is to being ideal.

Figure 4a shows the bed temperature profiles for the 30-77K span for a conventional bed and a layered bed. For the single material bed (GdNi_2) the profile exhibits downward curvature near the cold end of the bed. The middle portion of the profile is linear with some upward curvature at the hot end due to the Curie point of GdNi_2 at 75K. The layered bed consists of 18% erbium alloy and 82% GdNi_2 . The addition of the erbium alloy at the cold end eliminates most of the downward curvature and the overall profile is approaching an ideal profile.

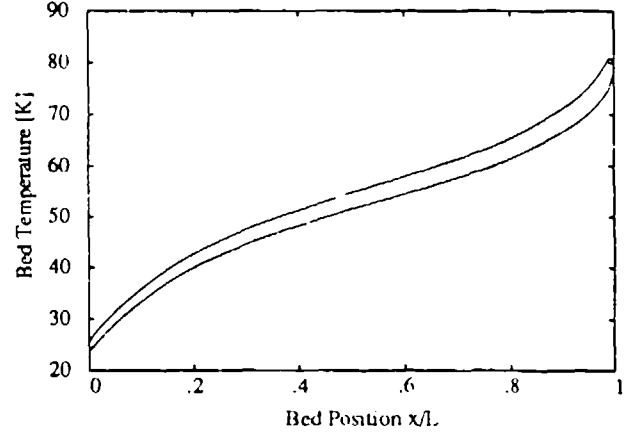
Figure 4b shows the bed temperature profile for the 25-77K span. For the 100% GdNi_2 bed the downward curvature is more pronounced at the cold end due to the deviation of GdNi_2 from ideal behavior. The adiabatic temperature profile for GdNi_2 becomes flat at lower temperatures. The layered bed consists of 26% of the erbium alloy and 74% GdNi_2 . The effect of the erbium alloy is the production of a more linear profile through the bed, which is responsible for the large increases in cooling power and efficiency.

Another feature to notice in figure 4 is the temperature at the material interface. In figure 4a the interface is at $x/L = 0.18$. The bed temperature here is near 40K, close to the Curie point of the erbium alloy. In figure 4b the interface is at $x/L = 0.26$. The bed temperature for this case is also near 40K. This confirms the expectations mentioned earlier.

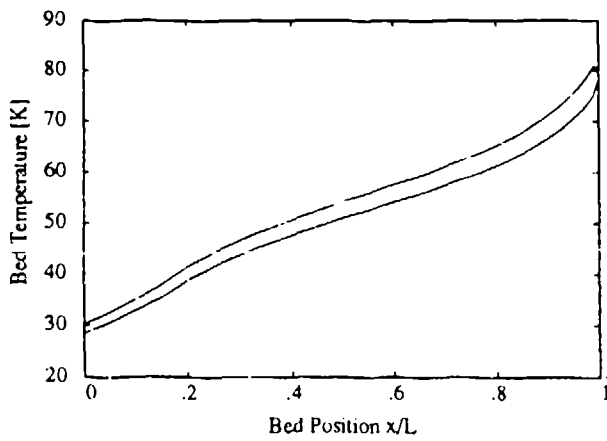
Bed Temperature Profiles for 100% GdNi₂ operating between 30-77K



Bed Temperature Profiles for 100% GdNi₂ operating between 25-77K

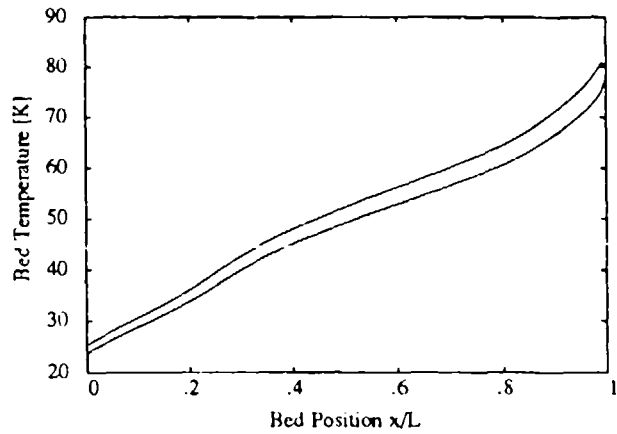


Profiles for 18% Erbium alloy, 82% GdNi₂ operating between 30-77K



(a)

Profiles for 26 % Erbium alloy, 82 % GdNi₂ operating between 25-77K



(b)

Figure 4. AMR temperature profiles for (a) 30-77K and (b) 25-77K temperature spans

Conclusion

One tentative conclusion that is drawn from figure 2 is that the adiabatic temperature changes for the materials in a layered bed should also follow ideal behavior (a straight line). This agrees with the data obtained from previous cases. If the adiabatic temperature increases at the Curie points for the two materials are too close in magnitude then the bed has very large temperature gradients appearing upon magnetization and demagnetization. This leads to excessive entropy generation from the conduction heat transfer in the bed and the AMR performance deteriorates.

Overall, the results look very promising. Layering the bed is a very simple procedure and the possible improvements in performance are worth further investigation. As mentioned before, these results are from a steady state model. A time dependent program is currently being modified to model a layered bed. The performance improvements will have a smaller magnitude due to the time constraint on the heat transfer but we still expect them to be significant. The next step should be to conduct experiments on an AMR with a layered bed.

References

1. C.R. Cross, J.A. Barclay, A.J. DeGregoria, S. R. Jaeger and J. W. Johnson, Adv. Cryogenic Eng. 33, p. 767 (1988)
2. A. J. DeGregoria, Adv. Cryogenic Eng. 37B, p. 867 (1992)
3. C. B. Zimm, E. M. Ludeman, M. C. Severson and T.A. Henning, Adv. Cryogenic Eng. 37B, p. 883 (1992)

LONG LIFE STIRLING CYCLE COOLER DEVELOPMENTS
FOR THE SPACE APPLICATION RANGE OF 20K TO 80K

B G Jones and R C Peddle
Cryogenic Cooler Group (FPC 740)
British Aerospace
PO Box 5
Filton
Bristol, BS12 7QW

1. INTRODUCTION

This paper features two Stirling cycle cooler developments at British Aerospace Space Systems (BAe), consisting of a single stage Stirling cycle cooler for the range 50K to 80K and a two stage Stirling cycle cooler for the range 20K to 50K. These coolers are based upon the well proven technology of the Oxford 80K coolers developed for ISAMS. This original development was carried out by Oxford University (OU) and Rutherford Appleton Laboratory (RAL), and later made available for commercial applications in the form of the BAe 80K cooler. The BAe 80K 800 mwatt cooler resulted from a BAe contract from the European Space Agency (ESA) to industrialise the ISAMS coolers, thus ensuring its future availability from industry.

The single stage cooler (50K-80K) is a further development of BAe's 80K cooler, for increased heat lift at lower temperatures and improved operating efficiency. A proof of concept cooler was manufactured and tested under a contract with LORAL of the USA, followed by a development model cooler built and tested under an ESA contract. The results of these activities are reported herein.

The two stage (20K-50K) cooler development has been completed under an ESA contract. BAe reviewed the original RAL design and generated a suite of manufacturing documentation for industrial manufacture. A pre-qualification testing programme has been completed and is reported herein.

Keywords: cooler, cryogenic, Stirling, space.

2. BACKGROUND

The Stirling cycle coolers described in this paper originate from the 80K cooler developed by Oxford University (OU) and Rutherford Appleton Laboratory (RAL), for use on the Improved Stratospheric and Mesospheric Sounder (ISAMS). (Ref. 1). ISAMS is part of the Upper Atmosphere Research Satellite (UARS) which was successfully launched into space during September 1991. The ISAMS coolers have continued to operate to specification, despite occasional switch-offs due to other instrument related problems.

This ISAMS 80K cooler was commercialised during 1986/87 at British Aerospace (BAe) under a European Space Agency (ESA) contract and a Development model cooler built and tested. Under a later contract (1989/91) from ESA, BAe manufactured an Engineering Model 80K cooler which successfully completed a pre-qualification test programme (ref. 2) in 1991. During this period BAe also manufactured two batches of six 800 mwatt 80K coolers which have been sold to customers in Japan, Canada, USA and Europe for evaluation purposes. One of these customers was the Jet Propulsion Laboratory in Pasadena who have completed and reported an extensive evaluation (ref. 3). During 1992 a third batch of six 80K coolers were manufactured at BAe, consolidating the design (Oxford Heritage), upon which these developments are based. Additionally a number of 80K coolers at OU, ESA, BAe and TRW have been undergoing long term life testing, (ref. 4).

The 50-80K single stage Stirling cooler development described is a direct derivative of the BAe 80K cooler. This has been developed during two separate contracts. The first in 1991 for LORAL (USA) for the Atmospheric Infrared Sounder (AIRS) resulted in a proof of concept 50-80K cooler capable of a heat lift of 750 mwatt at 55K being developed. The results of this programme are described in section 3, 'Proof of concept 50-80K cooler'. The second contract in 1991/92 from ESA resulted in the manufacture at BAe of a Development model cooler capable of significantly more heat lift than the earlier concept unit. The results of this programme are described in section 4, 'Development Model 50-80K cooler'.

The two stage 20-50K Stirling cycle cooler described is the continuation of a development started at RAL in the mid-1980's. RAL recognised the need for even lower temperatures, and based upon their involvement in the 80K ISAMS cooler development took this technology further. A prototype proof of concept cooler was built and tested at RAL during 1986, (Ref. 5), followed by a DM 20K cooler being manufactured and tested at RAL under an ESA contract in 1988. During 1990, ESA awarded a contract to BAe to commercialise this 20-50K cooler, to carry out a detailed review of design, and then to manufacture an Engineering Model (EM) and test it to Pre-qualification levels. It is the results of this test programme com-

pleted early in 1992 that is reported here in section 5, 'Engineering Model 20-50K two stage cooler'.

Figure 1 shows the development heritage of both the coolers described in this paper, it summarises the brief history given above.

Figure 2 shows a schematic representation of the single stage cooler, applicable to 80K or 50-80K types, whilst figure 3 shows a schematic of the two stage 20-50K cooler.

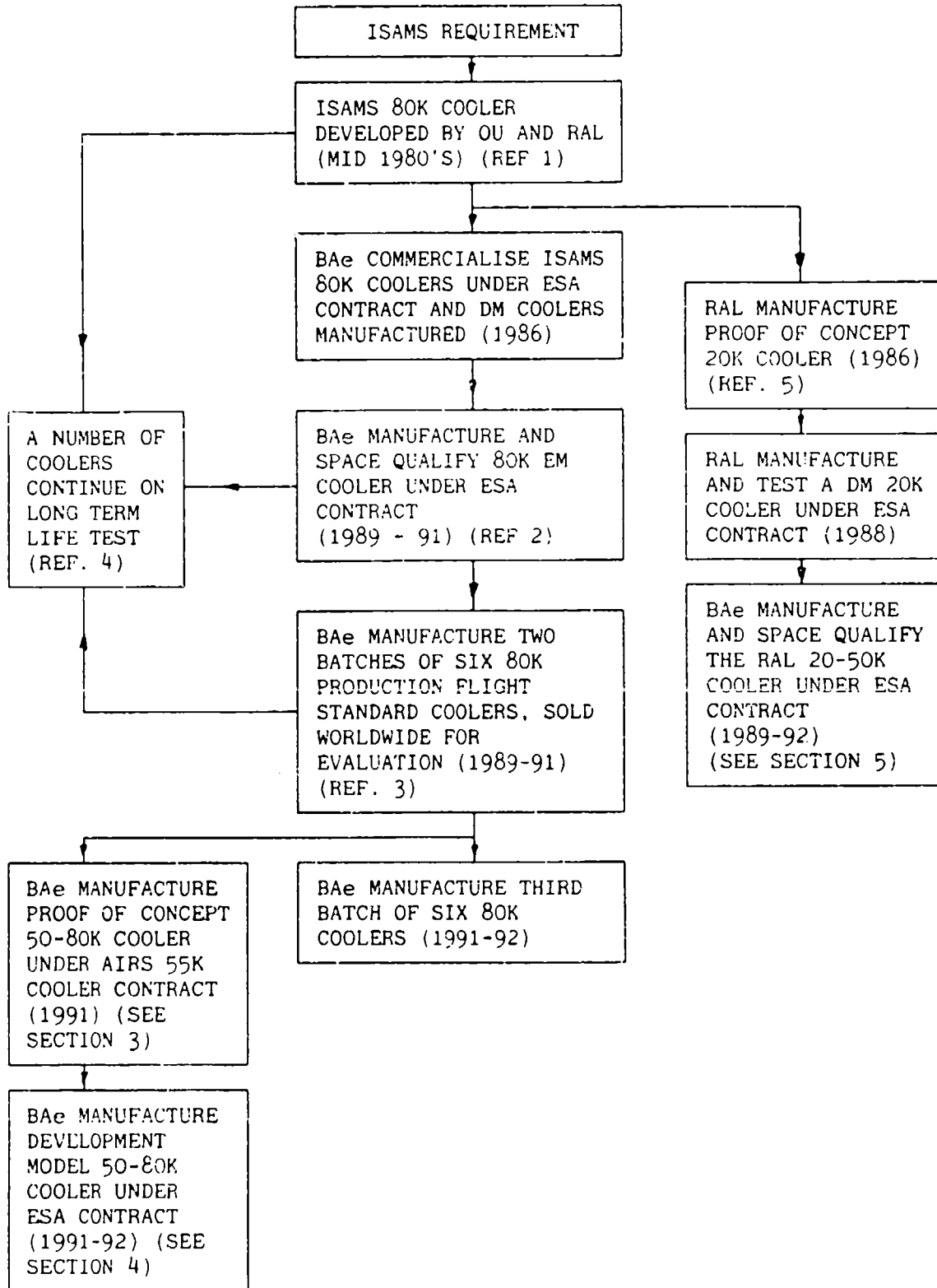


FIGURE 1 - BAe COOLERS DEVELOPMENT FAMILY TREE

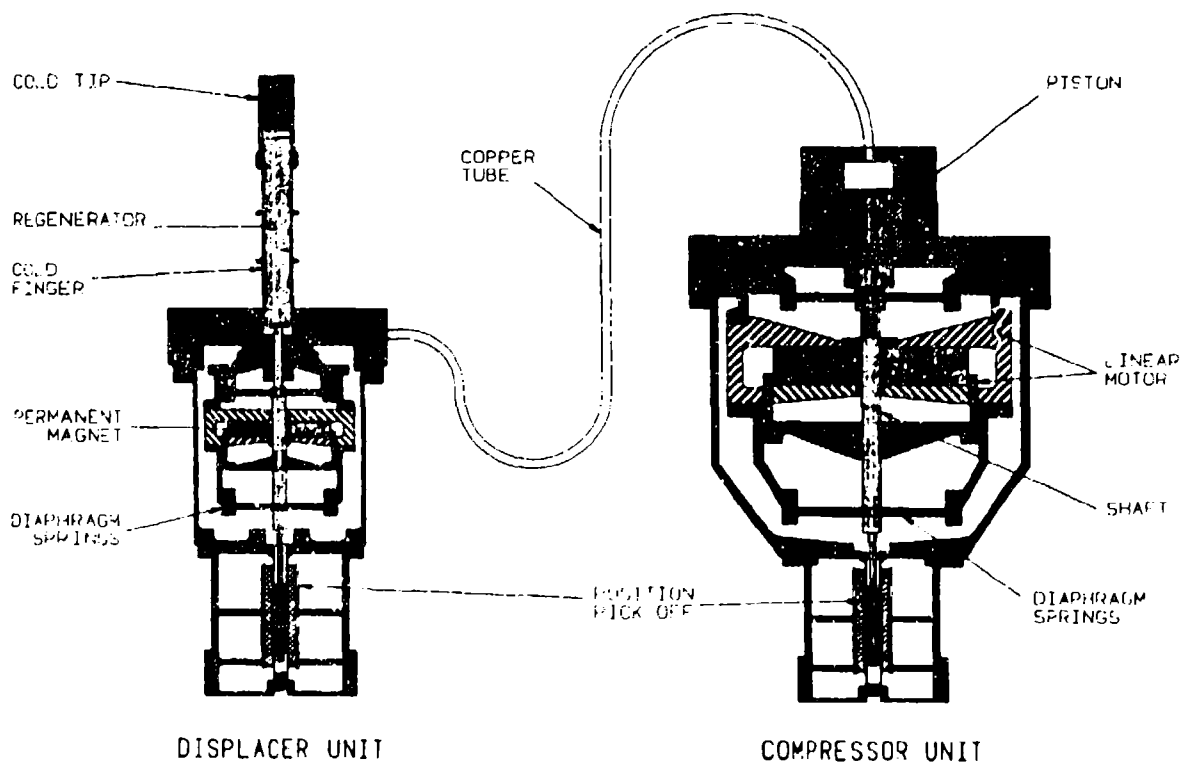


FIGURE 2 - SCHEMATIC REPRESENTATION OF THE 50-80K SINGLE STIRLING CYCLE COOLER

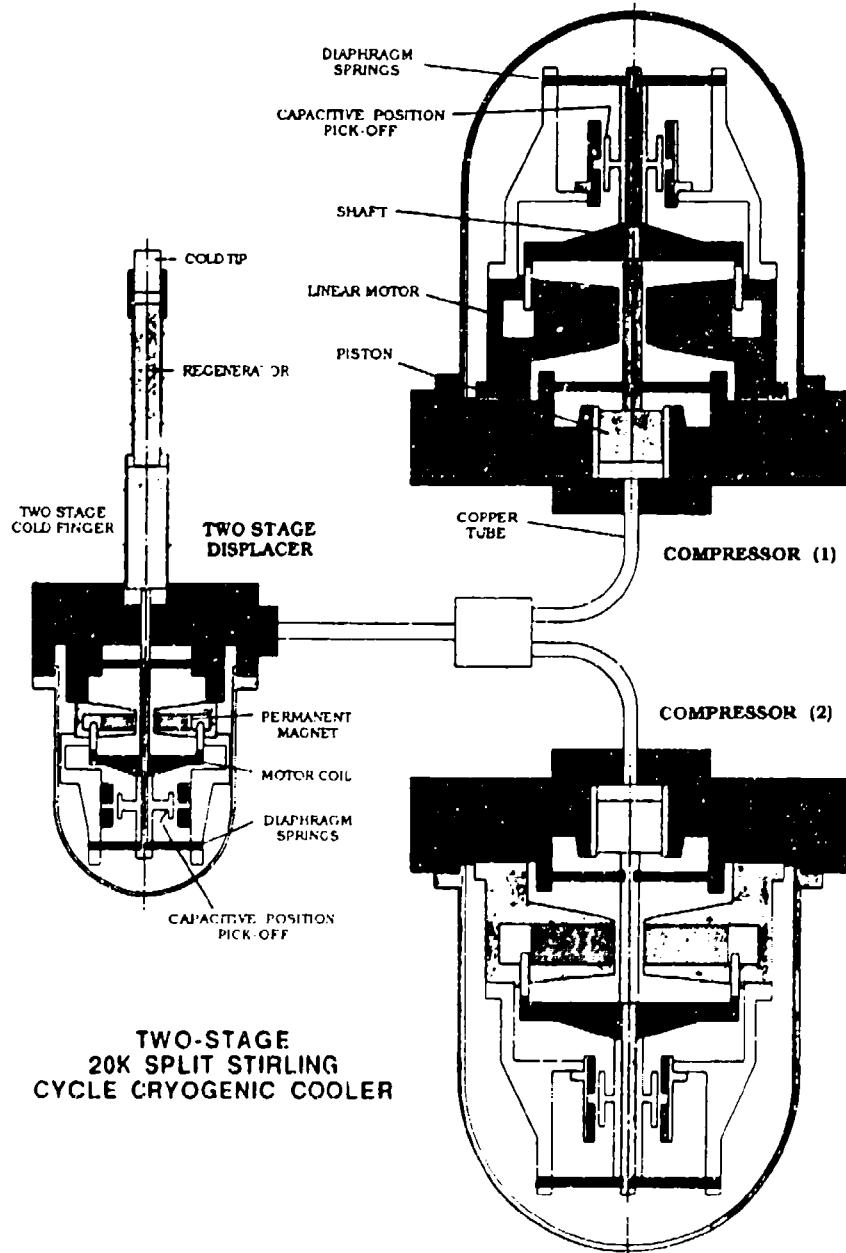


FIGURE 3 - SCHEMATIC REPRESENTATION OF THE 20-50K TWO STAGE STIRLING CYCLE COOLER

3. PROOF OF CONCEPT 50-80K COOLER

A proof of concept development was completed during 1991. This specifically required 750 mwatt of heat lift at 55K, thus demonstrating that a back to back dual cooler unit could achieve low induced vibration and a combined heat lift of 1500 mwatt.

The activity was funded under a contract from Loral Infrared and Imaging Systems, supported also by BAe funding, with the intention of providing a proof of concept for a cooler to meet the Advanced Infrared Sounder (AIRS) instrument primary requirements.

The basic design is adequately described by the schematic shown in figure 2. During the initial stages of the development RAL under contract to BAe undertook an extensive thermodynamic and thermal losses modelling exercise to identify the optimum cooler geometry. This resulted in only minor changes to the existing 80K cooler design, including, changes to the cold finger geometry both to reduce losses and to increase heat lift, interconnecting pipework, compressor capacity increased by using a bigger diameter piston, and a new compressor drive motor design. The Oxford heritage was retained in all the major features, to the extent that a practised eye is necessary to differentiate between the new 50-80K cooler and the existing flight qualified 80K cooler design.

Two displacer cold finger sizes were manufactured during this programme. One at 9mm diameter and 15mm longer than the existing 80K type, and another at 10mm diameter, that is the same size as the existing 80K cooler. Figure 4 shows a photograph of the completed cooler, note the valve that is still connected to the displacer, allowing the fill pressure to be varied during bench testing.

Bench testing with both types of displacers confirmed an optimum fill pressure of 11.5 bar and 13 bar absolute respectively for the 9mm and 10mm diameter cold finger configurations. Compressor drive motor efficiency measurements versus operating frequency tests showed the compressor resonant frequency to be about 55 Hz for the 10mm displacer cold finger, however with consideration to avoiding internal cooler resonances, 48.5 Hz was chosen as the operating frequency. Therefore the cooler compressor was run off resonance and was not necessarily optimum. Figure 5 shows the compressor drive motor efficiency plot, and figures 6 and 7 show the heat lift achieved versus gross compressor input power (includes I²R losses) at cold tip temperatures of 55K, 65K and 80K for both displacer cold finger configurations at optimised drive conditions, ie. optimum displacer stroke and phase.

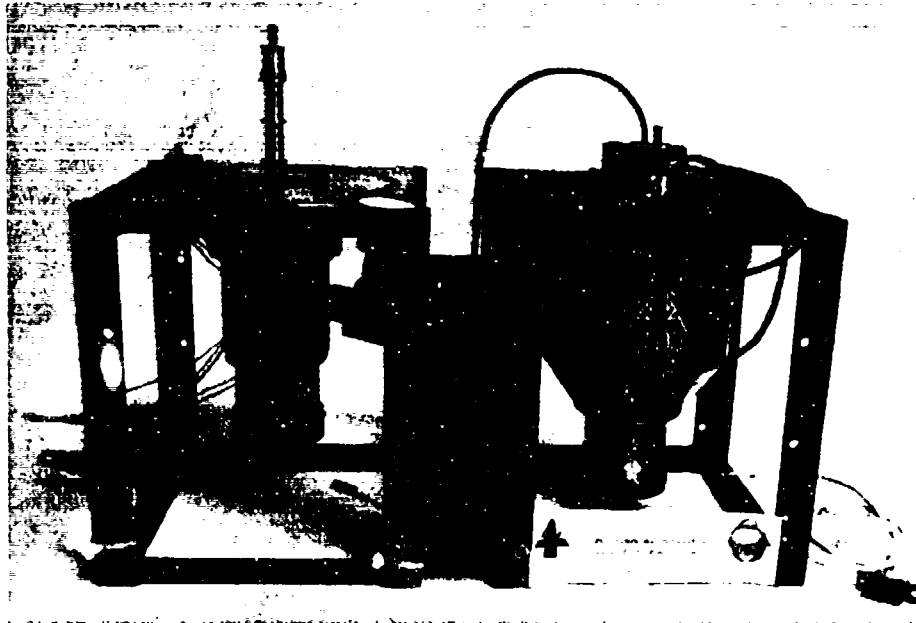


FIGURE 4 - PHOTOGRAPH OF PROOF OF CONCEPT 50-80K COOLER

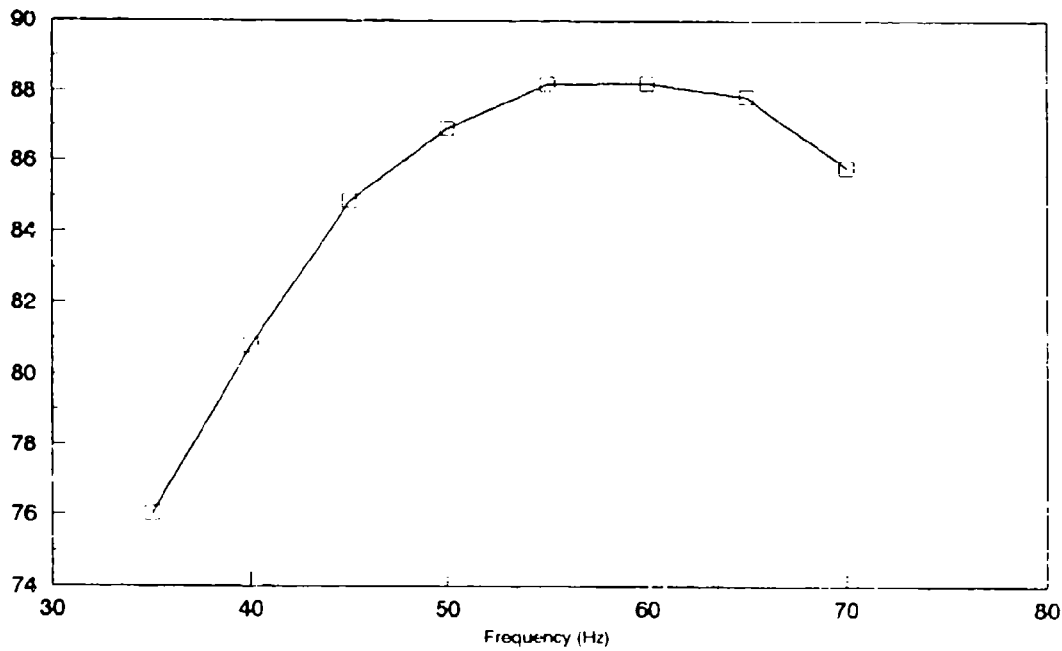


FIGURE 5 - 10MM COLD FINGER DISPLACER CONFIGURATION,
COMPRESSOR DRIVE MOTOR EFFICIENCY VERSUS FREQUENCY

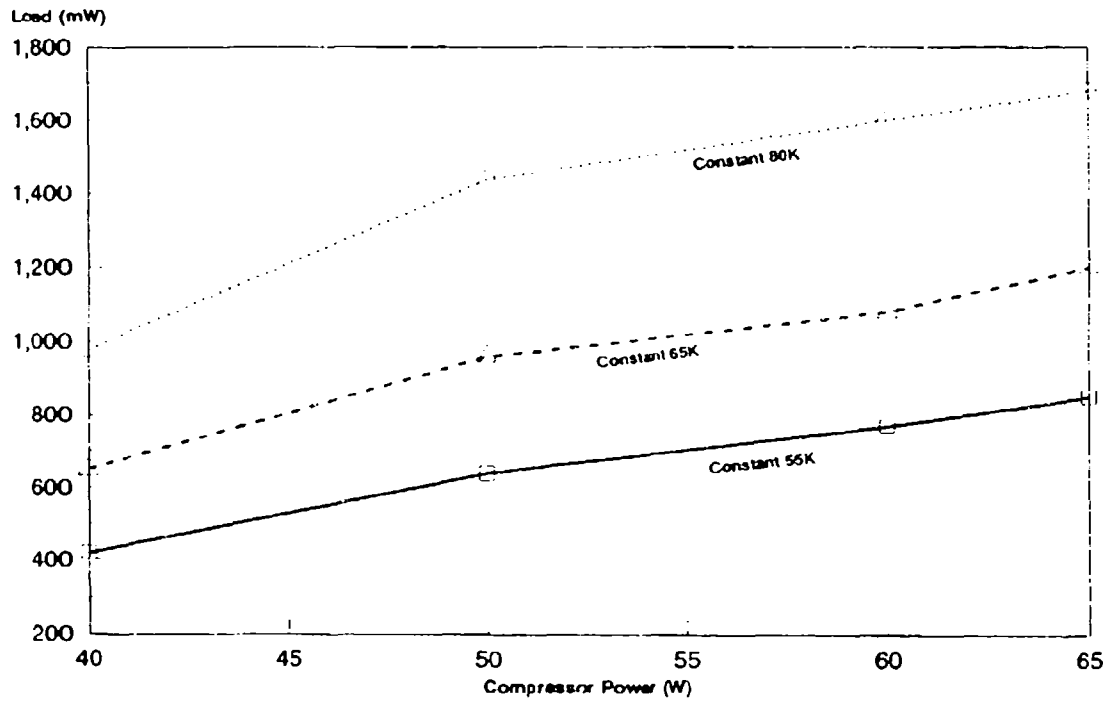


FIGURE 6 - HEAT LIFT V. GROSS COMPRESSOR INPUT POWER AT CONSTANT COLD TIP TEMPERATURES FOR 9MM COLD FINGER

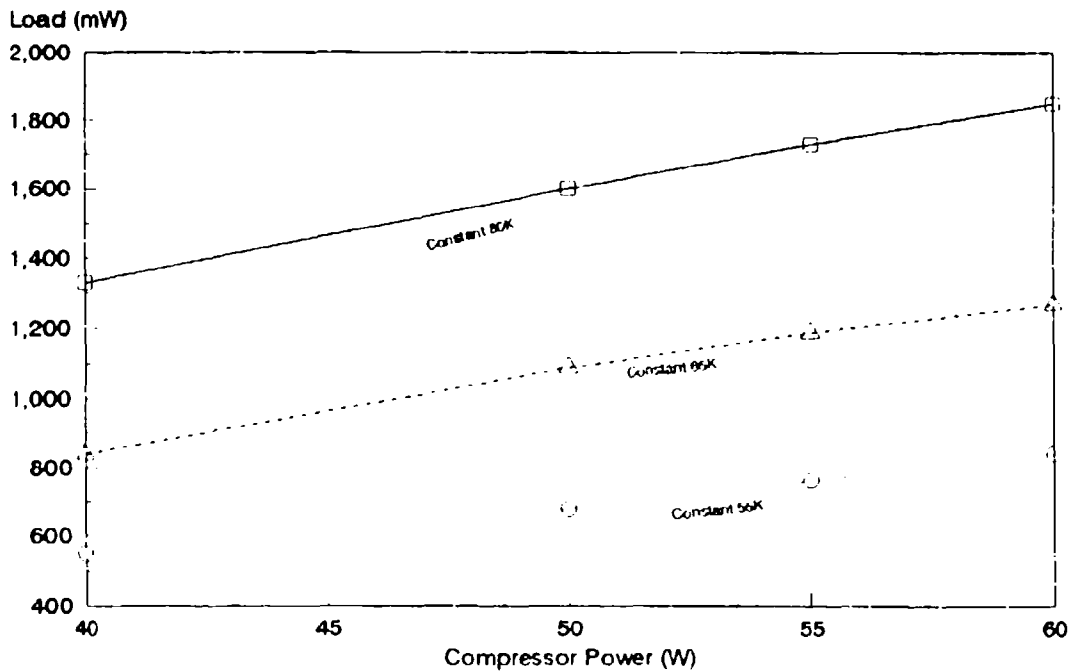


FIGURE 7 - HEAT LIFT V. GROSS COMPRESSOR INPUT POWER AT CONSTANT COLD TIP TEMPERATURES FOR 10MM COLD FINGER

These results demonstrated that this proof of concept cooler was capable of greater than 750 mwatt of heat lift at 55K, and significantly more heat lift in the range 50K to 80K than the existing BAe 80K cooler provides. Heat lift margin has been provided over a wide operating range without detracting from its 'Oxford Heritage'. Further work is necessary to optimise its performance, particularly with regard to operating efficiency. These aspects are addressed in the DM 50-80K cooler development which is discussed in the following section.

4. DEVELOPMENT MODEL 50-80K COOLER

A development model cooler was manufactured during 1991-92. The specific aims of this activity was to improve the heat lift performance of the BAe 80K cooler in the 50-80K range, with particular regard to operating efficiency. The previous proof of concept activity for a 50-80K cooler (section 3) provided a baseline start for this development.

The activity was funded under a contract from ESA, supported also by BAe funding. The basic design is the same as the previous proof of concept cooler, and is adequately described by the schematic shown in figure 2.

During the first phase of the contract several cooler design options were explored and a trade-off done to identify the optimum design. RAL were retained as consultants during this phase and completed extensive cooler performance modelling, and drive motor design modelling in order to assist in the trade-off. The adopted design changes again resulted in only minor changes affecting the 'Oxford Heritage'. These included displacer cold finger geometry, a longer cold finger at 10mm diameter, interconnecting pipework, same compressor capacity as the concept cooler, and significant optimisation of the compressor drive motor. Two different magnetic circuit designs were manufactured and evaluated at sub-assembly stages. The optimum drive motor design was then incorporated into the cooler build and the test programme started.

Figure 4 of the concept cooler is identical externally in all respects to this DM with the exception of the longer cold finger at 10mm diameter. (The Concept cooler comprised 9mm longer finger and 10mm standard finger configurations).

The bench testing of the cooler included measuring the compressor drive motor efficiency at room temperature versus operating frequency at various cooler fill pressures. These (shown in figure 8) indicate significant efficiency improvements at lower fill pressures, which is partly due to the effect of reduced pressure reducing the overall resonant frequency of the compressor. Therefore the frequency range of 40 to 52 Hz tested is closer to resonance at the lower fill pressures.

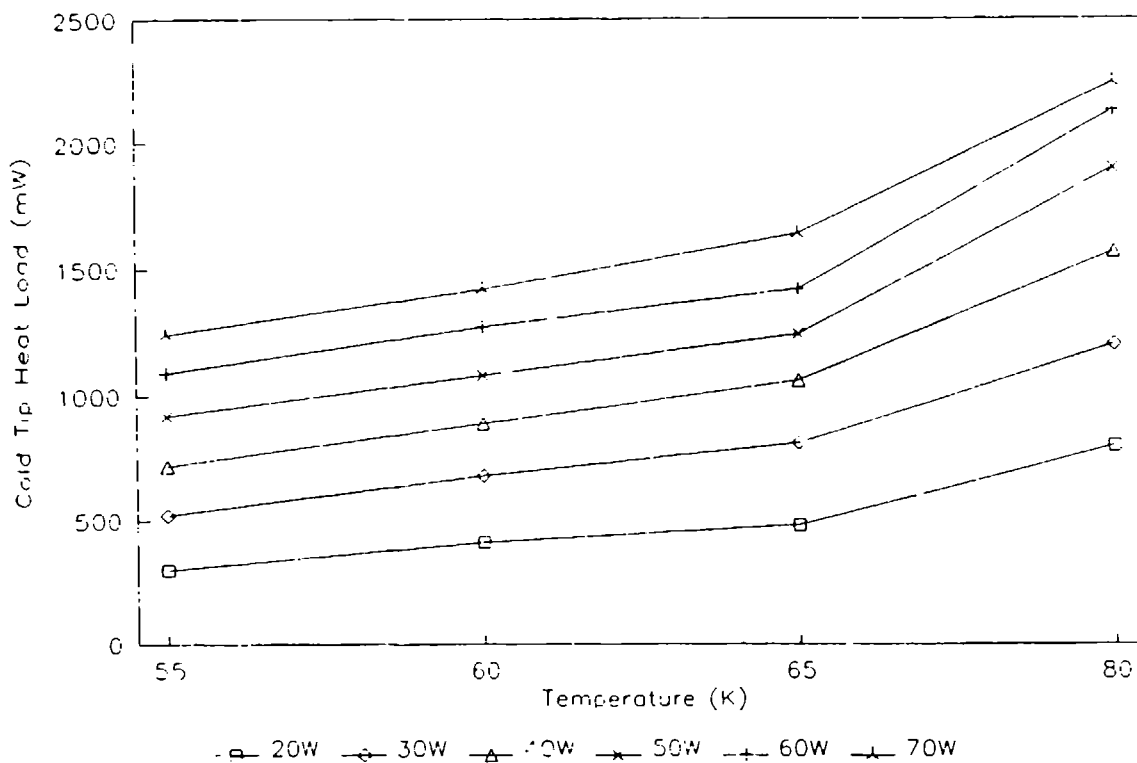


FIGURE 9 - HEAT LIFT V. COLD TIP TEMPERATURE FOR A RANGE OF CONSTANT GROSS COMPRESSOR INPUT POWER LEVEL

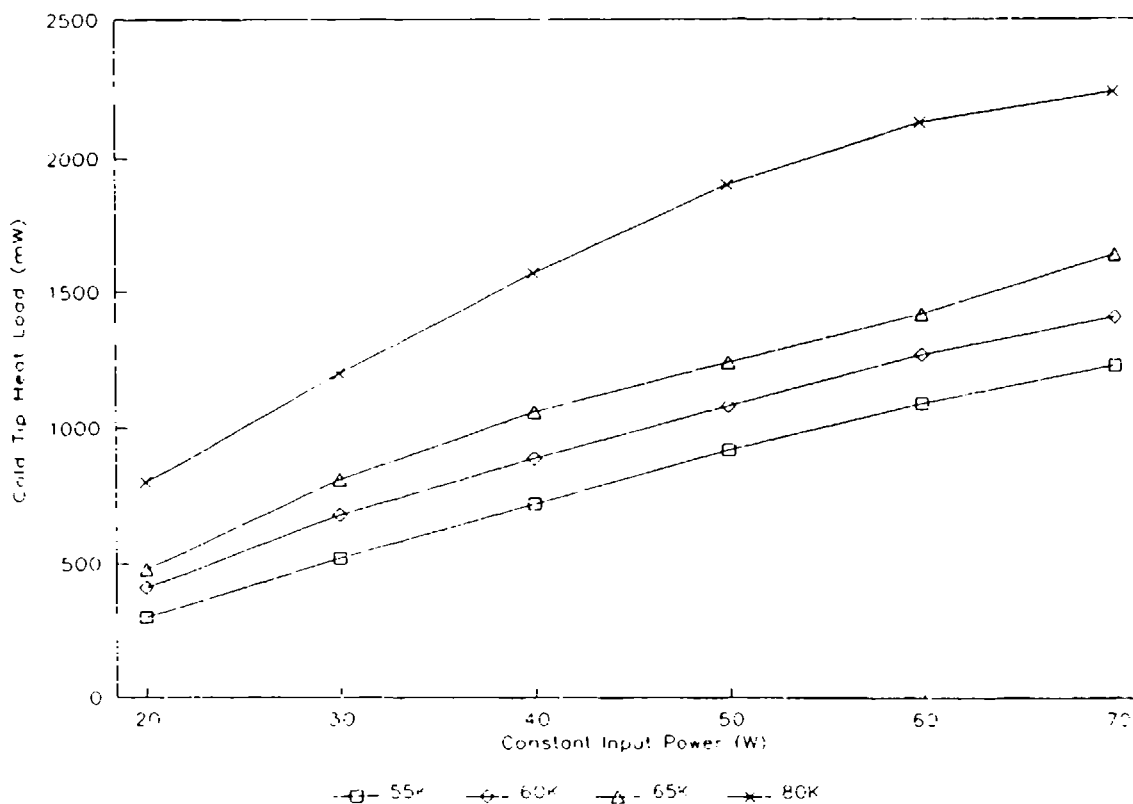


FIGURE 10 - HEAT LIFT V. GROSS COMPRESSOR INPUT POWER LEVELS FOR CONSTANT COLD TIP TEMPERATURES OF 55K, 60K, 65K AND 80K

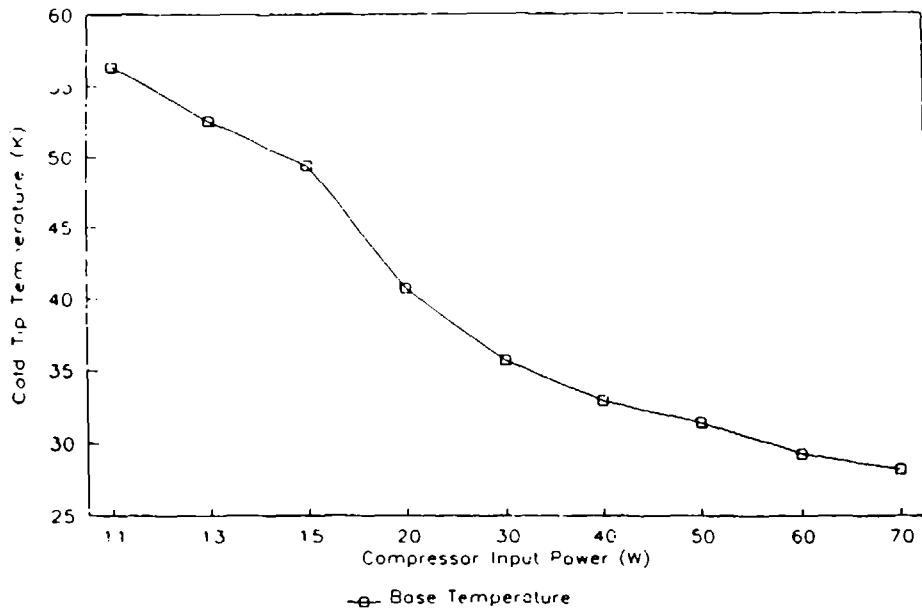


FIGURE 11 - COLD TIP TEMPERATURE V. GROSS COMPRESSOR INPUT POWER FOR ZERO HEAT LOAD CONDITIONS

These results were obtained at a cooler pressure of 13 bar absolute, operating frequency of 46 Hz, compressor heat sink temperature of 20°C, whilst other parameters such as displacer stroke and phasing were optimised for each test point. The test configuration included laboratory type drive electronics, and a vacuum environment provided by using a small thermally insulated vacuum enclosure around the cold finger. The heat load was applied by passing electrical currents through a resistive load at the cold tip, and the temperature measured with a Rhodium Iron temperature sensor. Connections to these were via very thin low conductivity constantan wire; ensuring that the thermal parasitic load was small, typically less than 50 mwatt.

Comparison of these results with the typical performance achievable from the standard BAe 80K cooler shows a 50% improvement in performance. For 30 watts compressor input power the 80K cooler has a specification of 800 mwatt, whilst the performance achieved here was 1200 mwatt for the same 30 watt input power. When compared to the concept 50-80K cooler (section 3), significant improvements can be seen here also, both in operating efficiency and overall heat lift capability.

This cooler has been demonstrated to have significant heat lift over the full operating range of 50-80K. It can be operated at higher power levels thus providing margin on heat lift performance, if required in applications with cooler redundancy for example. Operating at 60 watts the heat lift at 55K was 1090 mwatt, and 80K the heat lift was 2130 mw.

Its similarity to the existing BAe 80K ISAMS type cooler should ease the pre-flight qualification necessary, prior to usage in space instruments requiring cooling in the range 50-80K.

5. ENGINEERING MODEL 20-50K TWO STAGE COOLER

An Engineering Model 20-50K two stage Stirling cycle cooler was manufactured during 1990/91, and then completed a pre-qualification test programme during 1991/92. This qualification programme included, flight launch vibration, thermal vacuum testing, extensive performance characterisation, EMC testing, self-induced vibration measurements, and long term life testing. It is these tests that are reported here.

This activity to commercialise the RAL two stage cooler design was completed under an ESA contract, it was to ensure availability of a qualified industrial cooler for future space applications. The programme included a detailed review of the RAL design followed by the EM cooler manufacture and test programme.

The basic design is adequately described by the schematic shown in figure 3. Figure 12 shows a photograph of the cooler built and tested during this programme. The following sub-sections give the results of the test programme.

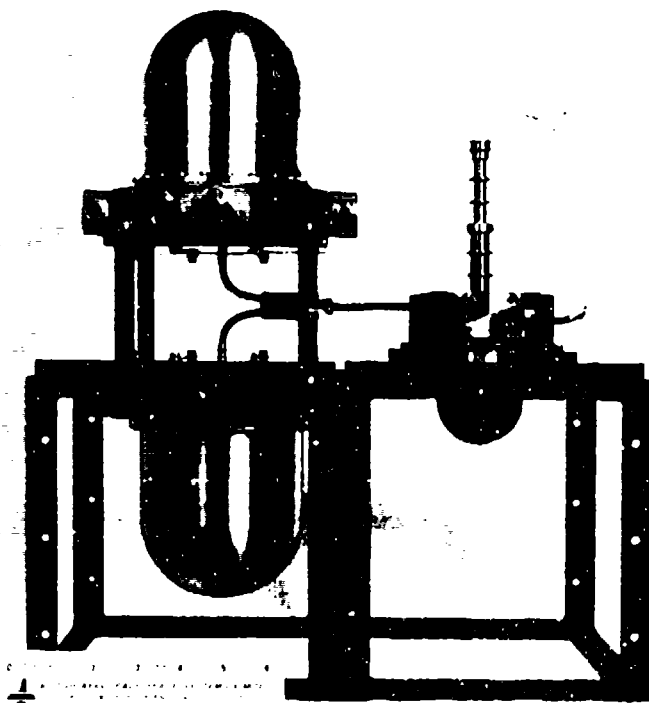


FIGURE 12 - PHOTOGRAPH OF ENGINEERING MODEL
20-50K TWO STAGE STIRLING CYCLE COOLER

BENCH TESTING Bench testing included measuring cooler heat lift versus cold tip temperature, both before and after vacuum bake-out. Vacuum bake-out consists of reducing the pressure internal to the cooler to high-vacuum levels, achieved through four separate pump-down ports into the four main volumes of the cooler. This vacuum is held for a minimum of one week at a temperature of 80°C. The process ensures that any residual moisture or organic materials contained within the cooler are fully outgassed, and the risk of gas type contaminants being released within the lifetime of the cooler is eliminated.

Figure 13 shows the heat lift performance of the cooler before and after the vacuum bake-out. 300mW of heat lift was achieved at 30K before bake-out and 300mW heat lift at 35K was achieved after bake-out. This performance was achieved for a total input power to the mechanical cooler of less than 70W.

The post bake-out performance shows a deterioration of about 5K. The causes for this are understood and the necessary detailed design changes are being incorporated into the future build standards for this cooler.

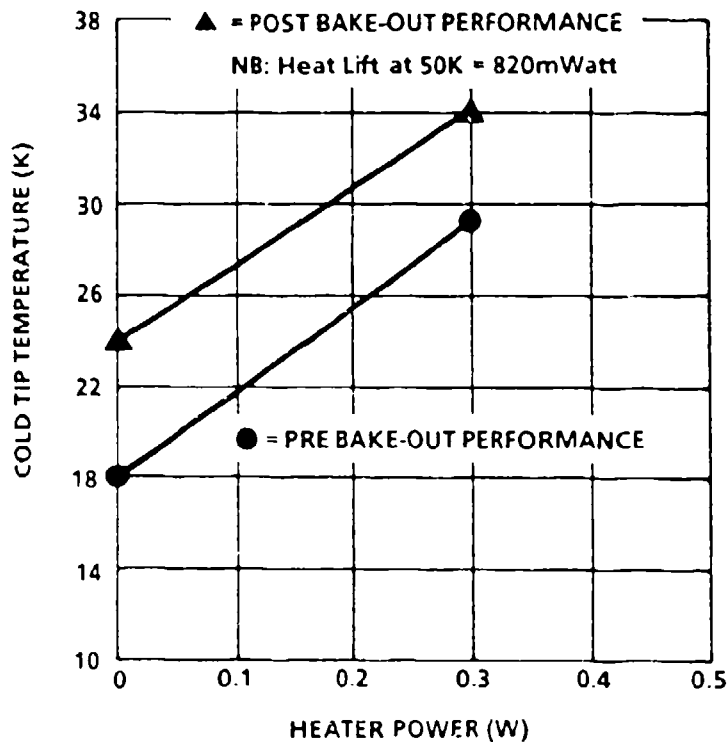


FIGURE 13 - HEAT LIFT PERFORMANCE OF ENGINEERING MODEL COOLER

Leak test measurements on the final gas sealed cooler confirmed the leak rate to be better than the specification requirement of 1×10^{-7} mbar litre/sec.

FLIGHT VIBRATION TESTING Figure 14 shows the 20-50K EM cooler on the vibration shaker ready for testing. The testing consisted of subjecting the cooler in turn to both Random and sinusoidal sweep vibration along each of its three principal axes.

Table 1 gives the random and sinusoidal sweep vibration levels tested. It shows when it was necessary to 'lock' the moving elements of the cooler to prevent over-travel and striking of internal end stops. Locking is achieved by powering the drive motor and holding compressor pistons and displacer regenerator to mid-stroke. The results show the cooler survived the full random and sinusoidal sweep vibration in the non-powered (not locked) condition with one exception. Locking was necessary for the case of sinusoidal vibration along the axis of the moving elements.

Launch locking required power in approximate proportion to the vibration level applied, with the compressors requiring 5W maximum each at the 15g peak, whilst the displacer required 3W maximum at 15g. The onset of the need for launch locking occurred at 1g for the compressors and 3g for the displacers.

Post flight vibration performance testing confirmed that no degradation had occurred to the cooler. The heat lift performance was the same as that demonstrated earlier in Figure 13. The leak rate was measured and no degradation was observed.

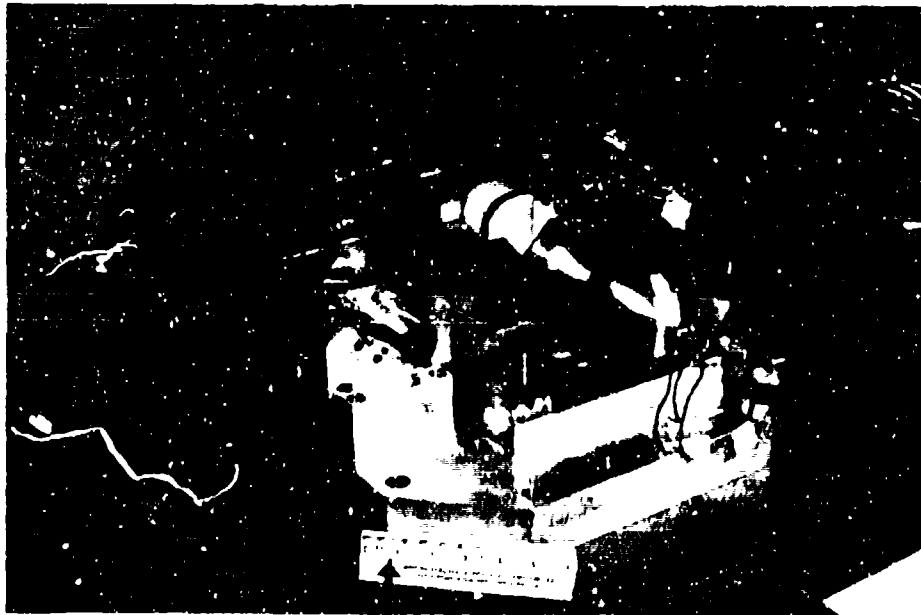


FIGURE 14 - 20-50K COOLER FLIGHT VIBRATION TESTING

Vibration test level	Comment on results/vibration axis		
	Along compressor and displacer drive axis	Perpendicular to plane of compressors/ displacers	Perpendicular to first two axes
Random vibration 20-80 Hz at +6dB oct ⁻¹ 80-500 Hz at 0.16 g ² /Hz ⁻¹ 500-2000 Hz at -3dB oct ⁻¹	The cooler survived the vibration level in the non-powered condition, for all three axes of vibration		
Sinusoidal sweep vibration 5-18 Hz at 11 mm peak 18-60 Hz at 15g peak 60-100 Hz at 6g peak ⁻¹ (sweep rate < 2 oct min ⁻¹)	Necessary to power up to compressors and displacers drive motor for launch locking, preventing over travel of moving elements. Cooler survived in this condition.	The cooler survived the vibration test in the non-powered condition for both these axes of vibration	

TABLE 1 - FLIGHT VIBRATION TEST RESULTS FOR EM 20-50K COOLER

THERMAL VACUUM TESTING Testing was carried out to confirm the ability of the cooler to survive temperature extremes without degradation in performance, and to identify its heat lift performance at other lesser temperature extremes. The cooler installation being fitted into the thermal vacuum chamber is shown in figure 15. A summary of the test results is given in table 2.

The cooler was mounted in the same fixture that had previously been used for flight vibration testing, its thermal design being suitable for heat sinking at the mounting interfaces of the cooler. Thermal blanketing was provided around the cold finger to minimise any parasitic heat loads. A heater resistor and calibrated rhodium iron resistance thermometer, connected with low thermal conductivity constantan wiring were attached to the second stage cold tip for heat load and temperature monitoring purposes.

It should be noted that for each test point, the operational parameters of the cooler, amplitude of stroke, displacer phasing and input powers were optimised. The cooler was very sensitive to these changes, much more so than the single stage cooler, with each test point taking hours to stabilise. This sensitivity may have affected some tests and the performance achieved may not have been fully optimised.

The results show an expected degradation in heat lift performance at the elevated temperatures, with negligible improvements at the lower temperatures. However, the input power to the compressors at the lower environmental temperatures is significantly reduced. Further work will be undertaken at a later date to better understand this characteristic.



FIGURE 15 - THERMAL VACUUM TEST INSTALLATION
FOR 20-50K EM COOLER

Mounting Interface Temperature (°C)	Second Stage Cold Tip Temperature (K)	Heat Load (mwatt)	Total Compressors input power (watt)
-45	Survival Test	-	-
-25	25.6	0	54
	30.0	125	66
	36.6	300	72
-20	24.4	0	58
	30.0	140	67
	34.2	300	74
+26	24.1	0	69
	30.0	170	82
	34.3	300	84
+45	28.6	0	66
	30.0	120	80
	40.5	300	80
+60	28.7	0	81
	30.0	13	80
	40.5	300	82
+85	Survival Test	-	-

TABLE 2 - THERMAL VACUUM TEST RESULTS
FOR THE EM 20-50K COOLER

CHARACTERISATION TESTING To better understand the performance of the cooler it was subjected to an extensive series of characterisation tests. The cooler test configuration was a local vacuum environment around the cold finger provided by a vacuum jacket, heater resistors and thermometry were provided at the 1st and 2nd stages of cooling on the cold finger. The tests were carried out in a laboratory environment with the interfaces at nominally room temperatures.

A series of tests were taken for a range of second stage (20K) cold tip heat loads (0, 150, 300, 500, 800 and 1400 mwatt). For each of these conditions, the operating parameters of compressors stroke and power, displacer stroke and phase, and operating frequency (nominally 38 Hz), were adjusted to give optimum performance. Each of these parameters was then varied in turn to quantify its effect on performance, these results provided too vast an amount of data to present here. In addition, at each optimised second stage heat lift point, the first stage heat load was varied (without changing other parameters) from zero to 1000 watt, and the effect on both stages temperature monitored.

These results are shown in table 3, and show relative insensitivity of the second stage performance to heat loads on the first stage. The slight sensitivity seen in the no load condition for the second stage is believed to be due to a greater sensitivity to losses of that temperature. It clearly demonstrates a potential for additional heat shield capability from the first stage, as well as a second stage heat lift capability up to 1400 mwatt at 80K.

FIRST STAGE COOLING		SECOND STAGE COOLING		COMPRESSORS INPUT POWER (watts)
TEMPERATURE (K)	HEAT LOAD (mwatt)	TEMPERATURE (K)	HEAT LOAD (mwatt)	
140 182 225	0 500 1000	24 25 33	0	62 63.5 64.5
108 141 182	0 500 1000	30 30 31	150	79 77.5 77.5
108 138 172	0 500 1000	35 35.5 36	300	82 84 86.5
101 128 159	0 500 1000	41.5 42 43	500	82 84 88
104 126 154	0 500 1000	53 53 53.5	800	84 84 86
107 132 155	0 500 1000	80 84 84	1400	83 82 84

TABLE 3 - RESULTS OF 1st AND 2nd STAGE PERFORMANCE CHARACTERISATION TESTS FOR 20-50K EM COOLER

ELECTROMAGNETIC COMPATIBILITY TESTS Electromagnetic compatibility tests have been completed on the cooler driven by laboratory drive electronics. Therefore the tests were limited to those compatible with the mechanical cooler only and not the drive electronics. The tests included the measurement of the structure current, radiated electric field emissions, radiated magnetic field emissions and an assessment of the DC magnetic field.

The mechanical cooler structure current under normal operating conditions was measured by commoning together the three earth leads from the major components, and measuring the current with a current probe and oscilloscope. The structure current was less than 1.5 mamp P to P against an assumed requirement of 5 mamp P to P.

Figure 16 shows the radiated electric field emissions specification that the cooler was tested to, it includes narrowband and broadband in the range 14 KHz to 10 GHz. The only area where failure was indicated was a narrow region on the broadband measurement just below 30 MHz. Comparison of plots taken at various bandwidths showed it to be in the transitional region between narrowband and broadband. This could be considered a marginal failure and the use of laboratory drive electronics which was unavoidable could also have been contributory.

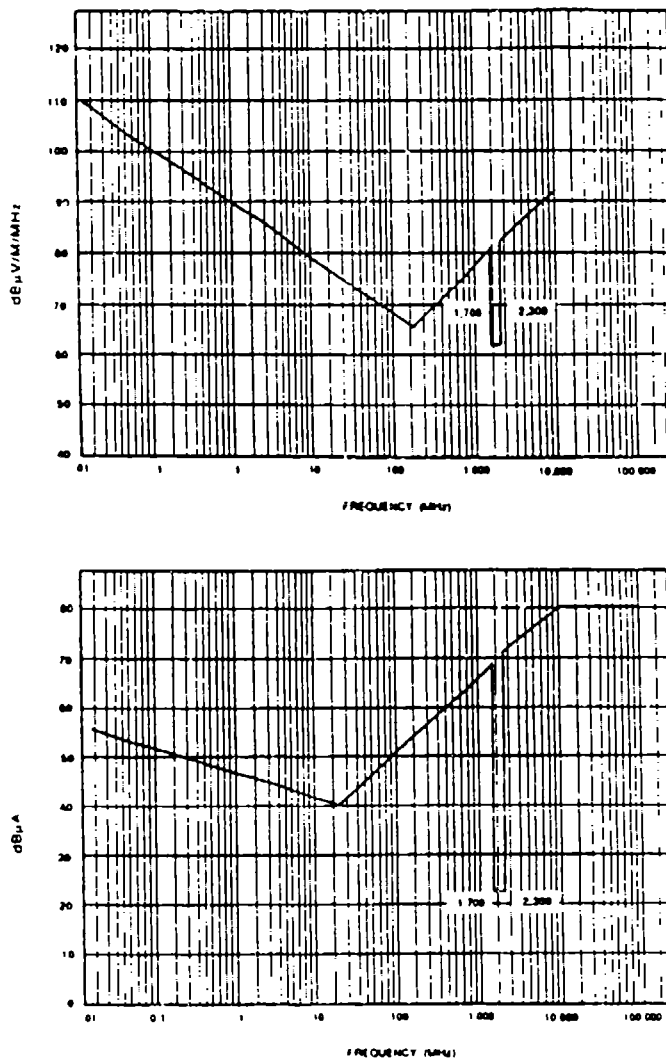


FIGURE 16 - BROADBAND AND NARROWBAND RADIATED EMISSION REQUIREMENT

The radiated magnetic field emissions requirement was to MIL STD 461B part 3 (April 1980). The results were generally satisfactory, with the specification being marginally exceeded at around 100 Hz.

The DC magnetic field was measured at a maximum of 1×10^{-4} Tesla at 28 cm distance from the compressor. The DC magnetic field associated with the displacer was 20% of the values measured for the compressors.

SELF INDUCED VIBRATION One of the major concerns for potential users of mechanical coolers is the level of vibration generated and its effect upon the host instrument. Vibration from these coolers is inherent in the design, with the piston and regenerator moving masses generating vibration forces. BAe are currently developing a low vibration drive system for a range of coolers from 4K through to 80K, and this would be suitable for this 20-50K cooler. The purpose of this work was to demonstrate sufficient similarity in the forces generated in the 20-50K cooler to those in the 80K cooler, which is the baseline cooler for the electronics development.

The vibration characteristics measured were shown to be similar to those of the 80K cooler, and that similar vibration suppression techniques could be employed here also. Ref (3) details the techniques employed for the 80K cooler, and confirms compressor forces of 0.22N, and displacer forces of 0.044N can be achieved for flight applications.

LONG TERM LIFE TESTS Following completion of the test programme and before commencement of life testing the cooler performance was measured to confirm that no degradation in performance had occurred. There was no degradation in heat lift performance or the leakage rate of the cooler.

The cooler was then put onto life test, operating at optimum settings in room ambient conditions, with local vacuum achieved around the cold finger by using a vacuum jacket.

An operating life of 11 months has been achieved with no degradation in performance up to 4th November 1992, with 3 months of this period achieved in a cold finger horizontal orientation. It is intended to continue this life test for a minimum period of 5 years.

6. DISCUSSION

Development of a cooler capable of operating over the range 50 to 80K has been completed to a development model standard. Heat lift performance has been demonstrated, and the further work that is necessary is to complete a pre-qualification programme demonstrating fully its suitability for space instrument applications. The 'Oxford Heritage' of the BAe 80K cooler has been retained in this improved cooler.

A pre-qualification programme has been completed on a two stage Stirling cycle cooler for the temperature range 20-50K, verifying its suitability and availability for future space instrument applications.

7. ACKNOWLEDGEMENTS

The author wishes to acknowledge and thank the workers at RAL and BAe that have made these programmes possible. These include but are not limited to T Bradshaw and A Orłowska of RAL, and J Harris and D Pidoux of BAe.

8. REFERENCES

1. Werrett S T et al. Development of a small Stirling Cycle Cooler for Space Flight Applications. Adv. Cryogenic Eng. (1986) 31 791-799
2. Scull S R et al. Pre-qualification testing of an 80K Stirling Cycle Cooler. Proceedings of the European Symposium on Space Thermal control. Florence Italy, October 1991
3. Ross R G et al. BAe 80K Stirling Cooler performance characterisation. Jet Propulsion Laboratory report. Ref. D-9912. May 1992
4. Jewell C I et al. Present Life testing status of 'Oxford-type' cryocoolers for Space applications, Proceedings of the 7th International cryocooler conference. Santa Fe, New Mexico, November 1992
5. Bradshaw T W. First results on a prototype two stage Stirling cycle cooler for space applications, Proceedings of the 4th cryocoolers conference. Easton, MD, September 1986, 303 - 309

STIRLING CRYOCOOLER WITH DUAL OPPOSED
DISPLACERS FOR SPACE APPLICATIONS

P. ARTER, D. BERRY, W. GULLY, AND C. VARNER
BALL AEROSPACE GROUP, PO BOX 1062
BOULDER, CO. 80306

INTRODUCTION

In an effort to make a low vibration Stirling cryocooler with a minimum of electronic compensation, we experimented with a novel configuration that used dual opposed displacers. We report here on the vibration and thermal characteristics of this cryocooler, and discuss other aspects that arose as we considered integrating it into specific applications.

BACKGROUND

Modern space instrumentation often requires cryogenic temperatures for optimum performance. Liquid and solid cryogenics have met this need in the past, but the desire for longer missions has led to the development of various miniature cryocoolers to fill this role. These cryocoolers must be robust, reliable, efficient, and quiet if they are to become acceptable alternatives. A number of papers (1,2,3) describe the detailed requirements for these coolers.

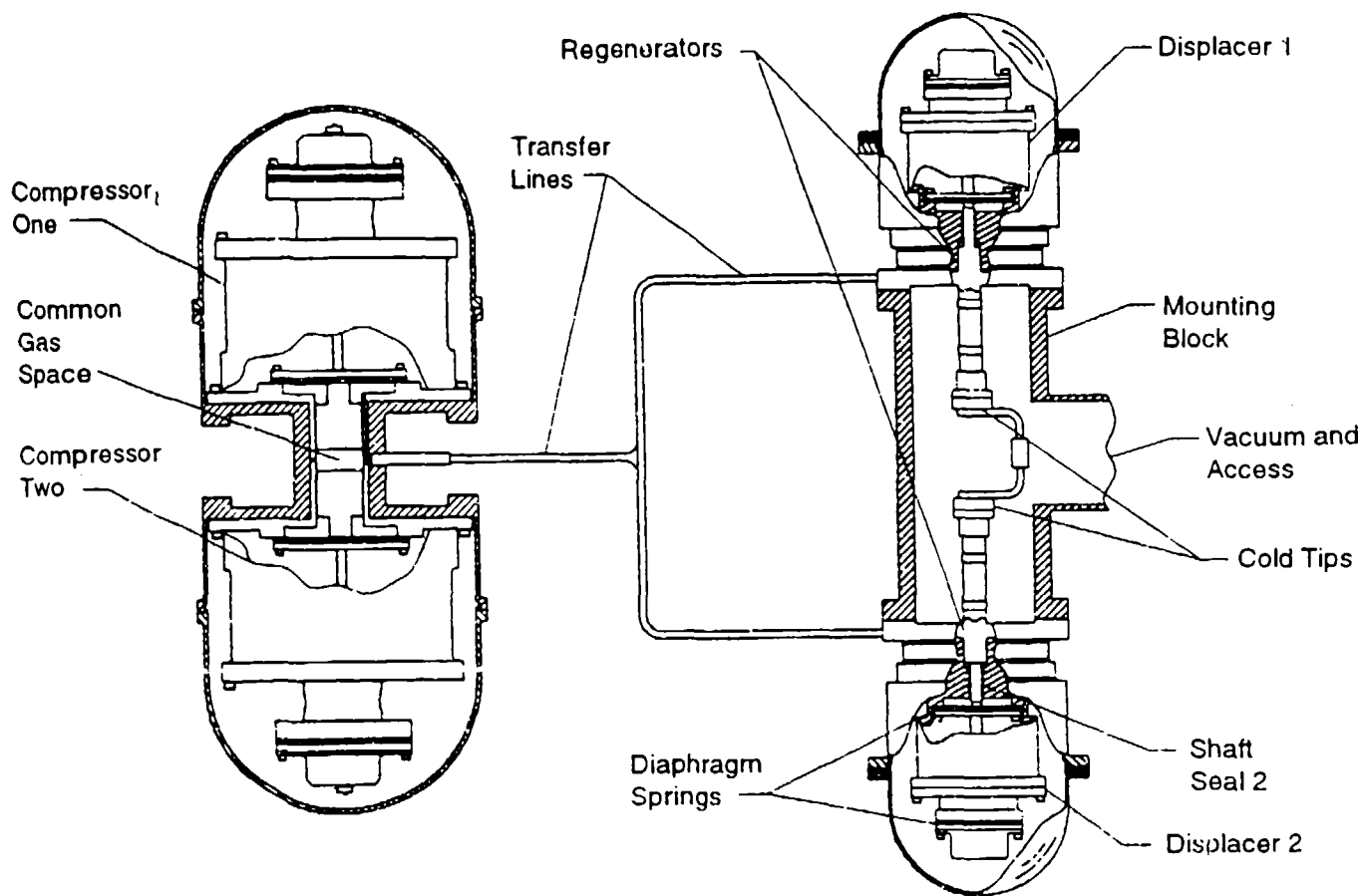
Linear Stirling cycle mechanical coolers have become popular because of the relatively simple motion of their moving parts and the ability of these parts to operate without rubbing by using

"Oxford" type diaphragm springs. In the simplest form of these cryocoolers the output vibration primarily comes from the compressor, which has a heavier armature than the displacer. This force can be balanced out by running compressors in opposition, as either separate units under electronic control or as an integrated unit where the compressors share a common compression space. In our cooler, an output force of 60N on one side can be balanced to better than 0.25N with a second compressor in opposition.

We now focus on the displacer, which is more difficult to deal with because it is intimately connected to the sensitive equipment being cooled. Our displacer, if unbalanced, would produce 4N of vibration at the fundamental and up to 0.5N at the harmonic frequencies. Our choices were to use counterweights with varying degree of electronic compensation, displacers of separate coolers electronically slaved in opposition, or dual opposed displacers that were parts of a single cooler. In this paper we describe our efforts to use two displacers operating from the same compressor in opposition to cancel vibration.

LINEAR COOLER WITH DUAL DISPLACERS

A schematic of our cryocooler is shown in **Figure 1**. We employ an integrated twin compressor with a common gas space to get the maximum natural cancellation of the opposed pistons. We employ two displacers mounted "face to face" on a block representing the vacuum structure that would house the load to be refrigerated. The displacers do not share a common pressure wave because of the flow impedance of the intervening transfer lines, but they do share a common pressure source. This configuration leads to balanced vibration to the extent that the regenerators are identical. Non-linear forces due to the pneumatic forces on the shaft seals and



RA3(968.A3880)005

Figure 1. Schematic of the Ball linear Stirling cryocooler with dual displacers

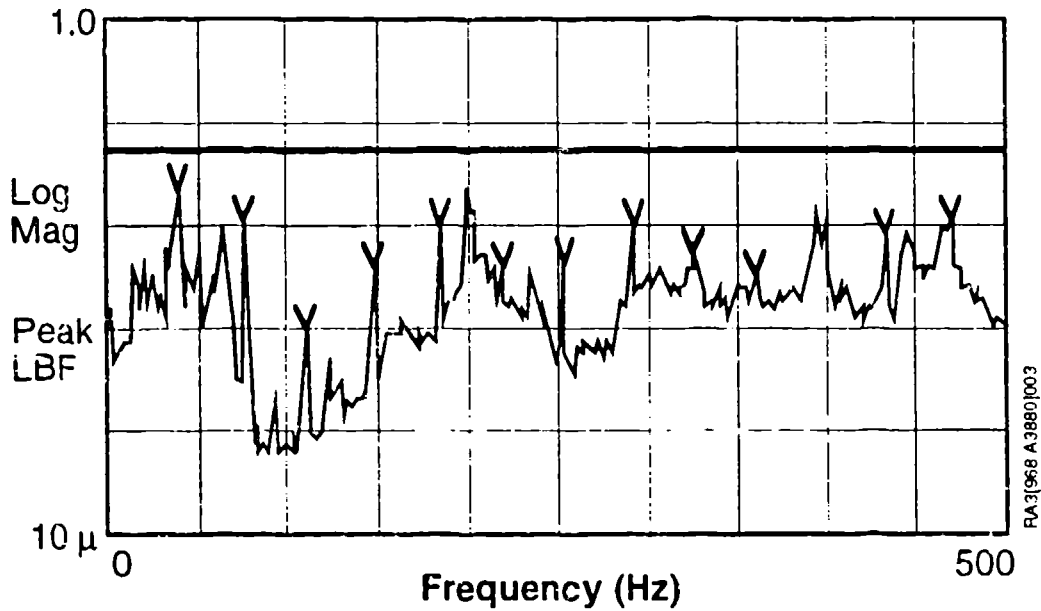
across the regenerator screens would balance, as would non-linearities in the motor since the displacers would require identical operating currents. Subtleties in the spring forces due to axial non-linearities should also be reproduced. The displacers are identical to within standard machine tolerances. The moving masses were within 1 gram of each other without adjustment, and alignment rings assured that the moving components are co-axial to within 50 micrometers.

VIBRATION TEST

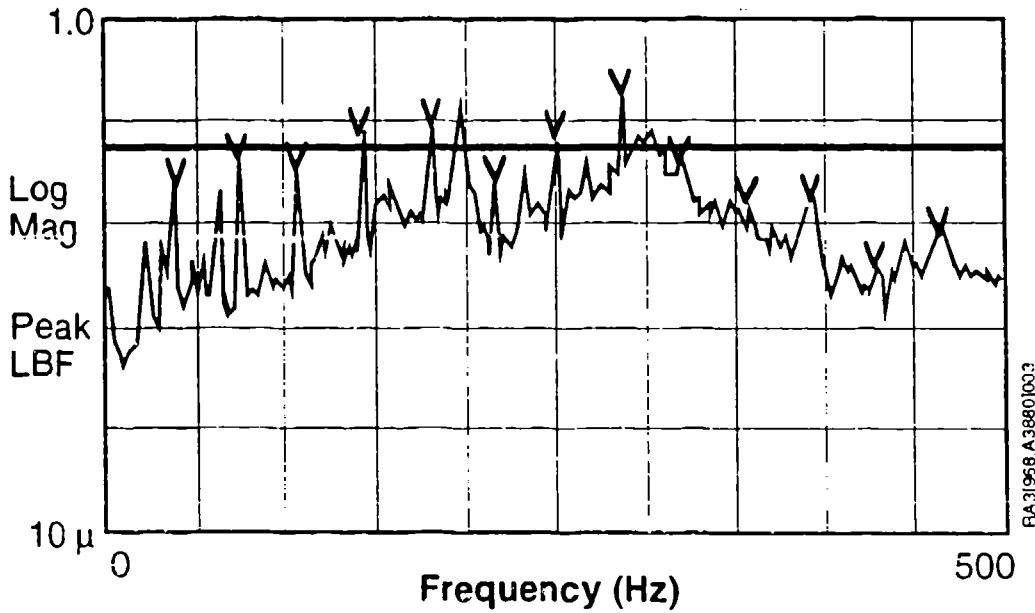
In this section we will describe the test configuration, drive electronics, and the vibration results. To record vibration we used a piezoelectric vibration head capable of simultaneous measurement of force along three axes. The sensor is in the form of a right circular cylinder approximately 8 cm in diameter. To perform this test we had to separate the displacer from the compressor and mount it alone on the transducer head, with the compressor mounted separately alongside. Both components were mounted in simple frames and oriented vertically. The compressor was coupled to the displacer through a 3.2mm Od. transfer line about 25cm in length. Output signals from the sensor were fed through charge preamplifiers into a dynamic signal analyzer which displayed the vibration spectra.

For this specific test we drove the compressors with identical sinusoidal voltage waveforms. We did not attempt to minimize the compressor's vibration since it was off the transducer, although this resulted in some unwanted background in the displacer vibration data. We drove the displacers with sinusoidal input signals that were the reference inputs into analog position control loops. These loops had relatively modest (5x) open loop gains and a low frequency range. They were primarily used to control the center of oscillation and the amplitude of the displacer motion, and did little to suppress the vibration at harmonics of the operating frequency.

In **Figures 2a** and **2b** we show the results for axial and lateral vibration with the displacers stationary and the compressors operating at full amplitude. These results should be zero except for coupling of compressor vibration in through the transfer line.



Transverse Forces



Axial Forces

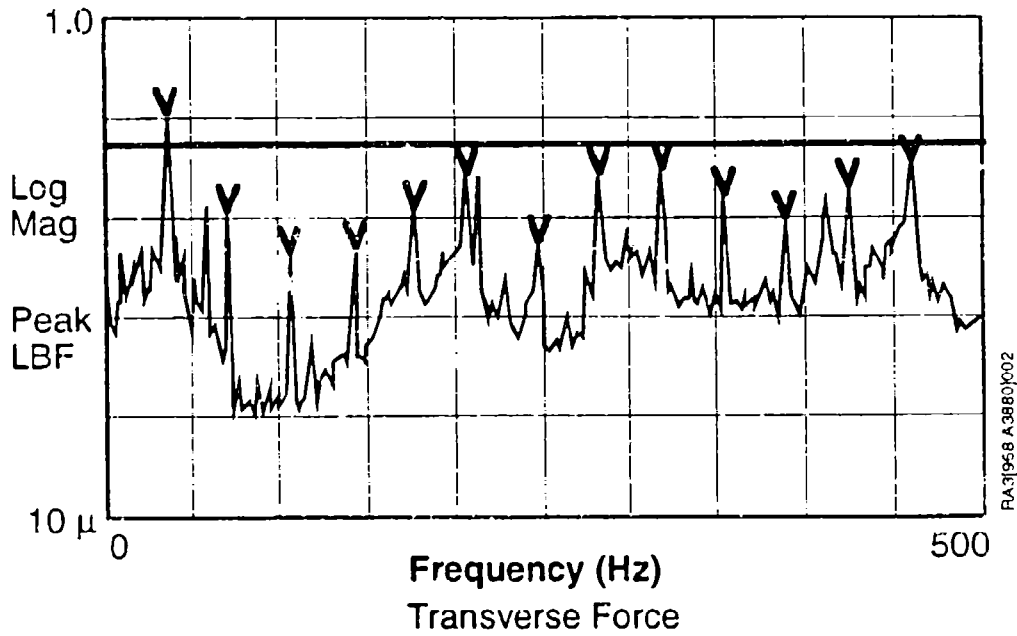
Figure 2 (a and b). Vibrations measured at the displacers with only the compressors running

Vibration at the first few harmonics is low, but above 150 Hz, we see broadband vibration and some narrowband vibration (indicated by the carats) in excess of 232mN (0.05lbf) peak force. Much of this background is associated with the relatively simple fixturing for this measurement. The result for one displacer operating is shown in **Figures 3a** and **3b**. We notice immediately the increased vibration output at all harmonic frequencies in the axial direction, and at the fundamental frequency in the lateral direction. In this test the single displacer was at approximately 60K, while the other was at room temperature. The vibration for dual displacers is shown in **Figures 4a** and **4b**.

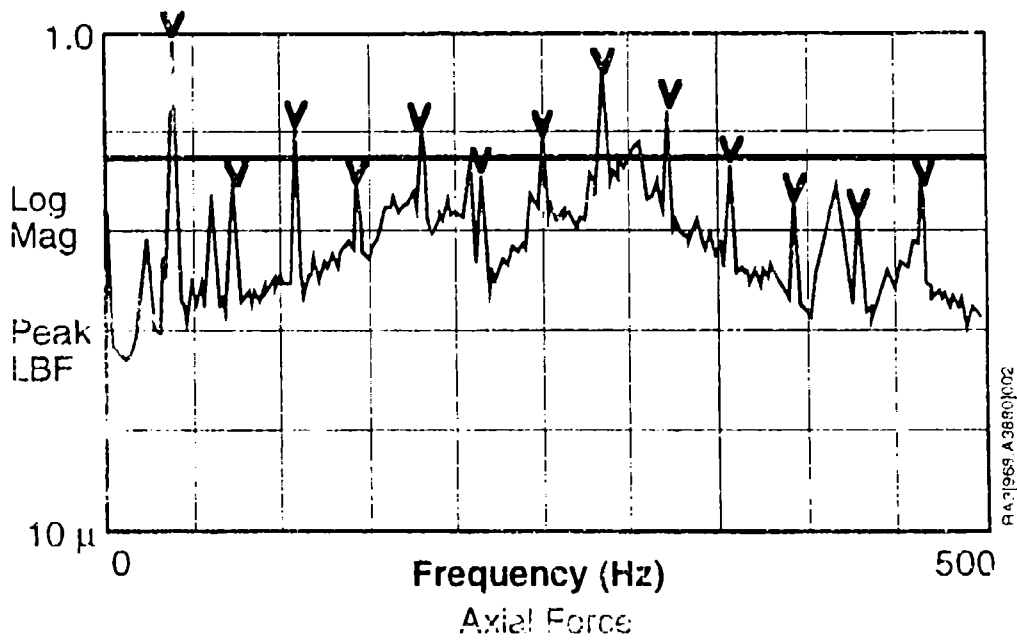
The axial results are summarized in **Figure 5**. The vibration is reduced by a factor of 25 at the fundamental, and at least by a factor of two at the higher harmonics. In some cases the vibration lies below that of the background, which evidently shifted as a result of the changing load of the displacers. The lateral results are shown in **Figure 6**, which shows that in this instance the opposed displacer has helped to reduce a lateral vibration at the fundamental, but has had no impact at higher frequencies. We conclude that the vibration in a system of dual displacers is significantly reduced at the fundamental operating frequency, is somewhat reduced at the lower harmonics, but at the higher harmonics the benefit of dual displacers has disappeared.

SYSTEM CONSIDERATIONS

The thermal performance for the cryocooler is shown in **Figure 7** for both ambient and elevated temperatures. The heat load applied is the sum for both displacers, while a temperature is reported for each independent displacer. The mean performance corresponds to approximately 30W of total compressor input power per watt of



PA-71958 A38801002



PA-71958 A38801002

Figure 2 (a and b). Vibration spectra showing output from single unbalanced operating displacer

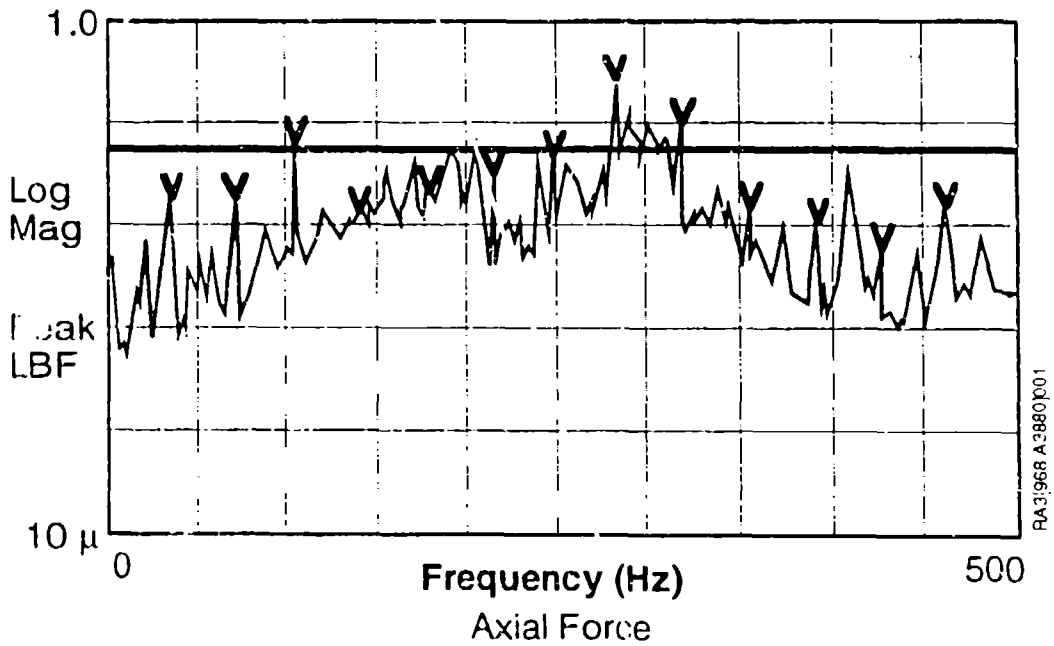
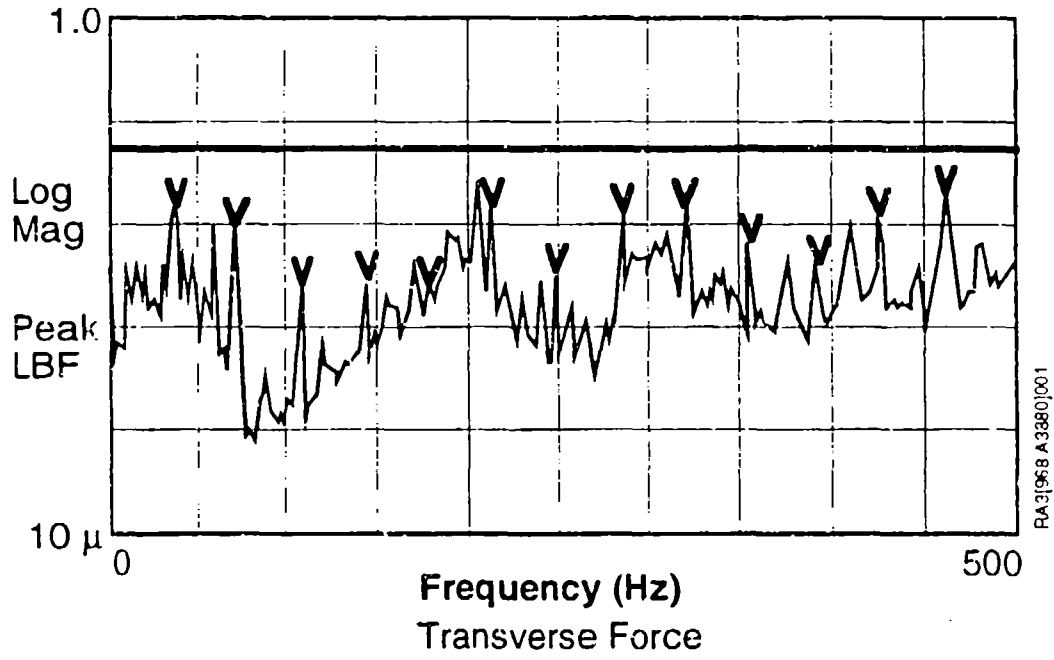


Figure 4 (a and b). Vibration output from dual opposed operating displacers

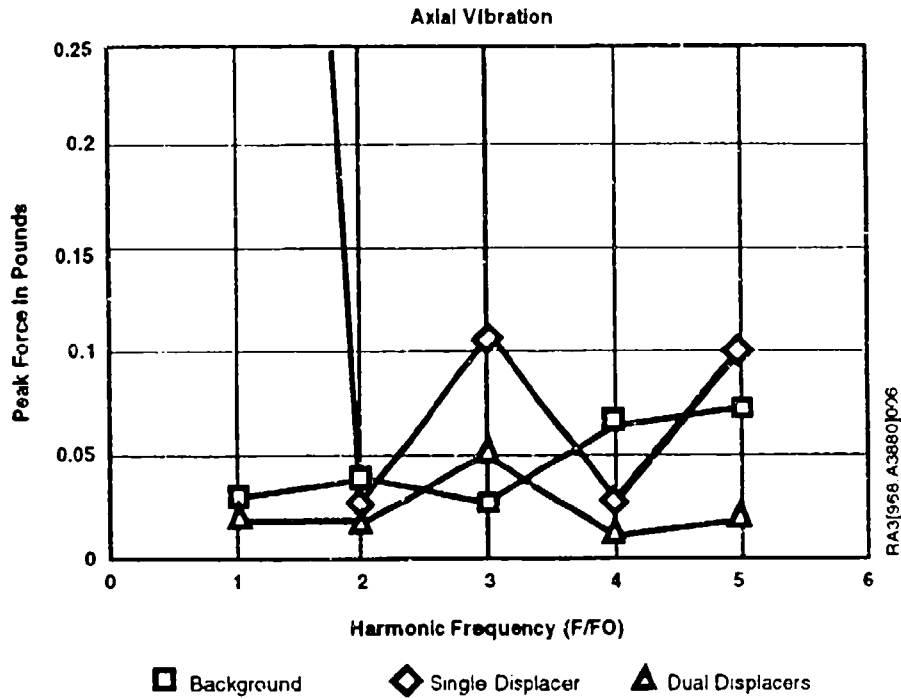


Figure 5. Summary of axial vibration

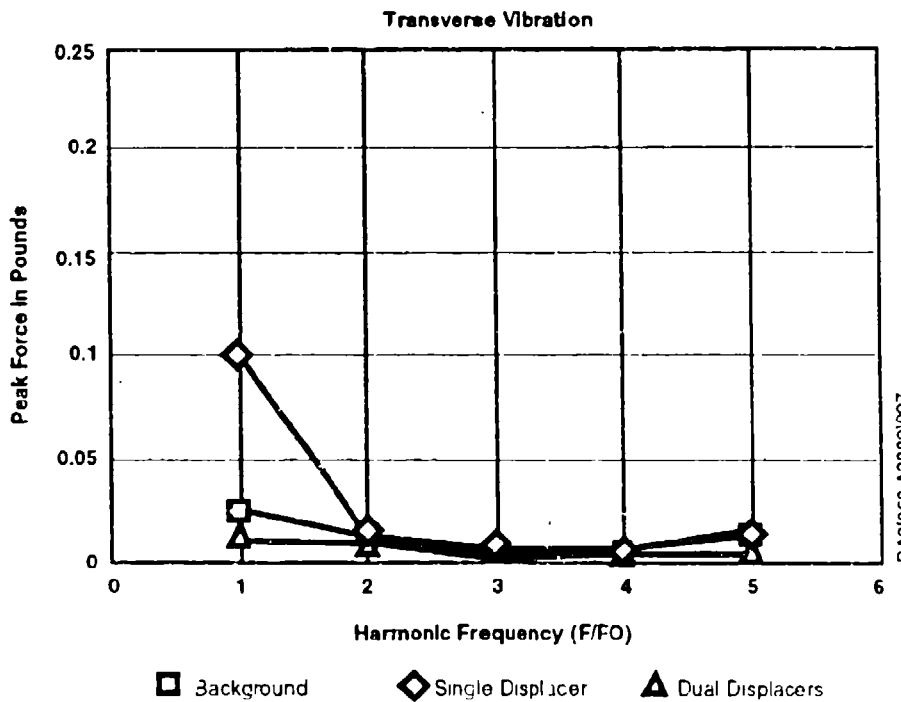


Figure 6. Summary of transverse vibration

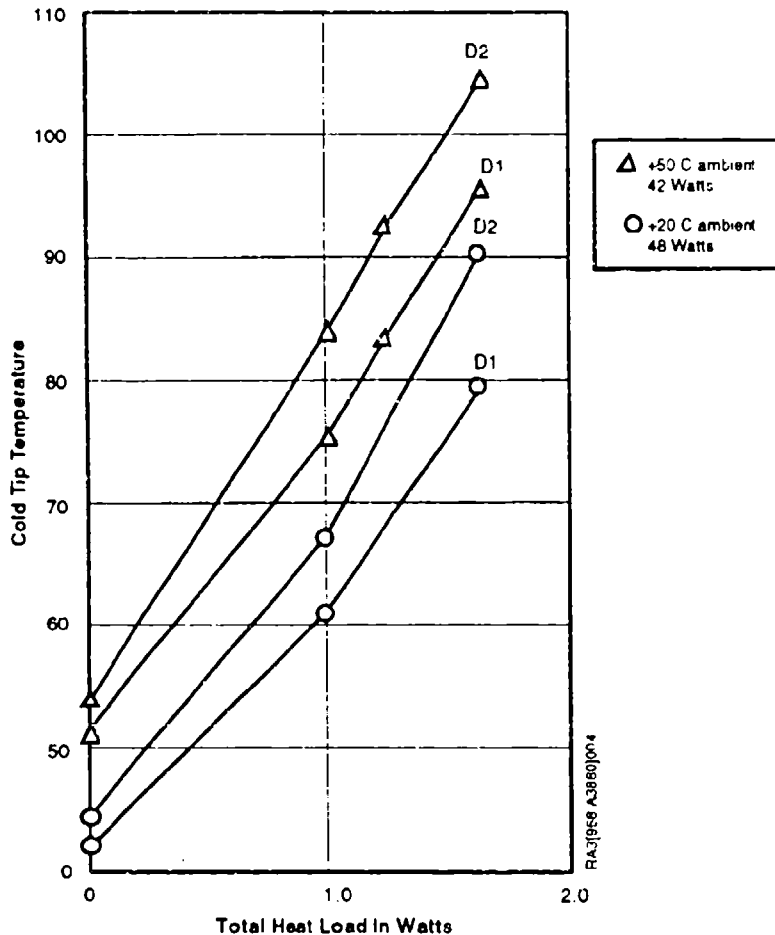


Figure 7. Thermal performances of dual displacers

heat lift at 80K for room temperature ambient conditions, similar to more conventional coolers of this type (4). However, we feel that the performance of two "half size" displacers must be somewhat less than a single full size displacer because of redundant transfer lines and duplicate conduction loads. We note that the performance of one displacer seems worse, but comment that on other occasions the displacers have behaved identically or even reversed roles. This difference could cause slight differences in dynamic behavior, but would disappear when the displacers were lashed together onto a common load.

We now turn to the long term control of vibration. We have seen that dual displacers do compensate for changes in pneumatics that could cause output vibration, such as during cooldown or during changes in ambient temperature. However, the long term reliability involves the resilience of the system to internal gaseous contamination. We go to great lengths to keep the contamination low in our cryocoolers. But if we allow the possibility of contaminants to accrue over the ten-year lifetime, they would tend to condense in the regenerators somewhere. The displacers would remain in balance if they happened to share the contamination equally. But obviously there is no way to control this, so we must assume that either displacer could be affected. We could be in a situation where the response of both components changed significantly and became difficult to control.

There were other concerns that arose during a consideration of the integration of dual displacers in a system. An obvious one is the limiting of access to the load to right angles to the line through the displacers. Another is the need for flexible links to the load, since the coldtips will contract in opposite directions as they cool, which probably means a separate support structure for the load. Another concern is that the integration of the displacer set is difficult because the displacers cannot be independently brought down on axial vacuum seals after the transfer lines are connected. Either one would have to interface to the mounting block as shown in Figure 1, or transfer lines would have to be connected after the displacers were installed in the bulkhead. Finally, one is using a relatively complex device as a counterweight. A great deal of effort goes into sustaining the tight clearances around the cantilevered displacer because of cryogenic considerations. These clearances must be maintained after launch vibration, and over time.

In applications where two independent coldtips are useful, for example, our results show that dual displacers do run easily from a single compressor and do compensate reasonably well. But for applications where the goal is simply to attain extremely high vibration cancellation, dual opposed displacers introduce a number of complications that have to be weighed against the modest degree of balance obtained.

REFERENCES

1. Requirements for long-life mechanical cryocoolers for space applications, R. Ross in Cryogenics , Vol.30 pp233, March 1990
2. Structural and Thermal Interface Characteristics of Stirling Cycle Cryocoolers for Space Applications, R. Boyle et.al., Adv. Cryo. Engr. Vol 37, 1991
3. Vibration characterization and control of Miniature Stirling-Cycle cryocoolers for Space Applications, R. Ross, et. Al. Adv. Cryo. Engr. Vol 37, 1991
4. Performance of the Oxford Miniature Stirling cycle refrigerator, T. Bradshaw et.al, Adv. Cryo. Engr. Vol 37, pp801, (1991)

**DEVELOPMENT AND SPACE QUALIFICATION TESTING
OF A RANGE OF MECHANICAL CRYOCOOLERS**

C WEIR BSc (Hons) AMIMechE
LUCAS AEROSPACE LIMITED
ENGINE AND ELECTRONIC SYSTEMS DIVISION
BIRMINGHAM
UNITED KINGDOM

7TH INTERNATIONAL CRYOCOOLER CONFERENCE
18 NOVEMBER 1992
SANTA FE, NEW MEXICO

1.0

ABSTRACT

Lucas Aerospace and Lockheed Missiles and Space Company have been jointly developing mechanical space cryocoolers since 1988 and are now well advanced with the development and space qualification of a number of systems. This paper describes the various cryocooler configurations under development plus their current performance results. Additionally a brief resume of the Space Qualification Test Programme will be presented covering topics such as launch vibration, magnetic moment tests, exported vibration and life tests.

2.0 BACKGROUND

An outline of cryocooler development is presented in Fig. 2.1. Initial work was directed towards the avionics market aimed at military infra red detectors. The Phase I study concluded that the reverse split-Stirling cycle machine offered the best prospect for success. A number of cryocooler prototypes were built and tested using concepts supplied by Dr Gordon Davey and Dr Anna Orłowska of Oxford University. With further development, enhanced reliability and excellent performance for a 7mm diameter cold finger displacer were achieved.

Phase 2 was instigated by the signing of an agreement with Lockheed to jointly develop a range of low vibration, long life mechanical cryocoolers for space applications. Between 1988 and 1990 both companies carried out a series of performance and vibration tests using existing Lucas cryocoolers. Furthermore a series of pre-space design sub-assembly tests tackled outgassing, helium leakage and other important space related issues. Two thermodynamic models and a suspension spring model were generated and verified.

The third and current phase saw the introduction of the CCS 1000 and 500 series space application cryocooler, which incorporated all the tried and tested design features of the previous phase's coolers. The Lockheed electronic controller was further modified to employ a hybrid analogue/digital controller. Active balancers and different configurations have since been developed.

Fig. 2.1 **PROJECT HISTORY**

PHASE 1 INITIAL DEVELOPMENTS (1978 - 1988)

- THERMO CYCLE/DESIGN EVALUATIONS - SPLIT REVERSE STIRLING CYCLE OXFORD COOLER CHOSEN
- INITIAL DEVELOPMENTS ON AVIONIC COOLERS
- DRs GORDON DAVEY AND ANNA ORLOWSKA CONSULTING

PHASE 2 PRE-SPACE PROGRAMME (1988 - 1990)

- JOINT DEVELOPMENTS WITH LOCKHEED
 - LUCAS - CRYOCOOLER AUTHORITY
 - LOCKHEED - CONTROLLER AUTHORITY
- PERFORMANCE/VIBRATION TESTS USING AVIONIC COOLERS
- SPACE SUB-ASSY. TESTS AND MODEL GENERATION
 - OUTGASSING OF MATERIALS
 - IMPROVED He SEALING
 - THERMO, DYNAMIC, SPRING MODELS ETC.
- BREAD BOARD CONTROLLER ETC.
- DEVELOPMENT OF INTERFACES - THERMAL BRAIDS, THERMAL SWITCHES ETC.

PHASE 3 SPACE CRYOCOOLER AND QUALIFICATION PROGRAMME (1990 -)

- PERFORMANCE TESTS ON DIFFERENT COOLER CONFIGURATIONS
- SPACE QUALIFICATION ON FLIGHT SYSTEMS
- FLIGHT ELECTRONICS
- ACCELERATED TESTS ON CANDIDATE COMPONENTS
- ADDITIONAL STRUCTURAL/DYNAMIC/THERMAL MODELS
- DEDICATED SPACE CRYOCOOLER BUILD FACILITY

3.0 Configuration and Performance

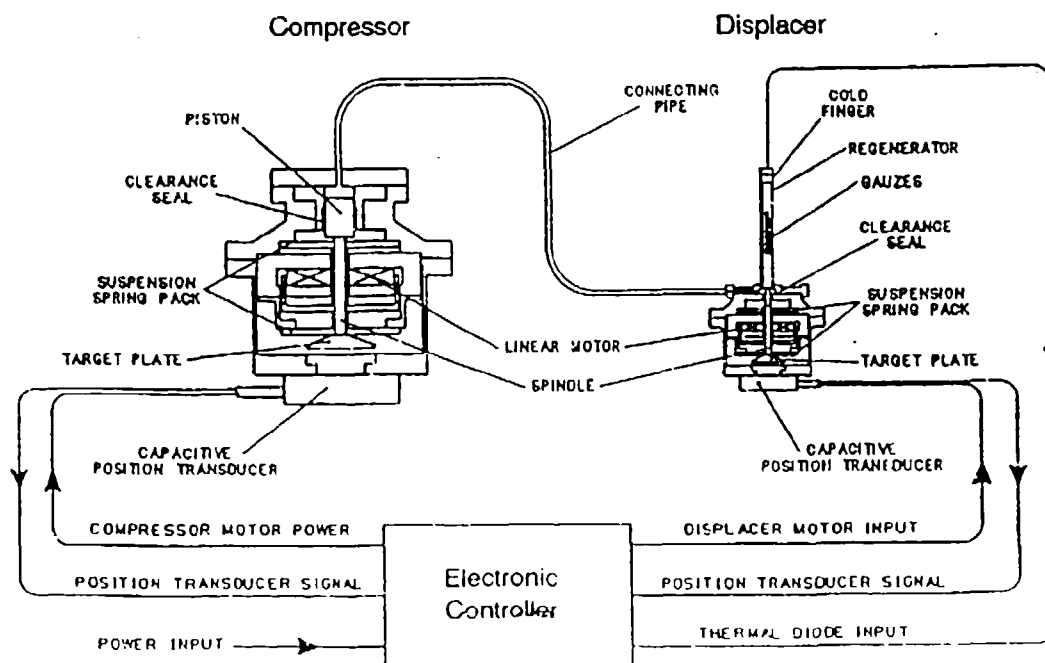
3.1 Basic Design

The principle features of a Lucas-Lockheed cryocooler system are shown in Fig. 3.1. The compressor piston provides the expansion-compression pressure cycle and the regenerator displaces a constant volume of gas cyclically through the heat exchanger.

Both compressor and displacer feature:-

- linear drive motors
- high radial/axial stiffness ratio springs (enabling operation in all orientations in a 1g environment)
- capacitive transducer position sensors
- non-contacting clearances which seal the working Helium gas from the motor casings.

Fig 3.1: Cryogenic Cooling System



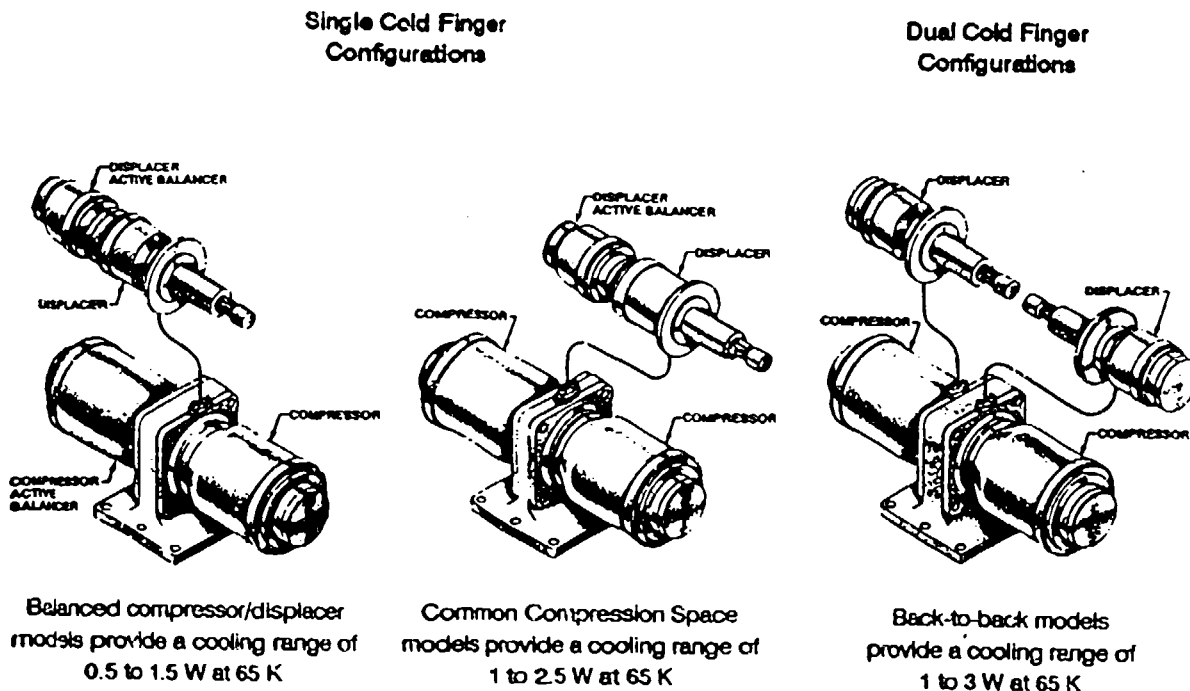
3.2 Configurations

A summary of the Lucas cryocooler configurations is given in Fig. 3.2. All benefit from exported vibration cancellation by either:-

- back-to-back models, or
- active balancers.

The role of the active balancer is purely to cancel exported vibration and does not contribute to the thermal cooling capacity.

Fig 3.2: Configuration Options & Performance



3.3

Performance

The configurations described in 3.2 are derived from the space base technology units of which there are two sizes. The model CCS 500 was originally designed to lift 0.5W at 65K whereas CCS 1000 was 1.0W at 65K. From Fig. 3.3 and 3.4 experimental results show that these performance goals were met with a margin.

Predictions generated by the Lucas Stirling cooler thermodynamic model (CMOD) shows close agreement with these results.

Fig 3.3: CCS 1000 Performance

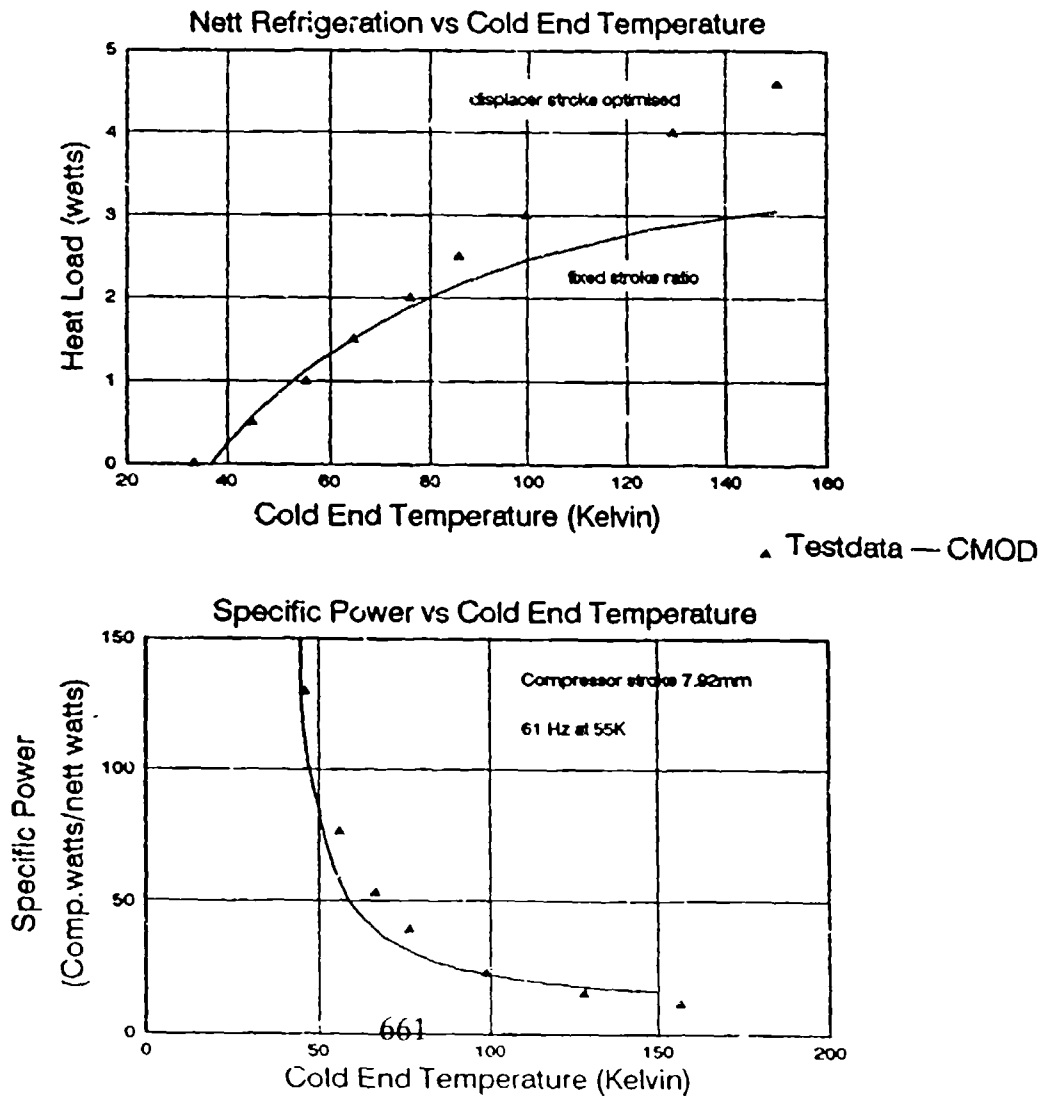
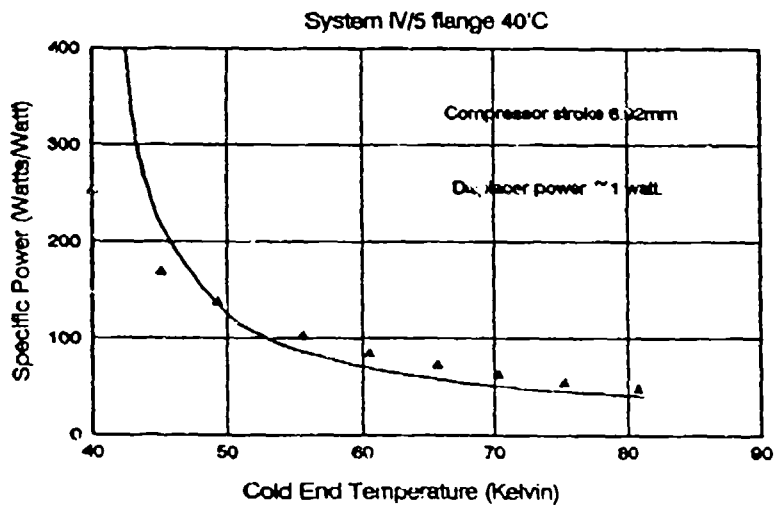
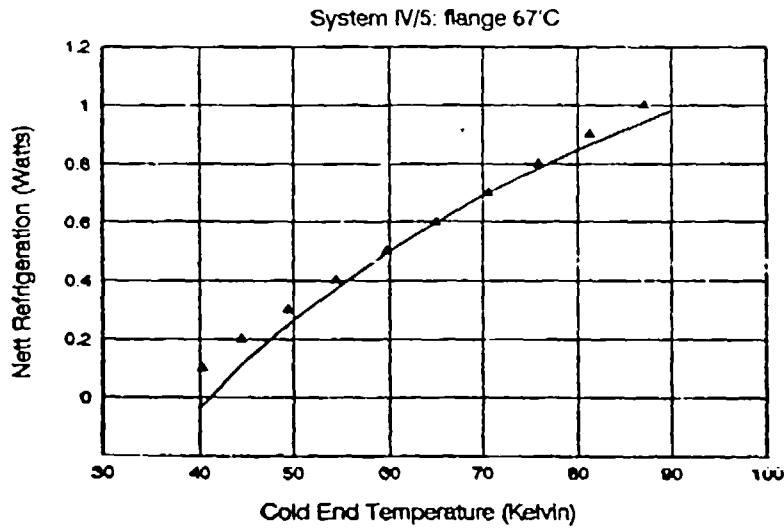


Fig 3.4: CCS 500 Performance

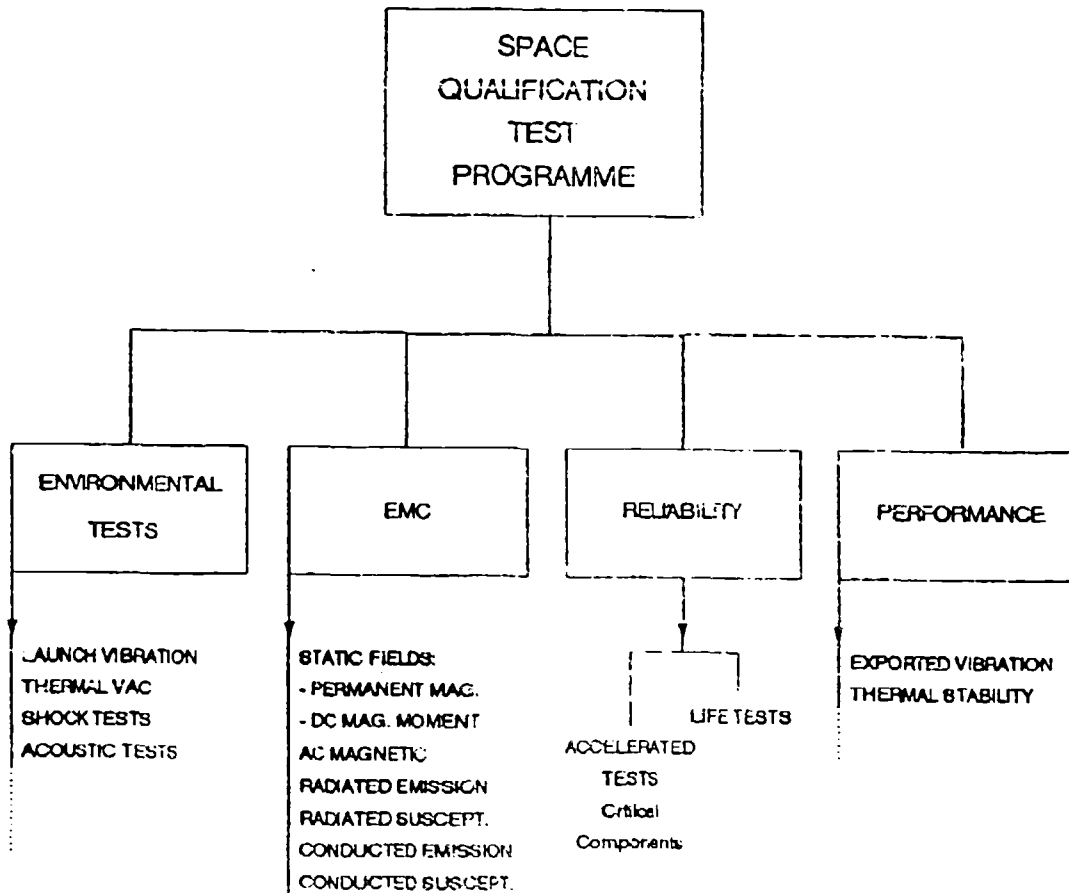


▲ Testdata — CMOD

4.0 Space Qualification Test Programme

Lucas-Lockheed cryocooler systems are undergoing space qualification testing. The test programme has been divided into four key areas of Performance, Environmental, Reliability and Electro-Magnetic Compatibility (EMC) testing as shown in Fig. 4.1.

Fig 4.1: Space Qualification Test Programme Structure



4.1 EMC

The comprehensive EMC programme is summarised in Fig. 4.1.

System level tests include AC magnetic fields and both radiated and conducted electrical emissions and susceptibility.

Permanent magnetic fields and DC magnetic moment measurements have confirmed the prediction made by Sheffield University's cooler motor FE model. Flux leakage primarily stems from the air gap as shown in Fig. 4.2. This stray flux is beneficial for motor performance and the launch damping technique described in 4.4. Outside the motor casing Lucas have minimised the permanent magnetic fields to ensure there is no interference with the cold end instrumentation.

Results for an unshielded single system are summarised in Fig. 4.3.

Even with a magnetic dipole of 12Am^2 - which can be reduced by shielding - the field in the vicinity of the cold end was less than 1 Gauss.

Field reduction techniques have been employed. For example, on the common compression space unit, the magnetically opposed motors of the compressor generated flux lines out towards the cold end (see Fig. 4.4). By reversing one of the magnets, the leakage flux has been restrained, as shown in Fig. 4.5.

Leakage minimisation is one of the design parameters for the modelling of the next generation of cryocooler motors.

Fig 4.2: FE Model of Motor showing Lines of Flux

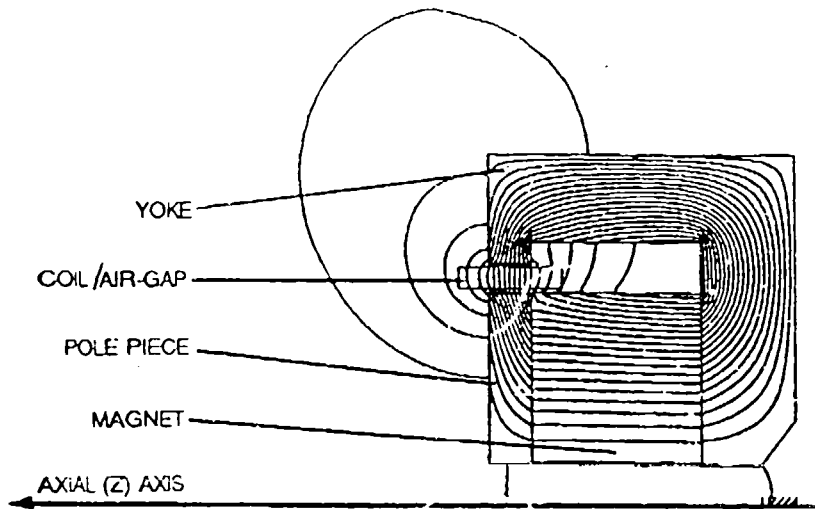


Fig 4.3: Permanent Magnet Leakage Field
Single System Results

	MAGNETIC MOMENT	MAGNETIC FLUX
EQUIPMENT	DEFENCE RESEARCH AGENCY	HALL PROBE
DISTANCE FROM UNIT:	0.5m & 1.0m	< 0.2m
FIELD STRENGTHS:	Max at 1m: 0.026 Gauss	Cold End: < 1 Gauss
MAGNETIC DIPOLE:	12Am ²	————

- Notes:
- Moment Test to ECA Spec
 - Effect of running unit < 3% of Field Strength

Fig 4.4: 'Opposed' Magnet Configuration

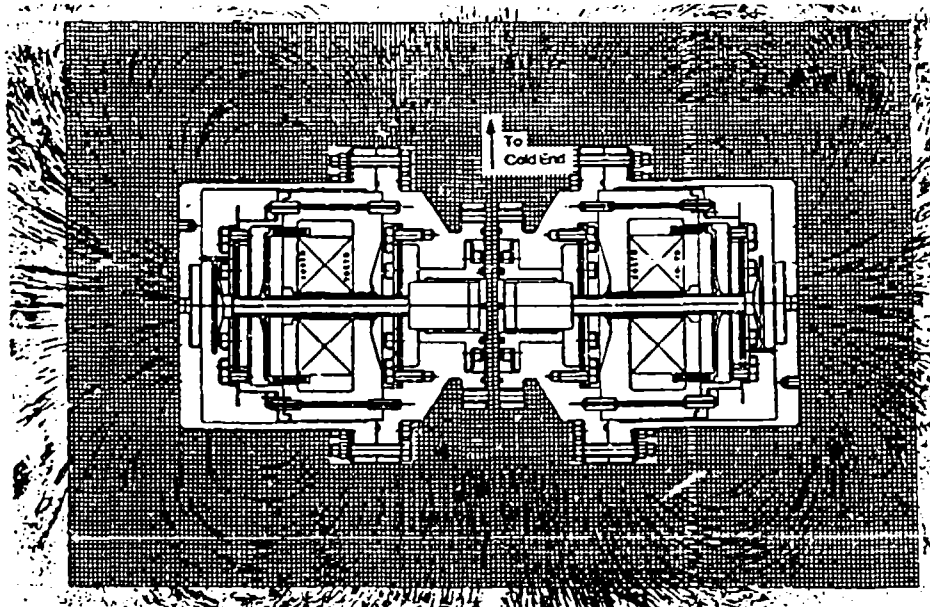
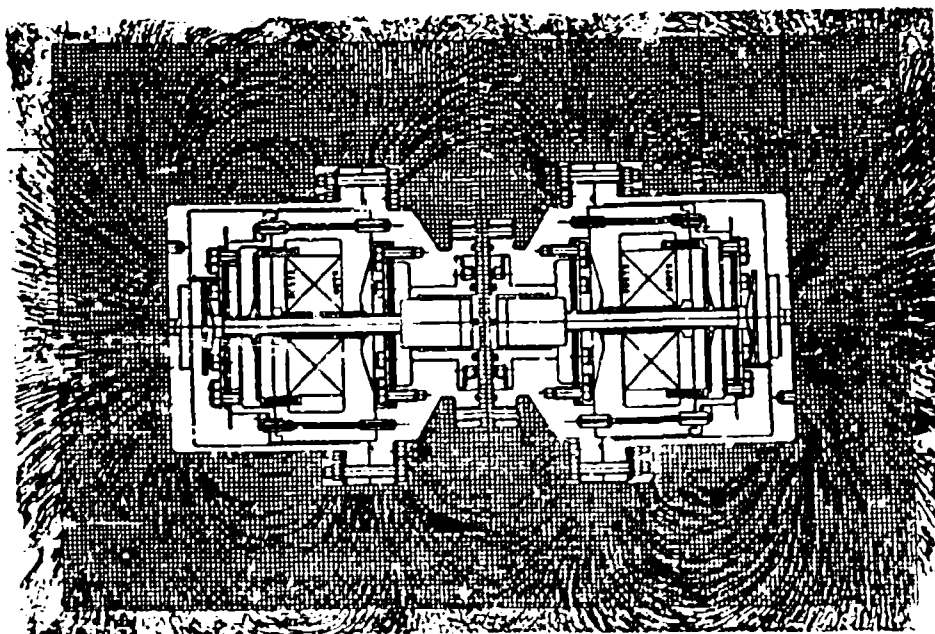


Fig 4.5: 'Aligned' Magnet Configuration



4.2 **Reliability**

To prove that the cryocoolers will outlive the duration of the mission, endurance testing continues at Lucas. The accelerated test programme will further increase the statistical confidence level of reliability data.

Reliability techniques are derived from standard Lucas processes used on safety critical systems.

4.2.1 **Life Tests**

A summary of Phase 2 endurance testing is presented in Fig. 4.6. System 3/1 completed 22,630 hours and 1000 on/off cycles. To prove the capability of the units to run horizontally in a 1g environment an endurance test is running both displacer and compressor horizontally. An automatic endurance rig capable of running six systems continuously has been developed.

Fig. 4.6 **PHASE 2 SYSTEM ENDURANCE SUMMARY**

SYSTEM	CONTINUOUS HOURS RUN	COMMENTS
3/1	22,630 HOURS INCLUDING 1000 ON/OFF CYCLES 3 YEARS RUNNING	TEST COMMENCED IN JUNE 198
1/2	590 HOURS	TEST STOPPED TO INSPECT PARTS
1/2	500 HOURS	RE-BUILD - DITTO
2/3	497 HOURS	TEST STOPPED TO INSPECT PARTS
11/3	1400 HOURS	VIBRATION WORK AT LMSC
21/4	800 HOURS	VIBRATION AND PERFORMANCE WORK AT LMSC
11/5	300 HOURS	PERFORMANCE WORK AT LUCAS
111R/2	100 HOURS	INTERNAL TEMPERATURE TESTS AT LUCAS
1R/6	200 HOURS	MODIFIED AT LMSC FOR LARGE PISTON WORK

4.2.2 Accelerated Test

Another approach to reliability testing is to overstress components. A requirement of high reliability is that the capability of a component must always be adequate for the demands imposed upon it. Suitable overstressing will cause the strength and stress distributions to overlap (see Fig. 4.8), providing a shorter time to failure. The resulting failures are analysed using a special form of Weibull' distribution to demonstrate that the reliability predictions are acceptable under normal stress. Shainin Consultants, Inc. are supporting Lucas with this overstress test programme.

The advantages of accelerated tests over life tests are that:-

- they provide greater confidence more efficiently (see Fig. 4.7);
- they verify failure rate data for FMECA reliability predictions, especially useful for mechanical components.

Accelerated tests do have limitations. The modes of failure must be known. The overstressing should increase only the failure mode undergoing study; care must be taken not to introduce new, unrepresentative causes of failure. The strength and strain distributions only need to overlap, not to be superimposed upon one another; to use Peter Shainin's expression "foolish failure" provides no useful information.

All critical cryocooler components - as highlighted in the reliability studies - will undergo accelerated testing. The parallel running of both life and accelerated test programmes will provide a high level of confidence for the systems' reliability.

Fig 4.7: Confidence Levels for Reliability Tests

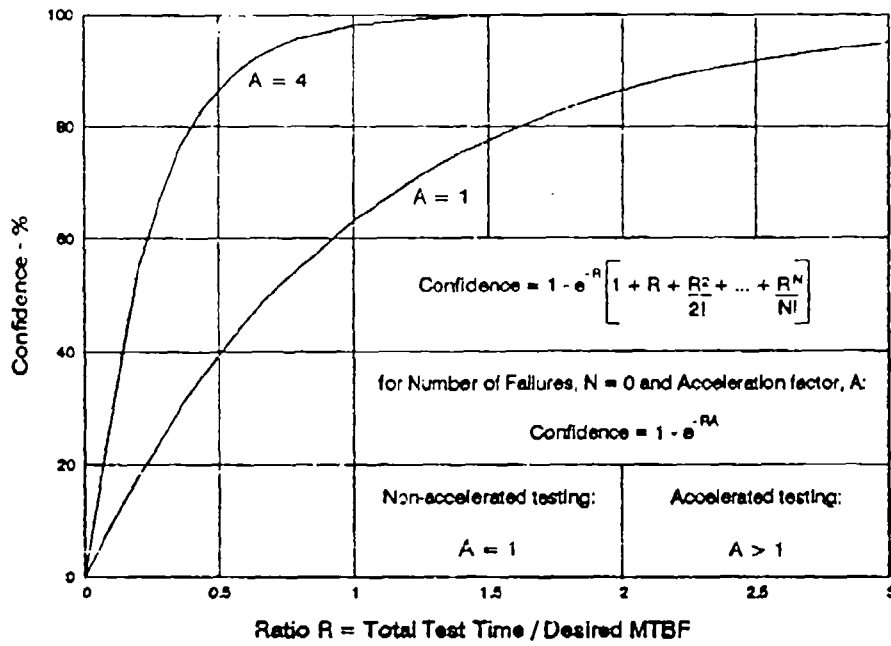
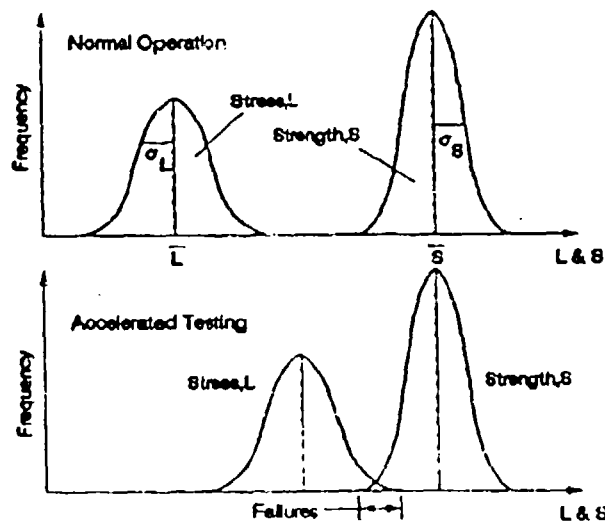


Fig 4.8: Strength & Stress Distributions



4.3 Performance - Exported Vibration

Infra-red detectors and their optical assemblies are highly sensitive to vibration. Very low vibration levels have been achieved using either active balancers or opposed units controlled by Lockheed's patented Digital Error Correction System (DECS).

Sponsored by ESA/ESTEC, absolute exported vibration levels from Lucas cryocoolers have been directly measured on a six-axis dynamometer. This high mechanical impedance system was specifically developed for such testing by Lockheed (see Fig. 4.9). The specimen table, to which the cooler components are mounted, is supported on a large granite block via six struts in a statically determinate configuration. The exported forces and torques from the cooler components are measured using six piezo-electric load cells located at the bases of the specimen table struts.

Exported vibrations have been measured for both single coolers and paired, actively balanced coolers when running with positional control (P-DECS). P-DECS accurately controls the positions of the moving masses of a system to be as close to sinusoidal as possible. The data has been analysed to determine the individual contributions from the cryocooler fundamental and harmonics in three axes. Further testing will include a force control loop (F-DECS), which actively reduces exported vibration levels.

Lockheed have also performed exported vibration tests utilising P-DECS, A-DECS (acceleration control) and F-DECS. As well as a 6-axis dynamometer, testing has been performed on an inertial platform rig. This rig is able to separately mount two compressors and two displacers on a spring platform.

With the aid of accelerometers mounted in three planes on each platform, residual compressor and displacer accelerations - and therefore out of balance forces - can be measured.

Typical results are presented in Fig. 4.10. P-DECS can provide 140:1 reduction for compressors running back-to-back. Initial tests at Lockheed suggest that a 500:1 reduction is possible with F-DECS.

Fig 4.9: Dynamometer Components

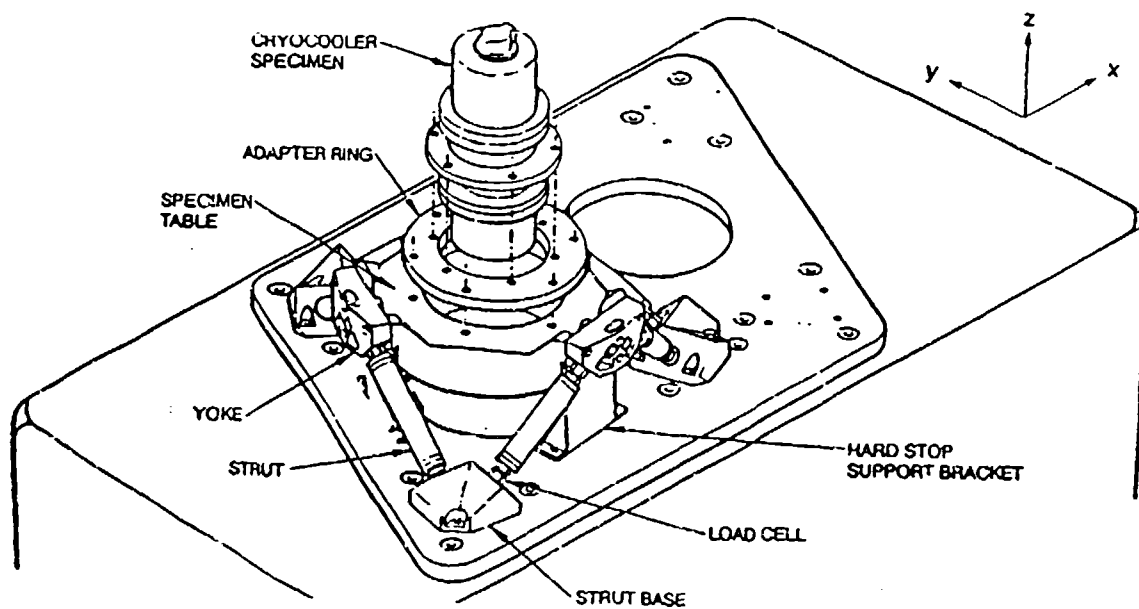


Fig 4.10: Summary of Position Control Exported Vibration Results

	COMPRESSOR 6mm stroke		DISPLACER 3mm stroke	
	SINGLE UNIT	BALANCED PAIR	SINGLE UNIT	BALANCED PAIR
Fx (N)	0.36	0.14	0.33	0.15
Fy (N)	0.38	0.17	0.73	0.13
Fz (N)	39.5	0.30	4.27	0.22
Mx (Nm)	0.09	0.020	0.102	0.017
My (Nm)	0.02	0.003	0.121	0.020
Mz (Nm)	0.05	0.004	0.022	0.010

RSS values up to 5th harmonic

4.4 Environmental Tests - Launch Vibration

To cater for the distinct characteristics of different launch vehicles, Lucas has subjected its cryocoolers to a composite specification for both sinusoidal and random vibrations at launch as detailed in Fig. 4.11.

Lucas has investigated the dynamic responses when sinusoidally excited with increasing g levels. For example, a CCS 1000 single system displacer with BeCu suspension springs required launch restraint over 4g, to ensure that the moving mass did not impact on its end stops.

Both analogue and digital control achieve this by restricting the moving masses up to the 15g maximum test level. Alternative restraint mechanisms have been devised should power not be made available to the cooler during launch. For example, magnetic damping significantly reduces the moving mass deflections. Fig. 4.12 clearly shows this damping effect on a displacer.

Fig 4.11: Laurich Vibration Spec

Composite Titan 4, Ariane 4 & 5 & Shuttle Spec

Sinusoidal:		Random:	
5 to 9 Hz	+/- 19mm	20 to 100Hz	+3dB/Oct
9 to 11.6 Hz	+/- 6g	100 to 400Hz	0.22g ² /Hz
11.6 to 22.5 Hz	+/- 11mm	400 to 2000Hz	-3dB/Oct
22.5 to 60 Hz	+/- 22.5g		
60 to 100 Hz	+/- 15g		

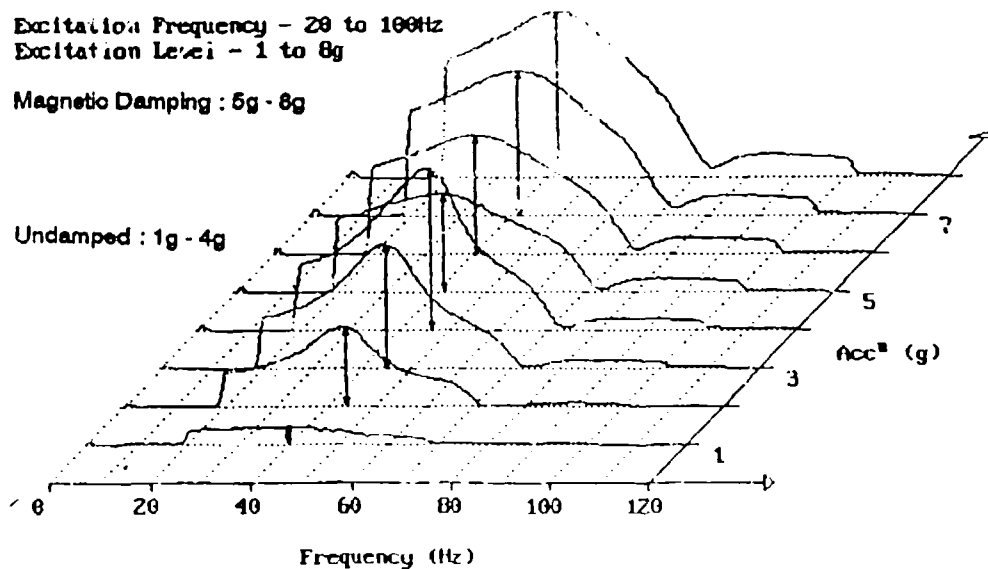
Fig 4.12: Effects of Magnetic Damping on Imported Sinusoidal Vibration

DISPLACER DISPLACEMENT SPECTRA

Excitation Frequency - 20 to 100Hz
 Excitation Level - 1 to 8g

Magnetic Damping : 5g - 8g

Undamped : 1g - 4g



5.0

CONCLUSION

Lucas has developed a range of cryocoolers which provides performance and configuration options to suit the customers' needs. Techniques used in the development and qualification of high reliability, safety-critical aeroengine fuel systems have been applied. Lucas is on schedule to achieve space qualification of its cryocooler systems to meet project requirements.

NOVEL LINEAR FLEXURE BEARING

T. E. Wong, R. B. Pan and A. L. Johnson
Vehicle and Control Systems Division
The Aerospace Corporation
2350 E. El Segundo Blvd.
El Segundo, CA 90245

ABSTRACT

Flexure bearings are a key technology for long-life, spacecraft borne cryogenic refrigerators (cryocoolers). The bearing provides frictionless, non-wearing, linear movement and radial support for reciprocating machines. It is used to maintain extremely tight clearances between piston and cylinder to form a gas "clearance seal". The objectives of the present work were to define the requirements for a cryocooler compressor flexure bearing design and to seek the best design which satisfies all these requirements.

A cryocooler compressor assembly with a typical flexure bearing, which is a spiral-cut diaphragm, was considered. An initial study to determine critical flexure design requirements for maintaining the "clearance seal" was then performed. A finite element analysis combined with a Taguchi method was used to optimize the spiral-cut flexure design. The principal goals were to minimize the flexure stress and axial stiffness while maximizing the radial stiffness. Analysis showed that (1) the flexure radial stiffness is precipitously reduced with the increase of the diaphragm axial motion; (2) high stresses occur at the edges of the diaphragm near the ends of the spiral cuts; and (3) an optimized flexure bearing with three spiral-cut fingers satisfies all of the design requirements. The analysis results of this optimized flexure bearing correlated very well with the experimental data. Review of the optimized spiral-cut flexure performance led to the invention of a novel linear flexure bearing.* This novel linear flexure bearing is a circumferential tangent cantilever cut diaphragm. A comparative analysis showed that this invention has 70% higher radial stiffness with 30% less stress than the optimized spiral-cut diaphragm. The novel linear flexure bearing requires mounting and clearance provisions that differ from the spiral cut diaphragm, however, it appears to be a superior design in that it can maintain tighter clearance seals with lower operating stress.

*Currently being considered for U.S. Patent Protection

I. INTRODUCTION

Long-life, high-reliability, space-qualified cryogenic refrigerators are a major enabling technology for infrared sensor systems on satellites. It has been shown that a linear drive, non-contacting bearing Stirling cycle cryogenic refrigerator concept is the best approach to satisfy these needs [1-2]. The key technology developments that enabled spacecraft applications of Stirling cycle cryocoolers were the use of flexure bearings and seals. The flexure bearings provide the frictionless and non-wearing support for the reciprocating components of the cryocooler. The high radial stiffness of these bearings allows for the use of non-contacting gas gap clearance seals. These bearings were first applied to cryocoolers by Oxford University [3], however, they had previously been used in an artificial heart application and in an ultraviolet sensor shutter system [4-5]. Fig. 1 shows some of the typical flexure bearing configurations used in various applications.

In general, the flexure bearing assembly consists of a stack of axially flexible cut-diaphragms with inner and outer rim/spacers. Fig. 2 shows a single diaphragm assembly. The inner rim/spacer provides support to the piston assembly. The outer rim/spacer is fastened to the compressor housing which provides support to the flexure diaphragm. An ideal flexure bearing should have the characteristics of very large radial or in-plane stiffness, minimal axial or out-of-plane stiffness, and low stresses when deflected. The radial stiffness is needed to maintain the extremely tight clearance between the piston and cylinder to form a gas "clearance seal". The axial stiffness needs to be kept low to avoid affecting the natural frequency of the spring-mass system composed of the piston and compressible gas. Low stresses in the cut-diaphragm are required to assure that the bearing will not fail due to fatigue stress. The objectives of this work were to define the specific design requirements for the cryocooler compressor flexure bearing and to

search for the best design which satisfied these requirements within practical restriction for the cryocooler.

In Section II, a cryocooler compressor assembly with a typical flexure bearing, which is a spiral-cut diaphragm, was considered. An initial study to determine critical flexure design requirements for maintaining the "clearance seal" was then performed. Other considerations, such as the allowable stress level which impacts the flexure fatigue life, are also discussed.

In Section III, the results of the nonlinear finite element analysis of a set of parametrically defined spiral-cut flexure diaphragms, analyzed using the Taguchi method to define an optimized spiral-cut flexure bearing, are presented. The analytical predictions for the optimized flexure bearing are compared with the experimental data. A review of the spiral-cut flexure stress plots involved the consideration of alternate geometry which led to the invention of a novel linear flexure bearing as presented in Section IV. A comparative analysis between this new bearing and the spiral-cut flexure bearings was performed, the results of which are presented in a summary graph comparing peak stresses and radial stiffnesses at full stroke position.

II. FLEXURE DESIGN REQUIREMENTS

A Standard Spacecraft Cryocooler (SSC) is being developed. The SSC is to provide 2 watts of cooling at 65 K and operate without maintenance for 10 years. The SSC is required to operate nearly vibration free to avoid disturbing the optics in the spacecraft. For the particular SSC considered, the compressor module was designed with two mirror-image pistons, housed within a common cylinder and operating in phase opposition for dynamic balance. Each piston, driven with its own moving coil linear motor, is supported by two stacks of spiral-cut flexure bearings. The compressor is designed with all metal components, and uses gas

gap clearance seals to avoid wear-out. The tight clearance seal between the piston and the cylinder is designed to separate the compressor working fluid from the plenum volume which contains the drive motor. Since the cryocooler must be extensively tested on the ground prior to flight, the clearance must also be maintained in a 1 G (gravity) environment.

To establish the cryocooler flexure bearing design requirements, a simplified model as shown in Fig. 3 was used to analyze the deflection response of the motor piston assembly under a 1 G radial environment. Excessive tip deflection causes loss of the clearance seal and potential rubbing of the piston on the cylinder. The assumptions made in this model are: (1) the flexure bearing mass is negligible when it is compared to the motor and piston mass; (2) the front and back flexures' centers of effort are located at the center of each group of springs; and (3) the piston radial stiffness is much higher than the flexure bearing radial stiffness. Based on this model, the piston tip deflection under one G gravity load can be estimated by the formula below:

$$\text{Tip Deflection} = \left\{ \frac{E/D}{1 + C(A/B)/(C + D)} + 1 \right\} (1 + C/D)(Fg/A) \quad (1)$$

where:

- A, B = Radial spring constants of front and back flexure groups, respectively
- E = Number of flexures within each group multiplied by the radial stiffness of a single flexure
- C = Distance between front flexure group and the piston assembly center of gravity (C.G)
- D = Distance between front and back flexure groups
- E = Distance between front flexure group and piston tip
- F = Total mass of the piston and motor
- g = Gravity acceleration, 9.8 m/sec²

According to the existing compressor design data shown in Table 1, using a piston tip deflection in Eq. (1) equal to the desired clearance seal gap, the required radial stiffness at full stroke is calculated to be 1890 N/cm. Based on the natural frequency of the piston assembly drive motor, the moving mass, and the combined mechanical and pneumatic spring rate, the allowable axial stiffness of the flexure assembly is determined to be less than 60 N/cm.

To assure a 10-yr fatigue life (10^{10} cycles for flexures), the peak stress (von Mises) in the flexure must be minimized. Fig. 4 shows the S-N fatigue resistance characteristics of a typical flexure material under reverse bending [11]. However, the problem in flexure design is that the stresses are not caused by bending alone, but are induced by a combination of bending, tensile, and torsional stresses. Unfortunately, fatigue data out to 10^{10} cycles has not been published. An approximate reliability analysis indicated that the peak stress for high quality stainless steel spring stock should be limited to approximately one half of the 50% endurance limit. For the particular material selected, this limiting stress is 415 MPa. All of the flexure design requirements were then summarized in Table 2. Several practical matters also influenced the study. These include: (1) maintaining the existing compressor configuration required retaining the original flexure inner and outer radii, and limited the total number of flexure diaphragms to 15; (2) the flexure thickness was constrained to be 0.12 mm due to material availability; and (3) the flexure rotation about its axis at full stroke (maximum axial deflection) was limited to about 1° in order to avoid any potential dynamic instability during operation.

III. SPIRAL-CUT FLEXURE DESIGN OPTIMIZATION

The geometry of a spiral-cut flexure finger can be defined by the equation

$$R = R_i + (R_o - R_i) f(\phi)^N \quad (2)$$

$$f(\phi) = a\phi + b\phi^3 + c\phi^5 + d\phi^7, \quad \phi = \theta / \theta_{max} \quad (3)$$

where R_i = Inner radius of the spiral

R_o = Outer radius of the spiral

θ = <Range from 0 to θ_{max} >

θ_{max} = Flexure finger sweeping angle

In order to determine the coefficients in the power series function $f(\phi)$, note that

$$f(1) = 1$$

$$df(\phi)/d\phi = S_i, \text{ at } \phi = 0 \text{ (the slope intercept of the function at inner radius)}$$

$$df(\phi)/d\phi = S_o, \text{ at } \phi = 1 \text{ (the slope intercept of the function at outer circle)}$$

$$\text{let } f(M) = M; 0 < M < 1 \quad (4)$$

In general, the coefficients of a , b , c , and d in Eq. (3) can be obtained by solving the 4x4 simultaneous equations when M , S_i , and S_o are given. To prevent any unrealistic spiral-cut flexure design with crossed fingers, the values of M and N in Eqs. (2) and (4) were limited from 0.4 to 0.6, and 1.0 to 1.25, respectively. The slopes of intercept S_i and S_o were also limited to be in the range of 0.8 to 1.2.

In the parametric study, three and six-finger flexures with 180° and 240° sweeping angles were examined. The Taguchi experimental design technique combined with the results of finite element analysis of the various configurations were used to optimize the spiral-cut finger geometry. The principal goal of this effort was to minimize the flexure stress and axial stiffness while maximizing the radial stiffness. Table 3 shows the six selected governing parameters and their variations. An analysis matrix of L_9 orthogonal array [6-10] was established to

study the criticality of these parameters (Table 4). The interaction effects between these parameters were also assumed to be negligible. Since the present parametric study only analyzes the impact on flexure performance of the spiral-cut finger geometry in Eqs. (2), (3), and (4), a parameter corresponding to the width of the spiral finger gap is not included in Table 3.

Coarsely meshed finite element models associated with the geometries defined in the L_8 orthogonal array in Table 4 are shown in Fig. 5. Each finite element model consists of about 500 shell elements and 600 nodes. The radial and axial stiffnesses and the peak stress were calculated at maximum stroke of the flexure. Due to the flexure's large deflection relative to its thickness, the nonlinear geometric analyses were performed with the ABAQUS finite element code on a CRAY supercomputer. The ABAQUS code is a general purpose finite element analysis program with special emphasis on advanced nonlinear structural engineering application. Thus, this code was chosen to characterize the flexure bearing performance. The analytical results of these eight models are listed in the last three columns in Table 4. A convergency study by refining some of these eight models was also performed and indicated that the coarsely meshed models in Fig. 5 can provide accurate results in radial and axial stiffnesses. However, the stresses in this table were underestimated due to the nature of coarse models and are only used for relative comparison between these eight models. The impact of the parameters on the flexure radial and axial stiffnesses, and the peak stress are shown in Figs. 6, 7, and 8, respectively. From these figures, it can be seen that parameters K and L, the number of fingers and flexure finger sweeping angles, have the most significant impact on the flexure responses. Parameter G is the next highest one on the list. Another approach to quantify the results is to use the analysis of variance method (ANOVA) [6-10]. For the case of the flexure radial stiffness, the ANOVA analysis results are shown in Table 5. The last column in this table shows the percentage of contribution of each parameter for the flexure radial stiffness. It can be seen that parameters K and L, with the highest

percentages, are the most significant parameters for the flexure radial stiffness. Using the ANOVA method, similar conclusions can be reached for the axial stiffness and the peak stress.

The parameter levels of G_1 , K_1 , and L_1 were chosen for the flexure design. The other three parameters in the flexure configuration were chosen to be H_2 , I_2 , and J_2 . Thus, the flexure geometry setting is selected to be $G_1H_2I_2J_2K_1L_1$. This parameter setting defines the preferred flexure configuration.

Analysis results indicated that the high stress concentrations were located at the two supporting ends of the spiral-cut finger. A flexure with six fingers will have twice the number of single-point failures compared to a three-finger flexure, and is thus less reliable. The three-finger flexure was thus chosen for further study. To improve the accuracy in peak stress calculation, a refined finite element model using the preferred parameter setting defined earlier was constructed with finer meshed elements at the ends of the spiral cuts (Fig. 9a). With a gap of 5.08 mm between the fingers, finite element analysis results indicated that the peak stress was 508 MPa (Table 6, first row), which is larger than the 415 MPa requirement. Therefore, additional modification was required on the flexure design. According to the data shown in Fig. 8f, it was estimated that peak stress can be reduced to within the design requirement by increasing the flexure finger sweeping angle from 180° to 220° . Another finite element model consisting of 1671 shell elements and 1762 nodes was then constructed (Fig. 9b), with the preferred parameter setting and a 220° sweep angle. The width of the spiral finger gap was also changed to 1.27 mm to compensate for the decrease of the flexure radial stiffness due to the increase of flexure finger sweeping angle. The results for the flexure radial and axial stiffnesses are shown in Figs. 10a and 10b. Fig. 10a shows that the radial stiffness is a function of the flexure axial displacement and is significantly lower at full stroke. The von Mises stress contour plot at full stroke is shown in Fig. 11a. It can be seen that the peak stress is again located at the hub and

wheel of spiral-cut fingers. The normalized displacement contour in Fig. 11b shows that the finger edge can curl up like a potato chip and deflect more than the hub. Analysis results of this design (Fig. 9b) are summarized in the second row of Table 6. This design satisfies the requirements of the flexure radial stiffness and the peak stress listed in Table 2.

In summary, a three-finger flexure with a 220° sweep angle and a 1.27 mm width slot is an optimized configuration. This design was fabricated and tested with success. The radial and axial stiffness measurements were within 5% of the finite element analysis prediction.

For the compressor module, the final design configuration required a combination of 8 and 4 flexures in the front and back flexure groups respectively. The maximum axial stiffness of the assembly at full stroke is calculated to be 39.6 N/cm with 12 flexures. As a consequence of the new design, all of the design requirements for the compressor in Table 2 are thus satisfied. From Eq. (1), the piston tip deflection at the full stroke was calculated to be 55% of the nominal gap clearance which is within the tolerance allowed for the piston clearance seal. Subsequent tests indicated that the compressor with the optimized three-finger spiral flexures maintained the clearance seal allowable dimension through out tests.

IV. LINEAR FLEXURE BEARING INVENTION

Earlier analysis results indicated that the high stresses in the spiral fingers were caused by a combination of bending, tensile, and torsional loads. To assure a high fatigue reliability of the flexure at 10^{10} cycles, the magnitude of these stresses had to be reduced by some means. One of the possible approaches would be to more effectively utilize the flexure material and redistribute the high stresses over a larger region. Another approach would be to eliminate the geometric stress concentration by "pushing" the peak stress away from the spiral

finger hub and wheel. By examining the earlier finite element analysis results, it was realized that the torsional warping of the spiral flexure is the major feature which contributes to high stresses. Therefore, a third approach to minimize the flexure stress is to reduce the torsional warping of the flexure.

A novel flexure design utilizes a translating spider to allow the incorporation of circumferential tangent cantilever flexures. These cantilever flexure blades are sandwiched between spacers. The flexure support points are defined by extensions to the spacers located at the hub and on the spider.

Under small deflections, the tangent-cantilever flexure blades behave like a simple beam under pure bending. Under large deflection, as in the case of the cryocooler compressor application, the amount of undesirable torsional warping of the blades is significantly reduced. Therefore, the deflected blades tend to be stressed primarily in bending. This argument was investigated by finite element analysis. A detailed finite element model, consisting of 1335 shell elements and 1450 nodes, was constructed to delineate the performance characteristics of the novel linear flexure (Fig. 12). Figs. 13a and 13b show the von Mises stress and normalized displacement contours in blades at full stroke. The results are also summarized in the third row of Table 6. Based on the deflection pattern in Fig. 13b, it was recognized that the peak stress can be further reduced by modifying the spacer pattern to provide better control of the flexure deflection. A refined finite element model of this new configuration (Fig. 14), consisting of 2430 shell elements and 2551 nodes, was constructed. The analysis results are summarized in the last row of Table 6. The stiffnesses and the stress and normalized displacement contours are shown in Figs. 15 and 16, respectively. The stress contour in Fig. 16a indicates that the stress has been almost uniformly distributed across the blade width. Peak stresses also tend to be less concentrated than those of the spiral-cut diaphragm. In a comparison of the results in Table 6, it can be seen that the novel linear flexure has 70% higher radial stiffness with 30% lower

stress than the optimized spiral-cut diaphragm. A summary graph comparing the peak stresses and the radial stiffnesses of the novel linear flexure bearing and the spiral-cut flexure bearings at the full stroke position are shown in Fig. 17. It can be also seen that this new bearing appears to be a superior design. Optimization of the novel flexure bearing design promises to result in even more significant improvements. The novel linear flexure is being incorporated into the next generation of the cryocooler designs.

V. CONCLUSIONS

Design requirements for flexure bearings were derived to ensure maintenance of the clearance seal between the piston and cylinder. The flexure radial stiffness at the full stroke position must be greater than 1890 N/cm with the existing configuration of the compressor module. A Taguchi experimental design approach, combined with a nonlinear finite element analysis, was used to seek an optimized spiral-cut flexure diaphragm with a limited number of the finite element analysis runs. Analysis showed that: (1) the flexure radial stiffness precipitously reduces with the increased axial displacement; (2) peak stresses occur at the extreme edge of the ends of the spiral cuts; and (3) an optimized flexure bearing with three spiral-cut fingers can be configured to satisfy all of the design requirements. The analytical prediction of this optimized flexure bearing correlates very well with the experimental data.

A review of the spiral-cut flexure stress contour maps led to the invention of a novel linear flexure bearing. This novel linear flexure bearing is a circumferential tangent cantilever-cut diaphragm. A comparative analysis shows that this new design has 70% higher radial stiffness with 30% less stress than the optimized spiral-cut diaphragm at the full stroke position. The novel linear flexure bearing is thus a superior design in both maintaining gas gap clearance seal dimension and reducing the probability of long life fatigue failure.

REFERENCES:

1. Johnson, A. L., "Spacecraft Borne Long Life Cryogenic Refrigeration Status and Trends," *Cryogenics*, pp. 339-347, July 1983.
2. Henderson, B. W., "U. S. Industry Close to Producing Long-Life Space Cooling System," *Aviation Week & Space Technology*, 6 April 1992.
3. Davey, C., "The Oxford University Miniature Cryogenic Refrigerator," *International Conference on Advanced infrared Detectors and Systems*, London, pp. 39, 1981.
4. Johnston, R. P., et. al., "A Stirling Engine with Hydraulic Power Output for Powering Artificial Hearts," Paper 75212, *IECEC Record* 1975.
5. Curtis, P. D., et. al., "Remote Sounding of Atmospheric Temperature from Satellites. V - The Pressure Modulator Radiometer for Nimbus F," *Proc. R. Soc. (London)*, A 337, pp. 135-150, 1974.
6. Schmidt, S. R. and Launsby, R. G., Understanding Industrial Designed Experiments, CQG Ltd. Printing, 1989.
7. Phadke, M. S., Quality Engineering Using Robust Design, Prentice Hall, Englewood Cliffs, NJ, 1989.
8. Ross, P. J., Taguchi Techniques for Quality Engineering, McGraw- Hill, New York, NY, 1988.
9. Quinlan, J., "Design Optimization: Application of Taguchi Methods to Finite Element Analysis," *ASI Taguchi Method Symposium*, pp. 233- 248, 1987.
10. Montgomery, D. C., Design and Analysis of Experiments, John Wiley & Son, 2nd edition, 1984.
11. SANDVIK Steel Company, Stainless Spring Material , S-3, 41-ENG, pp. 18, January 1984.

Table 1. Existing Configuration of Compressor Module

Radial stiffness of front flexure group (N/cm)	6xS*
Radial stiffness of back flexure group (N/cm)	4xS
Distance between front flexure group and C.G. of piston assembly (cm)	2.54
Distance between front and back flexure groups (cm)	5.59
Distance between front flexure group and piston tip (cm)	8.89
Total mass (kg)	0.364

* S = Radial stiffness of single flexure

Table 2. Flexure Design Requirements

Radial Stiffness of Single Flexure	> 1890 N/cm
Von Mises Peak Stress	< 415 MPa
Total Axial Stiffness (All Flexures)	< 60 N/cm

Table 3. Input Parameters in Spiral-Cut Flexure Diaphragm Parametric Study

Parameter	Description	Level one	Level two
G	Slope intercept of the spiral function at inner circle, S_i	1.2	0.8
H	Slope intercept of the spiral function at outer circle, S_o	1.2	0.8
I	Value of M in Eq. (4)	0.4	0.6
J	Value of N in Eq. (2)	1.0	1.25
K	Number of flexure fingers	3	6
L	Flexure finger sweeping angle, θ_{max}	180°	240°

Table 4. Parametric Study Matrix/Response in Spiral-Cut Flexure Diaphragm

Analysis Run	Parameter						Radial* Stiffness (N/cm)	Axial Stiffness (N/cm)	Peak* Stress** (Mpa)
	G	H	I	J	K	L			
1	1	1	1	1	1	1	6440	7.93	351
2	1	1	1	2	2	2	298	1.68	128
3	1	2	2	1	2	2	167	1.33	122
4	1	2	2	2	1	1	7890	8.63	362
5	2	1	2	1	1	2	2594	2.84	145
6	2	1	2	2	2	1	2093	3.80	243
7	2	2	1	1	2	1	1802	3.26	170
8	2	2	1	2	1	2	1599	3.61	161

* At full stroke position

** Stress concentrations are not included at the ends of spiral cuts

Table 5. ANOVA Table for Spiral-Cut Flexure
Taguchi Analysis in Radial Stiffness

Source	df	S (10 ⁴)	V (10 ⁴)	S' (10 ⁴)	F	P (%)
G	1	562	562	522	14	9
H	1	0	0	--	--	--
I	1	85	85	--	--	--
J	1	10	10	--	--	--
G*J	1	65	65	--	--	--
K	1	2507	2507	2467	63	45
L	1	2301	2301	2261	58	41
Error	4	160	40	280	--	5
Total	7	5530		5530		100

where df = degree of freedom
 S = sum of square
 $V = S / df$
 $S' = S - (df) (V_{error}), \quad V_{error} = 40 \times 10^4$
 $F = V / V_{error}$
 $P = S' / S_{total}, \quad S_{total} = 5530 \times 10^4$

Table 6. Flexure Diaphragm Characteristics

Flexure Type	Stiffness (N/cm)		Von Mises Peak* Stress (MPa)	Axial Rotation* (Degree)
	Radial*	Axial		
Spiral-cut Diaphragm in Figure 9a	3443	4.55	508	1.34
Optimum Spiral-cut Diaphragm in Figure 9b	2777	3.30	415	1.12
Cantilever-cut Diaphragm in Figure 12	5012	3.64	469	0.88
Cantilever-cut Diaphragm in Figure 14	4695	3.04	274	0.83

* At full stroke position

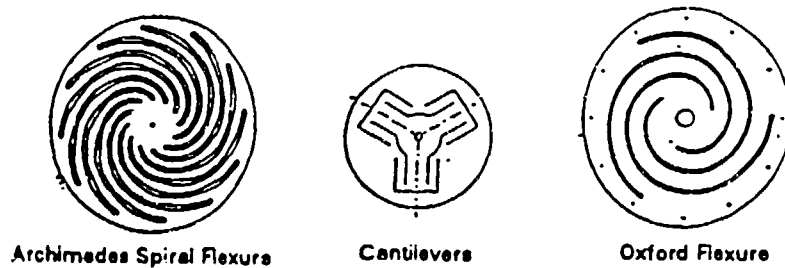


Figure 1 Typical Flexure Bearings

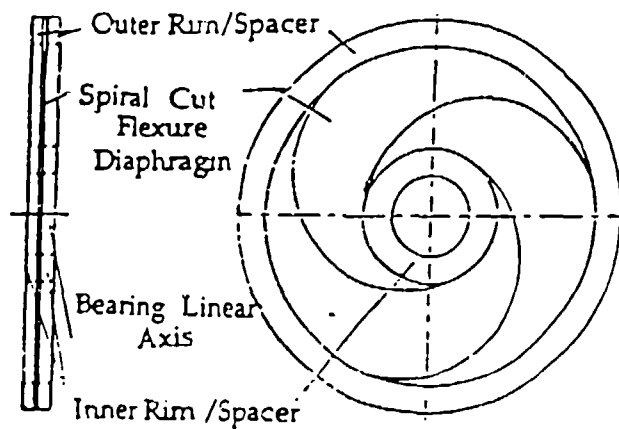


Figure 2 General Topology - Spiral Cut Linear Flexure Bearing

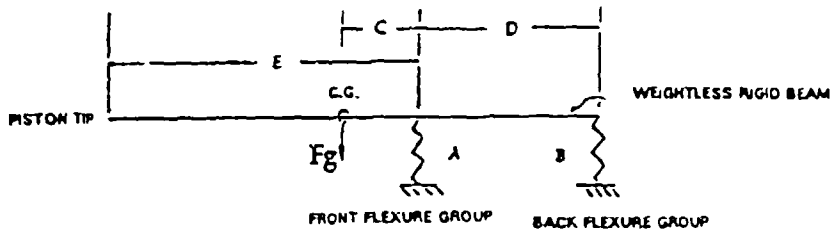


Figure 3 Compressor Module Mathematical Model

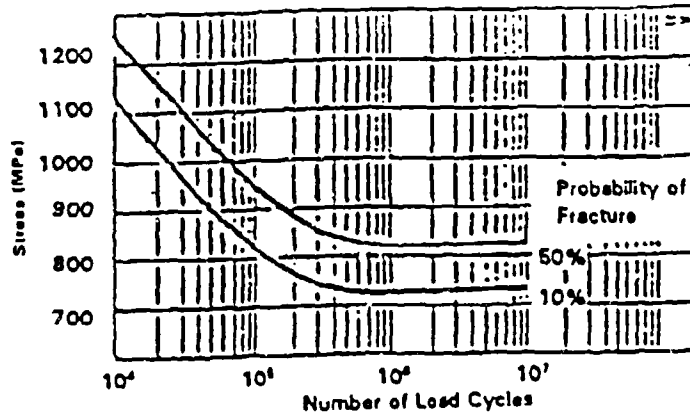


Figure 4 Typical Flexure Steel Reverse Bending Fatigue Failure Characteristics

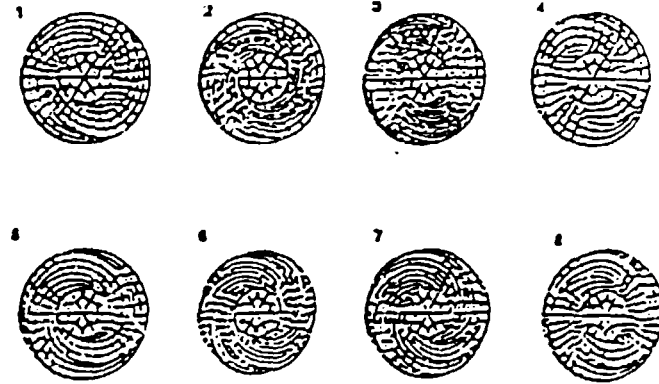


Figure 5 Flexure Finite Element Model

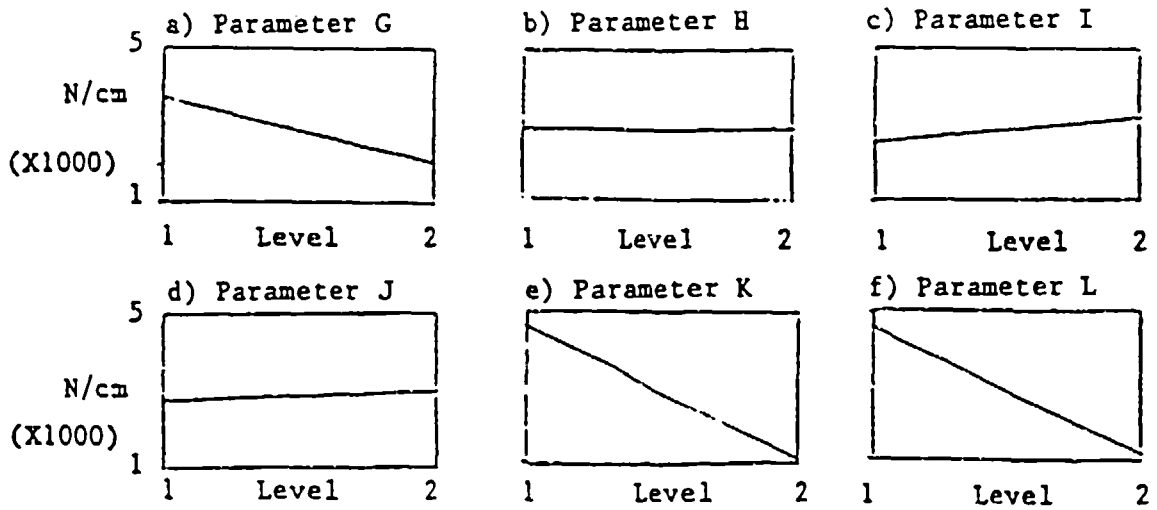


Figure 6 Flexure Parameter Effects on Radial Stiffness

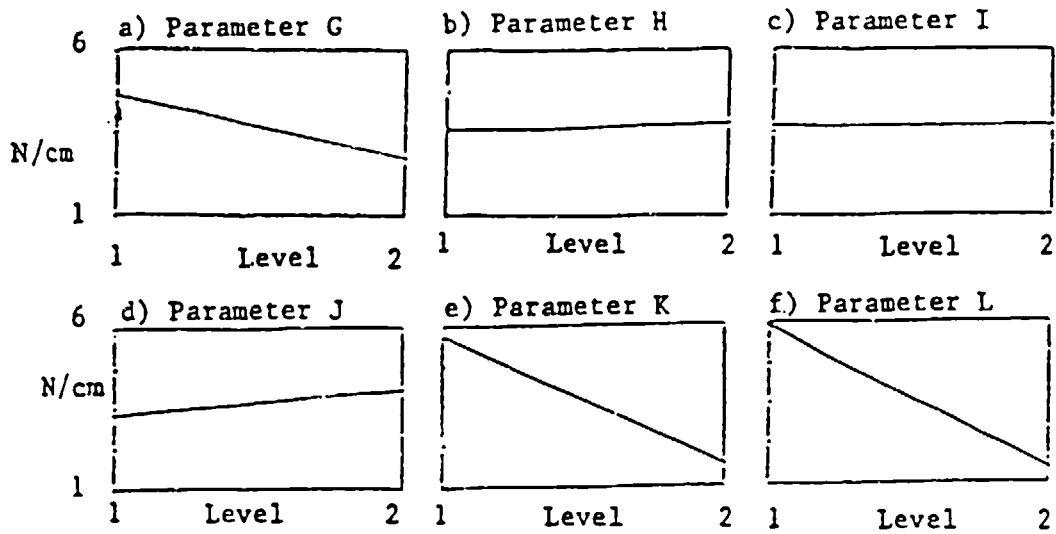


Figure 7 Flexure Parameter Effects on Axial Stiffness

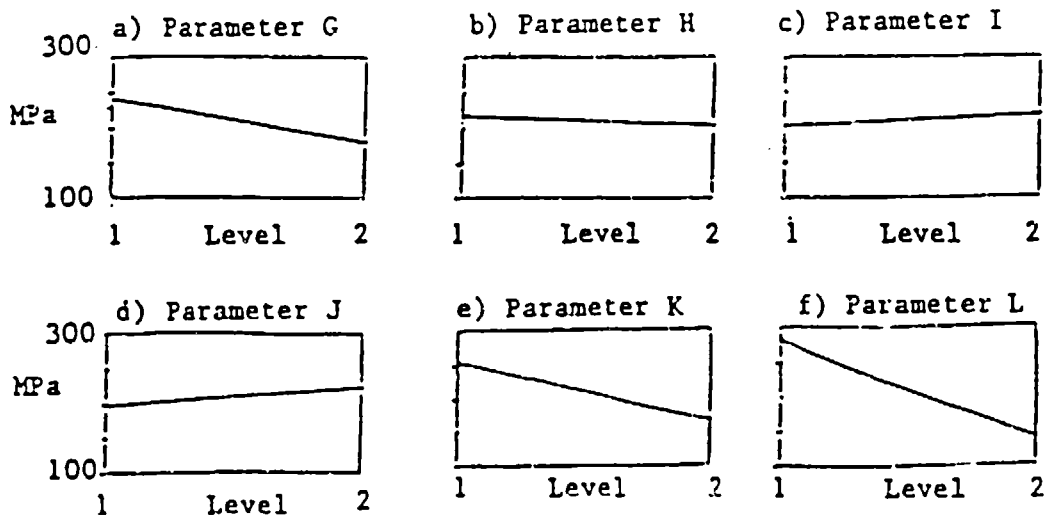


Figure 8 Flexure Parameter Effects on Peak Stress

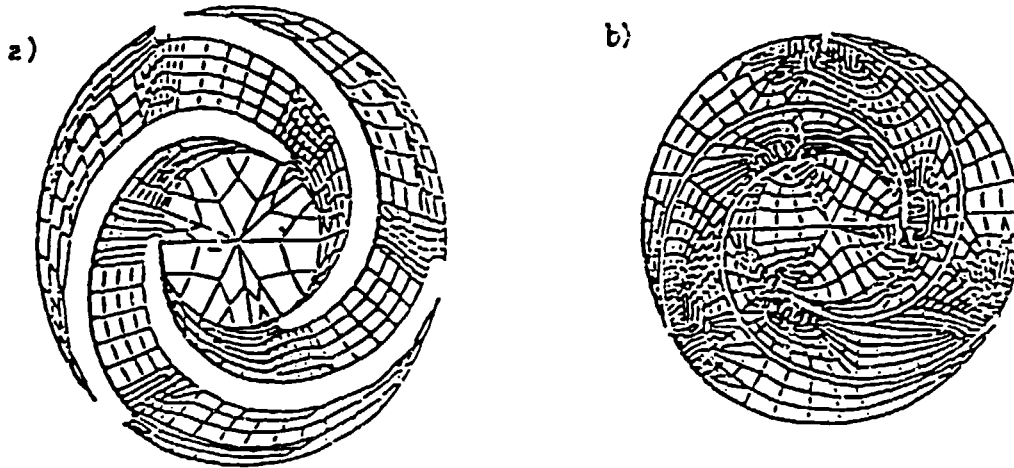


Figure 9 Flexure Refined Finite Element Models

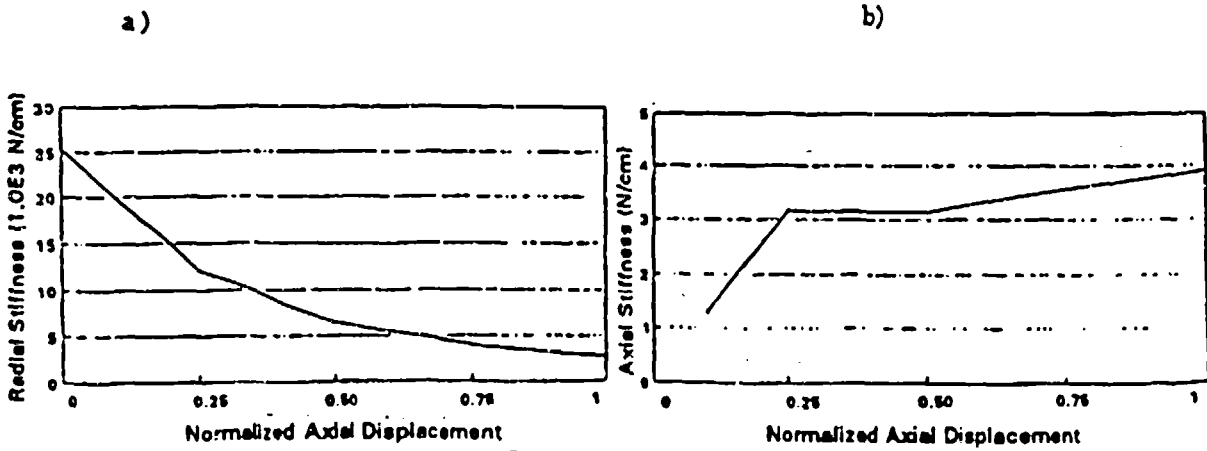


Figure 10 Axial and Radial Stiffnesses for Flexure in Figure 9b

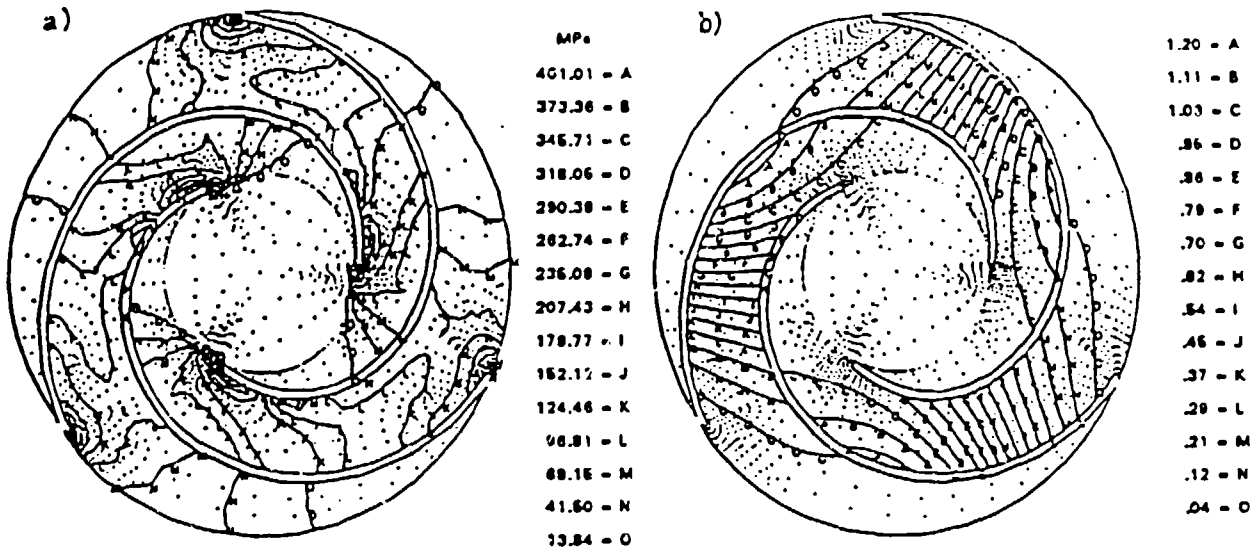


Figure 11 Von Mises Stress and Normalized Displacement Contours for Flexure in Figure 9b

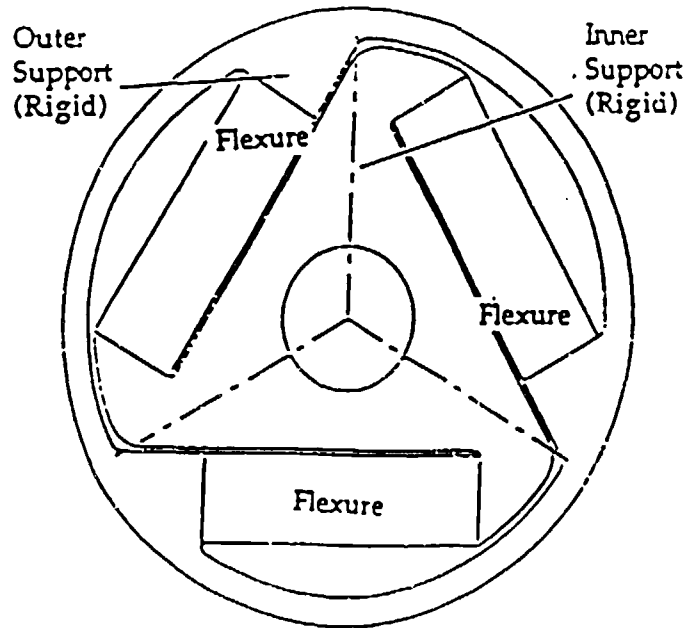


Figure 12 Circumferential Tangent Cantilever-Cut Linear Flexure Bearing

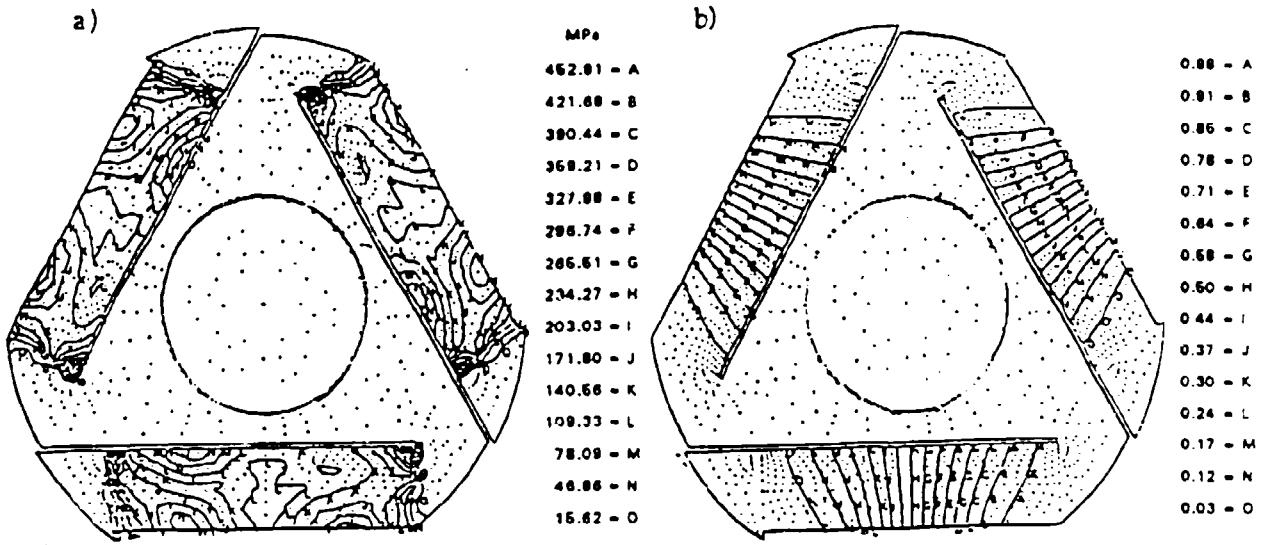


Figure 13 Circumferential Tangent Cantilever-Cut Linear Flexure Bearing von Mises Stress and Normalized Displacement Contours

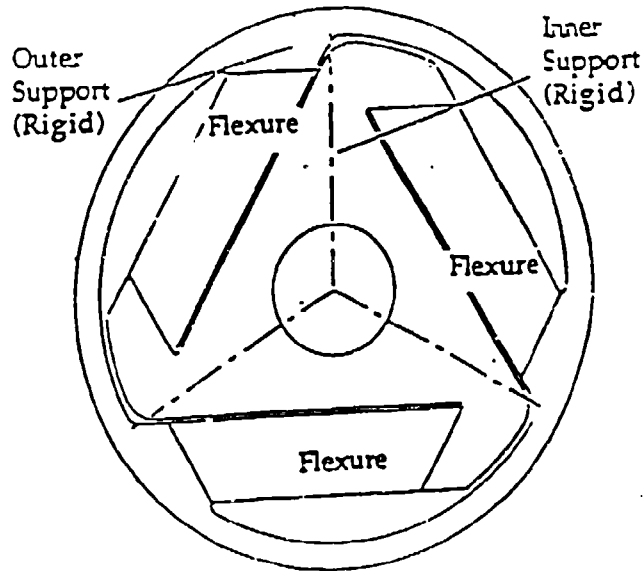


Figure 14 Novel Linear Flexure Bearing

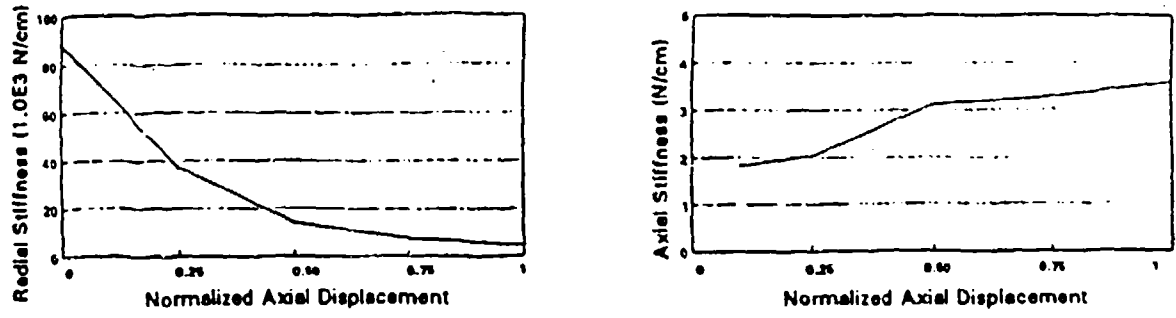


Figure 15 Novel Linear Flexure Bearing Axial and Radial Stiffness

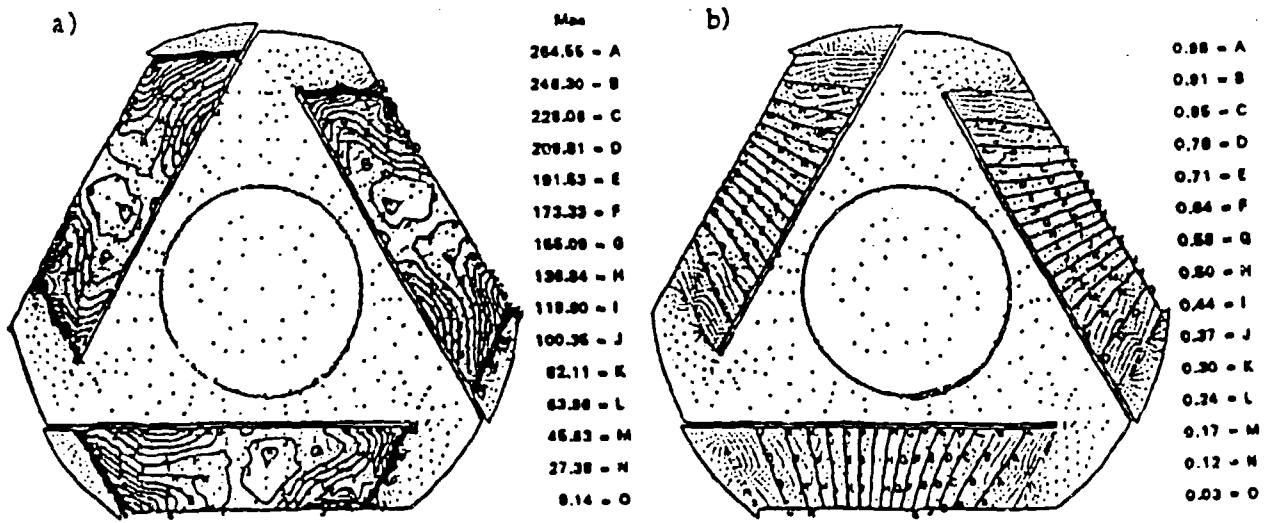


Figure 16 Novel Linear Flexure Bearing Stress and Normalized Displacement Contours

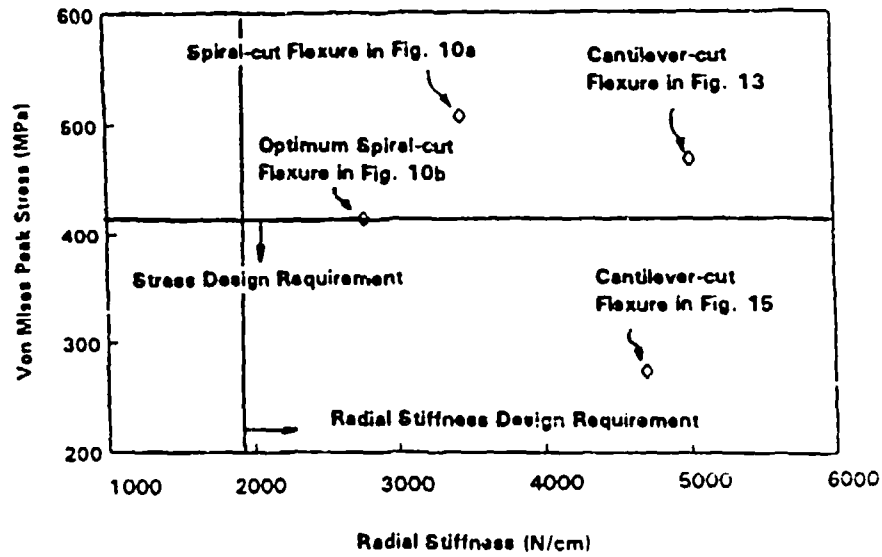


Figure 17 Flexure Diaphragm Characteristics

NASA/GSFC CRYOCOOLER TEST PROGRAM RESULTS

Leroy Sparr, Robert Boyle, Richard Cory and Frank Connors
Cryogenics, Propulsion and Fluid Systems Branch
National Aeronautics and Space Administration
Goddard Space Flight Center
Greenbelt, MD 20771

Edward James, Richard Fink
McDonnell Douglas Corp.
Greenbelt, MD.

Vincent Arillo, John Marketon
Hughes STX Corp.
Greenbelt, MD.

I INTRODUCTION

Evaluation testing of three single stage, split Stirling cycle, nominal 80K cryocoolers is underway at the cryocooler test facility at NASA, Goddard Space Flight Center (GSFC). These include a British Aerospace (BAe) unit, advertised as a flight qualified design, and cryocoolers from Lockheed/Lucas and Hughes Aircraft which were purchased as technology demonstration models. These cryocoolers have several common design features. The compressor piston and the displacer use non-contacting clearance seals, are driven by linear motors, and are supported by two stacks of flexure spring bearings. Stroke and phase adjustments are controlled by the electronics. Both the BAe and the Lockheed/Lucas cryocoolers use an organic material liner on the piston in the clearance seal area to avoid galling of moving metallic surfaces in the event of touch contact. Hughes uses an all metal design. All of the cryocoolers have a resistive heating element on the cold tip for the simulation of instrument heat loads.

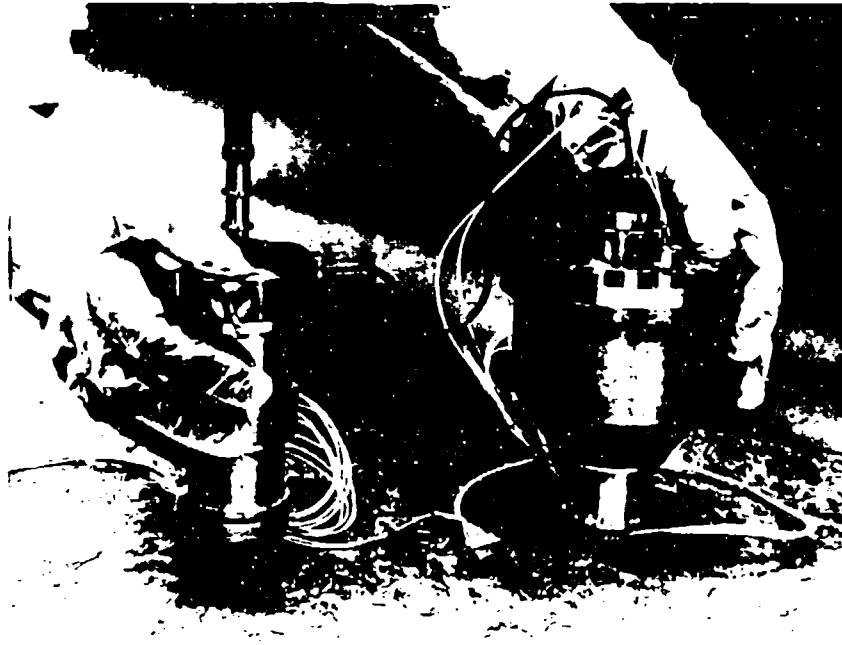
Since December, 1990, the BAe cryocooler has operated for over 2500 hours. Since mid-1992, the Hughes Aircraft and the Lockheed/Lucas cryocoolers have undergone over 100 hours of performance evaluation at GSFC. The Lockheed/Lucas cryocooler has also undergone over 350 hours of testing at Lockheed prior to delivery. The BAe cryocooler and the Lockheed/Lucas cryocooler have been operated in a vacuum environment at temperatures ranging from -25°C to +20°C. The BAe has undergone extended test runs for periods up to 40 days. The Hughes cryocooler has been operated only in ambient laboratory conditions. Similar thermal and residual vibration tests have been conducted on each of the three cryocoolers.

Some of the testing efforts required modifications to, and in some cases, replacement of, the electronics provided by the cryocooler suppliers. For each cryocooler, GSFC designed and fabricated a 6-axis force dynamometer and a heat removal system to permit the cryocoolers to be operated in the vacuum chamber. In addition, the vibration cancellation system, described by Boyle, et. al. in reference 1, was used to reduce vibration, and the results are compared to those measured in the as-received condition.

II CRYOCOOLER DESCRIPTION

IIa BAe CRYOCOOLER

The BAe cryocooler is hermetically sealed and provides a nominal 0.8 watts cooling at 80K with a compressor power of 35 watts. The single compressor and single expander assemblies are connected by a 10 inch copper transfer line. The compressor weighs approximately 3.5 kg and the expander weighs approximately 1.1 kg. The cryocooler housing is made of titanium with copper heat exchange surfaces on both the compressor and expander.



Photograph of the British Aerospace 80 K Cryocooler (courtesy of BAe).

Initial baseline vibration and thermal tests were conducted with the BAe supplied laboratory electronics. However, internal noise, the lack of a data collection system and insufficient

autonomous protection features led GSFC to design, fabricate, and integrate a custom electronics system. This system incorporated very low noise linear power amplifiers, general purpose interface bus (GPIB) programmable arbitrary waveform generators, high speed analog to digital converters, a precision power analyzer, and real-time, high speed positive and negative piston overstroke protection. The goal was to permit long term, unattended operation with automatic protection and graceful shutdown capability in the event of a hardware problem. User selectable data sampling rates of operational parameters were designed into the data collection system.

The cryocooler contains Linear Variable Differential Transformer (LVDT) position sensors for both the compressor and expander. The cold tip is instrumented with a platinum resistance thermometer to measure temperature, and its heat sink temperature is regulated while in a vacuum environment.

Additional instrumentation continually monitors the following cryocooler parameters:

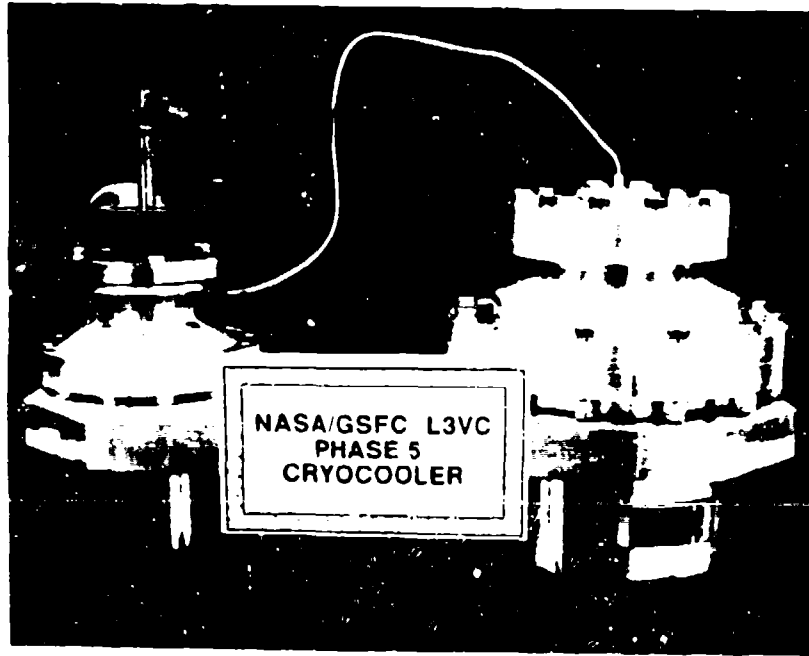
- hours of operation
- 14 thermocouples
- Cold tip temperature and heater power
- Cold tip bonnet vacuum level
- Chamber vacuum level
- Compressor
 - motor RMS current, voltage, and power
 - motor power factor
 - piston peak-to-peak stroke and offset (mm)
- Displacer
 - stroke level peak-to-peak and offset (mm)

The parameters which can result in an automatic shutdown are:

- Any one of 14 thermocouples exceeding 38 °C.
- Compressor power >40 Watts true power
- Uninterruptable power supply battery low indication
- Excessive compressor piston positive/negative travel
- Excessive displacer positive/negative travel
- A compressor power factor less than .75
- Heat load cutoff when cold tip temperature is >150 Kelvin

IIb LOCKHEED/LUCAS CRYOCOOLER

The Lockheed/Lucas Model 1707 cryocooler is hermetically sealed and provides over .9 watts cooling at 80K at maximum stroke. The single compressor and single expander are connected by a 10 inch stainless steel transfer tube. The compressor weighs 4.2 kg and the expander weighs about 0.8 kg. The compressor and expander housings are made of aluminum.



Photograph of the Lockheed/Lucas 80K Cryocooler (courtesy of Lucas).

The cryocooler includes capacitive position sensors for both the compressor and the expander. The cold tip is instrumented with a Lake Shore Cryotronics silicon diode temperature sensor. Electronics supplied by Lockheed permitted thermal testing of the cryocooler in the laboratory environment while controlling frequency, strokes, and phase. However, it was necessary for GSFC to assemble a data handling system and additional automatic shutdown protection features to permit unattended/autonomous operation in the thermal vacuum chamber. Additional instrumentation continually monitors the following cryocooler parameters:

- hours of operation
- 6 thermocouples
- Cold tip temperature and heater power

- Cold tip bonnet vacuum level
- Chamber vacuum level
- Compressor motor RMS power.

The parameters which can result in an automatic shutdown are:

- Any one of 6 thermocouples exceeding 38 °C.
- Uninterruptable power supply battery low indication
- Heat load cutoff when cold tip temperature is >150 Kelvin

The standard control system supplied with the cryocooler is the Lockheed developed Position Digital Error Control System (PDECS). This system alters the waveforms to achieve sinusoidal position movement of the compressor piston and the displacer. Since PDECS is fuse protected, if PDECS is running, no overstroke protection is required during unattended operation. During vibration testing when PDECS is turned off, unattended operation is not possible since the protective features are not adequate with this electronics configuration.

Two techniques to operate the cryocooler from arbitrary waveform generators were implemented. The first involved generating the waveforms from programmable waveform generators and feeding the signals directly into the Pulse Width Modulation (PWM) drive analog inputs. This kept the internal position loop in the Lockheed electronics still intact and resulted in no offset drift. The second technique involved breaking the cryocooler motor leads to permit driving the motors directly using low noise linear power amplifiers. The first technique was used to permit implementation of the NASA/GSFC developed vibration control algorithm (Reference 1), and the second technique is used for low frequency stiction testing.

The GSFC data acquisition and control system can perform autonomous shutdown of the cryocooler in the event of a problem. This shutdown feature implemented on the Lockheed/Lucas cryocooler incorporates a keyboard splice which allows the data acquisition and control system to command "WAVE OFF" on the Lockheed PC via an RS 232 interface.

In addition to the vibration control drive electronics modifications, GSFC personnel designed and implemented a vibration cancellation system, and a heat removal system which permitted the Lockheed/Lucas cryocooler to be run under vacuum conditions at various heat sink temperatures.

IIc HUGHES 80 K CRYOCOOLER

The Hughes cryocooler capacity is 0.15 W at 80K. It is a balanced unit with dual compressors having a common compression chamber and a single expander with active counterbalancer. The compressor housing is made of aluminum and the expander housing is made of stainless steel. They weigh approximately 4kg and 3kg, respectively. The compressor assembly is connected to the expander via a 4 inch copper transfer line. There are four linear motors to drive the dual compressors, displacer and the active counterbalance. Stroke and phase adjustment are controlled by the Hughes supplied electronics.

The cryocooler does not have a hermetic seal. No plastics or non-organic materials are used in the clearance seals regions. With the exception that the motor is not canned, this is an all metal design.



Photograph of the Hughes IR&D Cryocooler .

The electronics are rack mounted and were supplied by Hughes with the cryocooler. The cryocooler includes LVDT position sensors for the compressors, expander, and counterbalance. The cold tip is instrumented with a silicon diode cryogenic temperature sensor. The cryocooler electronics provided by Hughes are designed to permit very flexible experimentation with the thermodynamics and provides some vibration cancellation capability. In addition, other features were provided with the cryocooler such as a pressure tap on the cryocooler and auxiliary inputs on

the control electronics, which simplified implementation of the GSFC vibration characterization effort.

The testing at GSFC was primarily focused on the uniqueness of the back-to-back compressors and expander/balancer assemblies. The Hughes supplied electronics incorporates a control scheme which is very effective at nulling in-line force at the fundamental frequency, but does little to cancel higher harmonic vibrations. This cryocooler was used as a test bed for the NASA/GSFC vibration control system development effort.

Instrumentation continually monitors the following cryocooler parameters during testing:

- Cold tip temperature
- Heater power
- Cold tip bonnet vacuum level
- Compressor piston stroke level (mm)
- Displacer stroke level (mm)

The parameters which can result in an automatic shutdown are:

- Excessive compressor piston travel
- Excessive displacer travel

In addition to the drive electronics modifications, GSFC personnel supplied a vibration cancellation system interface and a heat removal system. Future tests are currently planned with the cryocooler installed in the thermal vacuum chamber.

III NON DESTRUCTIVE TESTING EVALUATION

It would be ideal if every cryocooler were equipped with a sensor that would provide a positive indication of touch contact at the clearance seals. However, since such a sensor is not presently incorporated into most cryocoolers, several attempts were made to find non-destructive examination procedures that could assist in verifying whether or not touch contact occurs at the clearance seals. The three cryocoolers were used to experiment with some possible testing alternatives.

Initially, experimentation was done with microfocus X-ray techniques to determine clearance seal gaps and alignment of expander and compressor parts. The compressor piston clearance seals could not be imaged in any cryocooler since there was too much metal for the X-rays to penetrate

into the cryocooler body. This technique was somewhat successful on the BAe cryocooler expander cold finger. The Lockheed/Lucas clearance seals could not be imaged and the expander cold finger clearance was determined to be smaller than the resolution of the X-ray machine.

Experimentation with stiction tests was also done on all three coolers. When the piston is driven at low frequency, if touch contact occurs at the clearance seals, hysteresis losses should be evident in the measurement of current as a function of position. Tests were performed in different physical orientations and at different operating temperatures.

Several different stiction waveforms were tried: sinusoid and triangle wave drive signals, at various frequencies and amplitudes, with positive and negative position offsets, in vertical and horizontal orientations, and also with various working gas and cryocooler body temperatures.

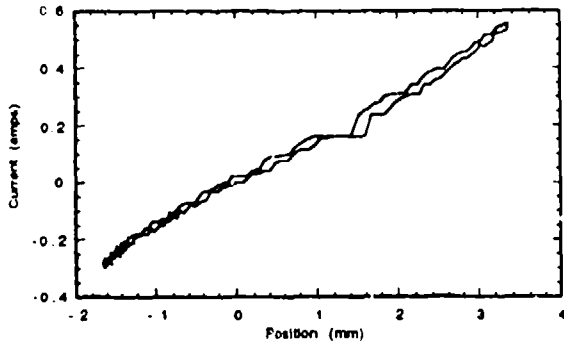
Data acquisition of the current and position signals proved increasingly difficult as lower frequencies were used. Stiction tests were performed at frequencies of 4, 10, and 100 mHz. The lowest frequency that allowed automatic data acquisition with existing hardware turned out to be 4 mHz. In an attempt to maintain consistency in testing, a 4 mHz triangle wave was used to test all three cryocoolers described in this paper. It is believed that this frequency may not be low enough for a clean hysteresis loop to be measured for systems with small clearance gaps.

IIIa BAe CRYOCOOLER

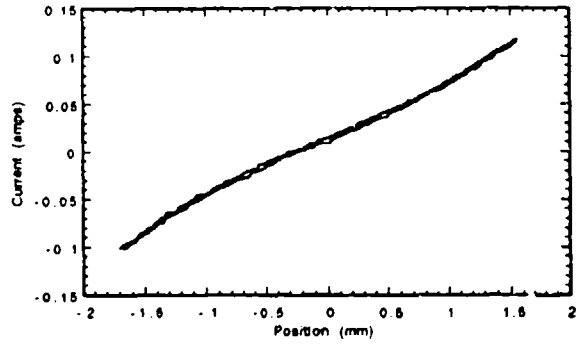
The plots below illustrate the results of the BAe cryocooler driven with a 4 mHz triangle wave with the cryocooler in the vertical orientation, at ambient air temperature, and with the working gas at approximately 75 K. The body of the cryocooler was maintained at approximately 20 °C.

Repeated stiction testing of the BAe compressor under these operating conditions did occasionally reveal an abrupt change in position with no change in current at a position between 1 and 1.5 mm at 4 mHz. At slightly higher piston velocities, this effect did not manifest itself.

The BAe displacer was also tested under the same conditions. The plot below illustrates what is considered to be a very clean stiction test with no apparent touch contact.

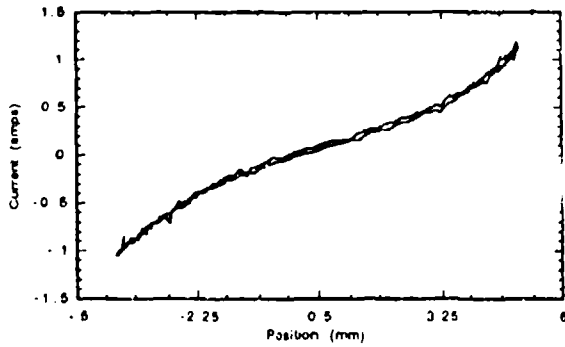


British Aerospace compressor position/current plot
Cooler structure at ambient temperatures

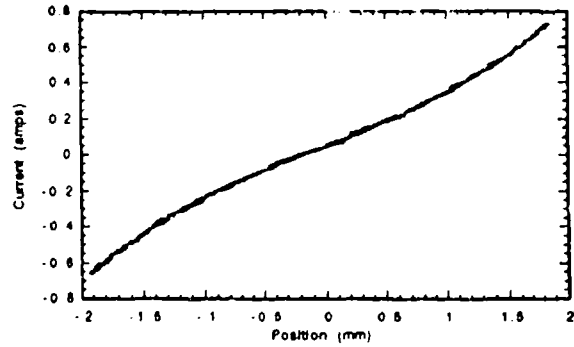


BAe Displacer position/current plot
Cooler structure at ambient temperatures

The BAe compressor and displacer also underwent low frequency testing with a cryocooler heat sink temperature of approximately -20°C . The following plots show little indication of stiction occurring; once again this test was performed in the vertical orientation.

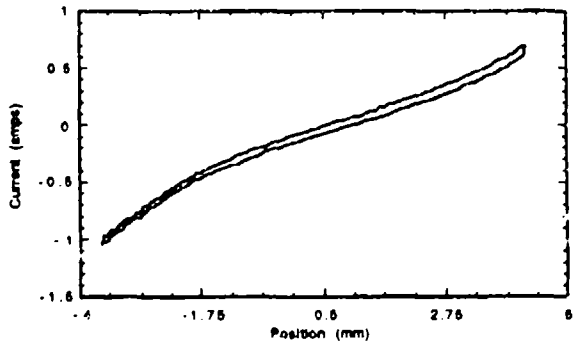


British Aerospace Compressor position/current plot
Cooler structure at -20 degree C

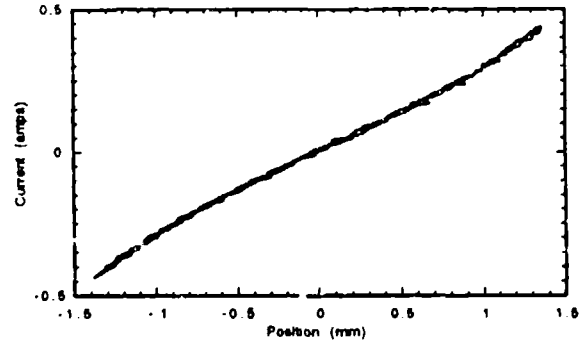


British Aerospace Displacer position/current plot
Cooler structure at -20 degree C

The plots below illustrate the effect of the low frequency testing with the cryocooler in the horizontal orientation. Once again the expander looks clean but an indication of compressor stiction is visible here.



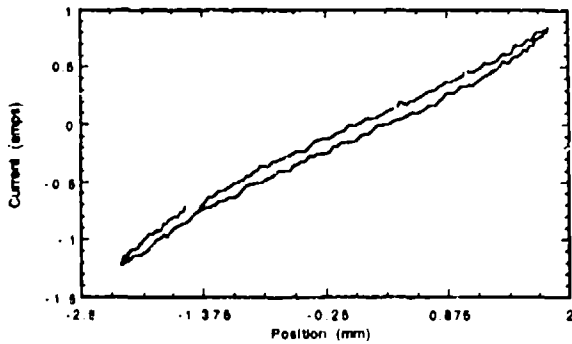
British Aerospace Compressor position/current plot Cooler in the horizontal orientation at 20 degrees C



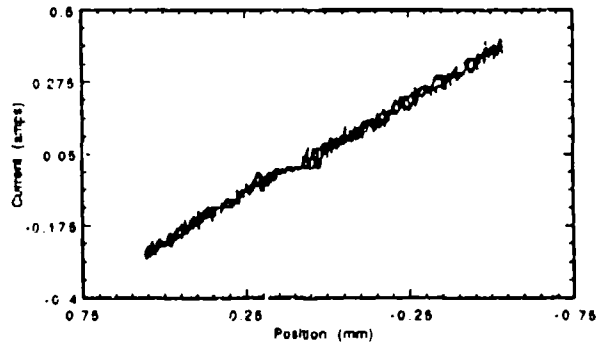
British Aerospace Displacer position/current plot Cooler in the horizontal orientation at 20 degrees C

IIIb LOCKHEED/LUCAS CRYOCOOLER

Stiction tests were conducted on a breadboard Lockheed/Lucas cryocooler at $-25\text{ }^{\circ}\text{C}$, and $+20\text{ }^{\circ}\text{C}$ in the vertical orientation. The ambient ($+20\text{ }^{\circ}\text{C}$) test results are shown below. Some hysteresis was seen in the compressor indicating either touch contact or that the frequency was too high. The latter may be in fact what is causing the hysteresis because vendor testing at .001 hz showed no such hysteresis.



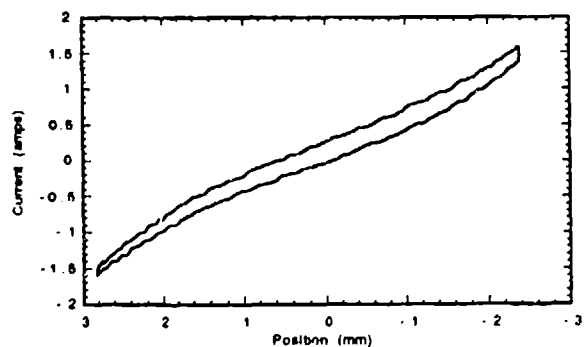
Lockheed/Lucas Compressor position/current plot Cooler structure at ambient temperatures



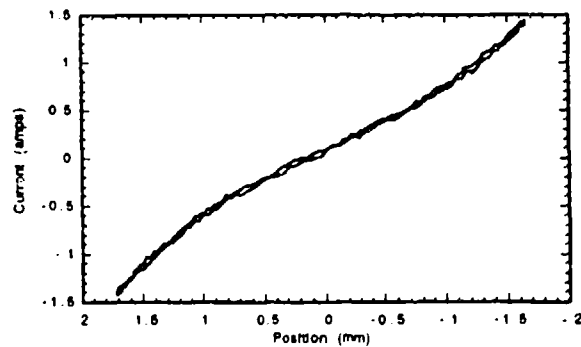
Lockheed/Lucas Displacer position/current plot Cooler structure at ambient temperatures

The displacer test results shown above provide no definite indication of touch contact. The unique characteristic of the displacer plot above is due to the fact that the digitization resolution was double that of the others.

The plots below show a repeat of the low frequency tests with the heat removal system temp at $-40\text{ }^{\circ}\text{C}$ and the cryocooler case at about $-25\text{ }^{\circ}\text{C}$. It appears that touch contact on the compressor increases substantially as temperature decreases.



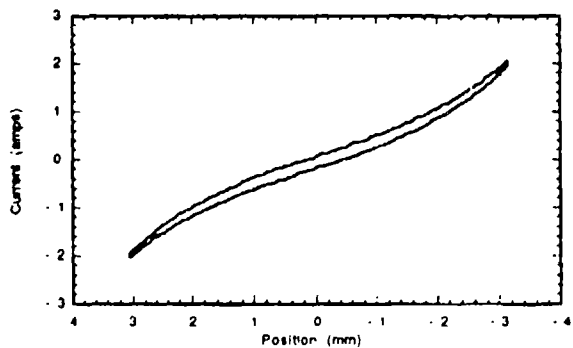
Lucas/Lockheed compressor position/current plot
Cooler structure at - 25 degree C



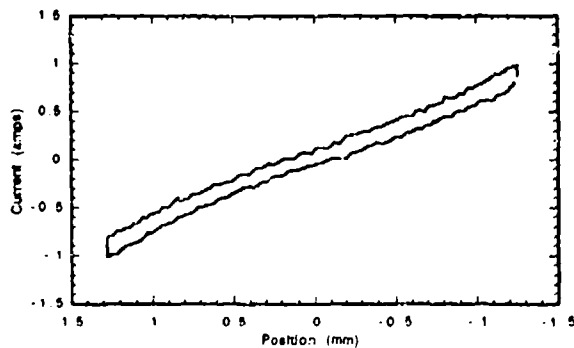
Lucas/Lockheed displacer position/current plot
Cooler structure at - 25 degree C

Once again the expander looks clean. No indication of contact is present. All other operating parameters except temperature where nominal.

A third test was performed in a horizontal orientation. Similar evidence of contact occurred in the compressor test as was seen in the vertical orientation. The expander stiction is now evident which could be attributable to three possible causes. The first is the effect of gravity causing misalignment. The second involves possible misalignment following temperature cycling and the third has to do with possible misalignment to the the cold finger which may have occurred when moving the cryocooler from the vertical to horizontal orientation.



Lockheed/Lucas compressor position/current plot
Cooler in the horizontal orientation at 20 degree C



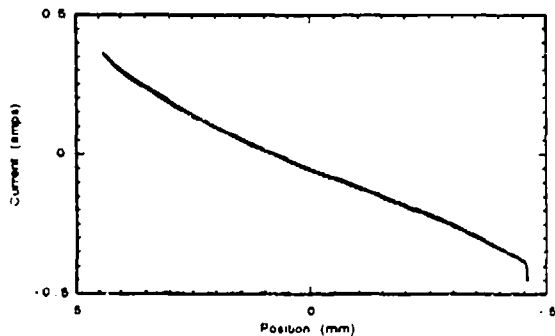
Lockheed/Lucas displacer position/current plot
Cooler in the horizontal orientation at 20 degree C

The third possibility is worth explaining because it may affect other cryocoolers. The cryocooler was received with a plastic vacuum fitting and during cryocooler reorientation this plastic fitting was bumped and it suffered a brittle fracture which should not have occurred since it was not cold. The plastic may have deteriorated under sustained vacuum conditions and lost its ductile properties.

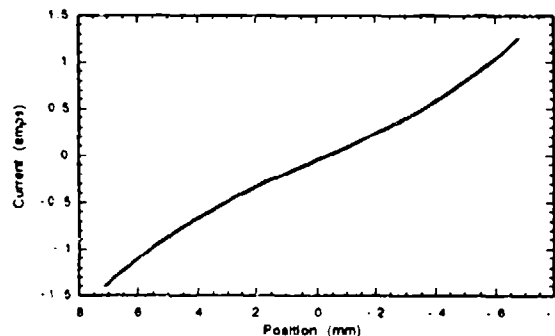
The cold finger was stressed although to what level is uncertain. No visible physical damage was sustained to the cold finger and the PDECS waveforms look normal. The cryocooler continues to perform thermodynamically as before.

IIIc HUGHES AIRCRAFT CRYOCOOLER

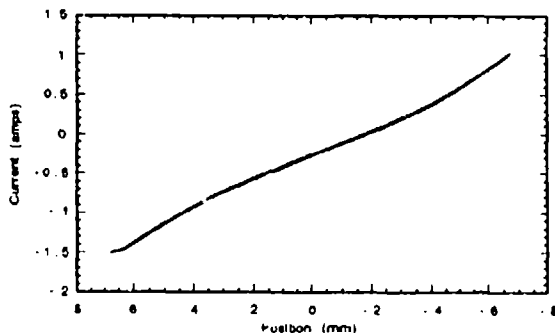
Stiction tests were performed on the Hughes IR&D cryocooler under ambient conditions (20°C) with the cryocooler mounted in only the horizontal orientation. Both the compressor assembly and displacer were tested. Plots of the resulting data are shown below.



Hughes 65K IR&D displacer position/current plot
Cooler structure at ambient temperatures



Hughes 65K IR&D compressor#2 position/current plot
Cooler structure at ambient temperatures



Hughes 65K IR&D compressor#1 position/current plot
Cooler structure at ambient temperatures

No indication of contact was visible in any of the plots. In the Hughes all metal design, experience has shown that if contact was to occur, one would expect that galling would cause the piston or displacer to seize in a short period of time.

IIIId Conclusions:

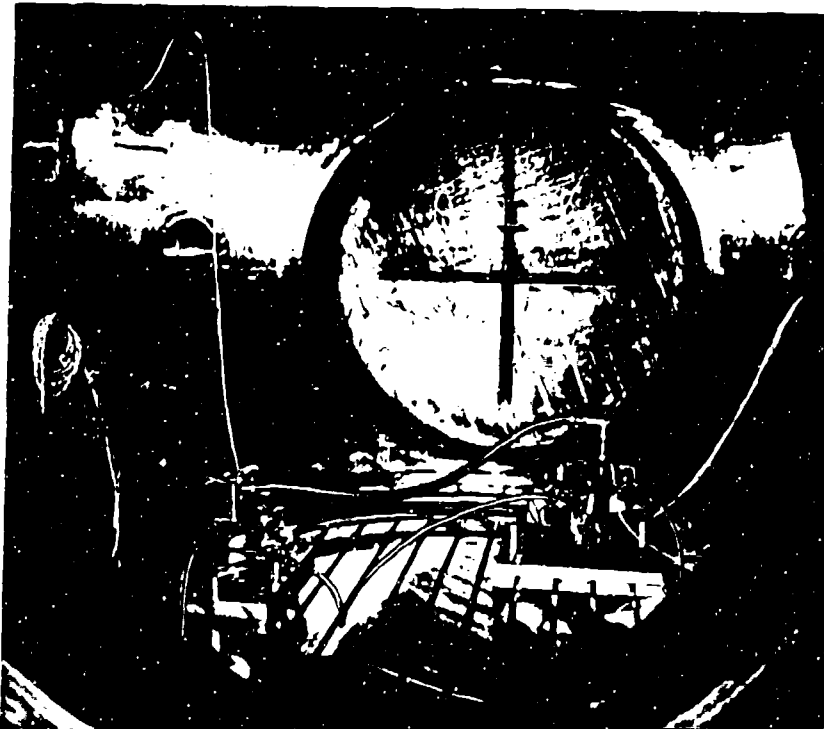
Microfocus x-ray techniques are of minimal value in evaluating alignment and touch contact in production cryocoolers. To some degree, indications of touch contact were seen using the stiction

test techniques. There is difficulty in interpreting the stiction plots in some cases, and even though momentary discontinuities occur, the cryocoolers still operate properly at their normal operating frequencies for the limited testing performed. The long term effects of stiction on cryocooler operation is not yet determined. In some cases, the test frequency may have been the cause of the indicated hysteresis.

Another technique which might detect contact is to periodically monitor the frequency response of the residual vibration for shifts in the magnitude of the dominant harmonic frequencies. These frequencies should be effected by any changes in the electromechanical system, including loss of damping from the gas spring caused by working gas leakage, additional friction caused by piston/wall contact, and changes in the spring constant caused by work hardening. This possible test method needs to be evaluated. The ultimate goal should be to incorporate design features that ensure no touch contact at the clearance seals. Any contact is potentially a serious concern.

IV THERMAL PERFORMANCE TEST

The thermal performance testing was performed in a Thermal Vacuum Chamber shown below.



Inside the NASA/GSFC vacuum chamber (BAe cryocooler left/Lucas cryocooler right).

The tests performed included cool down curves and families of cooling load curves with the coldfinger load ranging from no load to typically one watt. The heat sink temperature was regulated between -32°C to +20°C.

Every attempt was made to conduct all performance testing under steady-state cryocooler operating and environmental conditions. Some tests were performed multiple times over a period of months to ensure accuracy and test the repeatability of results. Estimated parameter uncertainties are as follows:

Table I: Estimated uncertainty for the thermal performance measurements

Parameter	Estimated Uncertainty
Cold Tip Temperature	± 0.1 K
Cold Finger Dewar Vacuum	± 2.2x10 ⁻⁶ torr
Compressor Power	± 0.005 watts*
Heat Sink Temp	± 0.6 °C
Cold Finger Heat Load	± 0.005 watts
Piston Stroke	± .1mm

*The estimated uncertainty of the compressor power measurement for the Lockheed/Lucas cryocooler is TBD.



NASA/GSFC cryocooler test station.

Cryocoolers were tested as received from the suppliers; no changes were made to reduce coldfinger parasitic loads. A new vacuum bonnet was manufactured and installed on the British Aerospace cryocooler. It should also be noted that all three cryocoolers were operated at recommended compressor and expander strokes. Additional cooling power is possible from all three cryocoolers if they are run with larger strokes.

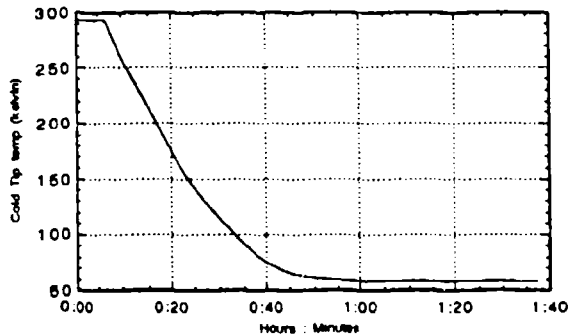
IVa BAe CRYOCOOLER

Cooldown curves were generated under ambient conditions with heat sink temperatures at 20°C.

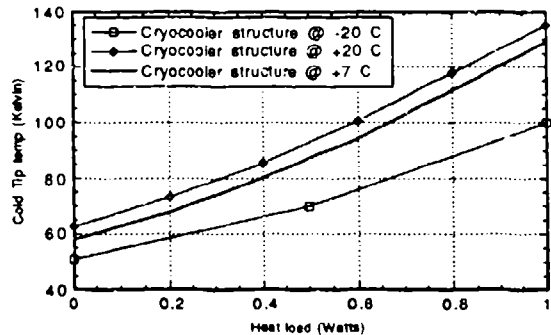
The BAe cryocooler cools down to operating temperatures in about 50 minutes. Cryocooler load curves were generated under both ambient and vacuum conditions with the heat removal system operating between -35°C and +20°C. Because the BAe cryocooler housing is titanium, it took a somewhat longer time for it to reach thermal equilibrium and typical housing temperatures were 10 to 15 degrees warmer than the heat sink.

Testing was performed under both constant power and constant stroke conditions. The charts below map the relationship between cold tip temperature and cooling load. The manufacturer's recommended values were used for all other cryocooler operating parameters. The constant stroke test procedure consisted of recording the steady-state cold tip temperature as a function of heat load while the compressor was operating at vendor recommended stroke. The cold tip heater was varied between 0 and 1 watt of cold tip heat load. Note that, because the compressor power was measured at the input to the motors, the results do not include power losses in the drive electronics.

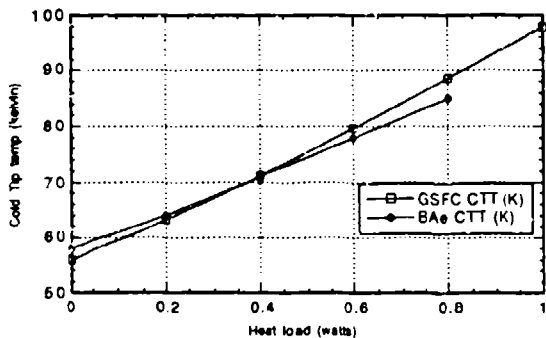
A constant compressor power load curve was generated for comparison purposes with BAe generated load curves. No indication of thermodynamic performance degradation is evident from our results. The GSFC load line slope and 'Y' axis intercept differ slightly from the BAe test results. The GSFC curve showed slightly better performance at low heat loads and slightly degraded performance at higher heat loads. This difference is probably due to differences in test hardware and procedures between BAe and GSFC.



British Aerospace 80 K cryocooler cooldown curve
compressor stroke at 6.9mm pp, displacer at 2.6mm pp



British Aerospace 80 K cryocooler load line
Constant stroke with multiple heat sink temps



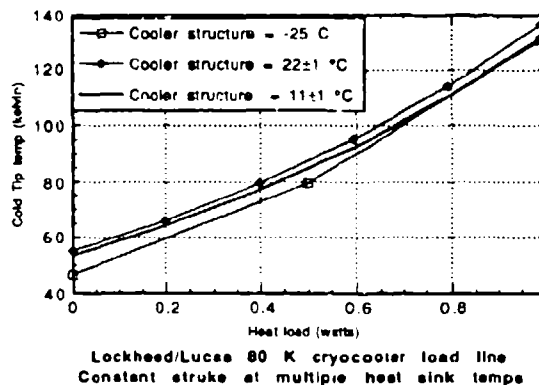
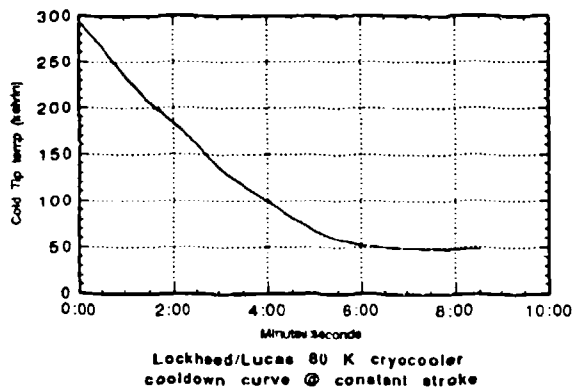
British Aerospace 80 K cryocooler load line
Constant compressor power = 33.75 watts

A second set of cooling curves were generated for a vendor recommended constant compressor stroke of 6.9mm and displacer stroke of 2.9mm at varying heat sink temperatures. As the heat sink temperature was decreased, the cold tip temperature dropped. This effect is clearly evident in the graph above. The curve at -20C is not parallel with the other curves. This may be due to the long thermal time constants of the cryocooler/dynamometer mass. It took a long time to stabilize temperatures at the low end of the load curve.

IVb LOCKHEED/LUCAS CRYOCOOLER

Lockheed/Lucas cryocooler performance testing was performed under both ambient and vacuum conditions with the heat sink temperature between -32°C and +20°C. The manufacturer's recommended values were used for all cryocooler operating parameters. A cooldown curve was generated under ambient conditions with heat sink temperatures at 20°C. The cryocooler cools down to operating temperatures in about 6 minutes under ambient conditions.

The performance curves generated below were with a compressor stroke of 4.80 mm peak-to-peak and an expander stroke of 3.05 mm peak-to-peak. These were the vendor recommended stroke levels.

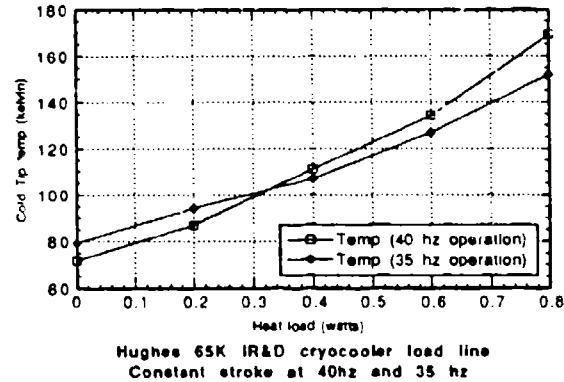
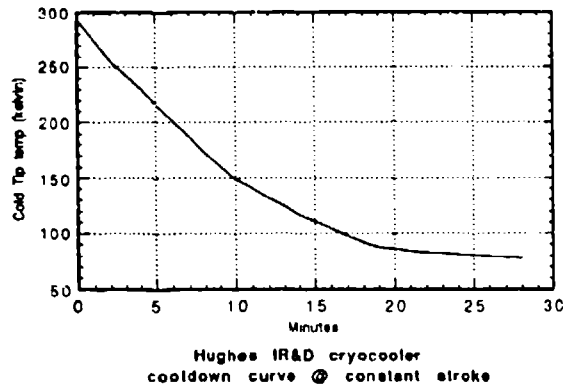


All thermodynamic performance testing was done with 'PDECS' on, so compressor and expander stroke levels were maintained constant throughout testing. As heat sink temperatures were decreased, the load line shifted downward. This effect appeared to be more pronounced at lower heat loads, probably due to the higher net cooling available due to lower cold finger parasitics.

IVc HUGHES AIRCRAFT CRYOCOOLER

Initially a mechanical problem was encountered with the Hughes cryocooler which required rework by Hughes. A metallic particle became entrapped in the clearance seal gap of the displacer which in turn caused abnormal vibration and piston motion to occur. A displacer with a larger clearance seal was installed. No further problems have been encountered in the test program to date. This change was acceptable for our testing efforts since the primary focus of NASA/GSFC work on the Hughes cryocooler was characterization of the vibration with the back-to-back compressor assemblies. Results are presented below.

Cooldown curves and load curves were generated for the Hughes cryocooler under ambient laboratory conditions with heat sink temperatures at typically +20°C. The results are presented below. The manufacturer's recommended values were used for all other cryocooler operating parameters. The test procedure consisted of recording the steady-state cold tip temperature while the compressor was operating at 20mm peak-to-peak and the expander was operating at 6.4 mm peak-to-peak. The cold tip heater power was varied between 0 and 0.8 watt .



Over a period of a month, two constant stroke load curves were generated. The results from the tests differ slightly. The cryocooler was not hermetically sealed and working gas pressure dropped approximately 2% between tests. Also, slightly different operating frequencies were used.

V VIBRATION CHARACTERIZATION TESTS

The objectives of this test were to quantify the residual vibration generated by each cryocooler while operating at the nominal stroke and to determine the effect of orientation and temperature on vibration signatures. A GSFC designed dynamometer and analog signal mixer were used to measure the vibration forces and moments for both the compressor and expander/counterbalance assemblies.

Each test was performed under steady-state, no-load conditions with the compressor running at nominal stroke. Tests were repeated for both the horizontal and vertical cryocooler orientations for all three cryocoolers. Additional tests were performed between -32C and +20C for the BAe and Lockheed/Lucas cryocoolers.

Two eight-channel A/D converters were used to record several cycles of the force and moment signals simultaneously. A spectrum analyzer was used to record each force & moment spectra through the first twenty harmonics. The force and moment measurements are believed to have an absolute accuracy to within $\pm 10\%$.

In addition to these characterization tests, each cryocooler was mounted on its dynamometer to test the performance of a narrow band vibration control algorithm in canceling the first twenty

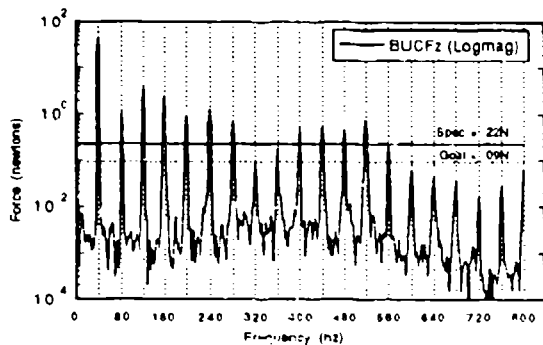
harmonics in the z-axis force spectrum. This cancelation was carried out for both the compressor and expander/counterbalance assemblies. A description of the GSFC control algorithm can be found in Boyle et al.: "Non-Real Time, Feed Forward Vibration Control System for Cryocoolers"¹.

The following convention is used for all cryocooler vibration tests: Fz is the force in the direction of piston/expander motion; Fx and Fy are forces transverse to the direction of piston/expander motion, and Mz is the moment about the axis of piston movement. Mz's magnitude is a function of dynamometer design. It is presented because it may be of interest to the user community.

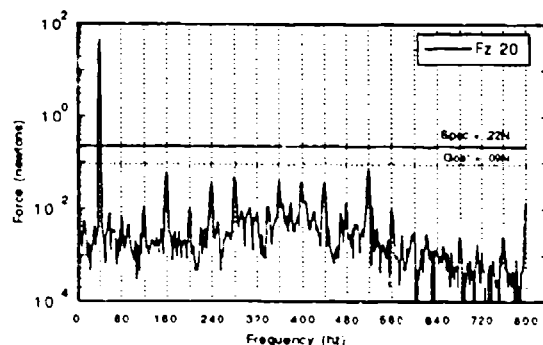
Va BAe 80K CRYOCOOLER

The plots below show the actual spectra of the BAe cryocooler compressor Fz both before and after the NASA/GSFC vibration control algorithm was activated.

An overlay of another force spectrum on top of this plot would be difficult to view and compare. Therefore, following this first set of full spectrum graphs, a second set of plots shows only the peak levels of each harmonic of the operating frequency. The reader should not interpret information between harmonics as residual force. Essentially all of the residual force occurs at the harmonics. Lines are used to connect the dots between harmonic peaks only to aid the reader in making comparisons between various cryocooler spectra.



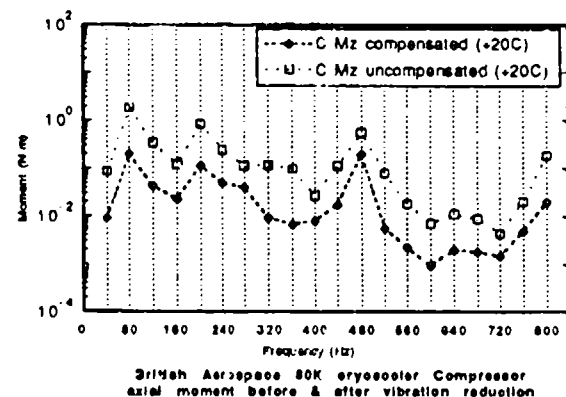
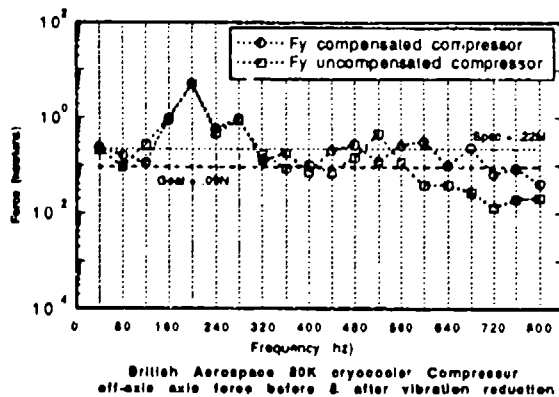
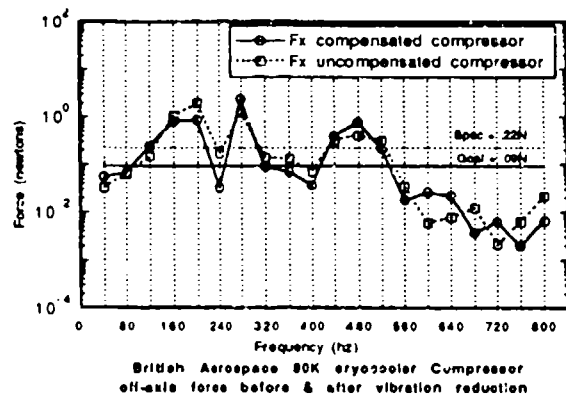
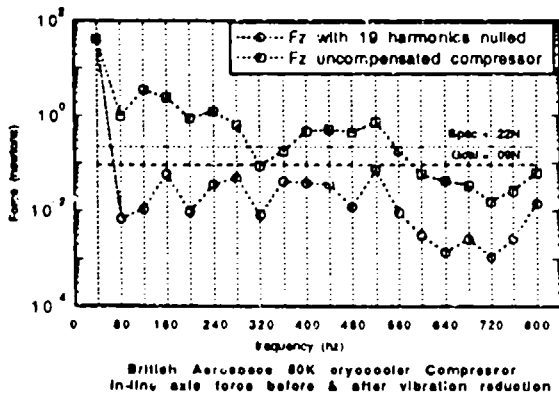
British Aerospace 80K cryocooler Compressor
Axial force as driven from open loop sinwave



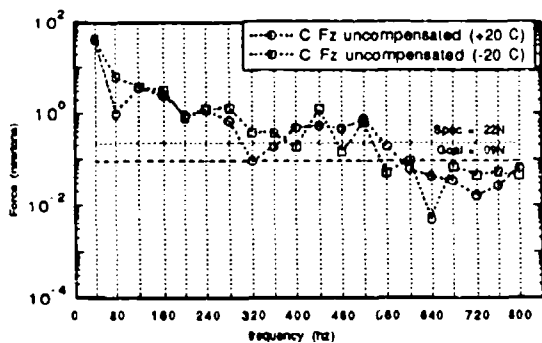
British Aerospace 80K cryocooler Compressor
Axial force with GSFC vibration algorithm on

The first plot on the left below shows the superposition of the two plots from above for the British Aerospace cryocooler compressor assembly before and after the GSFC vibration control algorithm

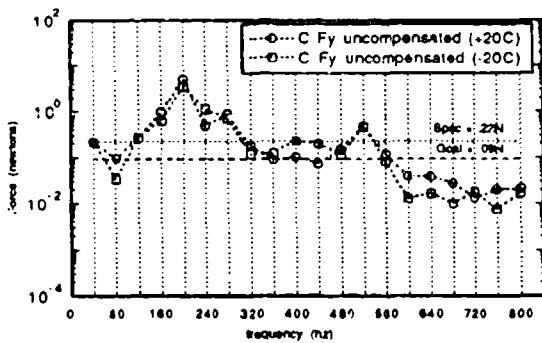
was activated. As can be seen 10 out of the first 12 harmonics were originally above the NASA/GSFC specification requirement for the 80K and 30K NASA/GSFC cryocooler contracts. Once the algorithm was activated, all of the first 19 harmonics were reduced below the specification goal. Since the BAe cryocooler is not a dual compressor/displacer configuration, the fundamental could not be nulled.



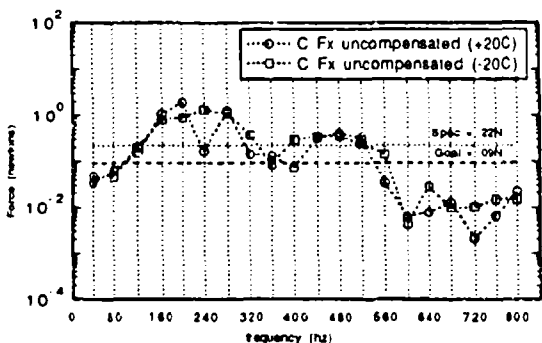
Vibration control of the BAe compressor did not result in a significant reduction in the off-axis forces; however the axial moment about the piston/expander movement axis was consistently reduced. Shown below are comparisons made between vibration signatures of both compensated and uncompensated cryocooler operation with the cryocooler operating at +20°C and -20°C.



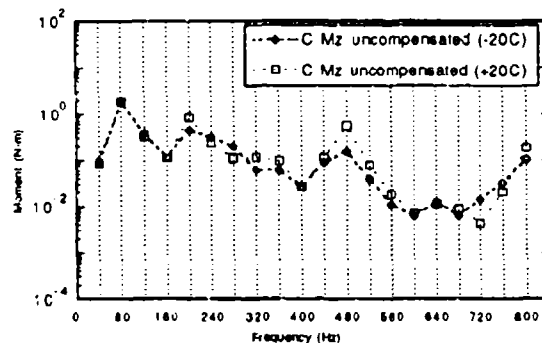
British Aerospace 80K cryocooler Compressor
axial force with multiple heat sink temperatures



British Aerospace 80K cryocooler Compressor
off-axis force with multiple heat sink temperatures

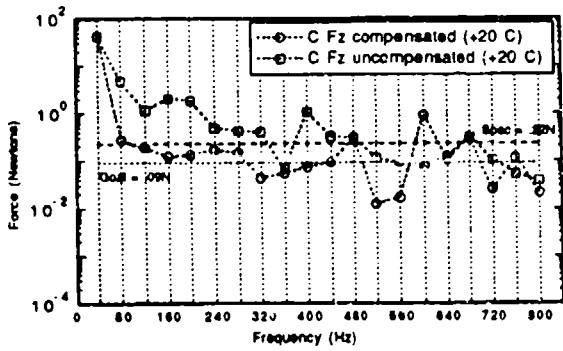


British Aerospace 80K cryocooler Compressor
off-axis force with multiple heat sink temperatures

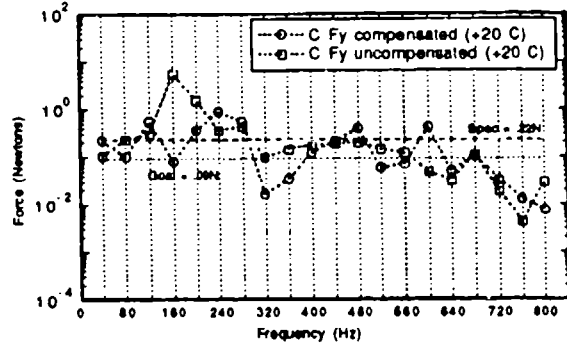


British Aerospace 80K cryocooler Compressor
axial moment with multiple heat sink temperatures

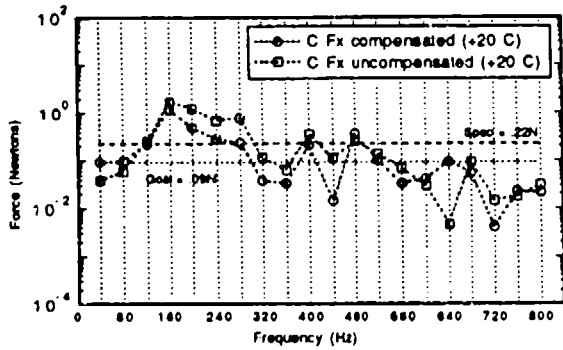
The following plots show spectra of compensated versus uncompensated waveforms for both the compressor and expander in a horizontal orientation (Fz) at ambient conditions. The NASA/GSFC algorithm was able to significantly reduce Fz at higher harmonics, although not as well as when the cryocooler was in the vertical orientation. The vibration control algorithm was not able to significantly reduce non-axial vibrations.



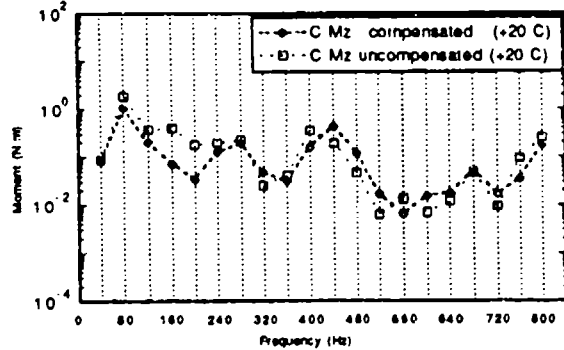
British Aerospace 80K Cryocooler Compressor axial force before & after vibration reduction Cryocooler in the horizontal orientation



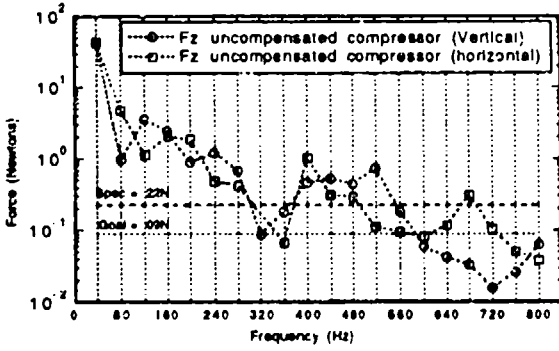
British Aerospace 80K Cryocooler Compressor off-axis force before & after vibration reduction Cryocooler in the horizontal orientation



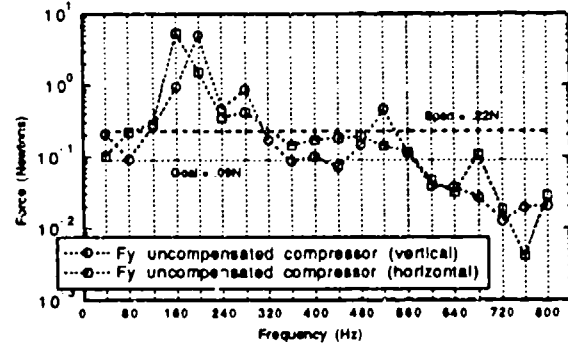
British Aerospace 80K Cryocooler Compressor off-axis force before & after vibration reduction Cryocooler in the horizontal orientation



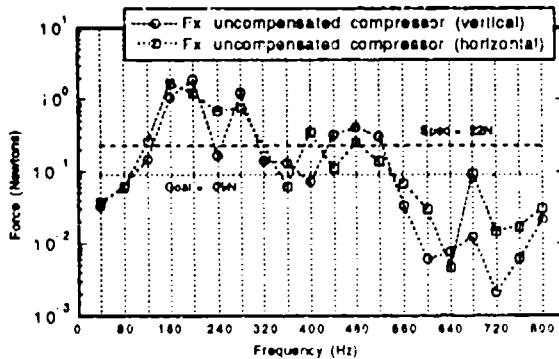
British Aerospace 80K Cryocooler Compressor axial moment before and after vibration reduction Cryocooler in the horizontal orientation



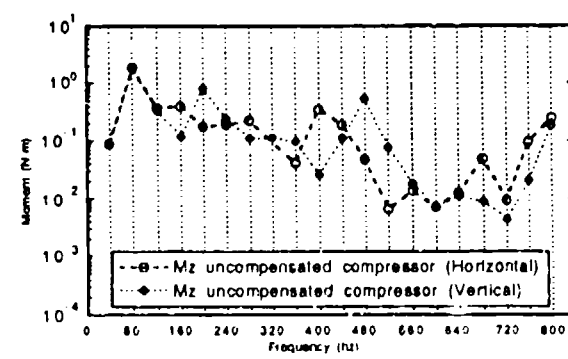
British Aerospace 80K Cryocooler: Compressor Axial force as driven from open loop sinewave Vertical versus Horizontal vibration signatures



British Aerospace 80K Cryocooler Compressor off-axis force as driven from open loop sinewave Vertical versus Horizontal vibration signatures



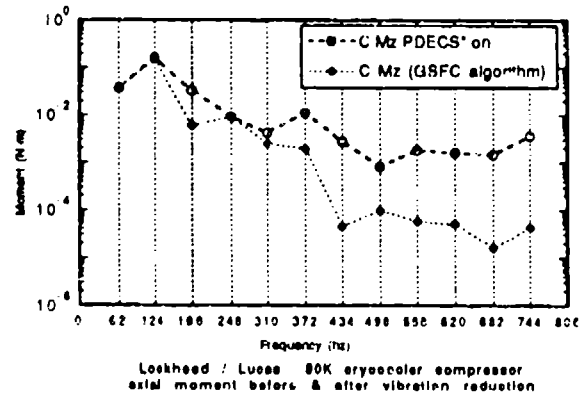
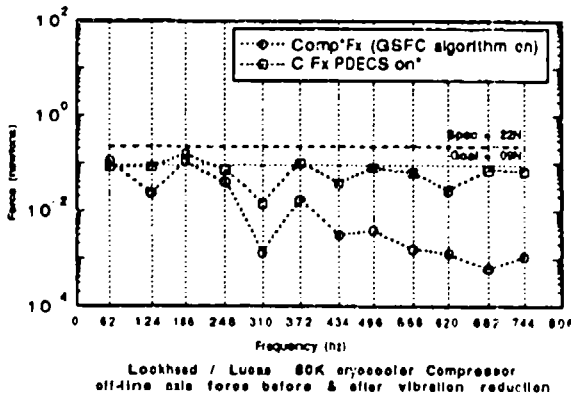
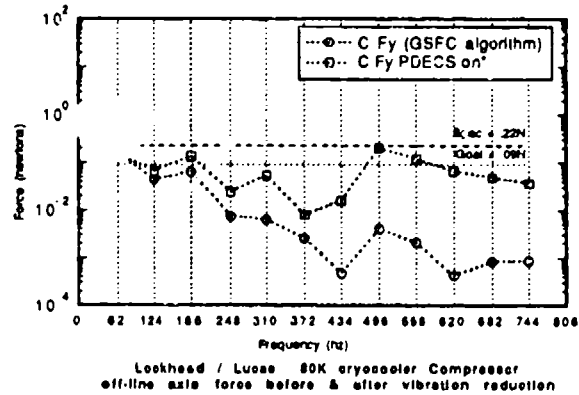
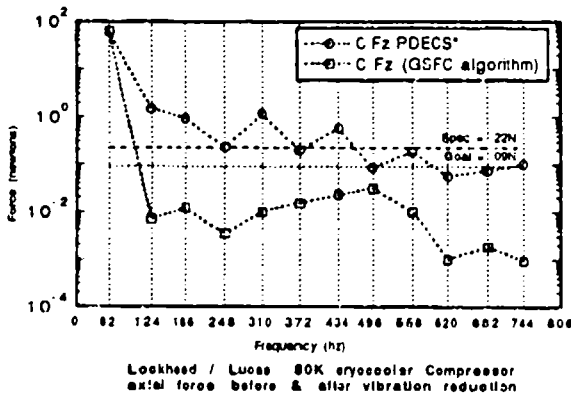
British Aerospace 80K Cryocooler Compressor off-axis force as driven from open loop sinewave Vertical versus Horizontal vibration signatures



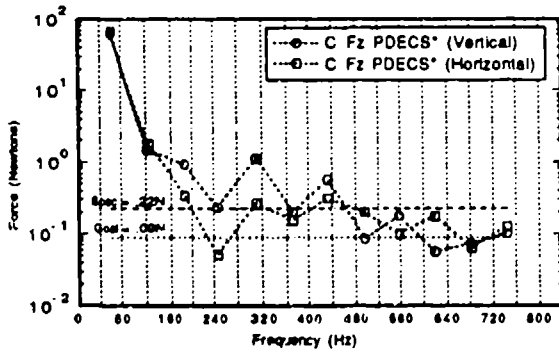
British Aerospace 80K Cryocooler Compressor axial moment as driven from open loop sinewave Vertical versus Horizontal vibration signatures

Vb LOCKHEED/LUCAS 80K CRYOCOOLER

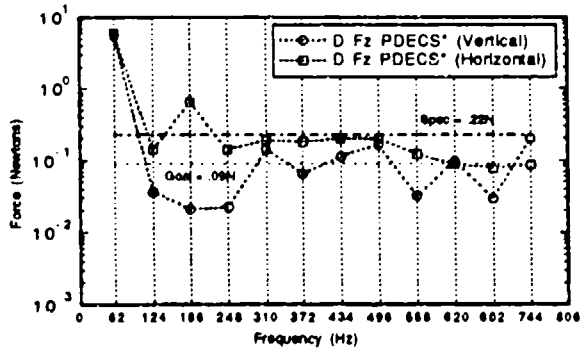
The plots below show the comparison of harmonic vibration levels of the Lockheed/Lucas cryocooler compressor when operated with the Lockheed control system to that obtained with the GSFC algorithm. It must be emphasized that this hardware does not represent the latest design available from Lockheed. 'PDECS' does not use force feedback. Rather, it drives the piston/expander motion in sinusoidal motion. The Lockheed/Lucas vibration signature, when driven with sinusoidal waveforms from the 'PDECS', exceeds NASA/GSFC vibration requirements. Lockheed has a more contemporary set of electronics which has a force feedback feature. The NASA/GSFC vibration control algorithm significantly reduced both axial and off-axis forces as well as Mz, over the performance demonstrated by 'PDECS' alone.



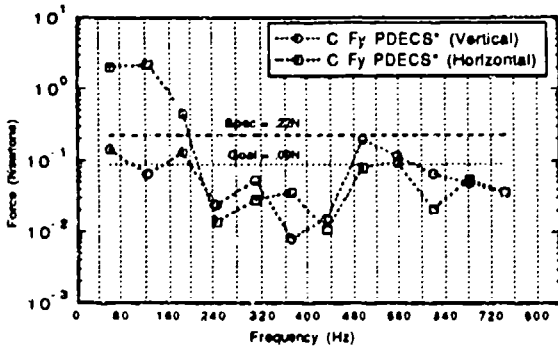
The plots on the next page show the vibration signature change between the operation of the Lockheed/Lucas compressor and displacer from the vertical to the horizontal orientation. The changes in the vibration signature are minor except for the low frequency, off-axis harmonics.



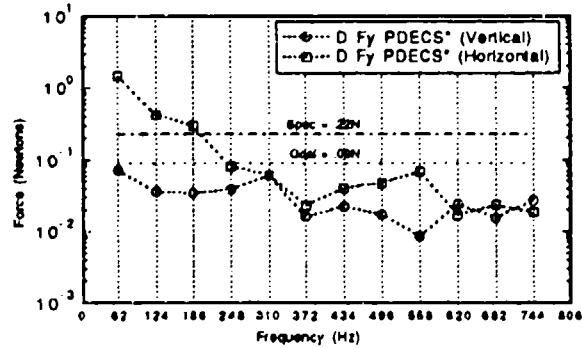
Lockheed/Lucas 80K Cryocooler Compressor axial force
Vibration signatures for vertical and horizontal orientations



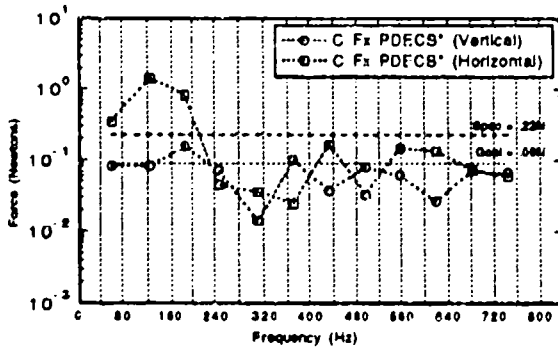
Lockheed/Lucas 80K Cryocooler Displacer axial force
Vibration signatures for vertical and horizontal orientations



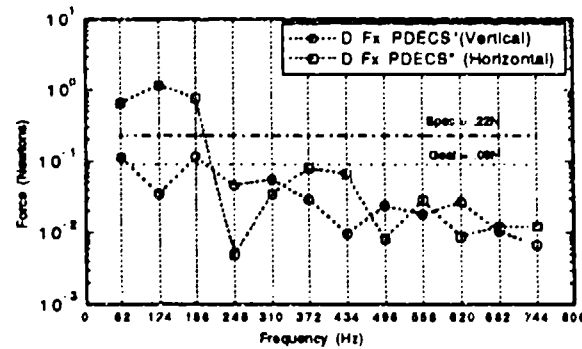
Lockheed/Lucas 80K Cryocooler Compressor off-axis force
Vibration signatures for vertical and horizontal orientations



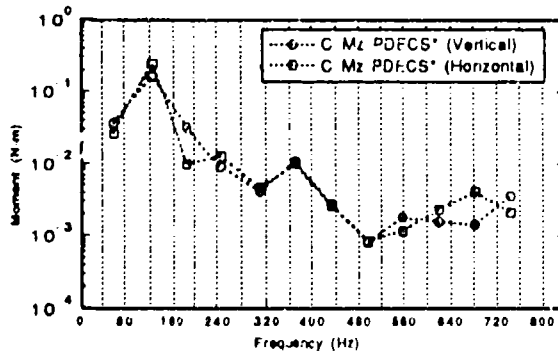
Lockheed/Lucas 80K Cryocooler Displacer off-axis force
Vibration signatures for vertical and horizontal orientations



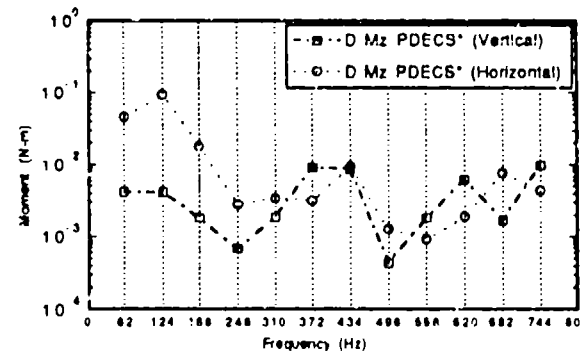
Lockheed/Lucas 80K Cryocooler Compressor off-axis force
Vibration signatures for vertical and horizontal orientations



Lockheed/Lucas 80K Cryocooler Displacer off-axis force
Vibration signatures for vertical and horizontal orientations

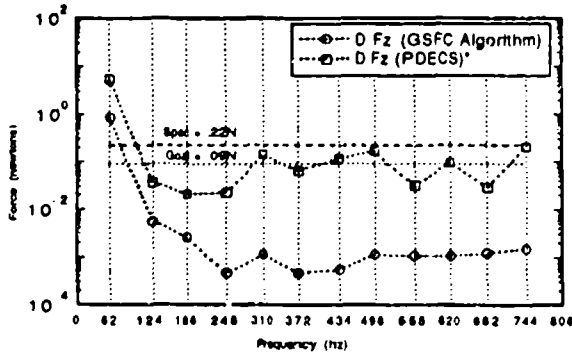


Lockheed/Lucas 80K Cryocooler Compressor axial moment
Vibration signatures for vertical and horizontal orientations

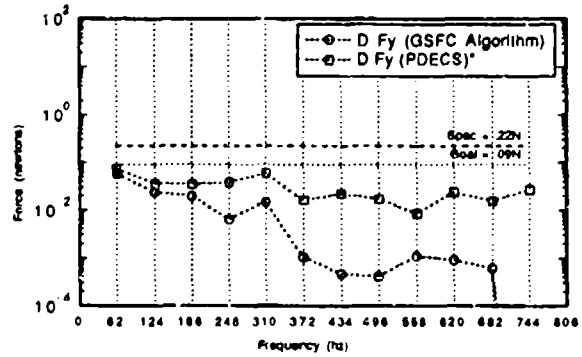


Lockheed/Lucas 80K Cryocooler Displacer axial moment
Vibration signatures for vertical and horizontal orientations

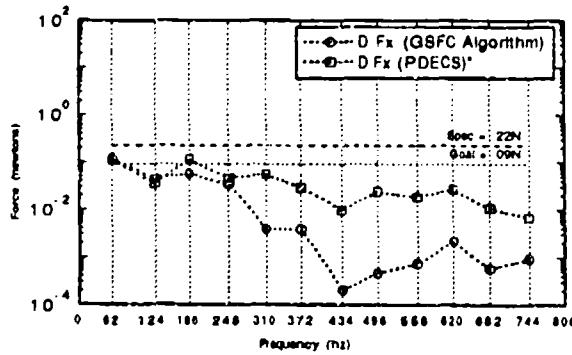
The plots below demonstrate the reduction of harmonic vibration levels in the Lockheed/Lucas displacer assembly when the GSFC algorithm is applied. Note that in addition to the reduction in F_z , the Lockheed/Lucas cryocooler experiences a marked improvement in off-axis forces as compared with the results from the BAe cryocooler tests.



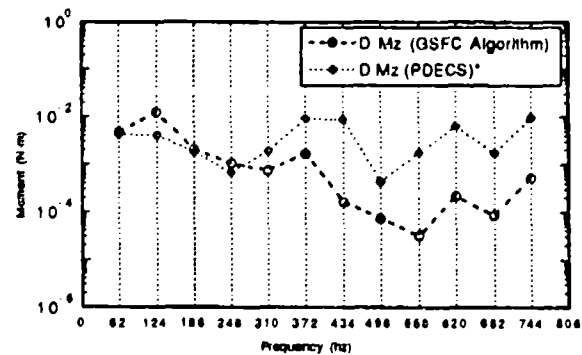
Lockheed / Lucas 80K cryocooler displacer axial force before and after vibration reduction



Lockheed / Lucas 80K cryocooler Displacer off-axis force before & after vibration reduction

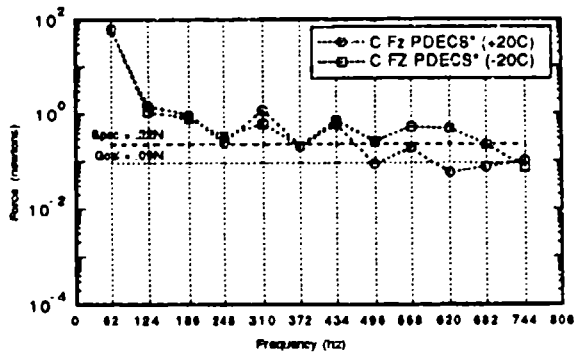


Lockheed / Lucas 80K cryocooler Displacer off-axis force before & after vibration reduction

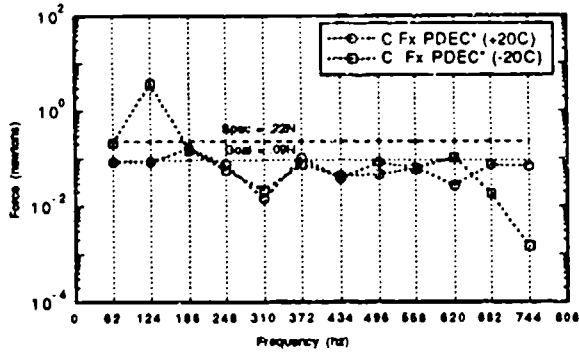


Lockheed / Lucas 80K cryocooler compressor axial moment before & after vibration reduction

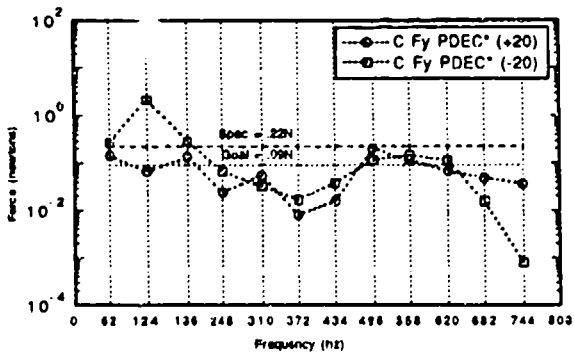
The cryocooler was also operated with its heat sink at $-20\text{ }^{\circ}\text{C}$ to determine the effect of this thermal environment on the vibration signature. The comparisons are once again made on the specific harmonic frequencies with the heat sink temperature at $+20\text{ }^{\circ}\text{C}$ and $-20\text{ }^{\circ}\text{C}$ with PDECS operational at the lowest no load cold tip temperature. The data consistently reveals a reduction in force at the higher frequencies when the heat sink is at $-20\text{ }^{\circ}\text{C}$. There is, however, an increase in off-axis forces at the lower harmonics.



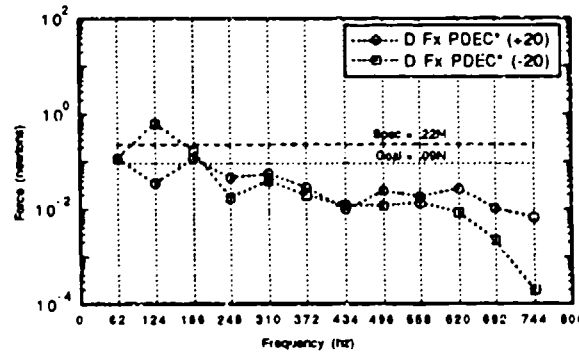
Lockheed / Lucas 80K cryocooler Compressor
axial force operating at two different heat sink temperatures



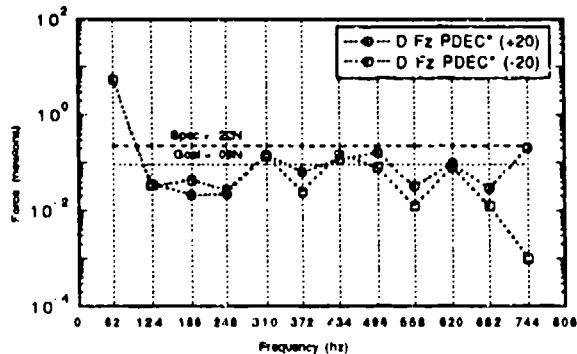
Lockheed / Lucas 80K cryocooler Compressor
off-axis force operating at two different heat sink temperatures



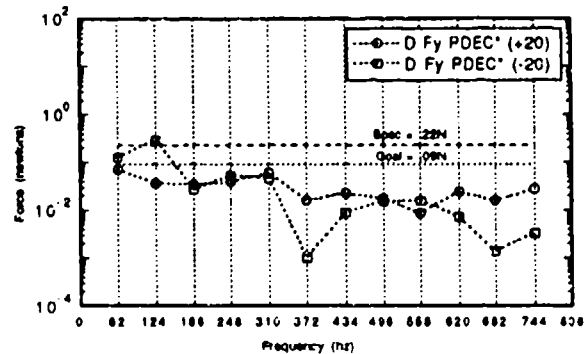
Lockheed / Lucas 80K cryocooler Compressor
off-axis force operating at two different heat sink temperatures



Lockheed / Lucas 80K cryocooler Displacer
off-axis force operating at two different heat sink temperatures



Lockheed / Lucas 80K cryocooler Displacer
axial force operating at two different heat sink temperatures

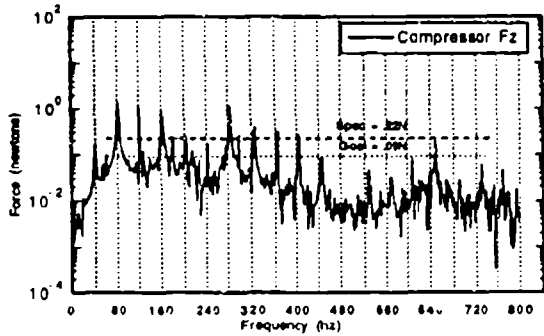


Lockheed / Lucas 80K cryocooler Displacer
off-axis force operating at two different heat sink temperatures

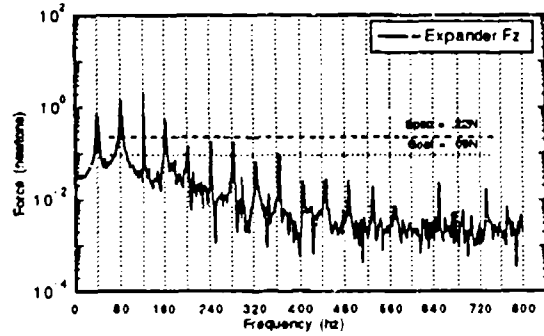
Vc HUGHES AIRCRAFT CRYOCOOLER

The following plots represent the baseline vibration spectra for the Hughes Aircraft dual compressors and displacer/counterbalance assemblies. The balanced design nulls out the

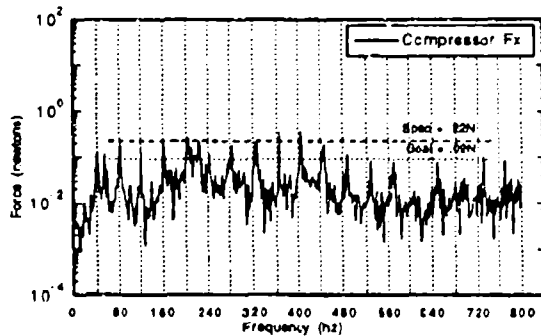
fundamental vibrations and does result in fairly low forces at the higher harmonics. Vibration signatures were taken with both compressors and displacer operating at full stokes.



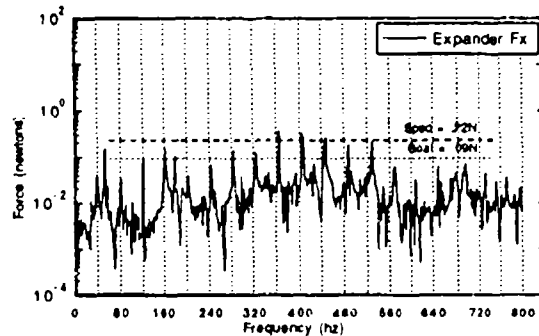
Hughes 85K IR&D cryocooler Compressor
axial force with fundamental nulled



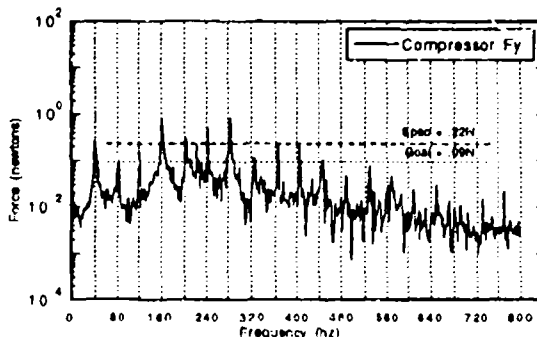
Hughes 85K IR&D cryocooler Displacer
axial force with fundamental nulled



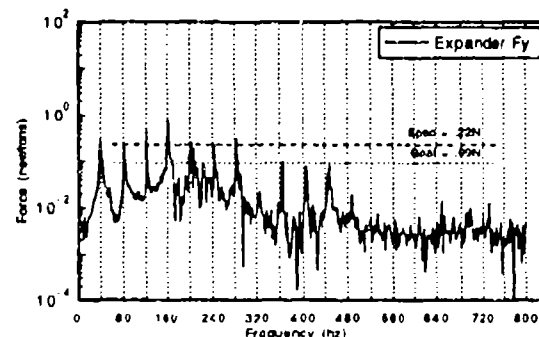
Hughes 85K IR&D cryocooler Compressor
off-axis force with fundamental nulled



Hughes 85K IR&D cryocooler Displacer
off-axis force with fundamental nulled

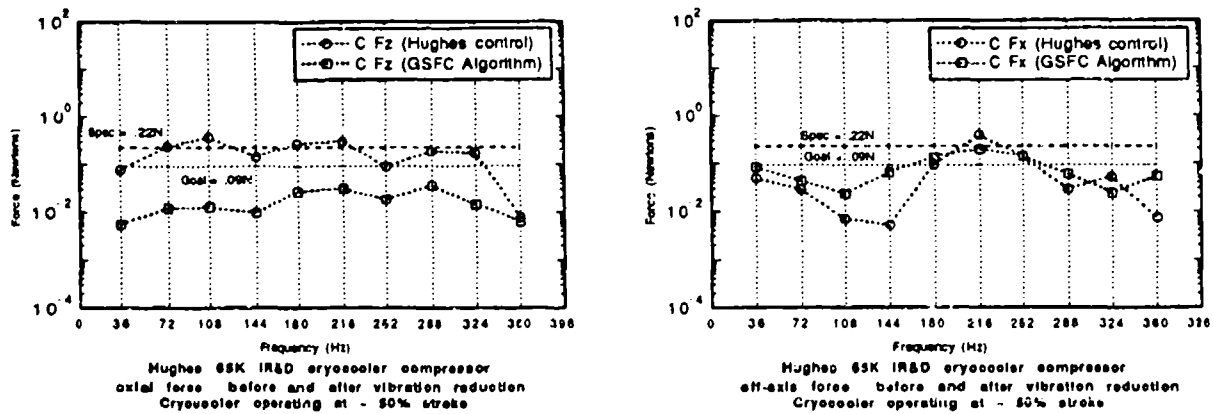


Hughes 85K IR&D cryocooler Compressor
off-axis force with fundamental nulled



Hughes 85K IR&D cryocooler Displacer
off-axis force with fundamental nulled

Additional hardware modifications must be implemented before testing can be completed with the NASA/GSFC control algorithm nulling up through 10 harmonics with the cryocooler running at full power. Until hardware modifications can be completed, it was only possible to run the compressors and displacer at 50% stroke. The following plots demonstrate that the NASA/GSFC vibration control algorithm will work on a dual compressor cryocooler but the plots do not represent actual nulled vibration levels under full stroke conditions. Actual hardware modifications will be completed in late 1992, and additional vibration testing is planned for early 1993.



VI CONCLUSIONS

NASA/GSFC test results from three cryocoolers have been presented in this paper. Two of the cryocoolers are single compressor units and one is a balanced dual compressor unit. Thermal performance data and residual vibration data is presented. As of the publication date of this paper, no thermodynamic degradation has been seen in any of the cryocooler as a result of operation at various temperatures; operation in a vacuum; and operation in vertical and horizontal orientations.

The data indicates that the use of stiction testing is useful. However, the sensitivity of stiction tests and determination of acceptable levels of stiction, if any, remain elusive. The stiction test results presented herein indicate touch contact under some operating conditions. In the next generation of cryocoolers, some manufacturers are designing to eliminate touch contact.

Reduction of residual vibration continues to be an important issue for space flight instruments. The results presented herein demonstrate that axial vibration can be reduced to acceptable levels with a good vibration control system. Unfortunately, the results indicate that off-axis residual vibration can not be consistently reduced to acceptable levels by such a system. Off-axis vibration must be minimized by proper cryocooler design.

Vibration control systems may need to be adaptable over time to account for changing operating conditions. However, the results presented herein demonstrate that a real-time control system may not be required. The GSFC vibration control system has performed well on three different coolers, manufactured by three different suppliers. For all cryocoolers, the residual vibration signatures are stable over periods of many minutes. The GSFC vibration control system has successfully and repeatably demonstrated vibration cancellation out to the 19th harmonic. This cancellation has been demonstrated under a wide variety of operating conditions.

REFERENCES

1. R. Boyle, et al., "Non-Real Time, Feed Forward, Vibration Control System", Presented at the 7th Annual Cryocooler Conference, Santa Fe, NM, 1992.

Performance of the Signaal Usfa Stirling Cooling Engines

D.Verbeek, H. Helmonds, P. Roos

Signaal Usfa,
PO Box 6034, NL 5600 HA Eindhoven, The Netherlands.

INTRODUCTION

More than 40 years ago SIGNAAL USFA entered the Stirling cooler market under the name Philips Usfa B.V. Since 1990, when Philips decided to relinquish its activities in the military market, USFA became a member of the Thomson group and operates from its location in Eindhoven, The Netherlands, under the name SIGNAAL USFA. Within the Thomson-CSF organization, SIGNAAL USFA is a subsidiary of Thomson TRT Defence (TTD) and operates alongside the French company, Cryotechnologies, which is located in Toulouse/Blagnac.

The product ranges of both companies are complementary, with SIGNAAL USFA producing linear cooling engines and Cryotechnologies producing rotary engines and Joule Thomson equipment, including the compressors.

SIGNAAL USFA produces a range of miniature cooling engines for cooling the detectors in thermal imaging systems. These coolers operate at approximately 80 K and have capacities of 0.25 W, 0.5 W and 1.0 W.

During the conference in 1988, we presented the results of various tests that were performed with the single piston cooling engine. In this paper, we present the results of tests performed on a recently developed dual-opposed piston version.

Basic Technical Principles of the Cooler

The principle of these coolers is based on the well-known Stirling-Cycle, using a free piston and free displacer. The piston, which is driven by a linear motor, creates a pressure wave while the displacer moves in such a way that the expansion takes place mainly at the top of the coldfinger and compression occurs in the space between the piston and the displacer.

The mass of the piston/coil assembly, in combination with the mechanical spring and gas forces (gas spring), creates a mass-spring system which is tuned to the drive frequency of 50 Hz. The side loads are extremely low because the driving forces on

both the piston and the displacer act only in the direction of movement. Indeed, this is the main reason for the very long operational lifetime provided by this type of cooler.

The recently developed dual-opposed piston cooler uses two pistons in order to balance the axial forces. This results in an extremely low level of mechanical vibration. In figure 1 is given a schematic cross section of the dual opposed piston linear cooling engine.

Specified Performances of the SIGNAAL USFA Cooling Engines

When specifying cooling engines with capacities of 0.25 W, 0.5 W and 1.0 W, SIGNAAL USFA is given performances which have been measured at the top of the interface and are valid at the specified high ambient temperature level and at the end of the guaranteed lifetime. As shown by the tables 1 and 3 the cooling power at room temperature is much higher.

Performances of the Single Piston Cooling Engines

Technical specification:

SIGNAAL USFA produces single piston cooling engines with performances of 0.5 W (type number UA 7041) and 1.0 W (type numbers UA 7043 and UA 7069). The detailed technical data can be taken from the table 1 and figure 2.

Lifetime test:

The lifetime tests were carried out according to the cycle of the NVEOL B2 Specification. Although the results of the tests for the single piston engines were presented during the 1988 conference, they were not complete at that time since the engines were still running. The final result of these tests, which can be found in table 2, is a measured MTTF of 5557 hours.

Performances of the Dual-Opposed Piston Cooling Engines

Technical specification:

In recent years, SIGNAAL USFA has developed a range of dual-opposed piston cooling engines based on the same principle as the single piston version. However, instead of using one piston for creating the pressure wave, the new version uses two pistons moving in opposite directions. This enables the induced vibrations to be substantially minimized.

In addition, the coil/magnet configuration has been modified to reduce both mechanical dimensions and the static magnetic field which provides the system designer with much more flexibility for integrating the cooler into the system.

The detailed technical data are shown in table 3. Figure 3 and 4 give the performances of these engines as a function of ambient temperature and input power.

This version is fully compatible with USCM detectors.

Qualification test:

For qualification of these coolers in various European programmes, tests as specified in the NVEOL B2 Specification have been performed on the 1.5 W version, type number UP 7058, under the supervision of the Dutch and German Ministry of Defense (MoD) quality departments.

Environmental tests:

The specified environmental tests, which were carried out in a test centre under the supervision of the German MoD, verified that the UP 7058 cooler meets all environmental requirements.

Lifetime tests:

Lifetime tests in accordance with the 24 hours temperature cycle of the B2 Specification were performed in SIGNAAL, USFA's laboratories under the constant supervision of the Dutch MoD. For these tests, eight coolers were taken at random from one production batch and placed in the test set-up in two sessions.

Results:

It was specified that one of the criteria for discontinuing and removing a cooler from the test should be the input power exceeding 55 W. In the graphs of the eight coolers, shown in figure 5 two distinct groups are clearly visible. The degradation in the first group is explained by the instable functioning of the test set-up. After rectifying the weak points, the discontinued coolers were replaced by the second group of 4 identical coolers.

The report of the test results, therefore, can be divided into the two sessions which are shown in table 4. Two coolers are currently still running without any signs of degradation. The results available at this time indicate a measured MTTF of 3582 hours and 4429 hours respectively.

Thermal interfaces

To minimize the thermal losses between coldfinger and the dewar/detector SIGNAAL USFA has developed a wide range of thermal interfaces tailored to the various

dewars. The flexible interfaces on top of the coldfingers will compensate the tolerances in the length of the bore in the dewar and produce a relatively constant pressure to the detector for optimum contact within the operational temperature range. In specifying the cold production of the various coolers SIGNAAL USFA has taken in account the thermal resistance of the interfaces. Next to the thermal advantages the use of the interfaces will give less risk in the demounting of the cooler/detector combination. Figure 6 give some examples of the applied interfaces including the thermal resistance.

Comparison single piston to dual opposed piston cooling engines

After concluding that the overall thermal performances of both versions cooling engines are at a equivalent level we have to notice that big advantages of the dual opposed piston versions are the lower weight and smaller dimensions which make them compatible with the USCM. But the extreme low levels of acoustic noise, EMI, and mechanical vibration make the dual opposed piston version superior to the single piston version and will give the designers a greater flexibility in the system configuration. A glossary of the key data are given in the table 5.

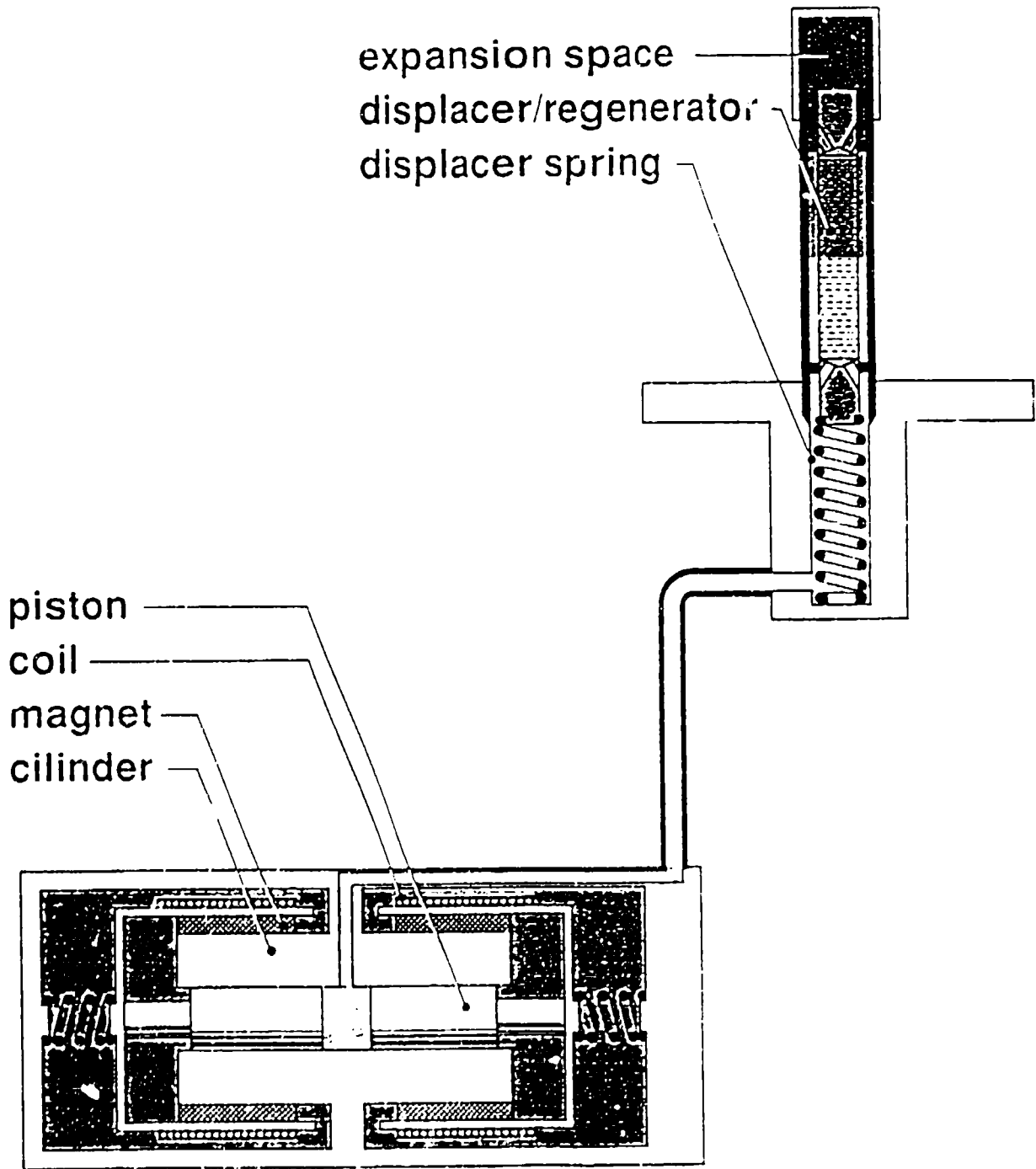


Figure 1 Schematic cross section of the dual opposed piston cooling engine

TECHNICAL DATA
 NOMINAL VALUES @ 23°C

SINGLE PISTON COOLING ENGINES

COOLER UA.	7041	7043	7069
COOLING POWER	0.5W	1.5W	1.3W
COOLDOWN TIME minutes	< 7	< 10	< 10
COOLING TEMP	80K	80K	80K
I/P POWER	50W	55W	55W
30V, 50Hz	max	max	max
COLDFINGER diam	7 mm	10 mm	10 mm
COMPRESSOR diam	71 mm	71 mm	71 mm

GENERAL

MTTF 3500 OPERATING HOURS
 STORAGE LIFE 10 YEARS
 TEMPERATURE RANGES:
 OPERATING - 40 °C TO + 71 °C
 STORAGE - 40 °C TO + 90 °C

Table 1

COOLING POWER @ 80K
 Single Piston Engines

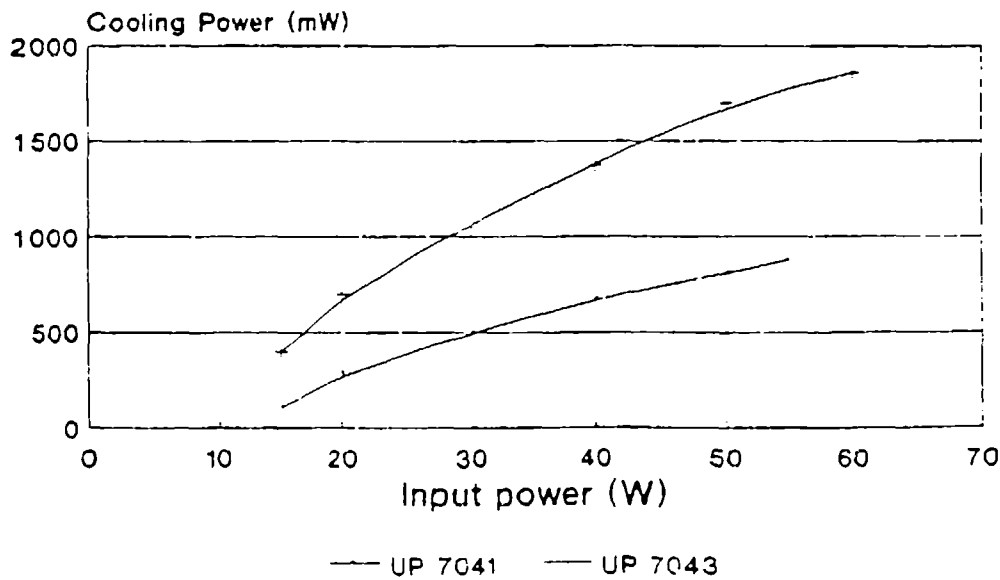


FIGURE 2

RESULTS LIFETIME TESTS UA 7041
SINGLE PISTON COOLING ENGINE

	1988	END TEST
COOLER 1339	2525*	2525
COOLER 1355	2809	8805
COOLER 1357	1408*	1408
COOLER 1362	2625	4410
COOLER 1504	1351	8478
COOLER 1515	591	7718
TOTAL		33343 HRS

AVERAGE 33343 / 6 = 5557 HRS

Table 2

TECHNICAL DATA
NOMINAL VALUES @ 23°C

DUAL OPPOSED PISTON COOLING ENGINES

COOLER UP.	<u>7056</u>	<u>7057</u>	<u>7058</u>
COOLING POWER	0.5W	0.7W	1.5W
COOLDOWN TIME	< 5	< 5	< 5
minutes			
COOLING TEMP	80K	80K	80K
LP POWER	30W	50W	55W
10V, 50Hz	max	max	max
COLDFINGER diam	5 mm	7 mm	10 mm
COMPRESSOR diam	44 mm	55 mm	55 mm

GENERAL

MTTF	3500 OPERATING HOURS
STORAGE LIFE	10 YEARS
TEMPERATURE RANGES:	
OPERATING	- 52 °C TO + 71 °C
STORAGE	- 55 °C TO + 90 °C

Table 3

Cooling power @ 80 K Dual Opposed Piston Engines

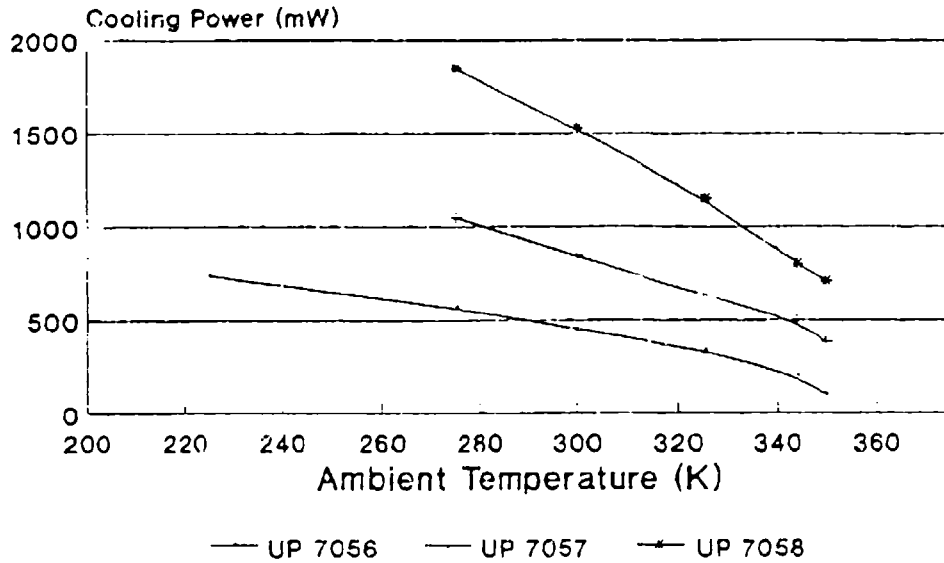


FIGURE 3

Cooling Power @ 80K Dual Opposed Piston Engines

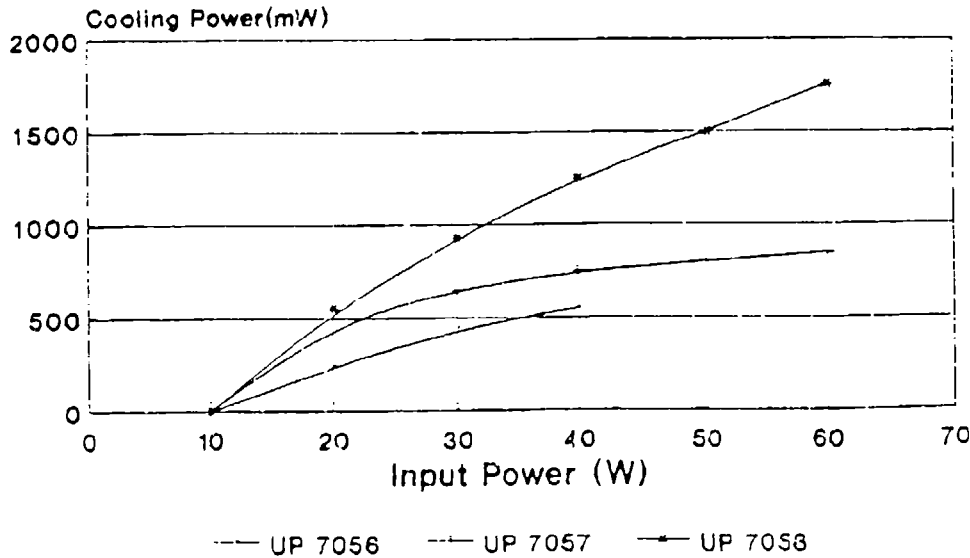


FIGURE 4

RESULTS LIFETIME TESTS UP 7058

DUAL OPPOSED COOLING ENGINE

COOLER	START	END	RUNNING HOURS
0632	18 06 1991	30 09 1991	1853
0634	18 06 1991	03 12 1991	2643
0638	18 06 1991	04 01 1992	3331
0639	18 06 1991	05 01 1992	3112
0635	09 10 1991	06 07 1992	4171
0633	16 12 1991		5356 **
0627	03 02 1992	06 10 1992	3951
0628	03 02 1992		4240 **

MTTF

COOLERS 1 TO 8 3582 hrs **
 COOLERS 5 TO 8 4429 hrs **

** COOLERS ARE STILL RUNNING

Dated: 1st November 1992

Table 4

Lifetime Test UP 7058

at +23 C ambient, (X : events)

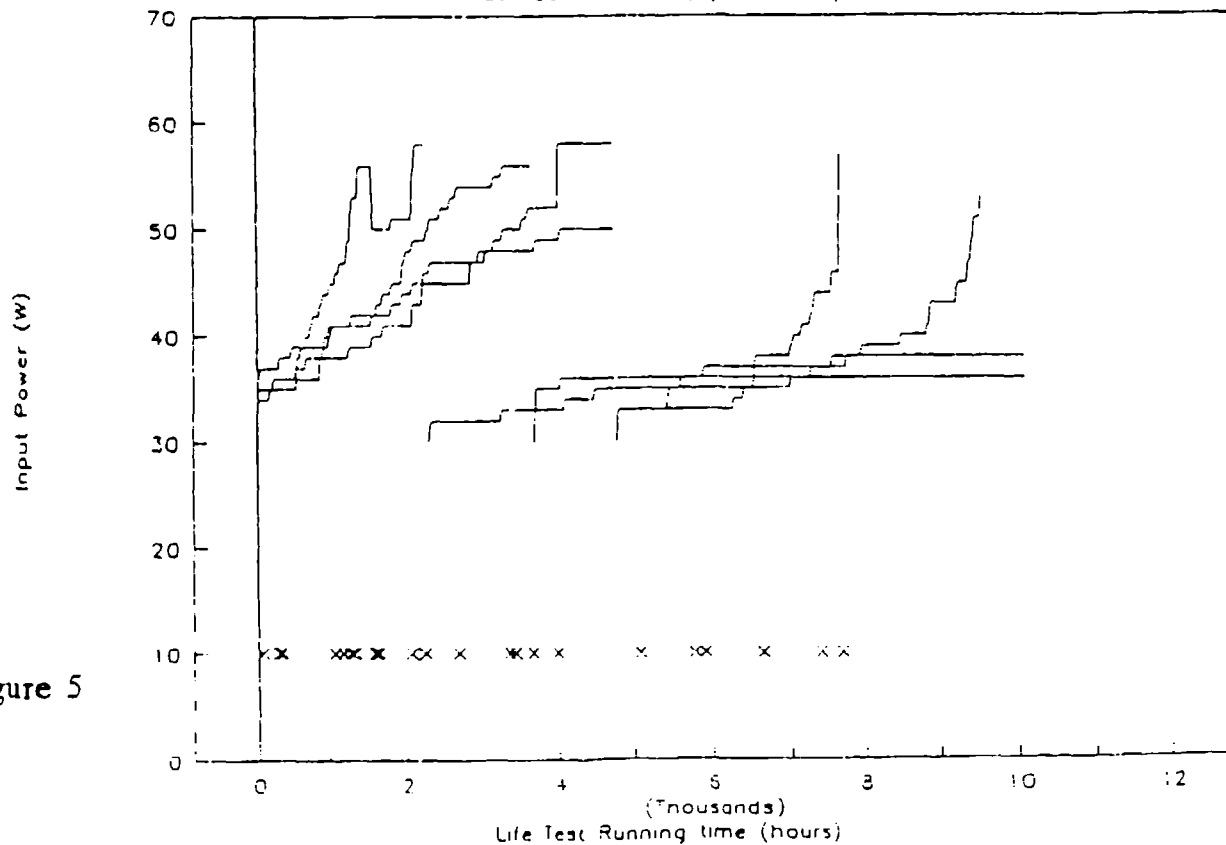


Figure 5

COMPARISON
DUAL AND SINGLE PISTON ENGINES

TYPE	<u>UA 7043</u>	<u>UP 7058</u>
VERSION	SINGLE PISTON	DUAL PISTON
COMPRESSOR dia	71 mm	55 mm
length	145 mm	122 mm
WEIGHT	2.1 kg	1.8 kg
VIBRATIONS	< 25 N peak with balancer	< 1.1 N peak
E.M.I.	82 dB uA/m Typ.	58 dB uA/m Typ.
STATIC FIELD	< 70 mT	< 0.5 mT
INPUT POWER	55 W	55 W
VOLTAGE	30 V rms	10 V rms
CURRENT	1.9 A rms	5.6 A rms

Table 5

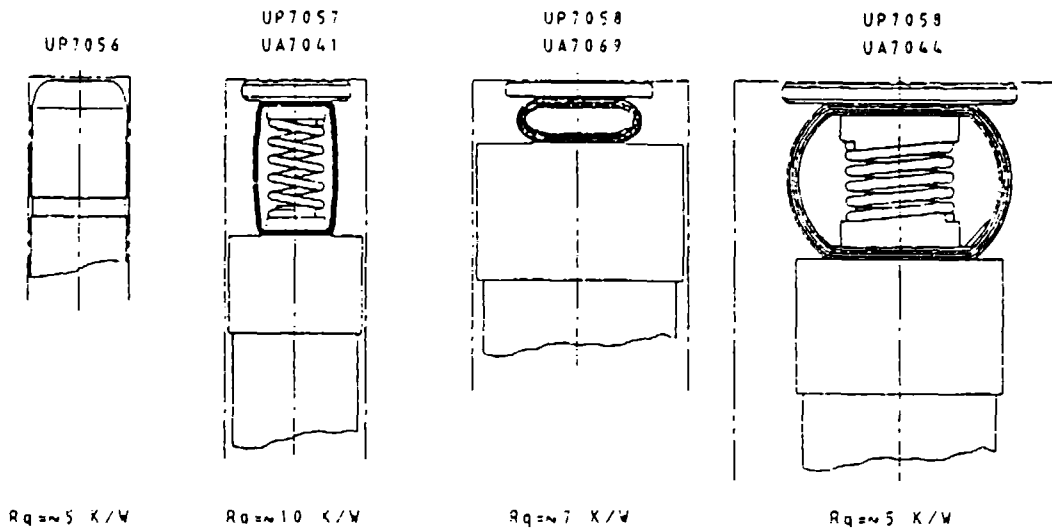


Figure 6 Some examples of applied thermal interfaces

**PRESENT LIFE-TESTING STATUS OF "OXFORD TYPE" CRYOCOOLERS
FOR SPACE APPLICATIONS****C Jewell¹, T Bradshaw², A Orlowska², and B Jones³**¹ Thermal Control and Heat Rejection Section, ESA, 2200AG Noordwijk, The Netherlands² Rutherford Appleton Laboratory, Chilton, Oxfordshire, UK.³ British Aerospace PLC, Bristol, UK.**ABSTRACT**

Both in Europe and the USA, numerous "Oxford type" cryocoolers are being baselined for multi-year space missions. One of the main reasons for such a choice is the belief in the above coolers long term unattended operating ability. This paper, while concentrating on work performed at ESA/ESTEC, Oxford, BAe, and RAL, collects data from several sources in an effort to investigate the confidence for such long term operation. It concludes that the "Oxford type" cryocooler has indeed a proven multi-year potential, with a strong likelihood of reliable operation over periods in excess of five years.

Keywords: cryocooler, long-life, space.

1. INTRODUCTION

Since the early 1970's a strong requirement has existed for multi-year cryogenic cooling in space. Such a requirement came mainly from earth observation and scientific instruments where strict mass and volume constraints inevitably led to the need to develop the only technically feasible solution - a cryocooler for space applications. Unfortunately, initial cryocooler development programmes were not as successful as hoped for, with machines that were either too heavy, too power hungry and failed after limited operating times. However, after a development programme initiated in the late 70's by the University of Oxford and continued by RAL and ESA, a single stage Stirling cycle cryocooler based on the "Oxford type" design (ref 1) now seems to be generally accepted as a viable basis for most cryocooling applications in space. Initial confidence that such "Oxford type" coolers were capable of long term unattended operation came from a design which eliminated all rubbing surfaces, and the experience with flight proven pressure modulator mechanisms (section 2). Increased confidence which comes with long-term life testing, by its very nature, has not progressed as fast as would have been wished, although three units have now operated for over one year each in space. Therefore, with such potential European projects as MIPAS, FIRST and Meteosat Second Generation requiring operational life times of approximately 3years, 3 to 6 years, and 7 years respectively, a life testing programme with the goal of increasing confidence in the coolers reliability predictions is still of major importance.

This paper will try to give an overview of the "Oxford type" reliability status with emphasis on the single stage Stirling cycle cooler, although references are made to further developments such as 20K & 4K coolers (ref 2) which are based on similar mechanisms. In section 2 the cooler mechanism is described and the initial reasons for confidence in the long life operation of the cooler given. In section 3 the accumulated hours of several "Oxford type"

coolers are given with details on certain selected coolers, and finally in section 4 the results and future work are discussed.

2. THE BASIC MECHANISM

The basic mechanism on which all the "Oxford type" Stirling coolers (Fig 2.1) are based is a motor similar to that used in loudspeakers, driving an oscillating piston suspended on diaphragm springs. A clearance around the piston acts as a seal with the motor operating at approximately 40 Hz and the radial position of the piston maintained by the springs. The drive is via the moving coil motor and the shafts axial position is sensed by an inductive or capacitive pick off. The oscillation is maintained by a servo loop which now according to the level of exported inherent cooler vibration required can be amplitude, acceleration or even force controlled. Initially such a mechanism was used by the University of Oxford as a pressure modulator which selectively absorbed molecular emissions at pre-selected wavelengths. In the 70's such pressure modulators were successfully used in space on three instruments (PMR on NIMBUS 6, SAMS on NIMBUS 7, and VORTEX on Pioneer Venus) for operating lifetimes of 3, 7, and 1 year respectively. Therefore, with the absence of any rubbing surfaces, the operation of the diaphragm springs at a maximum stress below the fatigue failure level, and the above in-orbit "life tests", in the early 80's there was already a high confidence in the long life potential of a cooler whose design was based on the mechanism described above.

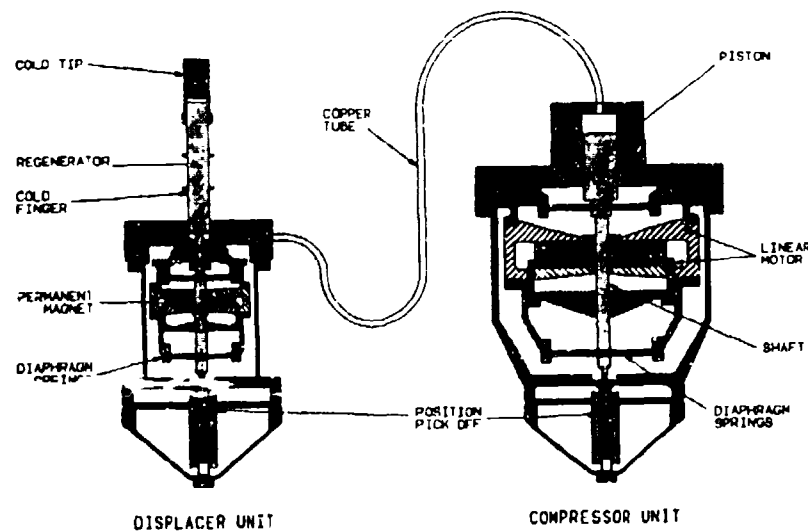


Fig 2.1

3. LIFE TEST COOLERS

In the ideal world an identical set of a 100 or more coolers would have been on life test since the mid 1980's. However, the need to continue development work and the prohibitive cost involved in setting aside such high numbers of coolers has led to a rather haphazard approach to the problem of life testing. Table 3.1 is an attempt to summarise the number of

"Oxford Type" Cryocoolers - Hours Completed			
Cooler	Hours	Last Update	Comments
ISAMS 1 Oxford	7984	May 18, 92	Two flight units (4984 hrs. in orbit)
ISAMS 2 Oxford	3000	June, 91	Two flight spare units
ISAMS Life Test	30560	Sept, 91	Failed Sept 91. Re-built
ESA/ESTEC	41933	Nov 9, 92	Presently running
ATSR	>10600	Nov, 92	One unit in orbit
BAe DM1	1396	Oct, 90	Re-furbished AIRS cooler
ESA DM2	1470	Oct 90	Re-furbished 65K cooler
BAe 2-Stage Cooler	7519	Nov, 92	2058 hrs horizontal
BAe Prod. Coolers			
1. NLR	690	Feb, 92	One cooler to be launched on HTSE expt. in 1993
2. NLR	1080	Feb, 92 □	
3. JPL	2850	Mar, 92	Extensively tested
4. TRW	8125	Aug 3, 92	5672 hrs horizontal
5. GSFC	750	May, 90	
6. ESA	8835	Oct 6, 92	Tested to pre-qual. levels
7. Fujitsu	400	Sep 90	Hours at delivery
8. Fujitsu	404	Sep 90	Hours at delivery
9. Toshiba	418	Jan 91	Hours at delivery
10. BAe	10750	Oct 6, 92	BAe life test cooler
11. Toronto Univ.	1143	Aug, 92	Evaluation coolers for MOPITT
12. Toronto Univ.	1843	Aug, 92 □	
Pressure Modulators			
NIMBUS 6 (PMR)	3.0 yrs	-	2 units in-orbit
NIMBUS 7 (SAMS)	7.0 yrs	-	7 units in-orbit
Pioneer Venus	1.0 yr	-	1 unit in-orbit

Table 3.1

operating hours for present day "Oxford type" coolers that are running as sealed units. The rest of this section gives a more detailed view of certain selected coolers:

3.1 ESTEC Cooler

3.1.1 History & Test set-up.

The ESTEC cooler (Fig 3.1) was ordered from Dr S Werrett (University of Oxford) on the 14th May 1986, and delivered to ESTEC on the 4th May 1987. It was built to an earlier design of the coolers presently flying on the instrument ISAMS (section 3.3) The original objective of the cooler was not that of a life test cooler but one of assisting instrument testing in the Space Science Division within ESTEC. When it became clear that the coolers original goal could no longer be realised the cooler was put on life test in the Mechanical Systems Laboratory at ESTEC. This life test was only intended to demonstrate the long life potential of the cooler mechanism and the cooler has never undergone environmental testing (i.e thermal vacuum or vibration testing). Unfortunately the cooler build is practically undocumented and information relating to the cooler prior to its delivery to ESTEC has been obtained verbally from its "builder" Dr S Werrett. Tragically with the recent death of Dr S Werrett this source of information is no longer available. However, it should be noted that the ESTEC cooler was certainly not baked-out to the same level as the Oxford lifetest cooler (section 3.2) and a possibility exists that it had indeed not been baked out at all (private communication 02/06/89).

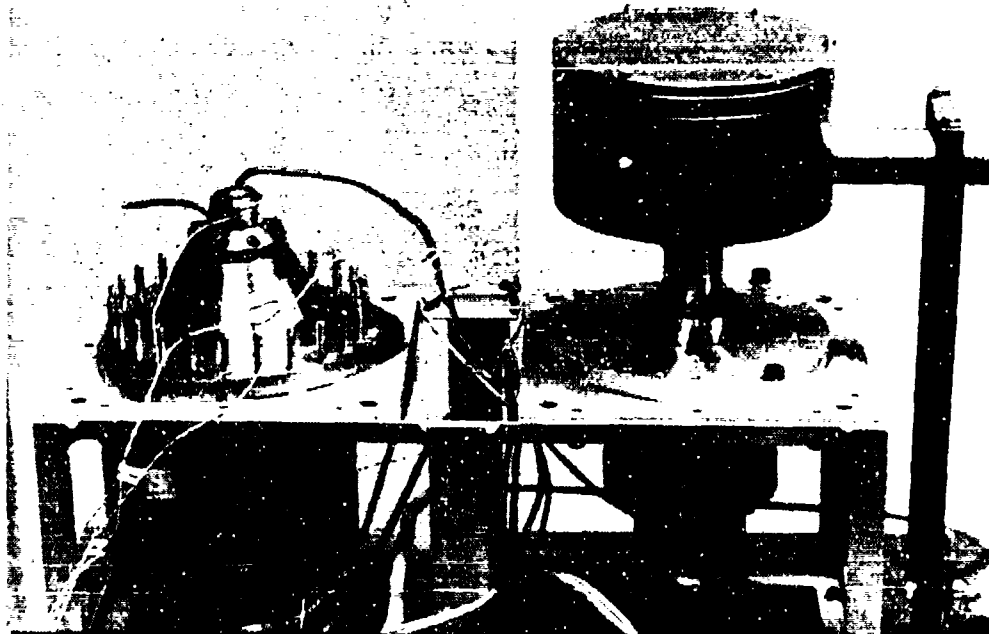


Fig 3.1

In the life-test bench set up at ESTEC the following points are worth noting:

- the temperature sensor is a calibrated 100 ohm platinum resistor, measured with a 4-wire resistance bridge.
- there are six 80micron diameter copper wires of 100mm length between the vacuum feed-through and copper cold finger. This is estimated to give an increase of approximately

30mW to the parasitic heat load.

- the temperature sensor and a 820 ohm metal film resistor used as a heater have been glued into a block of aluminum (16 x 8 x 8 mm) which is clamped onto a copper cold finger adapter with two M3 bolts.

- the vacuum housing is made of stainless steel and after initial pump down with a cryo-pump is left connected to a 20l/sec ion pump.

- laboratory electronics built by Oxford University are used to control the cooler.

- true rms wattmeters were used to measure the compressor and displacer power input from 15/03/89 onwards.

3.1.2 Life test data & discussion

The life testing of the ESTEC cooler started as a very low key affair with no pre-defined test programme in mind. Therefore the results presented in this section are open to criticism with respect to the scientific approach taken. Nevertheless the data is considered of particular interest when it is taken into account that this cooler as a sealed unit and with no servicing has operated for over 41,000 hours (4.7 years), which is thought to be a world record.

Before finally sealing the gas via crimping in early 1987, the ESTEC cooler was filled at Oxford to 1.4MPa at 20 C, and since transportation to ESTEC has run in a laboratory environment at an ambient temperature of 20 +/- 2 C. For the vast majority of the time the cooler has been run at fixed control unit settings corresponding to a frequency of 40.0 Hz and a phase angle between the displacer and compressor of 65 degrees. The compressor and displacer demands have also been left constant giving a peak to peak stroke of 7.96mm for the compressor and 2.56 mm for the displacer. No attempt has been made to simulate long term operation with a heat load, although the heater on the cold finger has been used during the life test period. The cooler offset was also checked to be correct and left unchanged during operation. Figs 3.2 to 3.4 show the evolution of the coolers base temperature with operating time, were the following points are of relevance:

1) Continuous cooler operation was started on the 29th February 1988, at which point the cooler had already run for 1443 hours.

2) After 918i, 10767, and 12055 hours of operation the heater was activated in order to measure cooler load lines, parasitic heat loads, etc.

3) At 14696; 17408; 19045; 20693; 26820; 31589; 35257; 37140; 38837; and 40134 hours the cooler, due to planned events or electrical trips was allowed to rise to room temperature for varying periods of time. The cooler was then re-started maintaining nominal cooler drive settings.

4) Cooler shell temperature, room temperature, level of vacuum, and true RMS power input into the compressor and displacer, were also measured but not presented here.

It can be seen from these results that there is a time dependent performance degradation, with a big "jump" at 12055 hours, which is systematically recoverable on warming up the cooler to room temperature and cooling down again. The following points should be noted:

- the vacuum installation was frequently tested and no leak has been found at the $< 10e-08$

mb litre/sec level. Also the degradation seen seems too high to be explained by water vapour condensing on the outside of the cold finger when an increase of 40% in the absorption would require 1-3 microns of ice.

- the degradation is still recoverable after only hours at 300K.

Since no drift away from the nominal cooler drive settings have been found, and the possibility of a mechanical fault with such a behaviour is not considered likely the authors believe that the performance degradation is due to internal cooler condensibles, probably in the regenerator. This hypothesis seems to be even more likely when it is re-called that the ESTEC cooler was probably not baked out but flushed prior to final crimping.

3.2 Oxford life test cooler

In the mid 80's a prototype Oxford cryocooler of a similar design to that which is presently running at ESTEC underwent a programmed lifetest (ref 3). This lifetest started with one unit being vibrated to levels shown in Table 3.2 and then operated for 6438 hours before the displacer failed. On strip down of the displacer (the compressor remaining intact) the failure was found to be caused by the short circuiting of one of the static wires leading to the drive coil which had been incorrectly positioned on assembly. Since no signs of wear or fatigue of the displacer mechanism were found, another displacer from the same batch of prototype coolers was connected to the lifetest compressor, the "new" cooler vibrated again to the levels shown in Table 3.2, and allowed to run in a continuous manner in a laboratory environment. After 21313 hours of displacer operation, and hence 27751 hours of compressor operation, problems were experienced with the displacer which eventually entailed the ending of the life test in September 1991. At which time the compressor had achieved 30,560 hours of operation.

Frequency (Hz)	20 - 120	120 - 600	600 - 2000
Power Spectral Density	+ 9 db Oct ⁻¹	0.08 g ² Hz ⁻¹	-9 db Oct ⁻¹

Table 3.2

Under strict QA control the cooler was "stripped down" and the problem identified to be one that had already been designed out at the late prototype stage. Therefore, the cooler was re-furbished and is expected to be put back on continuous life test in the near future.

3.3 In-Orbit Coolers

Although not strictly life test coolers there are presently "Oxford type" coolers flying on

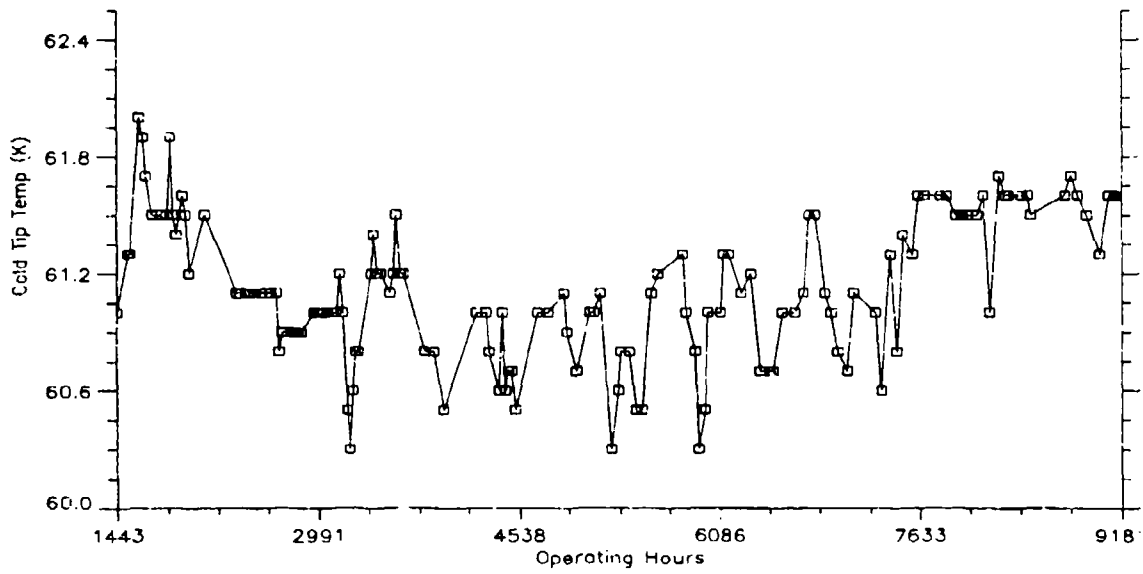


Fig 3.2 Cold Finger Temperature vs Time (1443 hrs - 9181 hrs)

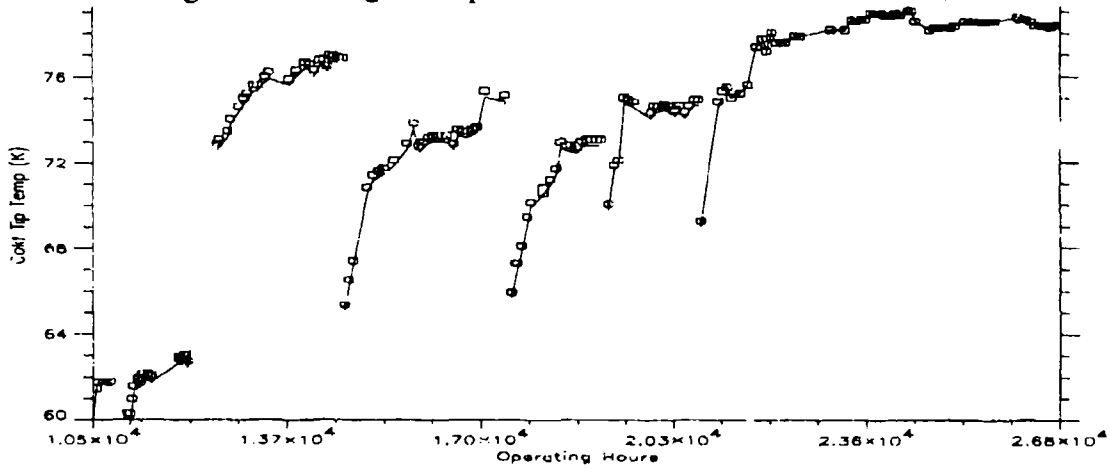


Fig 3.3 Cold Finger Temperature vs Time (10475 hrs - 26820hrs)

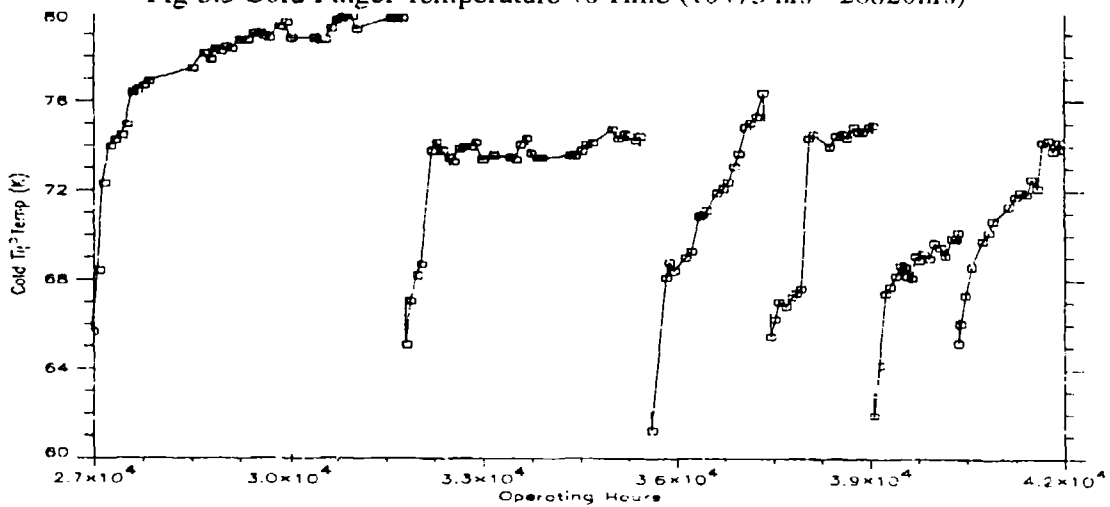


Fig 3.4 Cold Finger Temperature vs Time (26886 hrs - 41763 hrs)

two earth observational instruments in space. These instruments are the Improved Stratospheric and Mesospheric Sounder (ISAMS) on the american satellite UARS, and the Along Track Scanning Radiometer (ATSR) on the European satellite ERS-1. The ISAMS coolers consist of two split Stirling cycle coolers which have evolved from a design described in sections 3.1 & 3.2 of this paper. The ATSR cooler (built at RAL) uses the same diaphragm springs and clearance seal technology, but is built in one unit with two compressors working back to back directly feeding into a single displacer. Both coolers have been extensively documented up to their launch dates on the 16th July 1991, and the 8th October 1991, for ERS-1 and UARS respectively.

In orbit, the ATSR cooler has performed nominally since its commissioning in August 1991 with no sign of any cooler related performance degradation. It has presently (November 1992) run for approximately 10,600 hours with an instrument lifetime specification of 2 to 3 years. Further data is expected when a nearly identical cooler is to be flown on a follow-on mission: ERS-2 in 1994, for the instrument ATSR-2.

With respect to ISAMS technical problems not associated with the cooler have caused several long periods of non-operation. Presently, problems with the chopper drive motor have put in doubt the future operation of the instrument but the coolers when running have performed nominally, and have achieved the running hours mentioned in Table 3.1.

3.4 BAe Production Coolers

In 1986 in order to ensure a future supplier for potential European users the ESA placed a contract with BAe which transferred the Oxford cooler technology to industry. After the end of this contract in 1988 a cooler build standard was specified from which present BAe production coolers are built. So far the production model coolers that have been built to this standard are shown in Table 3.1 although six more coolers are presently on-line. The operating hours in Table 3.1 are frequently updated but unfortunately visibility is not always easy. While the coolers in Table 3.1 were delivered after a 400 hour "run in" period (with acceptance level testing baselined for future coolers) it should be noted that two of the coolers number 6 and number 10 have undergone extensive environmental testing (ref 4) to pre-qualification levels. This testing has included sinusoidal vibration testing to levels in Table 3.3, thermal vacuum testing, EMC testing and self induced vibration measurements. Both these coolers are operating nominally and are scheduled to continue their life tests.

Sinusoidal Vibration (each orthogonal axis)	
Frequency	Level
5 - 18	+/- 11mm (0 - peak)
18 - 60	+/- 15.0 g (0 - peak)
60- 100	+/- 6.0 g (0 - peak)
Sweep Rate	2 octaves/minute, 1 sweep up and down. No notching.

Table 3.3

Other production coolers worth mentioning in more detail are coolers 3 and 4 delivered to JPL and TRW respectively. The JPL cooler has been extensively used for characterisation work which has included measurements of cooler self induced vibration, cold finger parasitic heat leak, EMC and a comprehensive performance mapping (ref 5). The TRW cooler was intended as a demonstration model while gaining useful life test data and is now on loan to Los Alamos for system integration work. It is interesting to note that the TRW cooler has run 5672 hours in a horizontal position.

3.5 Other Coolers

Other coolers out of the initial batch of six Oxford prototype coolers have only been used for development purposes, but have been estimated to have run for periods ranging up to a few hundred hours each. While moving forward historically two development model coolers DM1 and DM2 were built in 1986. The BAe DM1 ran for 1396 hours before being re-configured into a 55K cooler for the US instrument AIRS, and the ESA DM2 ran for 1470 hours (despite being vibrated to qualification levels twice) before being re-configured into an optimised 65K cooler. Other single stage coolers based on the Oxford design have been operated over long periods but none are known to have run as sealed units.

Finally, as an example of the ability of the design in maintaining its long life potential, a 20K dual stage Stirling cycle cooler development based on the Oxford mechanism was initiated in 1985 by RAL, with the help of ESA funding. The 20K cooler has two separate compressors working back to back feeding a dual stage displacer. The RAL 20K cooler used as a pre-cooler in RAL/ESA's development model 4K cooler has run for a few hundred hours before being presently re-furbished. Of more significance a 20K cooler (ref 6) built at BAe under another ESA transfer of technology contract has completed over 1000 hours of operation without any performance degradation, 2000 of which were in a horizontal position. This ESA 20K cooler successfully negotiated a similar environmental testing programme as the ESA (No 6) production cooler and is due to undergo a minimum of 5 years life testing at BAe.

4. DISCUSSION

As can be seen from section 3 a significant amount of both terrestrial and in orbit data has, and is continuing to be collected on sealed "Oxford type" cryocoolers. This data is being acquired in a rather haphazard manner, but is still significant and adds enormously to the confidence in long life cooler operation, which was initially based on the design similarity with the pressure modulators described in section 2. At present nearly 8 sealed units have operated for over a year, with 2 units achieving over 3 years of operation. Since many instruments have lifetimes of the order of 3 years and are presently unlikely to be flown without cooler redundancy, a significant barrier is likely to be broken in early 1993 when a statistically viable number of coolers will have passed 18 months of operation. Of course such life testing should continue for as long as possible, but already with the Oxford and ESTEC life test coolers, reasonable confidence can be had in extremely long life times of the order of 5 years or more. Such long lifetimes start to raise further questions with respect to the reliability of other mechanisms in the instrument, such as choppers, moving mirrors, the need for cooler electronic controller redundancy etc etc. However, there does not seem to be any one weak point in the cooler design which would render the operation of a cooler for periods greater than 5 years impossible, or even difficult to achieve. Regarding future work, with the possible exception of the re-furbished Oxford University cooler (section 3.2), no new coolers are expected to start a life testing programme, in fact it is possible that

the ESTEC cooler is taken off lifetest in 1993 for a complete strip-down and testing under strict quality control. This is expected to resolve the problem of the recoverable degradation in performance, but if arguments for a longer running period were strong enough this might be postponed to a later date.

5. CONCLUSION

This paper has tried to bring together the operating lifetimes of various sealed cryocooler units using the "Oxford type" mechanism. Although not conclusive by itself, it does seem to strongly indicate that long term cryocooler operation in space is now a reality. In fact, with the ever increasing confidence in their long life potential, the use of such coolers is expected not only to render present cryogenic instruments more system friendly, but lead to new and exciting applications, such as the possibility of long life cooling down to very low cryogenic temperatures. The ESA is presently encouraging such an innovative development, and within Europe a programme for very low temperature cryocoolers should see by early 1993 a 4K cooler, originally developed at RAL, being built and tested at BAe to the pre-qualification levels mentioned in reference 6. A 2.5K cooler should also be bench tested at RAL by the third quarter of 1993. All these coolers rely heavily on the Oxford type mechanism, and could herald a new era in the domain of space cryogenics.

6. REFERENCES

1. Werret S & al 1986, Development of a small Stirling cycle cooler for spaceflight applications, *Adv. Cryog. Eng.*, 31, 791-799.
2. Jewell C 1991, An overview of ESA cryocooler activities, ESA SP-324, 195-199.
3. Werret S & Peskett G 1986, Development of the Stirling cycle coolers for the Improved Stratospheric and Mesospheric Sounder, *Proc. 4th Int. Cryocooler Conf.*, 289-301.
4. ESA Final Report Contract 8083/88 1992, Development of an engineering model 80K closed cycle cooler, CR (P) 3410.
5. Ross R & al 1992, BAe 80K Stirling cooler performance characterization, JPL Report D-9912.
6. ESA Final Report Contract 9004/90 1992, Development of an engineering model 50-20K two stage Stirling cycle cooler, CR (P) 3428.

DESIGN AND TEST OF A COMPREHENSIVE FACILITY FOR LIFE-TESTING SPACE CRYOCOOLERS

R. G. Ross, Jr. and D. L. Johnson

Jet Propulsion Laboratory
California Institute of Technology
Pasadena, California 91109

ABSTRACT

With the growing commitment of long-life Stirling cryocoolers to multi-year NASA and SDIO space applications, there is increasing need for quantitative data verifying the long-term performance of the coolers and identifying any possible time-dependent degradation or wear-out failures. To obtain such data, JPL has designed and fabricated comprehensive life-testing facilities for use by the Air Force Phillips Laboratory (AFPL) and the Jet Propulsion Laboratory (JPL). These life-test facilities are directed at acquiring quantitative cooler performance data in three areas: 1) refrigeration performance including thermal efficiency, long-term temperature stability and possible effects of contamination and wear, 2) level and stability of generated vibration including long-term performance of vibration cancellation technologies, and 3) illumination of any wear-out or random failure mechanisms that need to be corrected prior to flight hardware deliveries. To provide these functional capabilities, the developed life-test chambers incorporate a number of unique features including thermostatically controlled thermal-vacuum heatsink environments, continuous monitoring of cooler-generated vibration, and active fault detection.

INTRODUCTION

Worldwide cooler development programs involve the development of a number of long-life cryocoolers for future space applications. These coolers are intended to provide continuous cooling at cryogenic temperatures from below 10K to as high as 150K for periods of time up to 10 years; they utilize a variety of thermodynamic cycles such as Stirling, pulse tube, turbo-Brayton, and sorption. Although thermodynamic cooling performance is a necessary attribute, operational life and reliability is the critical parameter that separates these long-life space cryocoolers from the relatively short life (2000 to 5000 hour life) "tactical" coolers commonly used in ground and airborne applications.

There is an important need within the space-cooler community for thorough and accurate data on the reliability performance of these space cryocoolers to assist both systems developers in their design of cryogenic sensor systems, and cooler developers in their process of understanding design strengths and resolving identified limitations. Although early life-

test data has become available for the first of the long-life space cryocoolers, the Oxford/BAe 80K cooler [1], no life tests have yet been initiated on the emerging second-generation coolers containing the advanced thermodynamic and vibration-suppression features required for the most recent space-instrument programs.

To meet the growing requirement for comprehensive life-test data on emerging space cryocoolers, JPL has developed specialized facilities specifically addressed to the unique demands of conducting life tests in simulated space environments and accurately measuring the broad array of critical performance parameters. The development effort reflects a combined program between the Air Force/Phillips Laboratory, Albuquerque, NM, and the Jet Propulsion Laboratory under a combination of SDIO and NASA funding. This paper first discusses the detailed test objective and approach addressed by the facility design, and then describes details of the thermal-vacuum test chambers and the performance measurement and data acquisition system.

LIFE TEST OBJECTIVES AND IMPLEMENTATION CONSIDERATIONS

There are at least three key objectives of life testing: one focused toward management-level needs, one focused toward the needs of the cooler development teams, and the third focused to the needs of the cooler users or application system designers.

- 1) The first objective is to demonstrate the ability of a test cryocooler to operate with good reliability over an extended period of time. This is the most general of the objectives and is focused toward providing confidence to high-level program management needing to judge the maturity of a particular cryocooler design and its general suitability to long-life space missions. Meeting this objective does not require that a cooler never fail; rather it requires that the number of failures and the type of failure mechanisms be consistent with reliably correcting any identified weaknesses within the budget and schedule constraints of the build cycle of a typical flight program.
- 2) The second objective is directed at the identification of failure modes and inadequate design features that need to be corrected. In particular, this objective is directed at detecting generic long-time-constant failure and degradation mechanisms that do not become visible until after an extended period of operation and aging. Examples include contamination due to extended outgassing of internal materials, long-term wear of contacting or rubbing parts, long-term thermal degradation of the physical properties of polymers (e.g. embrittlement, cracking, shrinkage), fatigue of cyclically loaded elements, long-term breakdown of electrical insulation materials, loss of dimensional stability of close tolerance parts, long-term creep of materials operating at high homologous temperatures (solders, polymers, gasket materials), and long-term drift of electronic component parameters. Although every attempt is made to adequately address long-time-constant mechanisms during the cryocooler design process, extended life data covering such mechanisms is often unavailable, and some critical issues are likely to escape early detection. Because such mechanisms are often common to every

cooler of the same design, even a single test cooler is often quite effective in identifying such mechanisms. On the other hand, long-time-constant mechanisms that stem from inadequate process control--such as cooler cleaning and outgassing, or part machining and assembly accuracy--generally require multiple test coolers to quantify the likely variability.

- 3) The third objective is to accurately quantify any long-term change in cryocooler performance that occurs over time. Although many long-time-constant mechanisms identified as part of the second objective cause catastrophic cooler failure and need to be corrected, others can lead to gradual erosion of performance, and be quite acceptable if properly taken into account during the application design process. This third objective is to accurately quantify the level and nature of any gradual change from initial beginning-of-life performance so that system designs using the cooler can introduce the necessary performance margin to account for the expected change.

To meet the above objectives, particularly the second and third, it is necessary to: 1) identify the cooler performance attributes of interest and how they can best be accurately monitored, and 2) identify the operating mode and environment that will best surface the critical long-term degradation and failure mechanisms without causing extraneous problems.

Key Performance Attributes

The primary cooler performance attribute of interest is cooler cold-end heat capacity and its stability for a given set of fixed input conditions such as piston stroke and input power; that is, constancy of refrigeration efficiency over many years. Stability of cold-end temperature over lesser periods of time is also important and relates to the ability to hold the cold end at a fixed temperature over time without excessive closed-loop temperature control.

In addition to cooler thermal performance, the ability of the cooler to maintain acceptably low levels of generated mechanical vibration over many years is also a critical issue for most precision space-instrument applications.

Test Environment Considerations

Because the degradation rate of most aging mechanisms is strongly dependent on ambient temperature, utilizing elevated temperatures to shorten the required test time is common in the field of life testing. Unfortunately, the presence of tight temperature-sensitive alignments and tolerances in most cryocoolers makes exposure to abnormal temperatures likely to cause rapid unrealistic failures that are not coupled to the real failure mechanisms of interest. This, combined with the fact that refrigeration efficiency is also highly sensitive to temperature, suggests that achieving realistic levels and tight control of operating temperature is key to being able to accurately measure long-term performance trends. This high sensitivity to temperature also argues for testing the cooler throughout its allowable flight heat-sink temperature range, typically from 0 to 40°C for space cryocoolers, but not

significantly beyond this range.

A second important life-test consideration is the issue of continuous operation versus start-stop cycles. The length of operating periods has been found to be critical to the getting of both internal and external contaminants to the refrigerator cold-end. Long, multi-week continuous operating periods, typical of space-cooler applications, have been found to be more sensitive to contamination than short multi-hour periods typical of tactical applications. On the other hand, periodic turn-off cycles every few weeks, which are common in space flight, are also well known for initiating failures associated with differential-expansion and fatigue mechanisms. For example, Fig. 1 illustrates the power turn-off cycles required for the Oxford University ISAMS instrument to periodically decontaminate the cold-end components attached to the instrument's two Oxford 80K Stirling cryocoolers [2]. The fact that the rate of contamination in Fig. 1 decreases each cycle suggests that the contamination is external to the cryocooler; thus, the turn-off cycles provide valuable evidence about the nature and location of the contamination. Life-test data on tactical coolers also supports the importance of periodic turn-off periods involving warming to room temperature, and suggest that cycling can cause contaminants to redistribute in detrimental ways within the cold-end.

Life-test data gathered by the European Space Agency (ESA) on the Oxford University 80K cooler also shows that contamination mechanisms can be quite sensitive to the cooler cold-end temperature. In the ESA tests, the level of observed degradation was dramatically greater when the cooler was under load, than when the cooler was under no-load [1].

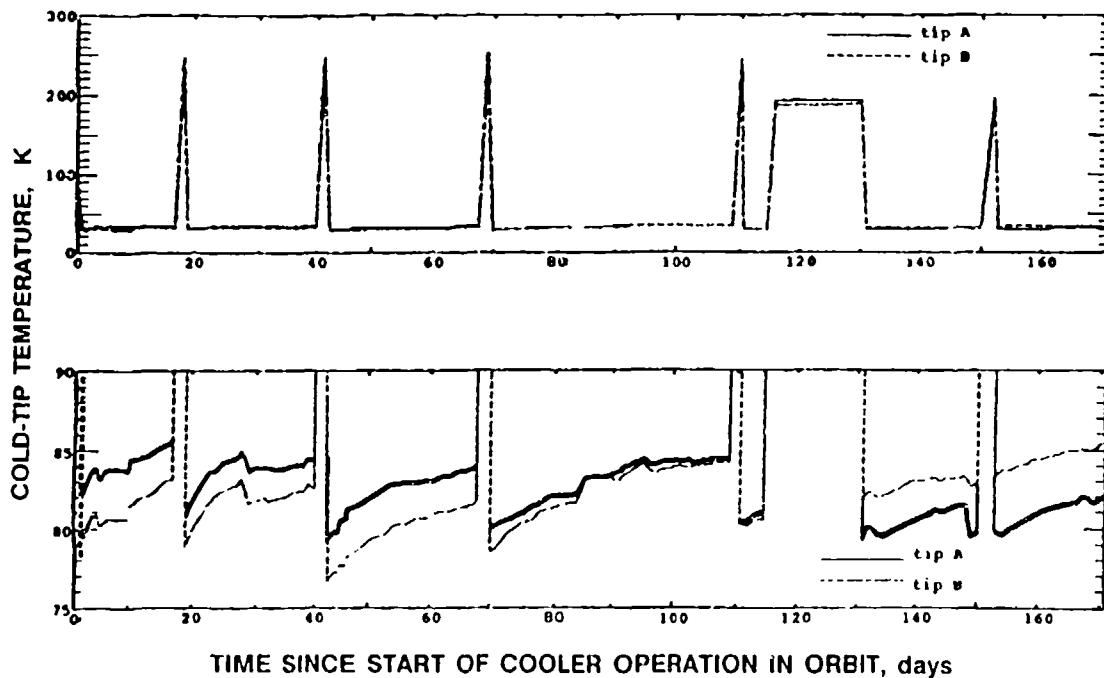


Fig. 1. ISAMS Oxford Stirling cooler performance in orbit aboard the NASA Upper Atmosphere Research Satellite (UARS).

We conclude from these data that a life-test cryocooler should be run at the expected application temperature (as opposed to under no-load conditions) and be periodically turned off and allowed to reach room-ambient temperature. Because buildup of contaminants has a relatively long time constant (many days), turn-off cycles should probably be conducted on the order of once per month for space cryocoolers, similar to the ISAMS flight history shown in Fig. 1.

As a last consideration, launch vibration can cause contact of otherwise non-contacting parts, thus leading to possible deterioration of critical alignments or generation of wear products. Since launch proceeds long-life operation in space, it is desirable to precondition the cooler prior to life testing by subjecting the cooler to flight-acceptance levels of launch vibration testing.

JPL LIFE-TEST IMPLEMENTATION APPROACH

In response to the above performance measurement needs and operating environmental sensitivities, the selected life-test implementation incorporates the following features:

- 1) The chosen fundamental measure of cooler performance is input power required to maintain the design cold-tip thermal load at the design cold-tip temperature (e.g. power required to maintain 2 watts at 65K). This power (or specific-power) performance can be most easily obtained by operating the cooler continuously at the desired fixed cold-tip temperature and cold-tip heat load. Unfortunately, many space coolers have only manual stroke control, and have no closed-loop means of temperature control. For manual-control coolers it is proposed to maintain operation near the desired load point (within 2°C) using periodic manual updating of the cooler stroke or applied heater load, and then to interpolate to the design-point specific power using the near-constant shape of the specific-power curve in the vicinity of the design point.
- 2) To provide the necessary stable environment to gather the power performance data, the life tests are conducted in a simulated space thermal-vacuum environment with carefully controlled heat-sink temperatures. This approach, which has been successfully demonstrated as part of JPL's extensive cooler characterization program [3,4], requires that the cryocooler reject its heat conductively--as in space; this results in realistic operating temperatures and thermal gradients within the cooler. Experience has shown that the heat sink temperature is accurately controllable and allows small deviations in cooler thermal performance to be monitored; the fluid-loop heat rejection system also allows the heat sink temperature to be easily varied throughout the flight temperature range (e.g. 0 to 40°C).
- 3) During life testing the cooler heatsink is slowly stepped throughout the flight temperature range; the cycle includes continuous cooler operation over sequential five-week periods; during each continuous-operation five-week period the heatsink temperature is varied weekly with sequential one-week operating periods at 20°, 0°, 20°,

40°, and 20°C, respectively. Each five-week sequence ends in a programmed cooler turn-off and warm-up to the 20°C heatsink temperature. The one-week duration at each heatsink temperature is chosen to allow adequate time for accurate temperature stability measurements to be made, and to allow repeat data to be acquired every two weeks at 20°C and every 5 weeks at the extreme (0°C and 40°C) temperatures. The turn-off excursion once every five weeks is bracketed by 20°C environments to allow accurate comparison of performance before and after the excursion.

- 4) In addition to the thermal performance, cooler generated vibration levels and spectrum are also measured over time; this is to assess changes in the vibration levels and spectrum caused by possible cooler degradation, or degradation of the vibration-suppression control electronics. The measurements are limited to qualitative measurements because precision multi-axis quantitative measurements would require a well-isolated, high-rigidity in situ vibration dynamometer for each cooler under test; this is considered beyond the scope of a life test. To achieve the high-quality qualitative measurements of vibration in the primary cooler axis requires that the thermal-vacuum test chambers be vibration-isolated from extraneous vibration sources such as vacuum pumps, chillers, and other coolers.

DETAILED TEST FACILITIES DESCRIPTION

Thermal Vacuum Test Chambers

The JPL developed thermal-vacuum test chambers, shown in Fig. 2, are custom-fabricated

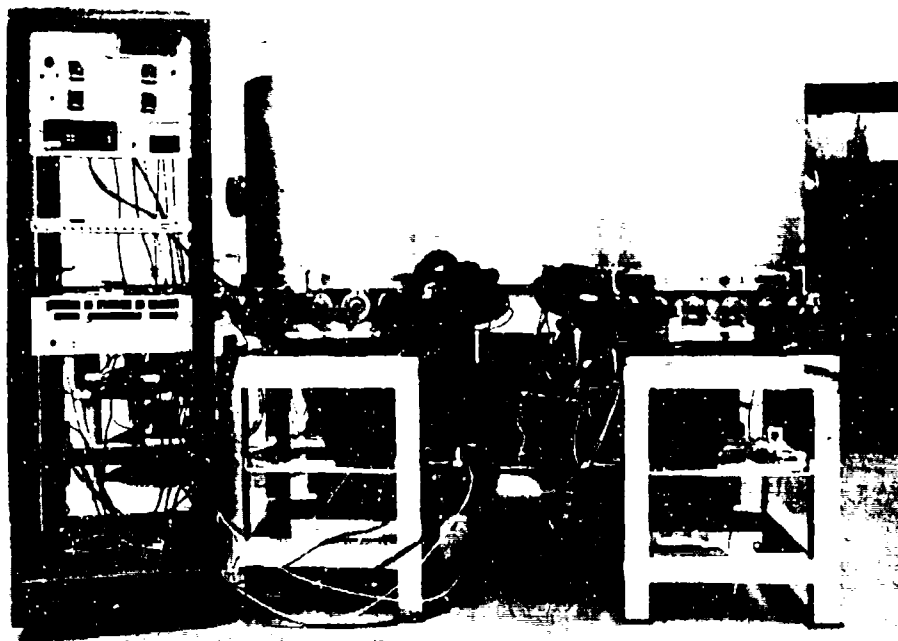


Fig. 2. JPL lifetest chamber installation overview.

24"-diameter bell jar assemblies connected to a central vacuum pumping system that uses a high-cleanliness turbo vacuum pump. Each chamber is equipped with an instrumentation collar to accommodate electrical and cooling-fluid feedthroughs, and a baseplate that is drilled with a pattern of tapped bolt holes to accommodate mounting of the test cooler within the chamber. An autoclosing gate valve is used to seal off each chamber from the central vacuum pumping system in the event of a pumping failure, and to allow a chamber to be opened while other chambers are under vacuum. Separation of the vacuum pumping system allows the pumps to be remote from the test chambers to minimize vibration, EMI and noise in the immediate vicinity of the cryocoolers under test. It also allows a single spare vacuum pump to back-up the total vacuum system in the event of a pump failure.

To allow cooler vibration measurements to be relatively free of background noise, each bell-jar assembly is vibration isolated from its structure using auto-leveling pneumatic air springs; this gives the bell-jar assembly a first natural frequency below 10 Hz, thus providing significant vibration isolation at the cooler drive frequency and harmonics.

Temperature control of each cooler is provided by a central fluid loop driven by a remotely located chiller system. The chiller system provides a flow of coolant at a temperature set approximately 10°C below the desired heatsink temperature for the cryocoolers. Like the central vacuum system, the remote location of the chiller and fluid pumping system minimizes vibration, EMI, noise and heat dissipation in the immediate vicinity of the cryocoolers under test.

To achieve accurate temperature control of each cooler heatsink (separate ones for each compressor and displacer) each bell-jar assembly is served by two fluid streams from the central chiller, and each stream is equipped with its own independent metering valve and temperature controller. Each fine-tuning controller actuates an inline immersion heater in its fluid stream to raise the individual heatsink assembly to the desired set-point value.

To provide for temperature control of each cooler element (e.g. compressor and displacer), a design-specific fluid-loop heat exchanger heatsink assembly is fabricated to interface to the cooler's heat rejection surfaces intended to be used in space. Each heatsink assembly also structurally supports the cooler element from the chamber base-plate via the vibration force transducers. Each cooler element is electrically connected to its manufacturer-supplied electronics via feed-throughs through the chamber collar. Fig. 3 shows the heatsink assemblies and structural supports for the British Aerospace (BAe) 80K cooler under life-test at JPL.

Following instrumentation of the cryocooler cold-tip with appropriate load heaters and cryodiodes, the cold finger is isolated from the chamber thermal radiation environment using a carefully manufactured canopy of multi-layer insulation (MLI).

Instrumentation

Life-test instrumentation includes all measurement transducers and their necessary conditioning electronics that interface to the data acquisition system. The total chamber

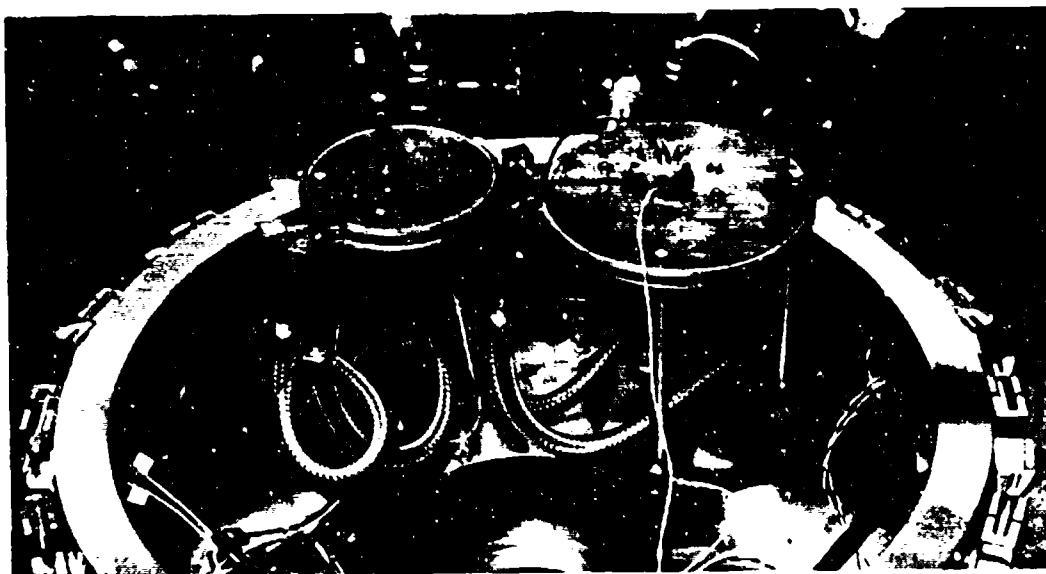


Fig. 3. Design-specific heatsink assemblies for JPL's BAe 80K cooler.

instrumentation falls into seven categories: 1) heatsink and cooler external case temperature transducers and conditioning electronics, 2) cold-tip cryodiode thermometry, 3) cold-tip heaters and power supplies, 4) cooler piston and displacer amplitudes, 5) compressor and displacer true-RMS power parameters, 6) vibration force transducers and conditioning electronics, and 7) chamber vacuum level instrumentation.

In the JPL-developed system, heatsink and cooler case temperatures are measured using thermocouples, as are ambient temperature and cooler drive electronics temperature. Cold-tip temperature is monitored via redundant Lakeshore Model 470 cryodiodes mounted to the cold tip. The level of vacuum in each bell-jar system is continually monitored using a cold cathode gage with integral alarm levels. The gage is used to shut the chamber gate valves in the event of loss of vacuum.

The cold-tip heater is either supplied by the cooler manufacturer, or is a (~ 500 ohm) precision thin-film resistor mounted in a custom fabricated mount for integration to the cooler coldfinger. It is important that the cold-tip heater only be actuated when the cooler cold-tip is cold and the cooler is operating; if the cooler is not running, application of cold-tip heater power can rapidly overheat and damage the cooler cold-tip. An important function of the data acquisition and control system is to protect against a misapplication of cold-tip heater power.

Conditioned analog signals (~ 1 volt per mm of stroke) representing the cooler piston and displacer amplitudes are monitored from the manufacturer-supplied cooler drive electronics. The input power to the cooler compressor and displacer are measured using a true-RMS digital power analyzer inserted into the cooler drive power cables. Correction to the power measurements must be made for I^2R power dissipation in the cooler leads

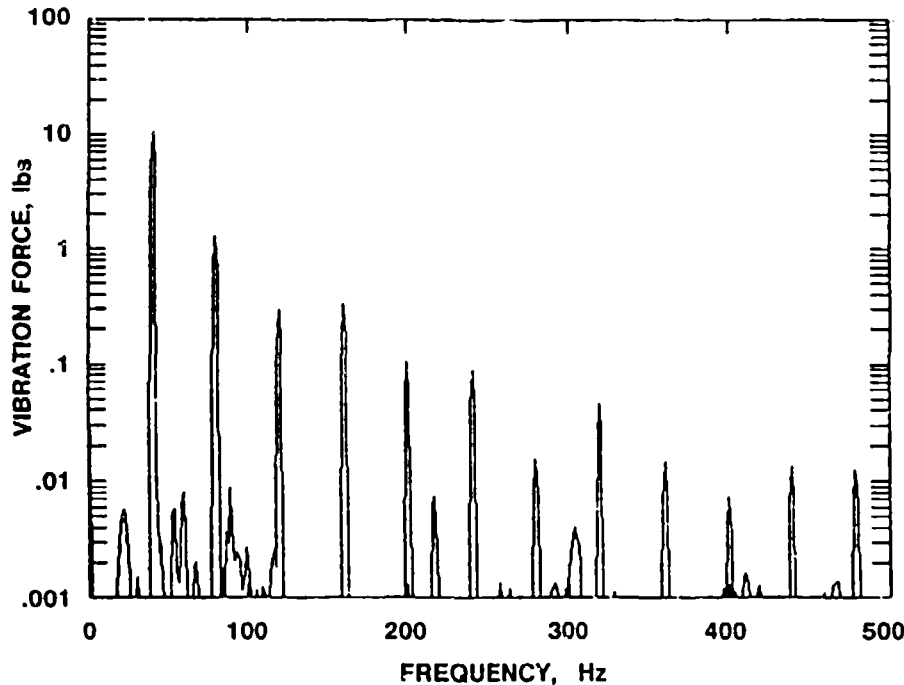


Fig. 4. Excellent low-noise vibration spectrum measurement of BAe 80K cooler in JPL lifetest chamber.

between the cooler and the power meter. This is done by subtracting the RMS current squared times the wire resistance from the power reading.

Cooler-generated vibration forces are measured using a piezoelectric force ring mounted between each cooler element (displacer and compressor) and the chamber base plate. These force transducers have a sensitivity range from 0.002 pounds to 100 pounds and are fed to the data acquisition system for spectrum analysis and A/D conversion. Figure 4 illustrates the excellent vibration spectrum achieved with JPL's BAe 80K cooler mounted in the life-test chamber. The low level of background noise achieved in the life-test facility compares favorably with the results achieved with JPL's 6 DOF force dynamometer with a 4000 pound seismic mass [5,6].

Data Acquisition and Control

The data acquisition and control system is responsible for sequencing the overall cooler test operations, logging the cooler performance and environment data in engineering units, archiving the measured data to mass storage (hard-disk, floppy, and back-up tape), providing realtime display of cooler performance parameters, and providing for cooler and system fault detection and safety shutdown. Final preparation of camera-ready plots of performance is done off-line, using the mass storage files, as part of the data reduction and documentation function.

The JPL data acquisition and control system is built around a 386 desk-top PC microcomputer that contains a GPIB board to interface to the IEEE 488 instruments, a

relay board for controlling external on-off functions, and a fast A/D converter for acquiring vibration analog data; standard hard disks, floppies, and back-up tape transports are used for data archiving.

In addition to measuring and archiving the data, the life-test PC also tracks key performance parameters relative to preset bounds that indicate acceptable performance or dangerous out-of-bound operation. If the occurrence of an out-of-bound performance parameter is noted, the computer relay board is commanded to turn off the cooler and light a visual warning indicator. Key performance parameters to be monitored against fault levels include: compressor and displacer stroke, compressor and displacer power, cold-tip temperature, cold-tip heater power, and heatsink temperature. Separate control of the cold-tip heater is provided to enable the cold-tip heater to be actuated only when the cooler is turned on and running and the cold-tip has a temperature below 200 K.

SUMMARY

The recent development of a number of long-life miniature cryocoolers has led to an explosion of interest in multi-year-life space cryogenic instruments. To assist the space-instrument user community in understanding and applying these important new cryocoolers, the JPL has undertaken the development of specialized cryocooler life-testing facilities under the sponsorship of SDIO/AF Phillips Laboratory and the NASA Eos AIRS project. Over the coming months important space cryocoolers are scheduled to begin life testing in these facilities at JPL and at the AF Phillips Laboratory in Albuquerque, New Mexico. These tests are expected to provide extensive life-test thermal-performance and vibration data on key cryocoolers of interest to the space instrument community.

ACKNOWLEDGEMENT

The work described in this paper was carried out by the Jet Propulsion Laboratory, California Institute of Technology, and was sponsored by the NASA Eos AIRS Project and the Strategic Defense Initiative Organization through an agreement between the Air Force Phillips Laboratory and the National Aeronautics and Space Administration.

REFERENCES

1. Jewell, C., Bradshaw, T., Orłowska, A. and Jones, B., "Present Life-Testing Status of 'Oxford Type' Cryocoolers for Space Applications", Proceedings of the 7th International Cryocooler Conference, Santa Fe, New Mexico, November 17-19, 1992.
2. Whitney, J., ISAMS Cooler Performance Log, Issue D, Atmospheric, Oceanic & Planetary Physics Div., Oxford University, U.K., March 16, 1992.

3. Kotsubo, V.Y., Johnson, D.L., and Ross, R.G., Jr., "Calorimetric Thermal-Vacuum Performance Characterization of the BAe 80 K Space Cryocooler", SAE Paper No. 929037, Proceedings of the 27th Intersociety Energy Conversion Engineering Conference, San Diego, California, August 3-7, 1992, P-259, Vol. 5, pp. 5.101-5.107.
4. Johnson, D.L., Mon, G.R. and Ross, R.G., Jr., "Spacecraft Cooler Characterization", Proceedings of the 7th International Cryocooler Conference, Santa Fe, New Mexico, November 17-19, 1992.
5. Ross, R.G., Jr., Johnson, D.L. and Sugimura, R.S., "Characterization of Miniature Stirling-cycle Cryocoolers for Space Application," Proceedings of the 6th International Cryocooler Conference, Plymouth, MA, DTRC-91/002, David Taylor Research Center (1991), p. 27-38.
6. Ross, R.G., Jr., Johnson, D.L. and Kotsubo, V., "Vibration Characterization and Control of Miniature Stirling-cycle Cryocoolers for Space Application," Adv. Cryo. Engin., Vol. 37B (1991), pp. 1019-1027.

**SIMULATION PROGRAM FOR MULTIPLE EXPANSION
STIRLING MACHINES**

G. WALKER, M. WEISS, R. FAUVEL, G. READER AND E.R. BINGHAM
DEPARTMENT OF MECHANICAL ENGINEERING
THE UNIVERSITY OF CALGARY
CALGARY, ALBERTA, CANADA

ABSTRACT

Stirling cryocoolers with a single stage of expansion routinely achieve cryogenic refrigeration temperatures of 70 K. Lower temperatures can be achieved with multiple expansion stages arranged 'in series', 20 K with two stages, and less than 10 K with three or four stages. Multiple expansion Stirling power systems are also in prospect particularly for exhaust heat recovery systems using different stages of progressively lower temperatures. Two or more stages can be combined in a single cylinder.

Multiple expansion Stirling machines have been a topic of interest at The University of Calgary for some years. Recently a second-order computer simulation program with integral graphics package for Stirling cryocoolers with up to four stages of expansion were developed and made available to the Stirling community. Adaptation of the program to multiple expansion Stirling power systems is anticipated.

This paper briefly introduces the program and presents a specimen result.

INTRODUCTION

The Stirling cryocooler was first developed commercially at the Philips Research Laboratories, Eindhoven, Holland in a program initiated in 1948 with first deliveries around 1953. Since then applications of Stirling cryocoolers have proliferated, particularly in the miniature versions used in night vision and

missile guidance systems. They are made nowadays by a dozen manufacturers at the rate of thousands a month (1).

The pioneer work on multiple-expansion Stirling cryocoolers was carried out at the Philips Research Laboratories (2). Temperatures of 20 K were readily achieved with two stages of expansion. Later, Daniels et al (3) described a three-stage Stirling cryocooler which achieved a minimum temperature of 7.8 K. This same engine was used by Keung et al (4) to study the effects of leakage through clearance seals on the cryocooler performance.

Zimmerman et al (5,6) described work on three and four stage Stirling cryocoolers intended for low power cryogenic electronic instrumentation.

Very little theoretical analysis or computer simulation of multiple expansion Stirling cryocoolers has been reported in the literature. The idealised cycle analysis for a Stirling refrigerator with multiple expansion stages, perfect regeneration and isothermal processes was published by Walker (7). A computer simulation program utilising this theory in BASIC, for personal computers was developed and tested but was not published.

The ideal adiabatic analysis of a Stirling cryocooler with multiple expansion stages in the form of a FORTRAN computer simulation program was presented by Urielli et al (8). The equations of the analysis do not have closed solutions. Rather the differential equation set is solved numerically and the authors found it necessary to use a main frame computer because of the non-linear complexities of the cycle. Neither of the two papers discussed above included any allowance for the various loss mechanisms present in all Stirling cryocoolers and arising from various thermal, fluid and mechanical friction effects. Walker (9) has summarised the principal loss mechanisms observed in small to miniature Stirling cryocoolers.

William Martini (10) of Richland, Washington was commissioned by the U.S. Bureau of Commerce, National Bureau of Standards, Boulder, Colorado (technical officer Dr. R. Radebaugh) to prepare a computer

simulation program for a four expansion space Stirling cryocooler. He delivered his draft report shortly before his death. On delivery the program was substantially complete but was only partially operational. The Martini draft report was not published but the original copy is held by Dr. R. Radebaugh, National Institute for Science and Technology, Boulder, Colorado. Copies of the report may be made available by Dr. Radebaugh to interested parties on application.

THE MARTINI MULTIPLE EXPANSION CODE

The partially operational computer simulation code for quadruple-expansion Stirling cryocoolers developed by Martini was specifically intended for a four stage expansion piston/displacer cryocooler. It consists of a stepped displacer, to form the four expansion spaces, and a separate compressor connected with the displacer cylinder by a connecting tube. The cylinders were arranged orthogonally. The code describing this cryocooler implemented a second order hybrid isothermal analysis which took into account the heat capacity of the solid parts but assumed perfect heat transfer from the working gas to the surrounding solid walls. It is assumed that, at each instant of time, the pressure of the working gas throughout the cryocooler was the same. Flow pressure losses were calculated separately at each time step, summed over the cycle, and then added to the required power input. Real gas properties of the helium working gas were included but a programming bug rendered them inoperable. Additionally, an extensive data base of material properties at cryogenic temperatures for several solids was incorporated in the code. This program served as the basis for the more general program which is the subject of this paper.

DESCRIPTION OF THE MULTIPLE EXPANSION CODE

The four-expansion space program described above was generalized to a multi-expansion space code which is capable of simulating low-temperature cryocoolers with up to four expansion spaces and in a variety of configurations and mechanical arrangements, two-piston machines, piston-displacer machines including parallel and tandem arrangements. The real gas properties of the helium working gas are now operable and the compressor and displacer drive mechanisms are separate, thus allowing dissimilar compressor and displacer strokes and a specified phase angle. Additionally, a simple but extensive graphics routine has been added to visualize the effect of important parameters. The code is written in FORTRAN 77 with GEOGRAF graphics routines and operates in the DOS environment.

Input to the program consists of the basic cryocooler dimensions, regenerator and displacer material and the operating conditions. The gas temperatures at each of the expansion spaces is assumed. Output includes the required power input and itemized heat transfer and losses in the compression and expansion spaces. Graphics of heat lifted and C.O.P. as a function of pressure and speed for each expansion space are available as is the total required input power. Future development of the program will include routines to simulate the operation of individual regenerators by having different forms and structures between given temperature levels. Initially it was anticipated the system would start from an arbitrarily specified temperature distribution and proceed automatically over many cycles to the steady-state temperature distribution. However, this depends to a critical extent on the external disposition of the refrigeration generated through radiation shields, convection, etc. and no simple way to account for the multifarious external factors has yet been devised.

PROGRAM TEST CASE

Actual operating and performance data for multiple expansion machines are generally not available. There is an urgent need for careful experimental measurements to be published before development of the computer simulation design aid can proceed.

Limited performance data and dimensions for a triple-expansion Stirling cycle cryogenic refrigerator are given by Keung and Lindale (4). The refrigerator dimensions, operating conditions and performance data are summarized in Table 1 and the refrigerator is shown schematically in Fig. 1. This test case was simulated using the new program and graphical displays of the results are given in Figs. 2 and 3 with sample tabular output in Table 2. The complete graphics package includes the production of 22 separate figures of different parameters calculated over a given range of pressure and speed levels.

These preliminary results (Table 2) confirm that the program is indeed functional, however, predicted values of heat lifted from the third expansion space are considerably higher than the actual measurements. This discrepancy is due primarily to the limitations of the models used to describe the compression space cooler and the regenerators. At present, the program can only model a simple connecting tube instead of a compression space cooler and solid regenerators with annular gaps rather than the packed regenerators present in the actual triple-expansion refrigerator.

From Keung and Lindale (4) it is not clear at which displacer and compression piston position the charge pressure is measured, thus the mean cycle pressure is not well defined. Furthermore, the temperatures of the compression space and the first and second expansion spaces are not given.

Considering the lacking input data coupled with limited regenerator models it is not surprising that the predicted results do not coincide with measurements.

MULTIPLE EXPANSION STIRLING POWER SYSTEMS

So far as is known no multiple expansion Stirling power systems have been made. However, recent work has indicated that this situation may soon change. The possibilities for multiple expansion Stirling power systems arise in connection with the development of engines utilising the waste heat of hot exhaust streams, ie. gas turbines, coke calcining plants, etc. Multiple stage Stirling power systems with progressively lower expansion space temperatures may be arranged mechanically to have two or more expansion stages arranged in the same cylinder.

It is anticipated the computer simulation program described above will be applicable also to Stirling power systems with multiple expansion spaces.

CONCLUSIONS

The computer simulation described here for multiple-expansion Stirling cryocoolers is still at an early stage of development. However, the ground work for a useful design and optimization tool has been laid.

ACKNOWLEDGEMENTS

Research on Stirling engine at The University of Calgary is supported by the Natural Sciences and Engineering Research Council of Canada. We would like to thank Dr. Ray Radebaugh for making available the original report and code of Martini. Thanks to H.C. Wong for assisting with the graphics routines.

AVAILABILITY

It is anticipated that when further developments are completed copies of the computer program described here will be available for

purchase from Brad Ross, 1923 Hummingbird Court, Richland, WA or from Marvin Weiss, Box 9, Site 7, R.R. 5, Calgary, Alberta, Canada, T2P 2G6. Experimental data for multi-stage expansion Stirling refrigerators is urgently required to validate and verify this computer program. Cooperation with those having functional multi-stage expansion machines is invited. Provide us with your experimental data and we will use the program to investigate optimising or improving your design.

REFERENCES

1. Walker, G., "Miniature Refrigerators for Cryogenic Sensors and Cold Electronics", Oxford University Press, Monograph Series of Cryogenics, Oxford, U.K., 1989.

2. Prast, G., "A Philips Gas Refrigerating Machine for 20 K", Cryogenics 3, pp. 156-160, Sept. 1963. See also, Prast, G., "A Gas Refrigerating Machine for Temperatures Down to 20 K and Lower", Philips Tech. Rev. 26(1), pp. 1-11, January 1965.

3. Daniels, A. and du Pre, F.K., "Triple-Expansion Stirling Refrigerator", Adv. in Cryo. Eng., Vol. 16 (Ed. K. Timmerhaus), Plenum Publishing Corp., 1971.

4. Keung, C.S. and Lindale, E., "Effects of Leakage Through Clearance Seals on the Performance of a 10 K Stirling Cycle Refrigerator", Proc. Third Intl. Cryocooler Conf., (Ed. R. Radebaugh, B. Louie and S. McCarthy), NBS Spec. Pubn. 698, US Govt. Printing Off., Washington, DC, Boulder, Colo, 1985.

5. Zimmerman, J.E. and Radebaugh, R., "Operation of a SQUID in a Very Low Power Cryocooler", Proc. Applications of Closed Cycle Cryocoolers to Small Superconducting Devices, (Eds. J. Zimmerman, T.M. Flynn), NBS Spec. Pub. 508, US Govt. Printing Office, Washington, DC, 1977.

6. Zimmerman, J.E., Sullivan, D.B. and Ives, J.T., "Operation of a Practical Squid Gradiometer in a Low-Power Stirling Cryocooler", Proc. Refrigeration for Cryogenic Sensors and

Electronics Systems, (Ed. J. Zimmerman, D. Sullivan and S. McCarthy), NBS Spec. Pub. 607, US Govt. Printing Office, Washington, DC, 1980.

7. Walker, G., "Cycle Analysis for Stirling Refrigeration with Multiple Expansion Stages, Perfect Regeneration and Isothermal Processes", Int. J. of Refrigeration, Vol. 13, No.1, Butterworths Scientific, Guildford, U.K., pp. 13-19, 1990.

8. Urielli, K. and Walker, G., "An Ideal Adiabatic Analysis of a Stirling Cryocooler with Multiple Expansion Stages", Proc. Low Temp. Eng. Conf., Univ. Southampton, Inst. of Cryogenics, U.K., June 1990.

9. Walker, G., "Low Capacity Helium Liquifier: A Ross-Stirling Engine with Zimmerman Displacer and Two Stage Compressor with Joule-Thomson Expansion", Proc. Fourth Intl. Cryocooler Conf., (Eds. G. Green, G. Patton and M. Knox), David Taylor Naval Ship Research and Development Center, Easton, Maryland, Sept. 1983.

10. Martini, W., "A Four Expansion Space Cryocooler Design Program", unpublished manuscript of a draft report prepared for U.S. Department of Commerce, National Bureau of Standards, Contract No. 40-RANP 5-B4748, Dr. R. Radebaugh, Project Officer, 1986.

TABLE 1 TEST CASE DIMENSIONS AND OPERATING CONDITIONS

	Comp. Space	1st Exp. Space	2nd Exp. Space	3rd Exp. Space
Diameter, mm	63.5	39.9	20.0	15.1
Stroke, mm	32	12	12	12
Regenerator				
length, mm	-	39.4	29.4	24.5
mesh material	-	phosphor-bronze	phosphor-bronze	lead
mesh fill factor	-	0.4	0.4	0.4
Temperature, K	300 (assumed)	120 (assumed)	60 (assumed)	20
Heat Lifted, W	-	-	-	1.0
Speed: 640 RPM				
Charge Pressure: 0.62 MPa				
Phase Angle: 60°				

TABLE 2 SAMPLE PROGRAM OUTPUT

<u>MECHANICAL POWER INPUT (Summation Method)</u>		<u>Watts</u>			
P-V power:		542.482			
Cooler flow loss:		0.772			
Regenerator flow loss (1st Stage):		0.568			
(2nd Stage):		0.078			
(3rd Stage):		0.009			
TOTAL POWER INPUT:		543.918			
 <u>TOTAL POWER INPUT (Mechanical Drive Method)</u>		 <u>Watts</u>			
Compressor drive:		544.705			
Expander drive:		-2.230			
Cooler flow loss:		0.772			
TOTAL POWER INPUT:		543.247			
 <u>ITEMIZED HEATS FOR CYCLE [W], (+ve is heating, -ve is cooling)</u>					
(ZONE)	Compression Space		Expansion Space		
	and Cooler	(1st)	(2nd)	(3rd)	
Heat Transfer from gas:	640.1	-121.8	-16.8	-20.1	
Cylinder Wall Conduction (in):	0.0	3.4	0.4	0.1	
Cylinder Wall Conduction (out):	-3.4	-0.4	-0.1	0.0	
Expander Wall Conduction (in):	0.0	0.2	0.0	0.0	
Expander Wall Conduction (out):	-0.2	0.0	0.0	0.0	
Shuttle Loss (in):	0.0	2.2	0.2	0.1	
Shuttle Loss (out):	-2.2	-0.2	-0.1	0.0	
Flow Friction:	1.1	0.3	0.0	0.0	
Net Heat (Sum):	635.3	-116.3	-16.4	-19.9	
Net Heat (DelT):	635.3	-116.3	-16.4	-19.9	

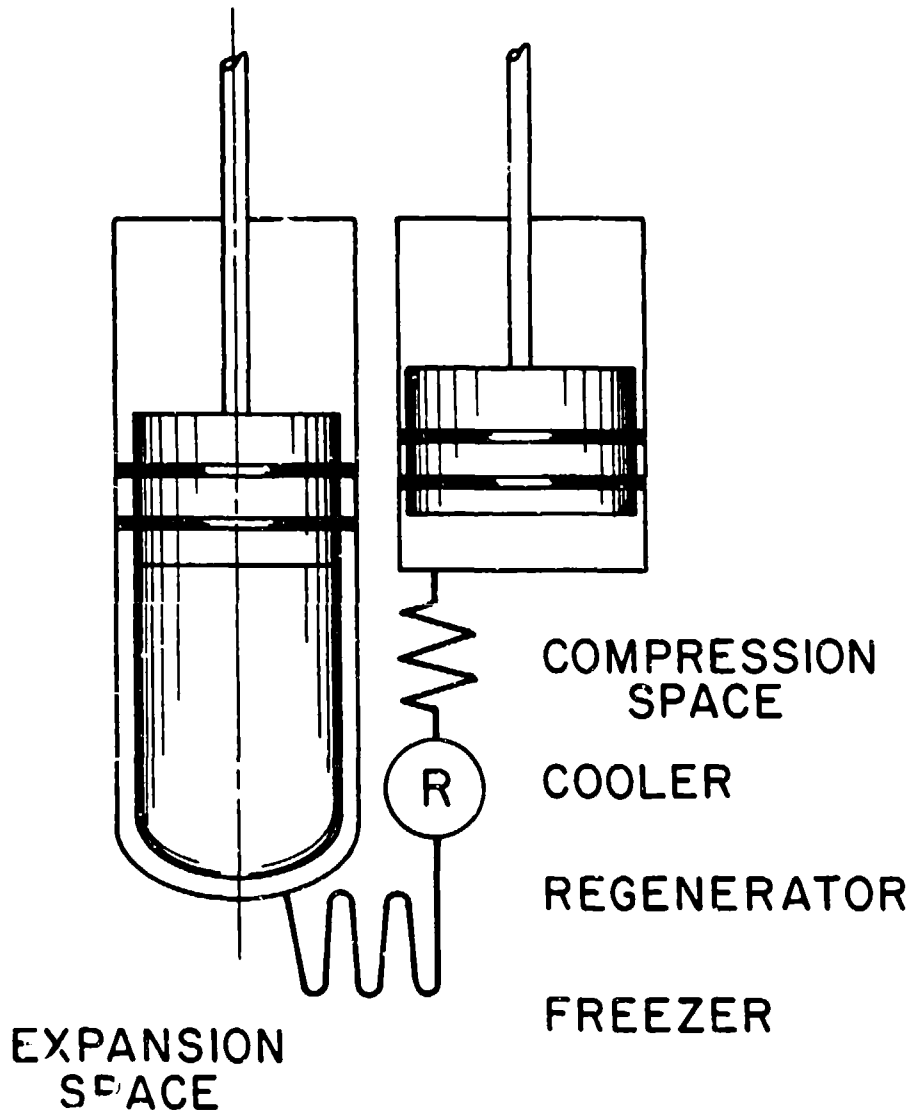
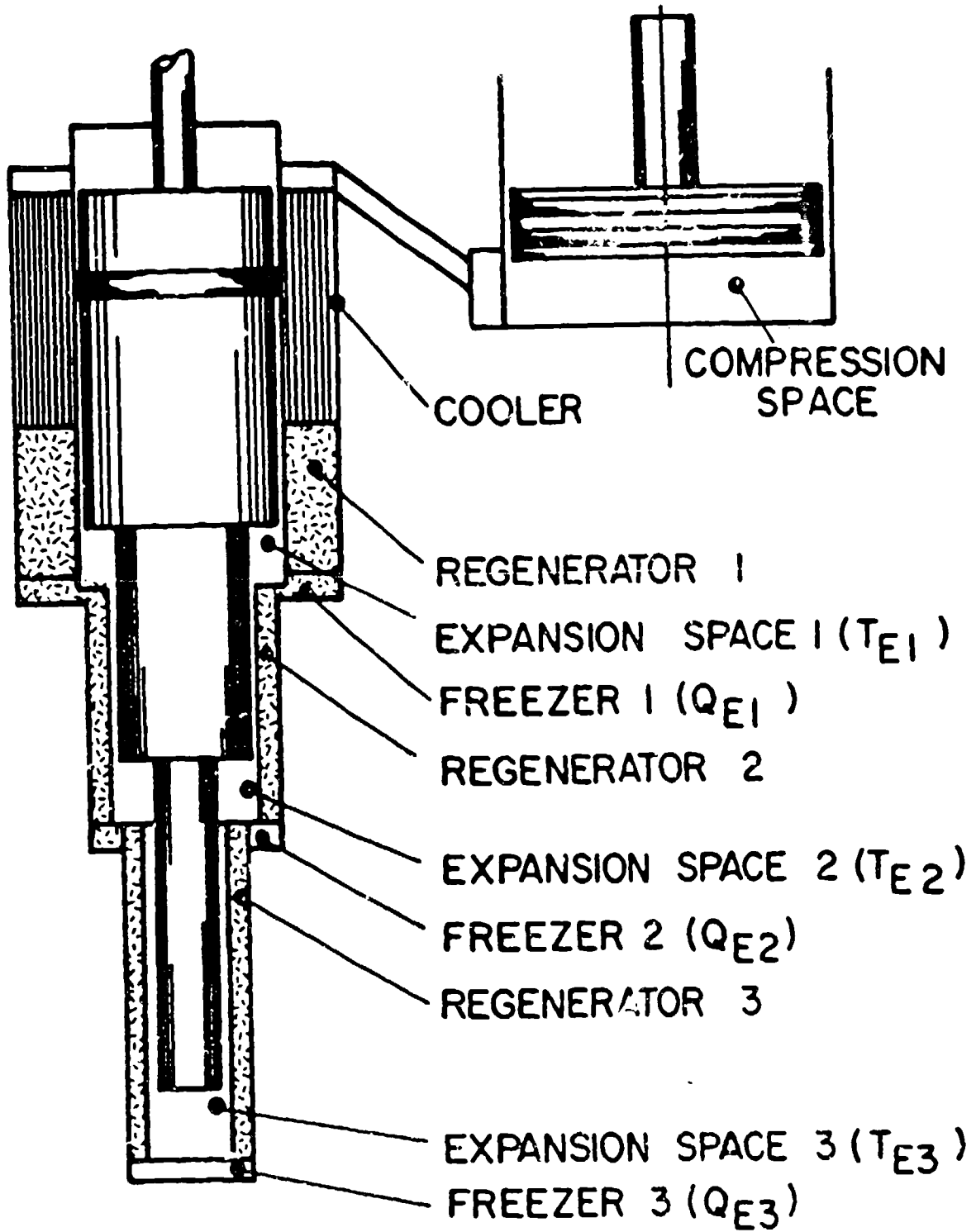
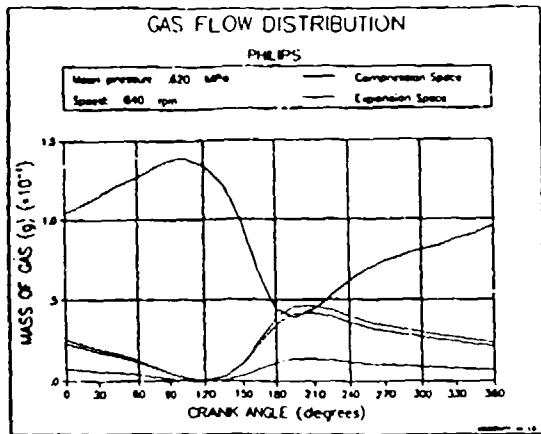


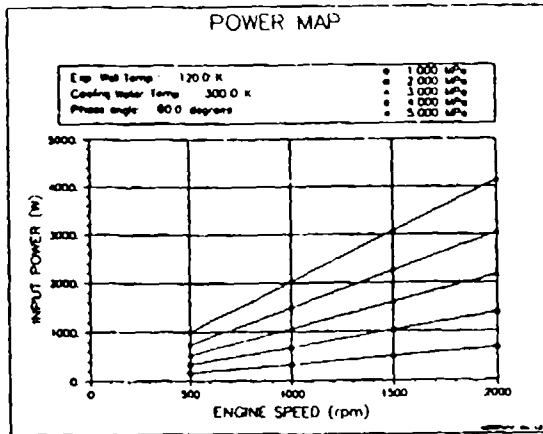
FIGURE 1: RIDER-STIRLING REFRIGERATOR ARRANGEMENT.



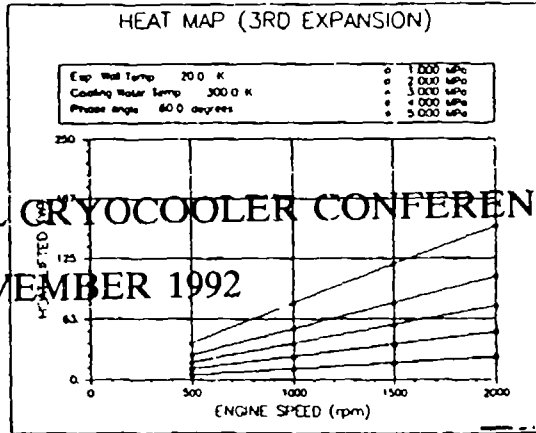
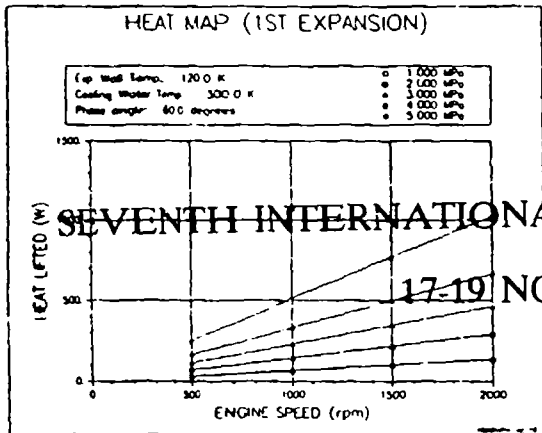
MULTIPLE EXPANSION STIRLING
CRYOCOOLER



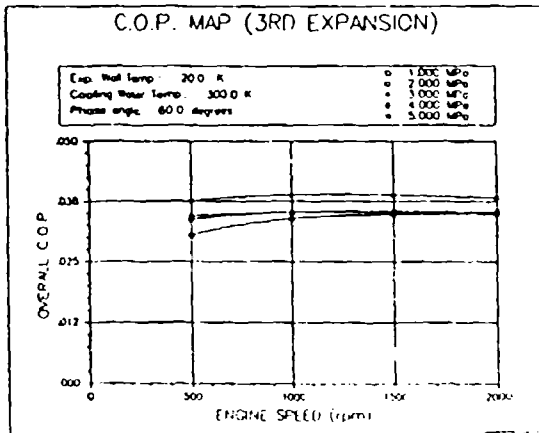
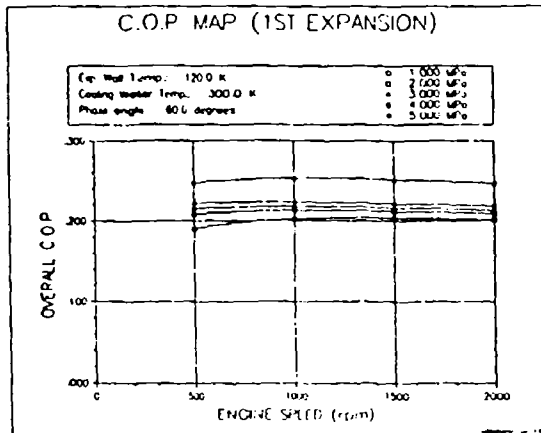
Gas flow distribution



Required input power



Heat lifted in the 1st and 3rd expansion spaces



C.O.P. for the 1st and 3rd expansion spaces

Computer modelling of Stirling Cycle coolers

T.W. Bradshaw, A.H. Orłowska and J. Heatt

Rutherford Appleton Laboratory
Chilton, Didcot
Oxon OX11 0QX, U.K.

INTRODUCTION

The Rutherford Appleton Laboratory (RAL) has been involved in the design and manufacture of single stage and two stage Stirling cycle coolers for space use for many years.¹ The design of these machines can be optimised for different temperature regimes and heat loads by analysis of the thermodynamic cycle and losses involved. This can yield the optimal dimensions of the machine and indicate the effect of varying operating parameters such as displacer and piston strokes, filling pressure and frequency on performance.

A computer model of Stirling cycle coolers is used at RAL to assist in cooler design and optimisation. The model analyses the cooler as a series of connected adiabatic and isothermal control volumes. This results in a calculation of the total refrigeration produced by a cooler of given geometry and displacements. The effect of the various loss mechanisms is then found. An important subroutine finds the effect of incomplete heat transfer and finite heat capacity in the regenerator matrix.

THE THERMODYNAMIC CYCLE ANALYSIS

The analysis is based on the Finkelstein model of a Stirling cycle containing

¹ T W Bradshaw, A H Orłowska, "Miniature closed cycle refrigerators", Proceedings of NATO Advisory Group for Aerospace Research and Development meeting on "Applications of superconductivity to Avionics", 7-9th May 1990, Bath, England, AGARD-CP-481.

adiabatic and isothermal regions.²

A representation of the cooler used in the thermodynamic cycle model is shown in Figure 1. The volume variations in the cooler are calculated from the specified geometry and operating parameters such as stroke and frequency. An isothermal model internal to the program provides the start conditions for the adiabatic analysis.

The adiabatic model assumes that there is no heat transfer in the cylinders, all of the heat transfer is assumed to take place in the heat exchangers. From the start conditions provided by the isothermal analysis the program integrates a series of simultaneous linear differential equations for the mass of the gas in each part of the cooler and the pressure around the cycle. A fourth order Adams Bashford method is used with a one degree step interval. The cooling power and various other parameters are calculated before the process is repeated. When steady state conditions are established (usually five cycles are required) the mass flows in the cooler are calculated.

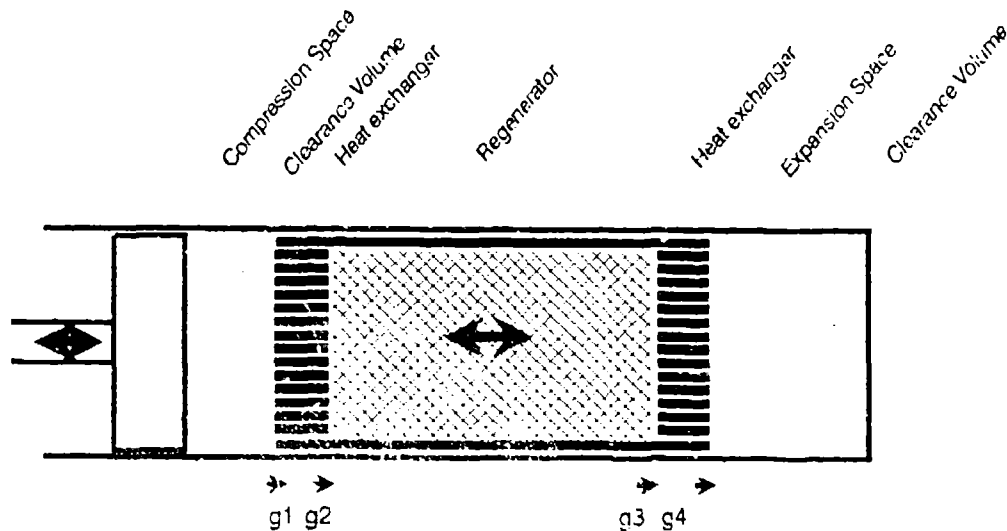


Figure 1. The series of control volumes used in the model

- ² Finkelstein, I. Generalised thermodynamic analysis of Stirling Engines. SAE paper 118B, SAE Annual General Meeting, Detroit (1960)
- ³ Halpern, V., and Shirickman, S., Cryogenics p687 (1980)

In the isothermal model heat exchangers are, by definition, redundant whereas in an actual cooler most of the heat transfer takes place in the heat exchangers. At the frequency of operation of these miniature cryocoolers (30 - 60 Hz), the thermal penetration depth in the helium is much smaller than the dimensions of the compression and expansion spaces. The adiabatic model only allows heat transfer to occur within the heat exchangers and makes the following assumptions;

- a) The compression and expansion spaces are completely adiabatic.
- b) The heat exchangers and regenerator are completely isothermal.
- c) There is no fluid dissipation ie:- the instantaneous pressure is the same throughout the system (but differences due to pressure drops and the finite speed of sound are calculated later).

For the purposes of this study the connecting pipe from the compressor to the displacer is considered as part of the heat exchanger.

There are important differences between this model and the isothermal model; the temperature of the gas in the compression and expansion spaces is no longer a constant and heat transfer takes place only in the heat exchangers and the regenerator.

The pressure drop through the cooler is calculated and used to find the reduction in pressure swing at the cold end (which decreases the cooling power available). The mass flows are used in a subroutine, described below, to calculate the regenerator loss. Due to the high operating frequency the finite speed of sound in helium cannot be neglected and an allowance for the phase shift in the pressure wave at the cold end, with respect to that in the compression space, is made.

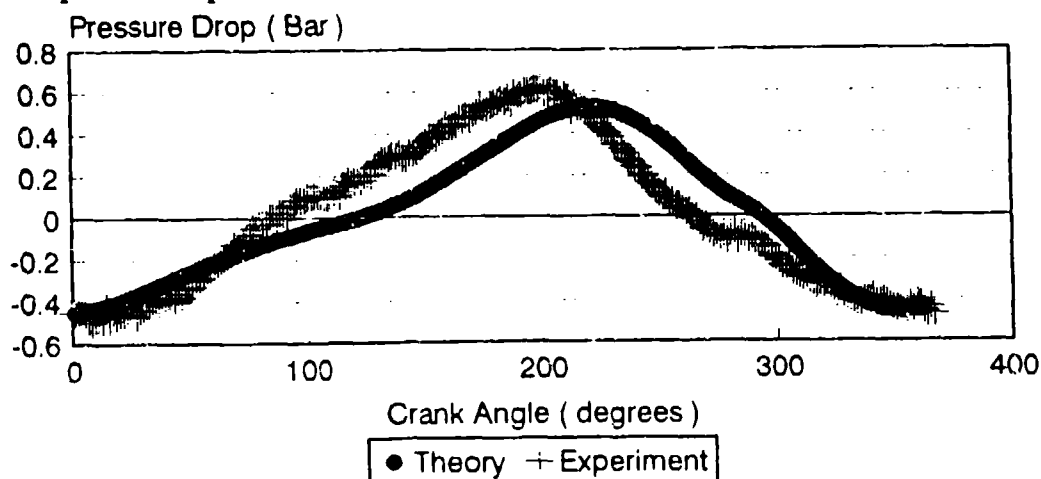


Figure 2. Pressure drop in connecting pipe, theory and experiment.

Adiabatic analysis including pressure drop

The pressure drops along the connecting pipework, heat exchangers and regenerator reduce the pressure swing in the cooler and hence the available cooling power. These are calculated using the expressions and flow correlations given by Martini⁴ and Kays and London.⁵ The calculated pressure drop along a cooler is compared to that measured in a working cooler⁶ in Figure 2.

These calculations allow the pressure distribution along the cooler to be calculated at any time interval. The PV integrals are then performed which give the revised cooling power.

Model Verification

The model has been verified in several ways;

- a) The program code has been checked against models presented in the literature and is verified each time a change in the source code is made.

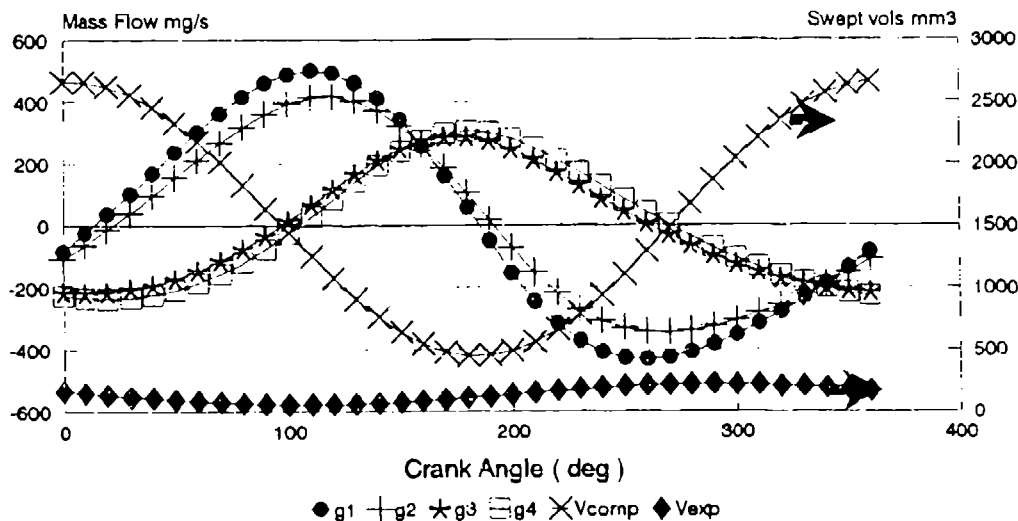


Figure 3. Mass flows and volume variations in the cooler

⁴ Martini W.R., "Stirling Engine Design Manual", NASA CR 135382

⁵ Kays, W., and London, A.L., Compact heat exchangers, McGraw-Hill, 1964

⁶ Measurements made by S T Werrett at Oxford University, private communication.

- b) Setting the specific heat ratio for the gas equal to unity makes the model isothermal and the results can be compared to an analysis such as the Schmidt closed form analysis.

This model provides a wide range of information about the cooler geometry including the mass flow at various points, cooling power, input power, heat transferred in the heat exchangers, and pressure swing (see Figure 3 for typical results). This figure shows the mass flow at four positions in the cooler, and the volumes in the compression and expansion spaces, as a function of 'crank angle', where g_1 is the mass flow at the exit of the compression space, g_2 , that at the exit of the first heat exchanger, g_3 , at the entrance to the cold end heat exchanger and g_4 at the entrance to the expansion space. These results can be output to files for further analysis and display as necessary.

PARASITIC LOSSES

The losses in the cycle fall broadly into two groups, those that can be treated as pure heat loads on the cold end and need only to be subtracted from the gross cooling power, and those that introduce departures from the ideal adiabatic cycle. The model assumes that the regenerator and pressure drop losses are perturbations on the ideal cycle and are calculated from the values of the mass flow derived from the program. The static, shuttle and regenerator losses are treated as parasitic heat loads and are subtracted directly from the gross cooling

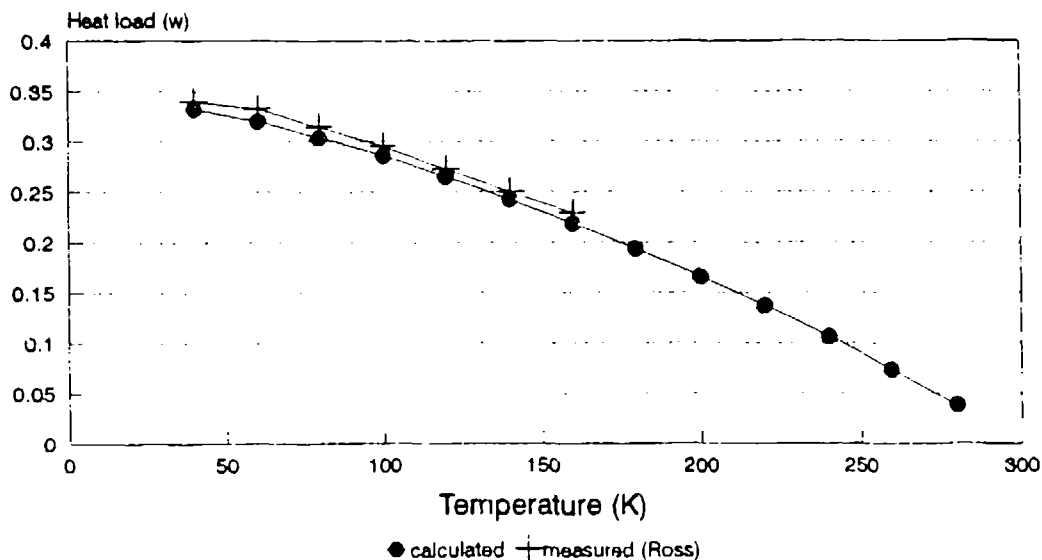


Figure 4. Static losses for the BA cooler cold finger

power. A correction to the temperature at which the modelling is performed was used in the model to allow for imperfect cold end heat transfer. This is described in detail later in the text.

Static heat losses

Measurements performed by Kotsubo et al⁷ indicate conduction losses down a cold finger of a non-operating cooler are lower than those obtained from warm up data probably due to differences in the temperature distribution.

The static losses in the cooler are determined by the temperature gradient and the conduction through the components of the cold finger and the radiation heat load. Conductivity data for the titanium alloy used in the cold finger was found for the temperature range 20 - 300 K.⁸ but the contributions from the plastic and especially the regenerator matrix were not so easily calculated. A search of the literature for data on these elements was unsuccessful, because of this, measurements of the conductivity of Vespel SP-3 were performed at RAL

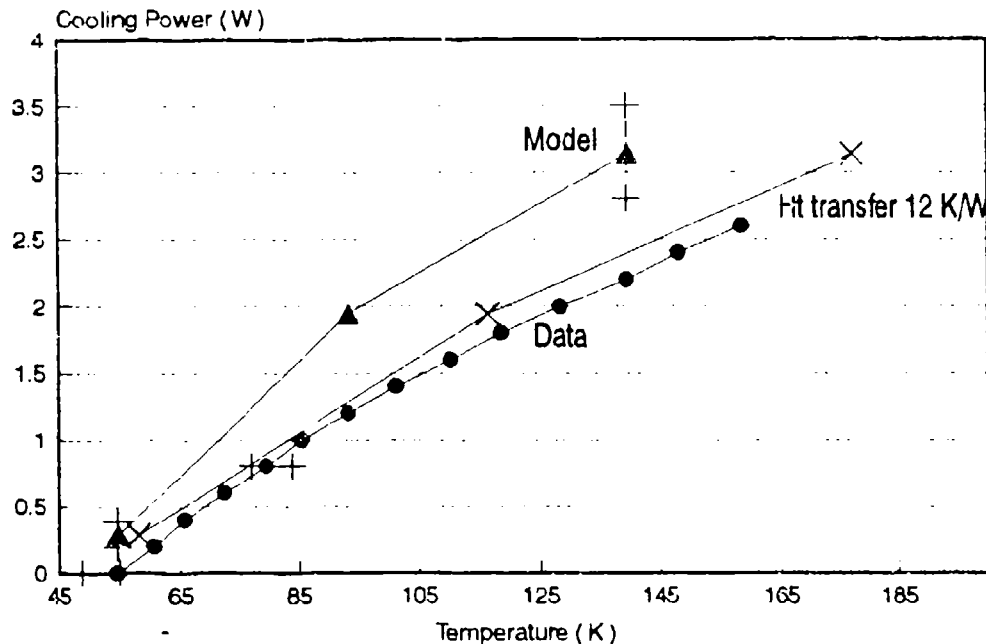


Figure 5. Computer modelling of BAe cooler performance: The effect of allowing for cold end heat transfer in the model is shown together with 5% variation in compressor and displacer strokes.

- ⁷ V. Kotsubo, D.L. Johnson and R.G. Ross, Jr. "Cold-tip off-state conduction loss of miniature Stirling cycle cryocoolers" To be Published in *Advances in Cryogenic Engineering* Vol 36
- ⁸ Purdue University, "TPRC Series - Thermophysical Properties of Matter" edited by Touloukian and Ho. Plenum.

between 70 K and 300 K and a recent RAL research programme has determined the conduction down a stack of metal gauzes in helium at a range of temperatures down to 60 K.⁹

Shuttle Heat Transfer

There is a heat load on the cold end from energy transport due to the reciprocating motion of the displacer. The equation derived by Zimmerman¹⁰ for the condition where the energy flow is limited by the conduction of the gas in the annulus between the displacer and the outer tube, is used in this model.

Regenerator loss

The regenerator loss, dominant in cryocoolers at low temperatures, is one of the least amenable to theoretical calculation since it depends on knowledge of forced convection heat transfer between the working gas and the matrix in unsteady flow. Most analyses make assumptions about the flow which are not applicable to conditions in small coolers operating at relatively high frequencies.

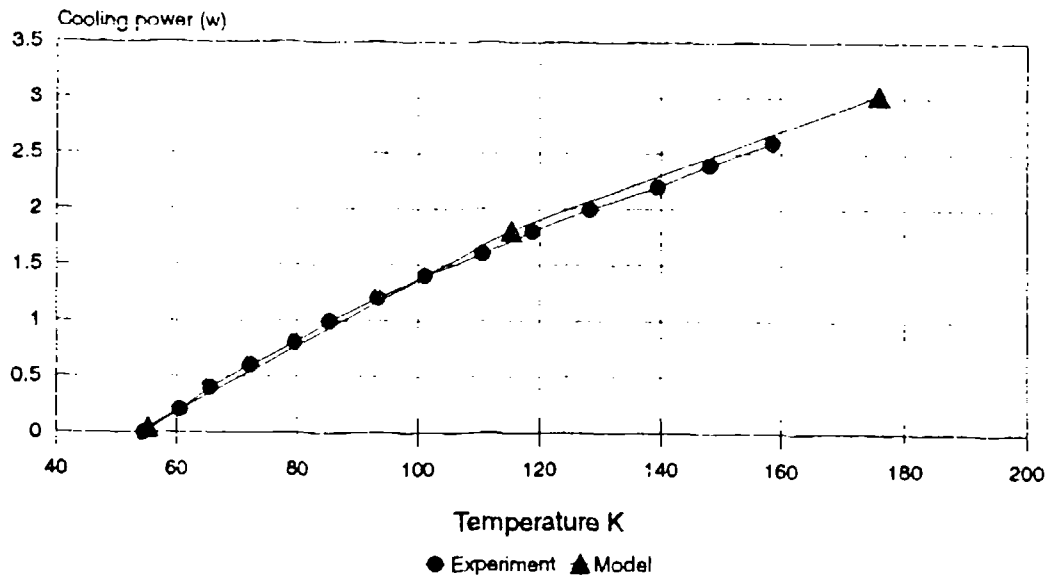


Figure 6. BAe cooler modelling at a compressor temperature of 306 K

⁹ to be published

¹⁰ Zimmerman, P.J. and Longworth, R.C. Lafayette College PA and Air Products Inc., PA. *Advances in Cryogenic Engineering* vol. 16, 1970.

The RAL cooler model includes a subroutine written to predict regenerator losses due to incomplete heat transfer and finite matrix heat capacity, using instantaneous mass flows and pressure data obtained from the main model. Regenerator loss measurements have been made in single stage coolers¹¹ and also in the coldest stage of two stage coolers. The losses predicted by this model are in good agreement with the experimental data at temperatures above approximately 50 K.

Governing equations

Helium is used as the working fluid and is assumed to be a perfect gas with a constant specific heat but with temperature dependent viscosity and conductivity. The matrix consists of gauze discs and has a temperature dependent specific heat.

The regenerator is divided into fifty cells with an initial linear temperature gradient between the temperatures of the cold and hot ends of the regenerator. These two temperatures are assumed to be constant during one cycle. Initially the gas temperature in each cell is the same as the matrix temperature in that cell and the temperature of the gas at the boundary between two adjacent cells is taken as the average of the gas temperatures in those cells.

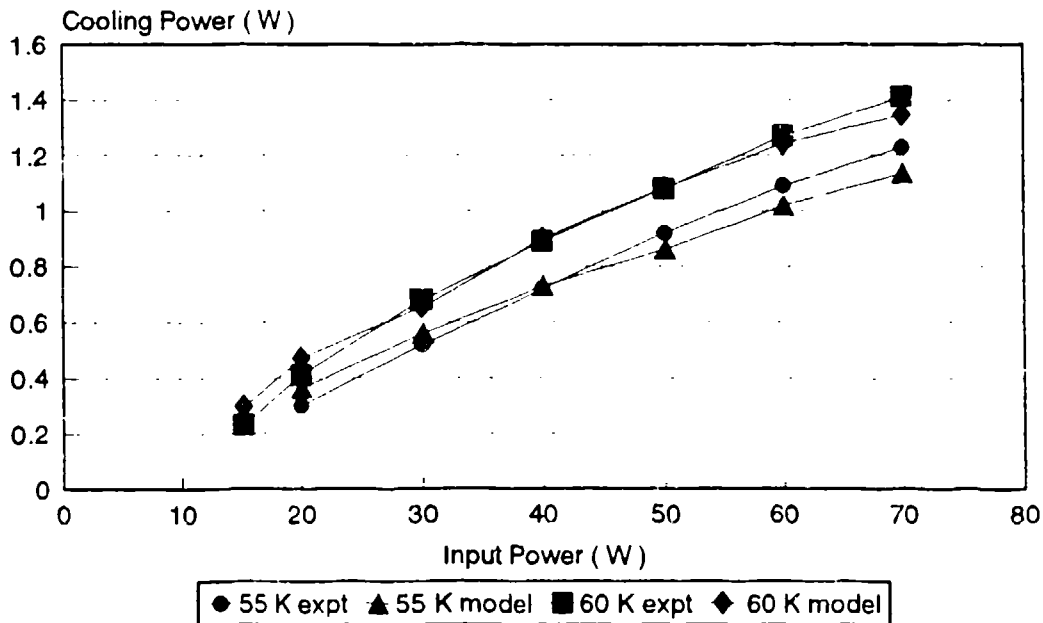


Figure 7. Optimised BAe cooler modelling at 55 K and 60 K

¹¹ Orłowska, A. H., and Davey, G. "Measurement of losses in a Stirling-cycle cooler" *Cryogenics* Vol 27 pp 645-651 (1987)

In each time interval the pressure changes by an amount calculated by the adiabatic cooler model and a quantity of gas enters the cell from the previous cell. This gas is at the temperature of the boundary between the cells. (For the first cell the mass input is taken from the adiabatic cooler model.) This results in a change in the mass of gas in the cell and in its temperature, and in the matrix temperature since a quantity of heat is transferred from the matrix to the gas (or vice versa).

The heat transfer correlation between the working gas and the matrix is crucial to any regenerator model and can be one of the weakest points. In this model a correlation is used which was proposed by Mikulin and Shevich¹² and found to give reasonable accuracy in measurements of regenerator losses in a single stage 80K cooler.¹³

Equations for the conservation of mass and energy are used together with the equation of state for the gas and the heat transfer correlation are solved to yield the mass and temperature of the gas entering the next cell. The program then moves on to repeat the calculations for the next cell of the regenerator. The program is cycled with the final gas and matrix temperatures from one cycle used as the initial values in the next.

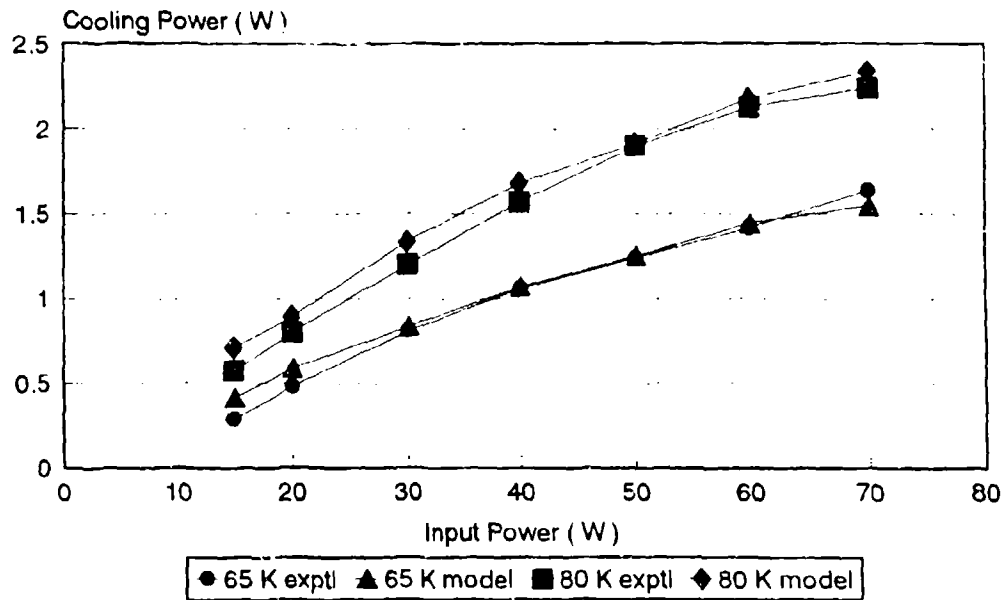


Figure 8. Optimised BAe cooler modelling at 65 K and 80 K

¹² Reported by Walker, G. in "Cryocoolers" Plenum Press (1983)

¹³ A H Orłowska, G Davey, Cryogenics 1987

THE EFFECT OF COLD END HEAT TRANSFER

It is known that when a heat load is applied to the cold end of a cooler the finite heat transfer leads to a temperature difference between the average gas temperature and the measured temperature on the cold tip. This ΔT will be a function of the external heat load and may also be dependent on operating parameters such as displacer stroke, frequency, cold end temperature and filling pressure, since all will affect the gas dynamics inside the cold tip.

Modelling of the flow conditions and heat transfer is difficult and several attempts have been made to measure the ΔT both directly and indirectly. Direct measurements using differential thermocouples were made in the Department of Engineering Science at Oxford in 1985 and yielded a ΔT of 10 ± 2 K/W. Measurements at RAL in 1983 of the temperature response to a step change in the heat load yielded a ΔT between 6 K/W and 10.2 K/W (for displacer strokes 3.5-3 mm). This was found to be a strong function of displacer stroke with a larger stroke giving the lower value. Similar measurements at the Department of Atmospheric Physics gave ΔT s between 8.6 and 19.3 K/W (for displacer strokes 3-2.5 mm), again with lower temperature differences corresponding to higher displacer strokes.

Cold end geometry is important in calculation of this parameter and results of ΔT between 13.2 K/W and 23.9 K/W have been obtained with various cold end heat exchangers. The large uncertainty in this data poses problems when this phenomenon is to be incorporated into models. For this reason it has been decided to assume a frequency and stroke dependent ΔT which gives a value of 12 K/W for a 2.6 mm displacer stroke at 40 Hz, which is in line with the data above.

BAE COOLER MODELLING

The model has been applied to the British Aerospace (BAe) single stage cooler¹⁴ and the results compared to the measured performance. The input data for this series of calculations was taken from BAe supplied drawings with a connecting pipe between the compressor and displacer of 300 mm.

¹⁴ Scull S. R. and Jewell C, "Pre-qualification level testing of an 80 K Stirling Cycle Cooler", Proceedings of the 4th European Symposium on Space Environmental and Control Systems, Florence, October 1991.

Static Losses

The total static loss calculated for the BAe cooler is shown in Figure 4 with the measured data of Kotsubo et al for comparison. The warm end temperature is taken as 295 K (the ambient temperature during the measurements of Kotsubo et al). The agreement between measured and calculated data is very good.

Cooler performance

The heat lift of the BAe cooler at 80 K with various compressor and displacer strokes was calculated, using a compressor temperature of 299 K, and the model results compared to the measured data.

The results of the analysis are shown in Figure 5. The figure shows the BAe experimental data. The horizontal error bars indicate the range of performance achieved with several different coolers of the same design at no applied heat load (base temperature), and with a heat load of 800 mwatts.

The results of the computer modelling are shown with and without the corrections to the model to allow for imperfect heat transfer in the cold end of the cooler. The vertical error bars are the results of the computer modelling with a 5% error on the amplitudes of the compressor and displacer motions.

Following discussions with BAe the cooler model was run at an increased compressor temperature of 308 K which represents an increase of 15 deg. C above the laboratory temperature. The results can be seen in Figure 6. There is an improvement in the fit to the experimental data.

Optimised single stage cooler

The model was used to optimise the single stage cooler geometry.¹⁵ The dimensions of the piston and displacer were changed in order to increase the cooling power, particularly at low temperatures (55 K-65 K).

Results are shown in Figure 7 and Figure 8. Very good correspondence between model and data has been obtained over a wide range of temperatures and input powers (from 55K to 80 K with input powers of 15 W to 70 W).

¹⁵ under ESA contract 9458/91/NL/FG

DESIGN EQUATIONS AND SCALING LAWS
FOR LINEAR COMPRESSORS WITH FLEXURE SPRINGS*

Eric Marquardt and Ray Radebaugh
National Institute of Standards and Technology
Boulder, CO 80303

Peter Kittel
NASA/Ames Research Center
Moffett Field, CA 94035

ABSTRACT

Linear-resonant compressors with flexure springs and clearance seals have recently been developed for use in long-life Stirling and pulse tube refrigerators. This paper describes a set of equations that are used to design the various components in the compressor given specified performance criteria. The components considered are the moving-coil linear motor, the mass of the moving components, the magnet assembly, the flexure springs, and the clearance seals. Both radially and axially magnetized magnets are analyzed and the criteria for selection are developed. Methods for reducing the compressor size and mass are discussed as well as the influence of the stroke-to-diameter ratio on the design of flexure springs. The design equations have allowed the development of scaling laws for linear motor compressors covering a wide range of compressor sizes from 3 watts to 4 kilowatts.

INTRODUCTION

This paper develops a set of equations for the geometrical parameters of a linear motor compressor in terms of the performance parameters. These equations then show how the dimensions are affected by the specified performance parameters. Figure 1 shows a schematic of a simple reciprocating compressor with a linear motor drive. The axial direction is parallel to the center line (defined here as the z axis), and the radial direction is perpendicular to the center line. These compressors use a current carrying wire (and thus, are called a moving coil design) within a magnetic field to impart a linear force in the axial direction to the piston while

*Research sponsored by NASA/Ames Research Center. Contribution of NIST, not subject to copyright.

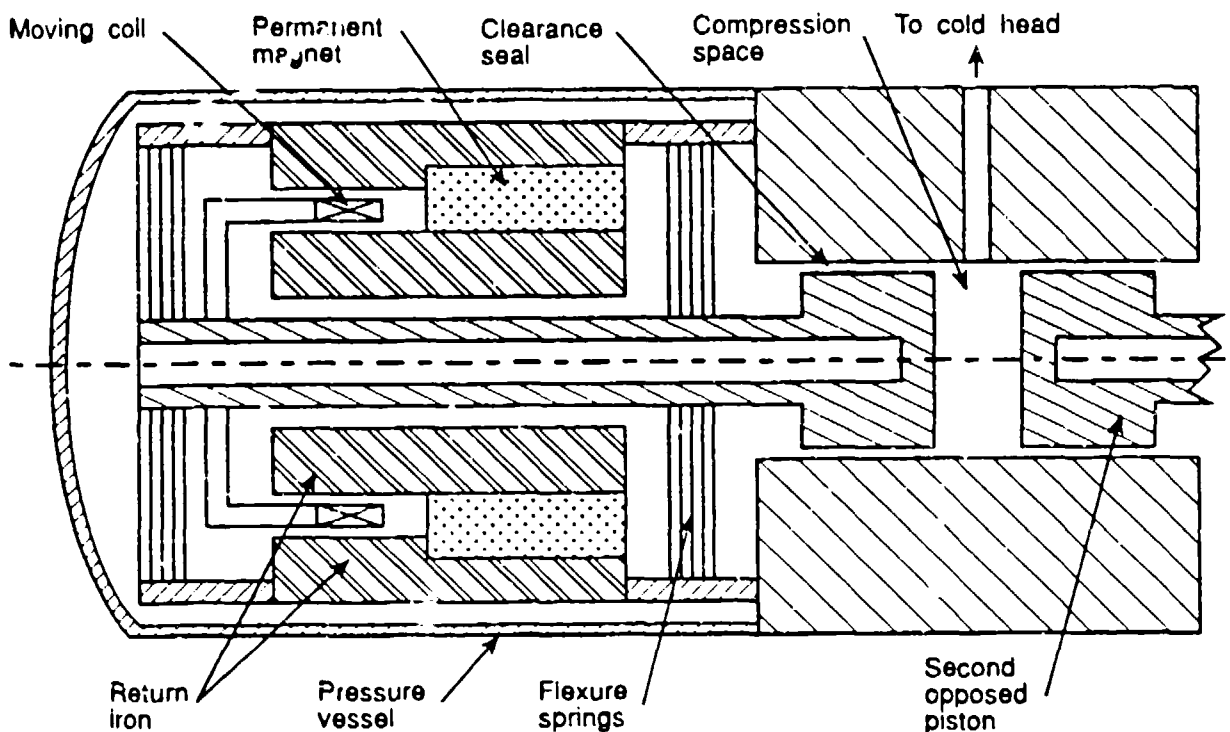


Figure 1. Schematic of a linear motor compressor. The drawing is axisymmetric about the dashed center line.

conventional rotary compressors use a crank shaft to provide this force. Rotary compressors apply large radial forces to the piston, which provide no useful work, cause a large amount of wear, and usually require lubrication. Lubrication is a problem in cryocoolers since contaminant can often migrate to the cold end of the refrigerator and liquefy or freeze. Linear motors eliminate radial forces completely since the force created in the wire is perpendicular to both the magnetic field and the direction of the current in the wire.¹ A linear motor compressor can operate at any frequency but is most efficient operating at a unique resonant frequency, usually in the range of 30 to 60 Hz.

Vibration of reciprocating compressors can be reduced by using a balanced-opposed design. In this configuration, the pistons are counter-balanced in-line, 180° out of phase, as shown in Figure 1. Traditionally the seal between the piston and cylinder has been accomplished using piston rings and is another source of wear in the compressor. Clearance seals can achieve the same effect while eliminating contact between the piston and cylinder wall, thus eliminating wear. A gap generally on the order of 15 μm is used and allows only a small percentage of the working fluid to pass through during a half cycle. The gas pressure on the backside of the piston is the average of that in the compression space, so there is no loss of gas from the compression space when averaged over one cycle. Clearance seals require very good alignment between the

piston and cylinder over the entire stroke. Traditional sliding bearings could be used to achieve this alignment, but there will be wear in the bearings and the alignment will be lost over time. Magnetic bearings could also be used but are large and complex. Flexure springs address this problem since they have no rubbing parts and are simple to construct. The flexure spring is constructed from a thin flexible material and is much stiffer in the radial direction than in the axial direction. They were first used in a Stirling refrigerator at the University of Oxford.²

The design of a linear motor compressor generally begins by specifying the performance parameters. These parameters are: (1) the required PV power \dot{W}_{pv} , (2) the desired efficiency of conversion of electrical power to PV power η , (3) the operating frequency f , (4) the average system pressure P_0 , (5) the pressure ratio P_r , defined as the maximum pressure over the minimum pressure, and (6) the phase angle ϕ by which the pressure leads the piston position. In some cases the compressor swept volume V_{co} may be used as an input parameter in place of the PV power. The compressor geometry, such as the stroke, clearance gap, coil dimensions, magnet configuration, return iron dimensions, and flexure spring dimensions must be optimized to give the minimum weight and/or system size that provides the specified performance parameters.

PHASOR ANALYSIS

Phasor analysis allows us to write simple algebraic equations in place of differential equations when solving sinusoidal steady-state problems.³ A phasor is a complex number expressed in polar coordinates as $v = V_0 e^{i(\omega t + \phi)}$ and whose projection on the real axis describes the sinusoid $v(t) = V_0 \cos(\omega t + \phi)$. The phasor v is represented by an arrow of length $|v| = V_0$ and an angle ϕ measured counterclockwise from the positive real axis at time $t=0$. The rotation of this phasor about the origin in a counterclockwise direction with angular frequency ω describes the time dependence of the phasor. It is necessary to show the phasors only at $t=0$, since all phasors for a linear system have the same frequency. Such a visual display is clearer than showing many time dependent sinusoids. The time derivative of a phasor is given as

$$\frac{d}{dt} V_0 e^{i(\omega t + \phi)} = i\omega V_0 e^{i(\omega t + \phi)}. \quad (1)$$

Since $i = e^{i\pi/2}$, we can write the derivative as

$$\dot{v} = \omega V_0 e^{i(\omega t + \phi)} e^{i\pi/2} = \omega V_0 e^{i(\omega t + \phi + \pi/2)}. \quad (2)$$

Equation (2) shows that the time derivative of a sinusoid leads the original sinusoid by $\pi/2$ radians or 90° . Phasors may be treated the same as vectors, but they are in complex space instead of real space. We represent phasors in this paper with bold variables.

Phasor analysis is useful for regenerative cryocoolers, such as Stirling and pulse tube refrigerators, because of the nearly sinusoidal variations of volume, pressure, mass flow, and temperature. Phasors are used here to represent all the forces acting on the sinusoidally driven piston of the compressor. The driving force F_{LM} that must be supplied by the moving coil of the linear motor is given by the force balance

$$\begin{aligned} F_{LM} &= m\ddot{z} + b\dot{z} + k_z z + PA - P_B A \\ &= F_I + F_w + F_s + F_p - F_B, \end{aligned} \quad (3)$$

where z is the position of the piston from its midpoint (positive numbers toward smaller compressor volume), m is the mass of the moving piston and coil assembly, b is the dissipation constant that gives rise to viscous losses, k_z is the flexure spring stiffness in the z direction, P is the dynamic pressure in the compression space, P_B is the dynamic pressure on the backside of the piston, and A is the piston cross-sectional area. Let the position phasor be given by

$$z = (s/2)e^{i\omega t}, \quad (4)$$

where s is the piston stroke and the phase angle of this reference phasor is made zero. The dynamic pressure in the working space P and in the backside P_B are given by

$$P = P_j e^{i(\omega t + \phi)}, \quad (5)$$

$$-P_B = P_{Bj} e^{i(\omega t + \beta)}, \quad (6)$$

where P_j and P_{Bj} are the amplitudes of the dynamic pressures with phase angles of ϕ and β respectively. Note that β refers to the negative of P_B . The resulting force balance from Eq. (3) is represented by phasors in Fig. 2. The magnitudes of the phasors are given by

$$\begin{aligned} |F_{LM}| &= L_w IB, \\ |F_s| &= \frac{1}{2} k_z s, \\ |F_B| &= P_{Bj} A, \\ |F_p| &= P_j A, \\ |F_w| &= \pi f s b, \\ |F_I| &= 2\pi^2 f^2 s m, \end{aligned} \quad (7)$$

where F_{LM} is the linear motor force, F_s is the mechanical spring force, F_w is the viscous dissipation, and F_I is the inertial force. The phase angle of F_s is 0° because it is in phase with the position. The phase angle for F_w is 90° since it is in phase with \dot{z} . The phase angle for F_I is 180° since it is in phase with \ddot{z} . The phase angle ϕ will depend on the particular cold head attached to the compressor. A typical value based on experiments may be about 35° to 40° for a pulse tube and about 40° to 45° for a Stirling refrigerator. Accurate values of this phase angle are needed for the proper design of the compressor. In most practical compressors, the volume

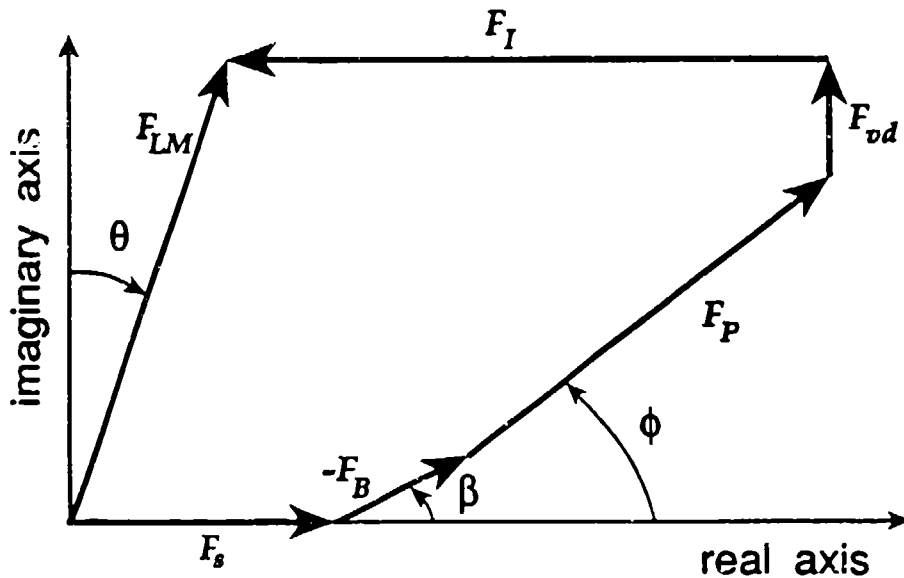


Figure 2. Phasor diagram showing the forces acting on the piston.

of the gas on the backside of the piston is much larger than that of the compression space. As a result F_B is negligible. Also the velocity of the moving components is usually small enough that the viscous dissipation term $b\dot{z}$ is negligible compared to the pressure term. The flow through the clearance gap results in a loss of some of the piston PV work that never reaches the cold head, however it has a negligible effect on the force balance. Figure 3 shows the phasor diagram without the backside pressure and viscous dissipation phasors. The relative magnitudes and phase angles are typical of most compressors, except θ may be zero or even slightly negative in some cases. Figure 3 shows that the motor force is minimized by adjusting m to make $\theta=0$. This condition is defined as resonance, which occurs when the inertial force is balanced by the sum of the real parts of the mechanical and gas spring forces. Since the motor force varies as $(1/\cos\theta)$, θ can be increased to $\pm 20^\circ$ with only a 6.4% increase in the motor force. For positive θ (F_{LM} lagging \dot{z}) the moving mass can be reduced, which reduces the vibration effects.

DESIGN EQUATIONS

Moving Mass

To operate the compressor at a predetermined frequency, it is necessary to determine the moving mass needed to achieve a resonant or near resonant condition. The moving mass is the entire piston assembly including the piston, piston shaft, coil, coil holder, and a portion of the flexure spring mass. To calculate the moving mass, the forces in Figure 3 are balanced in the real direction to give

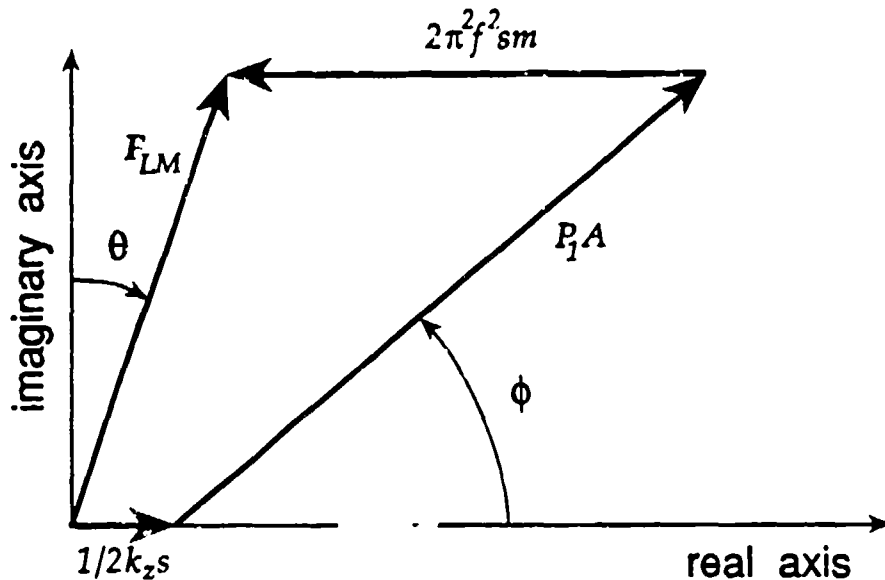


Figure 3. Phasor diagram used for the force balance on the piston.

$$|F_{LM}|\sin\theta + 2\pi^2 f^2 s m = \frac{1}{2}k_z s + P_1 A \cos\phi. \tag{8}$$

The area of the piston A is expressed in more fundamental parameters as

$$A = V_\infty / s, \tag{9}$$

where V_∞ is the compressor swept volume and is to be regarded here as a specified parameter.

The amplitude of the dynamic pressure is best expressed in the form of two components as

$$P_1 = (P_1/P_0)P_0, \tag{10}$$

where (P_1/P_0) is related to the pressure ratio P_r by

$$P_1/P_0 = \frac{P_r - 1}{P_r + 1}. \tag{11}$$

The motor force F_{LM} is calculated from a force balance along the imaginary axis in Figure 3,

$$|F_{LM}|\cos\theta = P_1(V_\infty/s)\sin\phi. \tag{12}$$

The term $|F_{LM}|$ from Eq. (12) is substituted into Eq. (8) and the moving mass is found to be

$$m = \frac{\frac{1}{2}k_z s + (P_1/P_0)P_0(V_\infty/s)\cos\phi(1 - \tan\phi \tan\theta)}{2\pi^2 s f^2}. \tag{13}$$

Compressor Power

The instantaneous PV power \dot{W}_{PV} produced by the compressor is given as

$$\dot{W}_{PV} = -P\dot{V}_{co}, \tag{14}$$

where \dot{V}_{co} is the time rate of change of the compressor volume. The time-averaged PV power $\langle \dot{W}_{PV} \rangle$ is given by

$$\langle \dot{W}_{PV} \rangle = -\frac{1}{2} \text{Re}[P\dot{V}_{co}^*] = \frac{1}{2} \text{Re}[P_1 e^{i\phi} |\dot{V}_{co}| e^{-i\pi/2}] = \frac{1}{2} P_1 |\dot{V}_{co}| \sin\phi, \tag{15}$$

where \dot{V}_{co}^* is the complex conjugate of \dot{V}_{co} and $\text{Re}[\]$ denotes the real part of the argument. In a simpler manner using phasors, the time-averaged PV power is given by

$$\langle \dot{W}_{PV} \rangle = -\frac{1}{2} P \cdot \dot{V}_{co} = \frac{1}{2} P_1 |\dot{V}_{co}| \cos\alpha, \tag{16}$$

where the dot product treats the phasors as vectors and α is the phase angle between P and $-\dot{V}_{co}$. Because $\alpha = \pi/2 - \phi$, Eq. (16) becomes

$$\langle \dot{W}_{PV} \rangle = \frac{1}{2} P_1 |\dot{V}_{co}| \sin\phi, \tag{17}$$

which is the same as Eq. (15). Because $|\dot{V}_{co}| = 2\pi f(V_{co}/2)$, the time-averaged PV power can be expressed as

$$\langle \dot{W}_{PV} \rangle = (\pi/2) f P_1 V_{co} \sin\phi. \tag{18}$$

Equation (18) is used to interchange input parameters between V_{co} and $\langle \dot{W}_{PV} \rangle$ in the design equations.

Clearance Seal

The gap thickness for the clearance seal must be made sufficiently small to keep the amplitude of the flow rate through the gap small compared with the amplitude of the flow rate between the compressor and the cold head. The PV work lost through the gap should be small compared with the total PV work delivered by the piston. Flow through the narrow gap is always laminar. Thus, the flow impedance Z_f of the gap is a function only of the gap geometry and can be expressed as⁴

$$Z_f = \frac{\Delta P}{\mu \dot{V}_{cg}} = \frac{12L_{cg}}{wt_g^3}, \quad (19)$$

where ΔP is the pressure drop across the gap, μ is the viscosity, \dot{V}_{cg} is the volume flow rate through the gap, L_{cg} is the gap length, w is the gap width, and t_g is the gap thickness. Because of the proportionality between ΔP and \dot{V}_{cg} , the amplitudes can be used for these two quantities instead of the instantaneous values. The dynamic pressure amplitude P_1 is equal to $|\Delta P|$ and the amplitude of \dot{V}_{cg} can be expressed as $\dot{V}_{cg} = |\dot{V}_{cg}| |\dot{V}_{co}| / |\dot{V}_{co}|$ where $|\dot{V}_{co}| = 2\pi f(V_{co}/2)$. The gap width is expressed as $w = \pi D = 2\sqrt{(\pi V_{co}/s)}$ for an annular gap. Substituting these terms into Eq. (19) and solving for the clearance gap thickness t_g gives

$$t_g = \left[\frac{6\mu L_{cg} f(|\dot{V}_{cg}|/|\dot{V}_{co}|) \sqrt{\pi s V_{co}}}{(P_1/P_0)P_0} \right]^{1/3}. \quad (20)$$

The time-averaged PV power loss due to flow through the gap is $\langle \dot{W}_g \rangle = \frac{1}{2} P \cdot \dot{V}_{cg} = \frac{1}{2} P_1 |\dot{V}_{cg}| \cos\beta$, where β is the angle between \dot{V}_{cg} and P , which is 0 from Eq. (19), leading to

$$\langle \dot{W}_g \rangle = \frac{1}{2} P_1 |\dot{V}_{cg}|. \quad (21)$$

Substituting Eqs. (21) and (17) into Eq. (20) yields

$$t_g = \left[\frac{6\mu L_{cg} f(\langle \dot{W}_g \rangle / \langle \dot{W}_{PV} \rangle) \sqrt{\pi s V_{co}} \sin\phi}{(P_1/P_0)P_0} \right]^{1/3}, \quad (22)$$

where $\langle \dot{W}_g \rangle / \langle \dot{W}_{PV} \rangle$ is the fraction of PV power lost to flow through the gap. Equations (20) and (22) are valid for a uniform gap. If the piston is not concentric with the cylinder, the flow loss can be significantly higher since the flow is proportional to t_g^3 according to Eq. (19).

Linear Motor

A linear motor can be made with a moving coil, moving magnet, or moving iron. Kerney⁵ compares these three types of linear motors. Because of its low weight, high efficiency, and zero radial forces, the moving coil motor is the one most often used for space applications of cryocoolers. With the moving coil motor, the magnet can be magnetized in either the radial or axial directions as shown in Figure 4. In order for a sinusoidal current in the coil to produce a sinusoidal force, the coil must be in a uniform magnetic field. The coil can be made short and

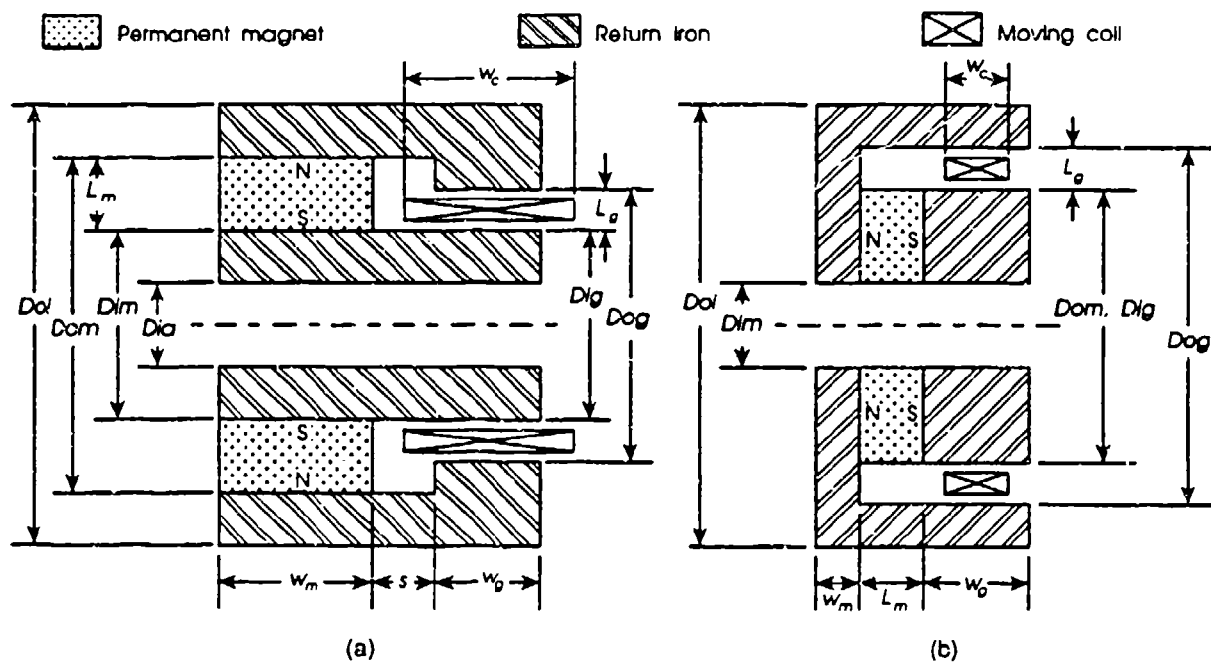


Figure 4. Geometry for (a) radial magnet and (b) axial magnet.

remain in the uniform magnetic field for the entire stroke (short coil as shown in Figure 4b) or a fixed magnetic field may remain within the coil for the entire stroke (long coil as shown in Figure 4a).

First the short coil design is discussed. The first step is to calculate the coil volume V_c , which is the volume of wire needed to produce the desired force including any insulation or epoxy used in construction of the coil. To determine the coil volume, the first step is to look at the magnitude of the force produced by a current I in a wire of length L_w in a magnetic field B

$$|F_{LM}| = |I|L_w B. \tag{23}$$

The time-averaged power generated by the force F_{LM} is

$$\langle \dot{W}_{PV} \rangle = 1/2 F_{LM} \cdot \dot{z} = (\pi/2) f s |F_{LM}| s \cos\theta. \tag{24}$$

When Eq. (23) is substituted into Eq. (24) the power output becomes

$$\langle \dot{W}_{PV} \rangle = \pi/2 (|I|L_w B) f s \cos\theta. \tag{25}$$

The volume of wire in the coil is $V_w = L_w A_w = p V_c$, where p is the packing fraction of copper in the total coil volume V_c . Solving this for L_w and substituting L_w into Eq. (25) gives

$$\langle \dot{W}_{PV} \rangle = \frac{\pi |I| p V_c B f s \cos\theta}{2 A_w} = \frac{\pi}{2} |j| p V_c B f s \cos\theta, \tag{26}$$

where j is defined as the current density $j=I/A_w$. Equation (26) can now be solved for V_c ,

$$V_c = \frac{2\langle \dot{W}_{PV} \rangle}{\pi |j| \rho B f s \cos \theta} \quad (27)$$

Because j is not a specified parameter, we express it in terms of known quantities. The time-averaged Joule heating in the coil for an oscillating current is

$$\langle \dot{Q}_j \rangle = \frac{|I|^2 \rho L_w}{2 A_w} \quad (28)$$

The value used for the resistivity ρ of the wire must reflect the increase in temperature of the coil due to Joule heating. The current density is now calculated in terms of known quantities by dividing Eq. (28) by Eq. (26) and solving for $|j|$,

$$|j| = \frac{(\langle \dot{Q}_j \rangle / \langle \dot{W}_{PV} \rangle) \pi B f s \cos \theta}{\rho} \quad (29)$$

where $\langle \dot{Q}_j \rangle / \langle \dot{W}_{PV} \rangle$ is the fraction of power lost to Joule heating. The current density in Eq. (29) can be used to determine the wire size for the available current. The coil volume can now be determined by substituting Eq. (29) into Eq. (27),

$$V_c = \frac{2 \rho \langle \dot{W}_{PV} \rangle}{\pi^2 \rho B^2 f^2 s^2 (\langle \dot{Q}_j \rangle / \langle \dot{W}_{PV} \rangle) \cos^2 \theta} \quad (30)$$

The coil volume in Eq. (30) is valid for both the axial and radial magnet configurations, but only for the short coil where the coil volume is in the magnetic field during the entire stroke.

Once the coil volume is known, the magnetic circuit, which includes the permanent magnet, air gap, and return iron, is designed. The short-coil, radial magnet will be discussed in this paper; similar steps can be used for the other cases. The volume of the air gap is the volume of the coil including clearance between the pole pieces and the coil plus the swept volume of the coil during the stroke. Since this volume is dependent on the final geometry of the magnetic circuit, a guess is made as to how much larger the air gap volume must be compared to the coil volume. Then the circuit is designed for this gap volume and it is determined if the coil will remain in the gap during the entire stroke. If the coil leaves the gap or the gap is too long, a new guess is made for the gap volume and the steps given below are repeated until the coil just remains within the gap during the entire stroke. Figure 4 shows the geometry of both a radial and axial magnetic circuit and defines the geometry variables. The only difference in the

magnetic circuit geometry between the long coil and short coil designs is the added length of the stroke to the return iron in the long coil, radial design. The first step in designing the magnetic circuit is to guess the ratio of gap volume to coil volume b_g then find the gap volume,

$$V_g = b_g V_c. \quad (31)$$

Next the volume of magnet can be determined from⁶

$$V_m = \frac{c_m B^2 V_g}{(BH)_{\max}}, \quad (32)$$

where $(BH)_{\max}$ is the maximum energy product of the magnetic material and c_m is a scaling factor used to account for magnetic losses due to the iron and fringing effects. Equation (32) gives the minimum volume of magnetic material needed to achieve the desired magnetic field in the air gap. Now it is necessary to decide on the length L_g of the air gap. This value is picked by the designer and the calculation should be done for a number of different values to see its effect on the magnetic circuit size and weight. Small values of L_g are better for heat transfer of the Joule heating produced in the coil. The optimum length L_m of the magnet can now be calculated by

$$L_m = \frac{b_m B L_g}{H_m}, \quad (33)$$

where b_m is a scaling factor used to account for imperfections in the magnetic circuit and H_m is the demagnetizing force in the magnet at the operating point. To minimize the amount of magnet material the operating point is taken at $(BH)_{\max}$ for the permanent magnet material selected. The largest $(BH)_{\max}$ values are currently obtained with NdFe permanent magnets. The cross-sectional area of the magnet perpendicular to the field is $A_m = V_m / L_m$. Similarly the cross-sectional area of the gap is $A_g = V_g / L_g$. Next the cross-sectional area of the return iron can be determined by $A_i = (B/B_i) A_g$, where A_i is the cross-sectional area of iron needed to keep the magnetic field in the return iron from saturating, and B_i is the maximum allowed magnetic field to keep from saturating the iron. Now the inner diameter of the magnet and air gap can be calculated using a center hole of specified size for the piston shaft and by using the cross-sectional area of the iron,

$$D_{im} = D_{ig} = \sqrt{4(A_i + A_s) / \pi}, \quad (34)$$

where A_s is the cross-sectional area of the hole needed for the shaft and D_{ig} is the inner diameter of the air gap, defined in Figure 4. The inner diameter of the air gap is placed at the smallest allowable diameter to reduce the extra volume introduced by the stroke of the piston. The extra

volume of the gap, due to the stroke, is dependent on the cross-sectional area of the gap. A larger gap cross-sectional area means a larger gap volume will be needed to contain the coil than would be needed if the gap cross-sectional area were smaller. This consideration also applies to the long coil design, a larger coil volume will be needed for larger diameter coils. Coils should be placed on the smallest possible diameter. The outer diameters of the magnet and air gap are given by

$$D_{om} = D_{im} + 2L_m; \quad D_{og} = D_{ig} + 2L_g. \quad (35)$$

Next the width w_m of the magnet can be determined by

$$w_m = \frac{4V_m}{\pi(D_{om}^2 - D_{im}^2)}. \quad (36)$$

The width w_g of the air gap, can be found using a similar equation. Since the length of the magnet will always be larger than the length of the air gap, the outer diameter D_{oi} of the iron can be found by

$$D_{oi} = \sqrt{D_{om}^2 + 4A_i/\pi}. \quad (37)$$

The inner diameter of the coil can be found by adding an appropriate clearance factor to the inner diameter of the air gap, while the outer diameter of the coil is found by subtracting a clearance factor from the outer diameter of the air gap. When deciding on the clearance factor for the inner diameter of the coil, allowance for the bobbin on which the wire is wrapped must be considered. Now that the diameters of the coil are known, the width w_c of the coil can be found using an equation similar to Eq. (36). The difference $w_g - w_c$ should be the stroke of the piston. If this is not the case, a new b_g guess in Eq. (31) is made for the volume of the gap and the procedure is repeated until $w_g - w_c = s$. A similar procedure can be used for the short coil, axial magnet, by using the appropriate geometry. This procedure should be repeated for a number of different piston strokes to determine the effect of the stroke on the size and weight.

The long coil designs always have the entire magnetic field within the coil. The difference in coil volume between the short and long coil designs is that for the same joule heating loss, the current density must be lower for the long coil design since it contains more wire than the short coil. The fraction of the coil within the gap is $w_g/(w_g + s) = [1 + (s/w_g)]^{-1}$. Thus Eq. (30) gives the volume of the coil within the gap if the relative Joule heating loss within this portion of the coil is also the same fraction of the total relative Joule heating loss ($\langle \dot{Q}_j \rangle / \langle \dot{W}_{pl} \rangle$). The total coil volume for the long coil design then becomes

$$V_c = \frac{2\rho \langle \dot{W}_{PV} \rangle (1 + s/w_g)^2}{\pi^2 p B^2 f^2 s^2 (\langle \dot{Q}_j \rangle / \langle \dot{W}_{PV} \rangle) \cos^2 \theta}, \quad (38)$$

where w_g is the width of the gap as shown in Figure 4. Equation (38) is valid for any long coil case. Using Eq. (38) for the coil volume and a procedure similar to the one given above, the magnetic circuit can be designed for both long-coil cases. The major difference between the procedures for the short and long coil cases is that a initial guess must be made for the width of the gap in the long coil case and for the long coil cases, $w_g + s = w_c$ is used to determine if the solution is correct.

The constants c_m , b_m , and B_i , must be adjusted to make these equations agree with more accurate results calculated from finite element techniques. By using finite element software for magnetic circuits, the proper values of the constants can be determined for a wide range of geometries. The constants vary some-what with the geometry. Using a finite element package, the constants have been determined to be: $c_m = 1.2$ to 3 , $b_m = 1.2$ to 1.8 , $B_i = 1$ to 1.6 Tesla.

The efficiency of the linear motor is given by

$$\eta_m = \langle \dot{W}_{PV} \rangle / \dot{W}_{input} = \frac{1}{(1 + \langle \dot{Q}_j \rangle / \langle \dot{W}_{PV} \rangle + \langle \dot{W}_g \rangle / \langle \dot{W}_{PV} \rangle + \langle \dot{W}_l \rangle / \langle \dot{W}_{PV} \rangle)}, \quad (39)$$

where \dot{W}_{input} is the electrical input power and $\langle \dot{W}_l \rangle$ represents all other losses not discussed previously. These other losses, such as windage and eddy current losses, are usually negligible. System size and weight are decreased by increasing the joule heating loss $\langle \dot{Q}_j \rangle$, but that leads to lower efficiency. A good compromise for satellite applications often gives $\langle \dot{Q}_j \rangle / \langle \dot{W}_{PV} \rangle = 0.1$ to 0.2 and $\langle \dot{W}_g \rangle / \langle \dot{W}_{PV} \rangle = 0.02$ to 0.05 . Motor efficiencies of 75% to 85% are typical.

Advantages and Disadvantages of the Different Magnetic and Coil Configurations

Long coil designs require more coil volume but a smaller air gap volume, giving an overall savings on system weight at the expense of adding to the amount of mass that must be moved. This is an advantage to smaller systems that must normally add additional moving mass to operate at the desired resonant frequency. Comparing Eq. (38) to Eq. (30) shows that the long coil volume is larger than the short coil volume by the factor $[1 + (s/w_g)]^2$. Typical values of s/w_g vary from 0.5 to 1 so that the long coil volume varies from 2 to 4 times the short coil volume. The magnet and iron weight of the long-coil configuration will be about 40% to 70% of that for

the short-coil configuration. The outer diameter of the long-coil configuration will be about 80% to 90% of that for the short-coil configuration. Long coils use more potting compound and out-gas more than short coils. A portion of the wire in the long coils experiences a magnetic field that varies from zero to the value in the air gap. The eddy currents induced within the wire diameter will lead to an additional heating effect that is on the order of 1% of the PV power.

Radial magnet configurations offer reduced system weight and size compared to axial magnet configurations. System weight for radial magnet configurations will be 50% to 70% of that for the axial magnet configurations. The outer diameter of radial magnet configurations will be 60% to 70% of that for axial magnet configurations. The cost of a radial magnet will be more than the axial magnet since radial magnets must be made in segments in order to be magnetized in the radial direction. If a radial magnet is designed properly, the epoxy used during assembly can be removed after the magnet is assembled.

Flexure Spring

Flexure spring bearings are used in place of traditional sliding bearings. They have the advantage of not having rubbing parts to wear out and contaminate the fluid. Flexure springs are constructed of a thin material having a high ratio of fatigue stress limit to Young's modulus. Stainless steel or beryllium copper are good candidates for such a material. The springs are designed to have a high radial stiffness and a low axial stiffness. This allows the clearance seal to maintain its close alignment while increasing the moving mass only a small amount due to k_r in Eq. (13). The desired radial stiffness k_r of the flexure springs in normal gravity is

$$k_r = \frac{mg}{C_r t_s}, \quad (40)$$

where g is the gravitational constant and C_r is the ratio of allowable radial displacement to the clearance gap thickness. The value of C_r should usually be about 0.5 or less to prevent channeling from occurring in the clearance gap that will cause an increase in the power loss. The desired axial spring stiffness is expressed as

$$k_z = 4C_z \pi^2 m f^2, \quad (41)$$

where C_z is the ratio of axial spring force to the inertial force. From a practical standpoint, C_z should not be less than about 15% or instability of the system may result when dual-opposed configurations are used. Values higher than 25% begin to significantly increase the moving mass. The desired ratio of radial to axial spring stiffness is then given by

$$\frac{k_r}{k_z} = \frac{g}{4\pi^2 C_r C_z t_g f^2} \quad (42)$$

As an example for $C_r = C_z = 0.20$, and $t_g = 15 \mu\text{m}$, then $k_r/k_z = 460$ at $f = 30 \text{ Hz}$ and $k_r/k_z = 204$ at $f = 45 \text{ Hz}$. Because there may be large gas side forces associated with slight axial misalignment, the actual value of C_r should be much less than 0.20 to prevent any possible contact during operation.

The Oxford-style flexure spring,² shown in Figure 5a, has been used for several years for small compressors. A problem with the Oxford spring is the highly localized stress concentration that occurs around the holes at the end of the photoetched slots. These stress concentrations occur because the flexing arms project out from the clamped region at an angle much different than 90° . As a result, in order to keep the peak stress below the maximum allowable stress for infinite fatigue life, the flexing arm has to be made quite long. Hence, the need for a spiral of at least a whole turn. The long flexing arm greatly reduces the radial stiffness. With properly shaped clamp rings, the flexing arms of the Oxford spring could project away from the clamp at nearly 90° and reduce this stress concentration. The arm length can then be reduced, leading to a greater radial stiffness while still keeping the peak stress below the allowable stress. Figure 5b shows the result of such a modification similar to that proposed by Wong et al.⁷ By

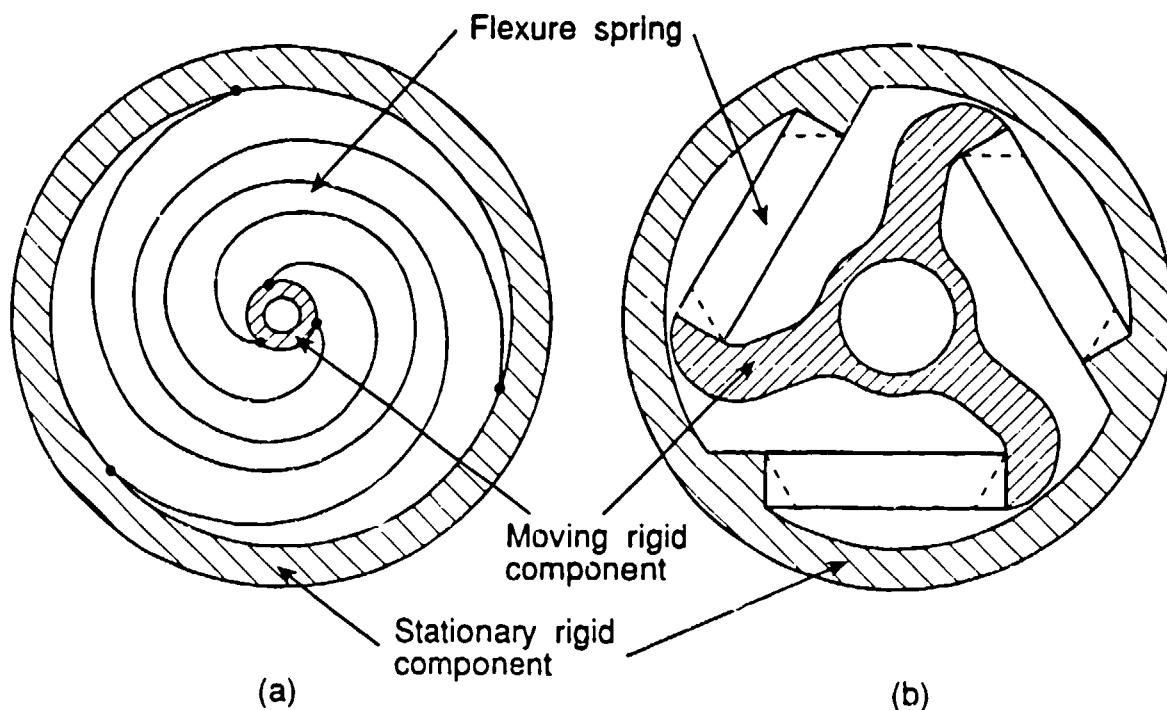


Figure 5. (a) Oxford flexure spring, (b) Linear flexure spring.

connecting the flexing arm to the moving rigid component at the maximum possible radius, the axial rotation is reduced although it adds additional mass to the moving component. The center hole for the shaft can be as much as 25% of the outer diameter of the spring, which allows for stiffer shafts with the same mass. Because of the axial rotation, the stress concentrations are minimized by having the clamped edge along the dashed lines in Figure 5b. For the sake of simplicity the following analyses of the spring ignore this effect and use a clamped edge shown by the solid lines in Fig. 5b.

Accurate calculations of stiffness and stresses in these springs can only be done with nonlinear finite element techniques. The straight arms of the linear flexure spring are more amenable to simple analytical calculations which help scaling the flexure springs to different sizes and serve as a good starting point for detailed design. By using simple beam analysis for a cantilever beam with both ends clamped, the maximum stress is found to be

$$\sigma_{max} = 3E(s/2)t_s/L_s^2, \tag{43}$$

where E is Young's modulus, t_s is the spring thickness, and L_s is the spring length. A large ratio, σ_{max}/E , allows for larger strokes. The axial and radial stiffnesses are

$$k_s = 3N_s E w_s t_s^3 / L_s^3 \tag{44}$$

$$k_r = 3N_s E t_s w_s^3 G(s/L_s) / L_s^3, \tag{45}$$

where w_s is the width of the spring arm, N_s is the number of springs, and the factor of 3 comes from the 3 arms of the spring. G is a function of (s/L_s) and is included to account for the decrease in radial stiffness with axial displacement. It has the property of $G(0)=1$. This function can be determined only from a finite element analysis of a particular spring design. The radial stiffness decreases rapidly as the axial displacement increases and at full displacement may be at least an order of magnitude less than that at zero displacement. Equation (45) is a poor fit to the finite element analysis performed on the linear spring. A better fit is achieved if it is assumed that one spring arm acts in pure tension to provide the radial stiffness which results in

$$k_r = N_s E t_s w_s G(s/L_s) / L_s. \tag{46}$$

The ratio of stiffness is given by

$$k_r/k_s = (L_s/t_s)^2 G(s/L_s)/3. \tag{47}$$

The required number of springs is found by comparing Eq. (44) with Eq. (41) to arrive at

$$N_s = \frac{4\pi^2 C_r m f^2 L_s^3}{3Ew_s t_s^3} \quad (48)$$

The resultant C_r from Eqs. (46) and (40) should be less than some established value such as 0.2. The desired number of springs will be in the range of 5 to 15 for most compressors. A thin spring (low t_s) leads to low stresses according to Eq. (43), high radial to axial stiffness ratio according to Eq. (47), but a large number of springs according to Eq. (48).

In the Linear design the spring length and inner diameter of the outer clamp ring are related by

$$L_s \approx D_s / 2, \quad (49)$$

where D_s is the inner diameter of the outer clamp ring. Likewise, the spring width is

$$w_s \approx D_s / 5. \quad (50)$$

Thus, Eqs. (43) through (47) become

$$\sigma_{\max} \approx 6E s t_s / D_s^2, \quad (51)$$

$$k_s \approx 3N_s (8/5) E t_s^3 / D_s^2, \quad (52)$$

$$k_r \approx N_s (2/5) E t_s G(s/D_s), \quad (53)$$

$$k_r/k_s \approx (D_s/t_s)^2 G(s/D_s) / 12. \quad (54)$$

Using Eq. (51) to solve for t_s in terms of the maximum allowed stress, Eq. (54) can be expressed in the alternate form

$$k_r/k_s = \frac{3(s/D_s)^2 G(s/D_s)}{(\sigma_{\max}/E)^2}, \quad (55)$$

and Eq. (48) for the linear spring design can be expressed as

$$N_s \approx \frac{180\pi^2 C_r m f^2 (s/D_s)^3}{E(\sigma_{\max}/E)^3 D_s} \quad (56)$$

For most spring designs the product $(s/D_s)^2 G(s/D_s)$ is an increasing function of s/D . Thus, according to Eq. (55) a high k_r/k_s is obtained by making s/D_s as large as possible. But according to Eq. (56) a large s/D_s leads to a large number of springs. A compromise is then needed. Typical s/D_s values range from about 0.10 to 0.15. Equation (56) also shows that D_s should be made as large as possible to reduce the number of springs. In practice the maximum D_s will be

about that of the magnet outer diameter D_{om} . The stroke should then be made as large as possible for a desired number of springs to maximize k_r/k_z and to minimize V_c and the resulting linear motor size and mass according to Eq. (30). We can express s in terms of N_s and D_s by first using Eqs. (48), (49), and (50) to solve for t_s in terms of N_s and D_s . This t_s is then substituted into Eq. (51) to obtain

$$s = \frac{(\sigma_{max}/E)}{6} \left[\frac{ED_s^4 N_s}{(5/6)\pi^2 C_s m f^2} \right]^{1/3} \quad (57)$$

Substituting this equation into Eq. (55) gives

$$k_r/k_z = \left[\frac{ED_s N_s}{(5/6)\pi^2 C_s m f^2} \right]^{2/3} \frac{G(s/D_s)}{12} \quad (58)$$

A material with the largest possible value of $E^{1/3}(\sigma_{max}/E)$ is desirable to increase the stroke and a large E is desirable to increase k_r/k_z . Thus, stainless steel is better than beryllium copper from both standpoints. Because D_s is related to the motor diameter, and the motor diameter was found originally by assuming a given value for the stroke, an iterative procedure must be used to find a consistent set of s , m , and D_s values that minimize the motor size and weight, yet provides the necessary k_r/k_z to prevent contact between the piston and cylinder.

SCALING LAWS

The set of equations developed in the previous section can be used for the original design of a flexure spring compressor. Finite element analysis is required for the calculation of the flexure spring radial stiffness and for more accurate values of the other spring parameters. It is also needed for more accurate sizing of the magnets and return iron in the linear motor. Calculations with finite element software can be time consuming since many trial and error calculations are required. These design equations minimize the amount of trial and error calculations necessary. Once a detailed design is developed for one size compressor, any other size can be quickly designed if the correct scaling laws are known. Two cases will be considered. The simpler case is that in which the frequency is allowed to vary as the size changes. That case is treated first and the case of constant frequency will be addressed later.

Variable Frequency

Let K be some constant which is used to form the scaling variable for the various dimensions and

the frequency. The base design corresponds to $K=1$, whereas an increase in size utilizes $K>1$ and a decrease in size utilizes $K<1$. The scale factor for each parameter will be some power of K . For the case of a variable frequency, use the following scaling laws:

frequency,	$f \propto 1/K$	magnet inner diameter,	$D_{im} \propto K$
stroke,	$s \propto K$	magnet outer diameter,	$D_{om} \propto K$
piston diameter,	$D \propto K^{3/2}$	magnet width,	$w_m \propto K$
piston length,	$L_p \propto K^{3/2}$	spring diameter,	$D_s \propto K$
coil inner diameter,	$D_{ic} \propto K$	spring thickness,	$t_s \propto K$
coil outer diameter,	$D_{oc} \propto K$	number of springs,	$N_s \propto K$
coil width,	$w_c \propto K$		

The parameters $P_o, P_r, (\dot{Q}_f / \dot{W}_{pv}), p, B, (BH)_{max}, \phi,$ and θ remain constant. Using the relevant design equation, the scaling factors for various related parameters are obtained. The selection of scale factors given above must satisfy the consistency equation that relates the coil dimensions to the compression space parameter, Eq. (30). This is shown in line 1 of Table 1. Scale factors for various performance parameters are given in lines 2 to 14 of Table 1. The terms $|j|, k_r/k_s,$ and σ_{max} are independent of the scale factor which is the ideal case. However, the relative deflections, lines 13 and 14, vary as K instead of being independent of K . Thus, these parameters place an upper limit on K , which depends on the initial values of $\Delta R/t_s$ and $\Delta z/s$. All values of K below 1 would be permitted although too small values of K lead to unacceptably high frequencies. Lines 9 to 12 show a scale factor of K^3 for all the force terms. Thus, their relative magnitudes will not change, which is desirable.

The scale factors for this case are particularly desirable since all the spring and linear motor dimensions vary as K . As a result there is no need for recalculations with finite element software for either of those two complex components. Because of the limitations associated with the non-ideal scale factor for the relative deflections as well as with the number of springs, this case is best used for size reductions rather than size increases.

Constant Frequency

A good (but not necessarily exclusive) set of scale factors for this case is as follows:

frequency,	$f \propto K^0$	magnet inner diameter,	$D_{im} \propto K$
stroke,	$s \propto K^{1/2}$	magnet outer diameter,	$D_{om} \propto K$

piston diameter,	$D \propto K^{3/2}$	magnet width,	$w_m \propto K^{1/2}$
piston length,	$L_p \propto K$	spring diameter,	$D_s \propto K$
coil inner diameter,	$D_{ic} \propto K$	spring thickness,	$t_s \propto K^{3/2}$
coil outer diameter,	$D_{oc} \propto K$	number of springs,	$N_s \propto K^0$
coil width,	$w_c \propto K^{1/2}$		

The resulting performance scale factors are shown in Table 1 for the constant frequency case. As shown in line 1, the selection is consistent and all terms of the force balance have the same scale factor. Non-ideal scale factors occur for $|j|$, k_r/k_s , and $\Delta z/s$. However, for the spring $s/D_s \propto 1/K^{1/2}$ in this case, which means that for large K the smaller s/D_s will contribute to a greater radial stiffness from the $G(s/D_s)$ factor that counteracts the $1/K$ dependence predicted from simple beam theory. Likewise, the larger $\Delta z/s$ at low K will also be compensated because of the larger s/D_s . The variable current density does not present any inherent problems as long as K is not

Table 1. Scale factors for derived compressor parameters.

Line #	Eq. #	Parameter	Proportionality	Scale Factor	
				variable f	constant f
1	30	Coil volume	$V_c = \langle \dot{W}_{pv} \rangle / (f^2 s^2)$ $w_c (D_{oc}^2 - D_{ic}^2)$ and $D^2 / (fs)$	consistency $K^3 \& K^3$	consistency $K^{3/2} \& K^{3/2}$
2	18	Power	$\langle \dot{W}_{pv} \rangle \propto fsD^2$	K^3	$K^{7/2}$
3	29	Current density	$ j \propto fs$	K^0 (ideal K^0)	$K^{1/2}$
4	22	Clearance gap	$t_s = [L_p fsD]^{1/2}$	K	K
5	46	Radial stiffness	$k_r \propto N_s w_s / D_s$	K^2	$K^{3/2}$
6	44	Axial stiffness	$k_s \propto N_s w_s^2 / D_s^2$	K^2	$K^{3/2}$
7	47	Radial/Axial stiffness	$k_r/k_s = (D_s/t_s)^2$	K^0 (ideal K^0)	$1/K$ (ideal K^0)
8	43	Maximum spring stress	$\sigma_{max} \propto t_s / D_s^2$	K^0 (ideal K^0)	K^0 (ideal K^0)
9	8	Force balance (flexure spring)	$1/2k_r s \propto N_s w_s^3 s / D_s^2$	K^3	K^3
10	8	Force balance (gap spring)	$PA \cos \phi \propto D^2$	K^3	K^3
11	8	Force balance (inertia)	$2\pi^2 f^2 sm \propto f^2 sm$	K^3 (for $m \propto K^4$)	K^3 (for $m \propto K^{3/2}$)
12	8	Force balance (motor force)	$F_{Lm} \sin \theta \propto D^2$	K^3	K^3
13	40	Relative radial deflection	$C_r = \Delta R / t_s = m / (k_r t_s)$	K (ideal K^0)	K^0 (ideal K^0)
14	-	Relative axial deflection	$\Delta z / s \propto m / (k_s s)$	K (ideal K^0)	$1/K^{1/2}$ (ideal K^0)

much larger than 1. This set of scaling laws is estimated to be good over the range of $0.25 \leq K \leq 2.0$. With a baseline design of $\langle \dot{W}_{PV} \rangle = 350$ W, these scale factors are good for the range of $\langle \dot{W}_{PV} \rangle$ between 3 W and 4 kW. Because the stroke and spring dimensions have different scale factors, a finite element analysis of the new spring will be necessary in this case. Likewise the different scale factors for the coil width and the coil diameters may require a new finite element analysis of the magnet and iron assembly to be certain of the magnetic field in the air gap of the new design. For $K > 2$, the ratio $D/D_{oc} \propto K^{1/2}$ may cause the piston diameter to become relatively large compared with the coil outer diameter.

CONCLUSIONS

A set of design equations has been derived to determine the optimum geometry (minimum size and mass) for a linear compressor using flexure springs. Input variables are desired performance parameters such as compressor PV power, frequency, average pressure, pressure ratio, pressure-to-volume phase angle, and compressor efficiency. The set of equations derived here easily show how these performance parameters affect the compressor design. These equations need to be supplemented by finite element calculations for the accurate and detailed design of the magnet system and the flexure springs. The equations were used to develop a set of scaling laws of the compressor system that is useful for changing the size of a previously designed compressor with a minimum number of design changes. These scaling laws should be valid over at least the range of 3 W to 4 kW of compressor PV power.

NOMENCLATURE

A	cross-sectional area of the piston	C_r	ratio of radial displacement to clearance gap length
A_g	cross-sectional area of air gap	C_s	ratio of axial spring force to inertial force
A_i	cross-sectional area of return iron	D	diameter of piston
A_m	cross-sectional area of magnet	D_o	inner diameter of outer clamp ring for flexure spring
A_s	cross-sectional area of piston shaft	E	Young's modulus
A_w	cross-sectional area of coil wire	f	operating frequency
b	coefficient of viscous drag	F_{LM}	motor force
B	magnetic field in air gap	g	gravitational constant
B_i	maximum magnetic field in iron	H_m	demagnetizing force in the magnet at the operating point
b_g	ratio of air gap to coil volume	i	$(-1)^i$
$(BH)_{max}$	maximum energy product of magnetic material	I	wire current
b_m	scaling factor for imperfections in the magnetic circuit		
C_m	scaling factor for magnetic losses		

k_r	total radial spring constant of flexure springs	V_{∞}	compressor swept volume ($V_{\infty} = sA$)
k_z	total axial spring constant of flexure springs	\dot{V}_{∞}	volumetric flow rate in compressor
j	current density (I/A_w)	V_g	air gap volume
L_{cs}	length of the clearance seal	V_m	permanent magnet volume
L_g	length of air gap	V_w	wire volume ($L_w A_w$)
L_m	length of magnet	w	width of the clearance seal ($w = \pi D$ for an annular gap)
L_s	length of spring arm	w_c	width of coil
L_w	length of wire in coil	w_g	width of air gap
m	mass of the piston assembly	w_m	width of magnet
N_s	number of flexure springs	$\langle \dot{W}_g \rangle$	compressor power lost to flow through the clearance gap
p	packing fraction (V_w/V_c)	\dot{W}_{PV}	instantaneous compressor PV power
P	instantaneous pressure	$\langle \dot{W}_{PV} \rangle$	time-averaged compressor PV power
P_o	average system pressure	w_s	width of spring arm
P_1	amplitude of the dynamic pressure in the compression space	z	spacial position of the piston
P_{B1}	amplitude of the dynamic pressure in the bounce space	\dot{z}	piston velocity
P_r	pressure ratio (maximum pressure / minimum pressure)	\ddot{z}	acceleration of the piston
ΔP	pressure drop through clearance seal	Z_f	flow impedance
$\langle \dot{Q}_j \rangle$	time-averaged joule heating in coil	β	phase angle between piston position and $-P_B$
R	coil wire total resistance	η_m	compressor efficiency
s	stroke of piston	θ	angle between the motor force and the imaginary axis
t_g	thickness of clearance gap	μ	working fluid dynamic viscosity
t_s	flexure spring thickness	ρ	wire material resistivity
V_c	coil volume	ω	angular frequency, $\omega = 2\pi f$
\dot{V}_{cs}	volumetric flow rate through the clearance gap	ϕ	phase angle between the position and dynamic pressure

REFERENCES

1. C. D. Zafiratos, in: Physics, John Wiley & Sons, New York (1985).
2. G. Davey, "Review of the Oxford Cryocooler", in: Advances in Cryogenic Engineering, vol. 35B, R.W. Fast, ed., Plenum Press, New York (1990), p. 1423.
3. S. E. Schwarz and W. G. Oldham, in: Electrical Engineering, Holt, Rinehart and Winston, New York (1984).
4. R. M. Olson, in: Essential of Engineering Fluid Mechanics, Harper & Row, New York, New York (1980).
5. P. J. Kerney, "Linear Drive Stirling Cooler Technology", in: Applications of Cryogenic Technology, vol 10, J. P. Kelley, ed., Plenum Press, New York (1991), p. 15.
6. L. R. Moskowitz, in: Permanent Magnet Design and Application Handbook, Krieger, Malabar, Florida (1976).
7. Wong, Pan, and Johnson, "Novel Linear Flexure Bearing", in: Proceedings of the 7th International Cryocooler Conference, this publication (1993).

NON-REAL TIME, FEED FORWARD
VIBRATION CONTROL SYSTEM
DEVELOPMENT & TEST RESULTS

Robert Boyle, Francis Connors
NASA / Goddard Space Flight Center
Greenbelt, MD 20771

John Marketon, Vincent Arillo
Hughes STX, Inc.
Lanham, Md 20706

Edward James, Richard Fink
McDonnell Douglas Astronautics Corp.
Lanham, Md 20706

ABSTRACT

The vibration generated by Stirling cycle cryocoolers has made it difficult to use them for cooling detectors in high-precision optical instruments. A simple technique has been developed for vibration control of linear-motor Stirling cycle cryocoolers. This technique takes advantage of the very stable harmonic content of the vibration forces by using simple signal processing and non-realtime control of the harmonic content of the drive signal. Laboratory testing of this technique has shown it to be very effective, even with imprecise information about the cryocooler's operating parameters. A possible chip set for flight implementation has been identified.

Key Words: Stirling refrigerators, cryocoolers, infrared instruments, periodic vibration, vibration control, flight electronics

INTRODUCTION

Many of the detectors used in infrared spectrometers and imaging cameras require cryogenic operating temperatures. A number of small cryogenic refrigerators (cryocoolers) are commercially available which meet the size, weight, and input power requirements for space flight science instruments. Most of these, such as the example shown in Figure 1, are Stirling cycle machines which use linear motors to drive reciprocating pistons, which do work on pressurized helium gas to produce

refrigeration. The pistons are driven at a fixed frequency and amplitude, with some fixed phase relationship between the motion of each of the components. These moving components cause reaction forces at the structural mount of the cryocooler which can disturb the alignment of an optical instrument, or cause microphonic pickup in some types of detectors.

One of the challenges in applying cryocoolers to science instruments has been to reduce the reaction forces to a level that does not degrade the performance of the instrument. The level of force that will be acceptable to a science instrument varies widely with the instrument's design, but has been estimated to be on the order of 0.1N^1 , which is much lower than cryocoolers usually produce. Measurement of the vibration produced by a single cryocooler compressor driven by a very pure sinusoidal motor current shows that the reaction force on the cryocooler's structural mount at the drive frequency may be on the order of 50N , and reveals that there are significant components at each of the harmonics of the drive frequency, equal to or greater than the acceptable level (Figure 2).² In instruments which are sensitive to vibration, pairs of pistons (two compressor pistons, or a displacer and a counterbalance) can be carefully aligned, and then driven in opposition to each other. This allows the reaction forces within each pair to balance one other at the drive frequency. Measurements on counterbalanced cryocoolers without a sophisticated control system show good cancellation at the drive frequency, but still show that the harmonics have not been balanced, and are above the acceptable levels.³

The origins of these harmonics are in the design and manufacture of the cryocooler itself. The cryocoolers have the common characteristic that the gas forces, motor forces, and in some cases, mechanical spring forces on the pistons are in some way non-linear with piston displacement. All these non-linearities produce harmonics of the drive frequency in the motion of the pistons, which in turn produces harmonics of the drive frequency in the reaction forces. The reaction forces at the drive frequency are easily controlled by balancing two pistons against each other, but the non-linear effects are not quite identical in each assembly, so the amplitude and phase of each will be slightly different. Broadband feedback control systems have been commonly used to control the position of the pistons in a cryocooler, but these have not successfully controlled reaction forces at the higher harmonics⁴. We have

developed an alternative to broadband controllers which takes advantage of the stable harmonic nature of the cryocooler vibration.

When the operating parameters of the cryocooler (piston stroke, piston offset, cold finger temperature, body temperature, etc.) have reached equilibrium, the harmonic content of the cryocooler vibration is very stable with time. Manual control of the amplitude and phase of the harmonics on the motor drive signal can reduce the magnitude of the force harmonics by 30-40dB for minutes at a time. This implies that a simple system for controlling these harmonics would be usable for vibration control in lieu of a broadband feedback control system. The fact that cryocooler operating conditions only change slowly with time also implies that the control system does not need to be fast, or operate real-time. One successful implementation of this concept is described here.

THEORETICAL BACKGROUND

Force Summation

A free-body diagram of the cryocooler piston or the cryocooler housing (Figure 3) shows that there are four forces interacting between the two bodies: the motor force F_m , the gas spring pressure force F_p resulting from the differential pressure between the buffer volume and the working volume acting on the piston face, the viscous forces in the clearance seal F_v , and the spring force F_s , resulting in a fixed-base reaction force F_r :

$$F_r = F_m - F_p - F_v - F_s \quad (1)$$

The non-linear relationship between force and position for each of these will introduce harmonics of the drive frequency. The object of the control system is to balance the motor force against the other forces so that the motion is purely sinusoidal, and the resultant force spectrum has no harmonic components.

The instantaneous force produced by each motor in the cryocooler can be assumed to be the product of a frequency-dependent motor force function times the motor current, plus some nonlinear function of the displacement:

$$F_m = G(\omega) I + g(x, I, \omega) \quad (2)$$

We take this non-linear component and treat it as an additional disturbance force on the cooler, so that for the simple case of a purely sinusoidal input current $I(t) = I_0 \sin \omega t$, the reaction force on the cryocooler housing will be a summation of harmonics

$$F_r = G(\omega) I_0 \sin(\omega t) + \sum_n f_n \sin(n\omega t + \alpha_n) \quad (3)$$

Unless we introduce some harmonic content into the motor current, it is easy to see that the reaction force will have components at harmonics of the drive frequency. For complete cancellation of the higher harmonics, the motor current must contain higher harmonics, such that for the n^{th} harmonic,

$$(F_r)_n = 0 = G_n I_n \sin(n\omega t + \phi_n) + f_n \sin(n\omega t + \alpha_n) \quad (4)$$

where the job of our control system is to find values for I_n and ϕ_n which satisfy this relationship. When the balance is not exact, the right side of equation (4) will have a non-zero reaction force at the n^{th} harmonic,

$$(F_r)_n \sin(n\omega t + \phi_n + \theta_n) = G_n I_n \sin(n\omega t + \phi_n) + F_n \sin(n\omega t + \alpha_n) \quad (5)$$

We can measure the reaction force F_r with a simple set of force transducers². With knowledge of the cryocooler characteristics and some simple signal processing, we can derive a drive signal which minimizes F_r .

Cryocooler Characteristics

The control system we are describing here is dependent on roughly knowing the transfer function between the motor current and the reaction force at each of the harmonics

$$H_n = \frac{(F_r)_n e^{i(\phi_n + \theta_n)}}{I_n e^{i\phi_n}} \quad (6a)$$

where we can say the magnitude of H_n is

$$h_n = \frac{(F_r)_n}{I_n} \quad (6b)$$

and the phase angle is θ_n .

The force balance within the cryocooler (equation 1) is sensitive to the design of the cryocooler's motors, and the interaction of the moving components with the working gas. These characteristics of the cryocooler determine the relationship between motor current and reaction force when the cryocooler is mounted to a rigid base. The motor characteristics do not change greatly with time or temperature, but the gas forces are very sensitive to the temperature of the coldfinger, the temperature of the gas in the buffer volume, the amount of blowby in the piston seals, loss of gas from the cryocooler, and the dimensions of the cryocooler components. H is also sensitive to the dynamics of the instrument structure and the cryocooler's structural interface, which typically has resonances in the 50-100Hz range.

Both the coldfinger temperature and the buffer temperature can undergo rapid changes. They both have an effect on the pressure of the gas in the cryocooler, producing changes in the gas spring pressure force F_p and the viscous force F_v . We have measured the amplitude and phase of H_n for four different cryocoolers at startup, and after thermal equilibrium has been established in the working gas, and we have seen very little difference between the two conditions. We are characterizing two of our cryocoolers at temperatures of +40°C and -40°C, which should quantify the sensitivity of H to changes in the gas charge pressure. Sensitivity of H to structural resonances is a bit harder to quantify. The major issue here is the change in boundary conditions between a 1-g test setup and the free boundary conditions of 0-g, and the resulting changes in the phase shift between F_m and F_r .

Since the machine is highly damped, small changes in F_v should not have a significant effect on H . The relatively small changes in gas pressure which will normally occur should not have a large effect on F_p or on internal resonances of the machine, and so should also have little effect on H . Loss of a large fraction of the working gas would have a large effect, but would also render the cryocooler effectively inoperable. Effects of the structural boundary conditions will have to be assessed for each instrument. If H only changes in small amounts during the normal operating life of the cooler, then each cryocooler may be characterized when

it is installed in an instrument with sufficient accuracy so that a control system such as ours can be effectively used.

Data Analysis

We need to obtain values for $(F_r)_n$ and θ_n from a digitally sampled force transducer signal. We can perform a Fourier transform of F_r , which gives a full spectrum of the components of $(F_r)_n$, but the actual force spectrum produced by a cryocooler, as shown in Figure 2, contains significant components only at the harmonics of the drive frequency. Since we only need to control the vibration at these harmonics, a Fourier series, comprised of the harmonics of the drive frequency, can be used instead, and the required calculations can be greatly simplified. By taking vibration data from an integral number of cycles of the drive frequency, the amplitude and phase at a single harmonic can be easily calculated.

For data collected over m cycles of the drive frequency ω , with a sample interval of Δt , we have $2\pi m/\omega\Delta t$ data points. We multiply each data point by sine and cosine functions of the harmonic frequency we are interested in, and make the summations

$$F_{x_n} = 2 \left(\frac{\omega}{2\pi m} \right) \sum_{k=1}^{2\pi m/\omega\Delta t} (F_r)_k \sin(n\omega k\Delta t) \Delta t \tag{7a}$$

$$F_{y_n} = 2 \left(\frac{\omega}{2\pi m} \right) \sum_{k=1}^{2\pi m/\omega\Delta t} (F_r)_k \cos(n\omega k\Delta t) \Delta t \tag{7b}$$

These summations may be further simplified by calculating the trigonometric functions in these summations in advance rather than in real time, and simply recalling the values from an array.

The quantities F_{x_n} and F_{y_n} can be thought of as a vector (Figure 4), whose magnitude is equal to the reaction force at the n^{th} harmonic

$$(F_r)_n = \sqrt{F_{x_n}^2 + F_{y_n}^2} \tag{8}$$

with a phase angle relative to the start of the data collection of

$$\beta_n = \tan^{-1} \left(\frac{F_{y_n}}{F_{x_n}} \right) \quad (9)$$

Control of a Single Harmonic

In principle, we can control the amplitude of any one of the harmonics very easily if we use the idea of a transfer function (equation 6). If the transfer function has a phase angle θ_n and an amplitude h_n , then a motor current of magnitude $(F_r)_n/h_n$ and phase $(\beta_n + \pi - \theta_n)$ would produce a motor force which would exactly cancel the reaction force (figure 5). For a cryocooler whose vibration is very repetitive with time, we can iterate on the amplitude and phase of the motor current, and reduce F_r to the noise limit even for θ_n and h_n which are not measured exactly.

We can look at successive iterations of the reaction force to determine the stability limits of our algorithm (Figure 6). The algorithm is stable for values of h_n and θ_n for which $(F_r)_n$ is equal or smaller in magnitude on each successive iteration. For a value of h_n which is known exactly, we see that the value of θ_n may be in error as much as $\pm 60^\circ$, and for a value of θ_n which is known exactly, the value of h_n may be in error as much as a factor of 2. This is analogous to having a phase margin of $\pm 60^\circ$ and a gain margin of 2. We can increase these margins by deliberately using a larger value for h_n , at the expense of slower convergence.

Control of Multiple Harmonics

A transfer function of a non-linear system like a cryocooler exhibits two characteristics that simple linear systems do not. The first is that the magnitude and phase of the transfer function are in general dependent on the amplitude of the input signal, and the second is that there is cross-coupling in the frequency domain. Not only is the response at a particular frequency dependent on the drive signal, but so is the response at other frequencies as well. The signal which nulls the reaction force F_r at one harmonic may increase F_r at another harmonic. An iterative solution will converge only if all the cross-coupling coefficients for each harmonic are smaller in magnitude than the self-coupling coefficient.

EXPERIMENTAL SETUP

A simple version of the control system described above was implemented on experimental setups like the one shown in figure 7. One cryocooler used for this test

was a 3W 80K machine, built by the Stirling Technology Co under a NASA Small Business Innovative Research (SBIR) contract. It had back-to-back compressor pistons and a free displacer; all control over the displacer/counterbalance assembly was effected via a counterbalance motor. We also tested our control system on a British Aerospace (BAe) 80K cryocooler, a CCS500 cryocooler built by Lucas Aerospace with electronics from Lockheed R&DD, and a small counterbalanced cryocooler built by Hughes under IR&D funding.

The control system itself was written in LabVIEW⁵ on a Macintosh desktop computer. We used a 16-bit A/D converter, sampling at 2kHz, for signal acquisition, and a 12-bit arbitrary waveform generator, sampling at 16kHz, to generate waveforms. Two 200W voltage-controlled servo amplifiers were used for power amplification. This voltage-controlled system is more difficult to handle conceptually than the current-controlled system described above, but did not alter the basic functioning of the algorithm, or adversely affect its performance. Our choice of hardware did lead to some major challenges in synchronizing the A/D and the D/A functions to sufficient accuracy. A system which used a common clock for both functions while still allowing different sample rates would have been much easier to use.

EXPERIMENTAL RESULTS

On the STC cryocooler, the control system succeeded in reducing the cryocooler reaction force (figure 8) below 0.03N for each of the harmonics to which it was applied (four on the compressor and six on the displacer/counterbalance assembly), where the broad band noise floor for the system was approximately 0.01N. On the BAe 80K cryocooler, the harmonics were reduced to 0.05N with a noise floor of 0.005N. In neither machine was the control system able to get the reaction force at the harmonics down to the level of the noise floor.

On the Lucas and Hughes cryocoolers, the harmonics were reduced to 0.01N with a noise floor of 0.01N. We noticed that the vibration force on these machines was more repetitive to begin with, perhaps reflecting differences in their design and construction.

Comparing reaction forces with and without our control system, we saw that the second harmonic axial force on the Lucas cryocooler was reduced by 45-50dB, while

the lateral forces were affected very little. On the BAe cryocooler, reductions were 30-40dB in the axial direction, and 10-15dB in the lateral direction. We saw on the BAe and STC cryocoolers that the axial reaction forces could be controlled to levels well below the lateral reaction forces⁴. Since the lateral forces are not easily reduced with the addition of a control system, it falls to the cryocooler designer to control the sources of the lateral reaction forces throughout the mechanical design of the cryocooler, including alignment of the motor windings, concentricity of the pistons with their bores, and spring dynamics.

Strong coupling between the DC offset of the pistons (the zero harmonic) and the rest of the harmonics was seen in all our testing, but cross-coupling between the higher harmonics was not seen. The phase and magnitude of H also did not seem to be dependent on the amplitude of the drive signal or of F_r at the accuracy to which we were measuring H.

DISCUSSION

Performing the signal processing off-line did not prevent the control system from driving the reaction force down into the noise when applied to the Lucas/Lockheed cryocooler, and did not prevent the control system from meeting our force specification¹ on the other two machines. The forces produced by the cryocoolers were apparently repetitive enough that a quiet drive signal could be derived from data which was seconds old.

One of our concerns prior to testing this system was the potential complications introduced by a voltage-controlled system. In practice, we saw no problems with its use, nor any disadvantages relative to a current controlled system. Though the motor force should have no appreciable phase shift relative to the drive current, the reaction force in general does, so no effort is saved by going to a current-controlled system.

Another concern was the resolution in time and amplitude of the digital-to-analog conversion. We found that the D/A sample rate could be as low as 5-10 times the period of the highest harmonic being controlled, depending only on the amplitude of that harmonic relative to the desired force level. The output voltage amplitude ratio between the highest level harmonics and the lowest was greater than 2000:1 (or approximately 2^{11}), so a converter with a resolution of at least 14 bits would be

necessary. Our waveform generators, with 12-bit resolution, were able to achieve a control level of approximately 0.05N, but were not able to control forces down to the noise level of the system.

While control systems using a DSP chip have been successfully used for cryocooler vibration control⁶, these chips have not been qualified for flight use as of 1992, and may not be qualified in time for flight of the first long-life instruments which use cryocoolers. One of our objectives was to design a control system which can be implemented on a chip set which is already qualified for space flight. One possible set which was identified by our flight electronics branch is shown in Table 1.

Table 1. Candidate Chip Set for Flight Use

Function	Chip	Comments
A/D	MN5290	16 bit 25kHz max sample rate susceptible to SEU
D/A	AD7543	12 bit 2μsec settling time
CPU	80C86RH	rad hard 16 bit processor 5-6MHz clock
PROM	6617RH	rad hard 2k x 8
RAM	IBM2568CRH	rad hard 32k x 8

CONCLUSIONS

A simple control system may be constructed for Stirling cycle cryocoolers which takes advantage of the stable operating characteristics of the machines. Testing has confirmed that axial forces below 0.05N may be achieved at each of the harmonics for a representative cryocooler.

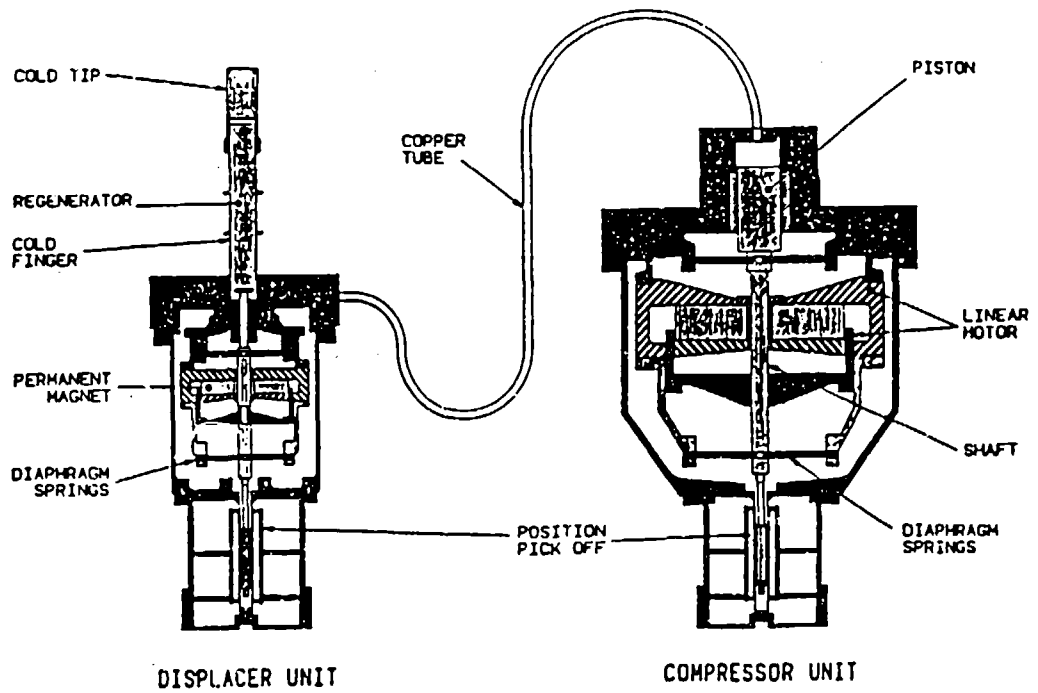


Figure 1 Typical cryocooler layout.

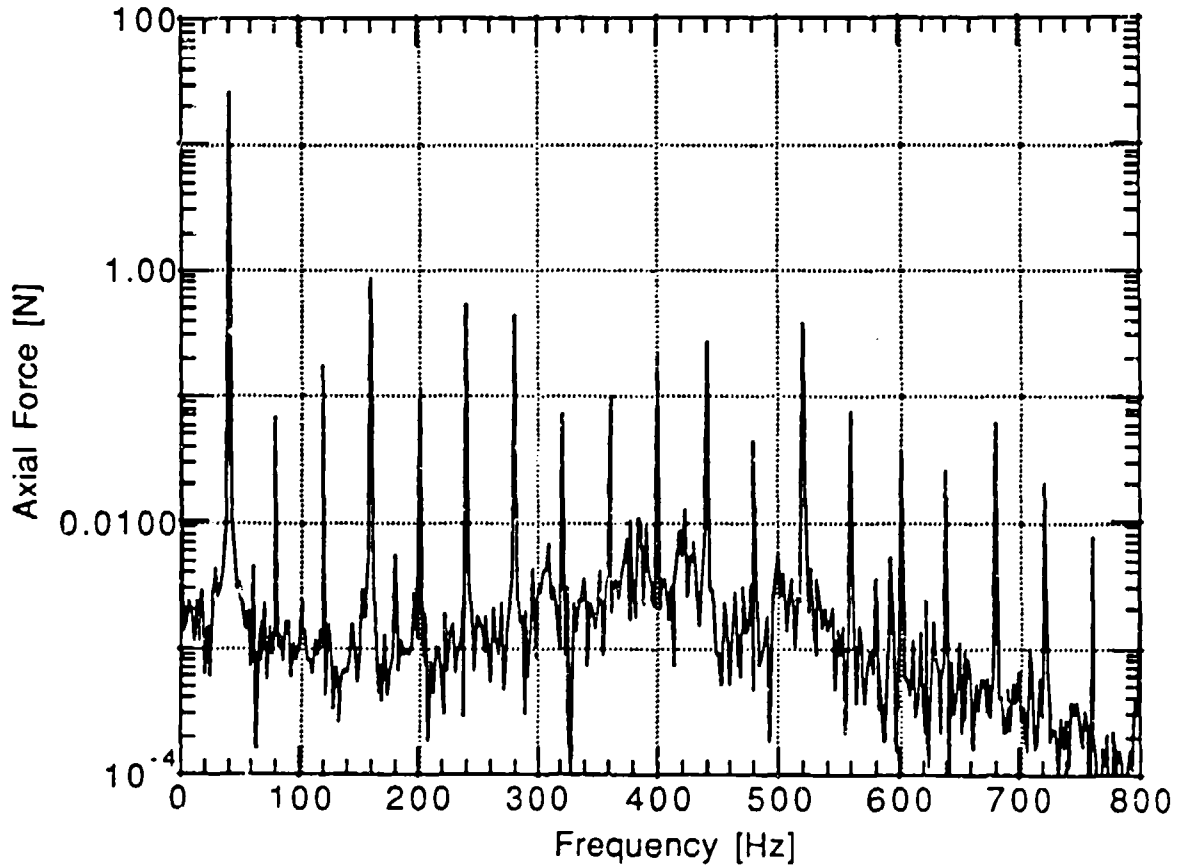
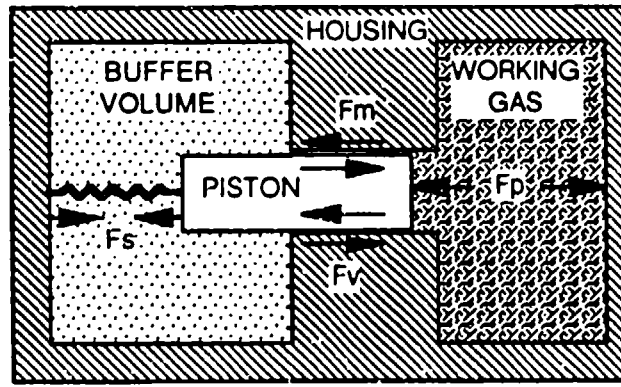


Figure 2 Harmonic distribution of cryocooler vibration (BAe 80K compressor).



Piston $\Sigma F = F_m - F_p - F_s - F_v$
 Housing $\Sigma F = -(F_m - F_p - F_s - F_v)$

Figure 3 A free-body diagram of a cryocooler piston or the cryocooler housing shows the four primary forces acting on them. If the housing is rigidly mounted, then the reaction force at the mounting interface equals the summation of the internal forces.

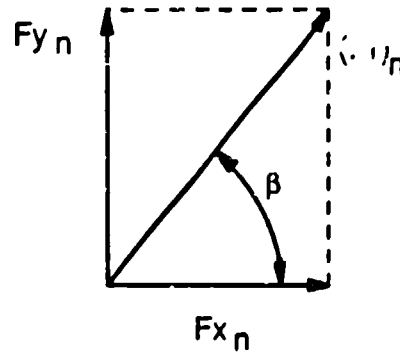


Figure 4 Vector representation of cryocooler reaction force $(F_r)_n$ in terms of F_{x_n} and F_{y_n}

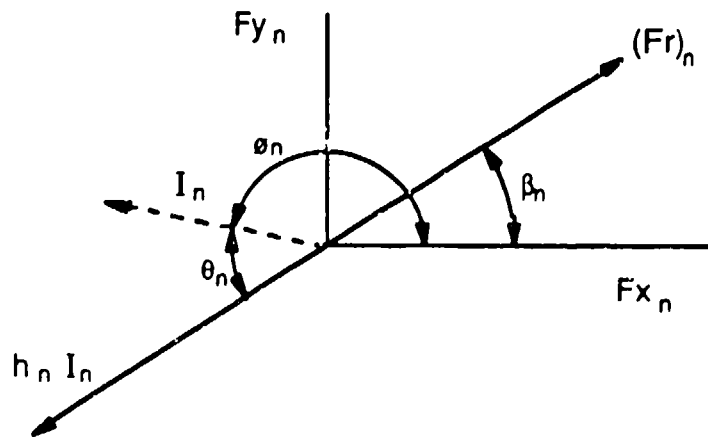


Figure 5 A motor current with phase angle θ_n and amplitude I_n will exactly cancel the reaction force for a single harmonic.

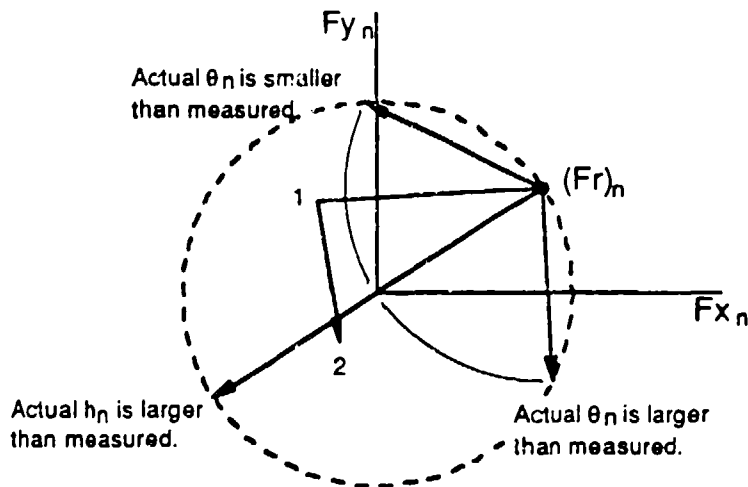


Figure 6 Iteration diagram for $(F_r)_n$. If h_n and q_n are known accurately enough such that for each successive iteration $(F_r)_n$ is smaller in magnitude than on the previous iteration, then the control algorithm is stable. The actual value of h_n can be as much as twice the value used by the algorithm; the actual value of q_n can be $\pm 60^\circ$ from the value used by the algorithm.

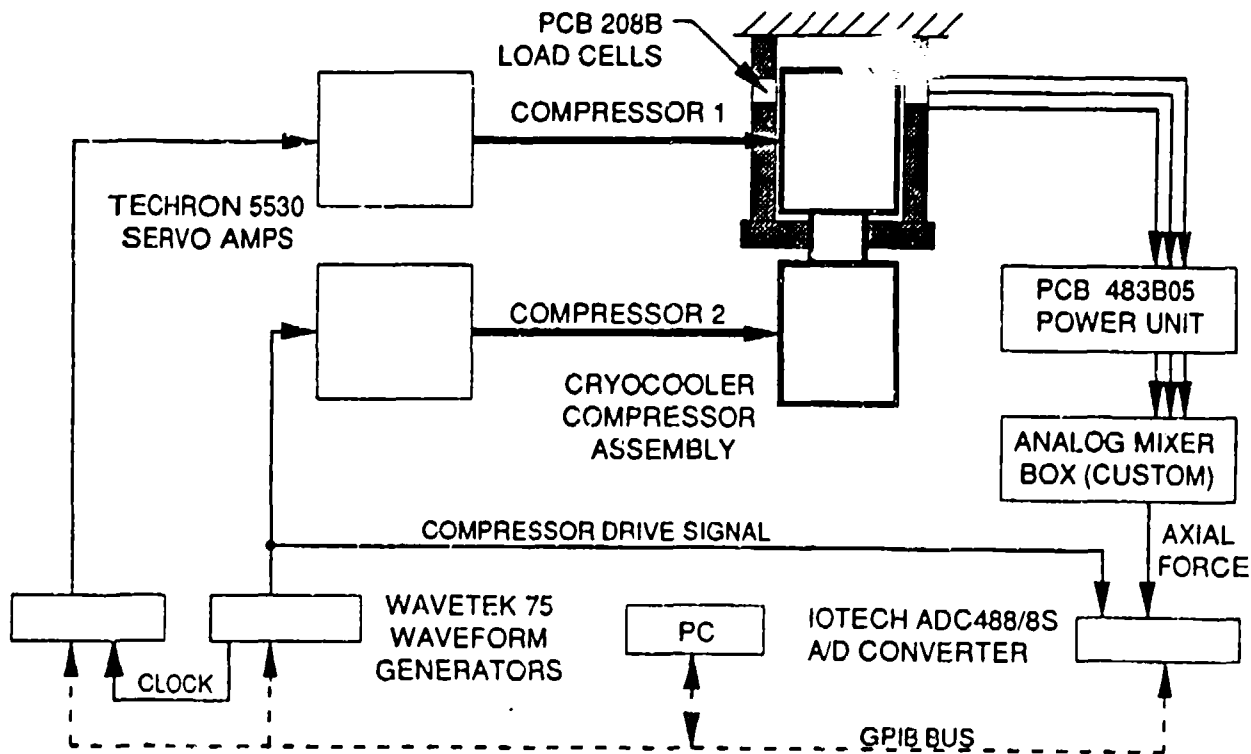


Figure 7 Schematic of control system interconnections for a back-to-back compressor assembly. A similar arrangement is used to control the displacer assembly.

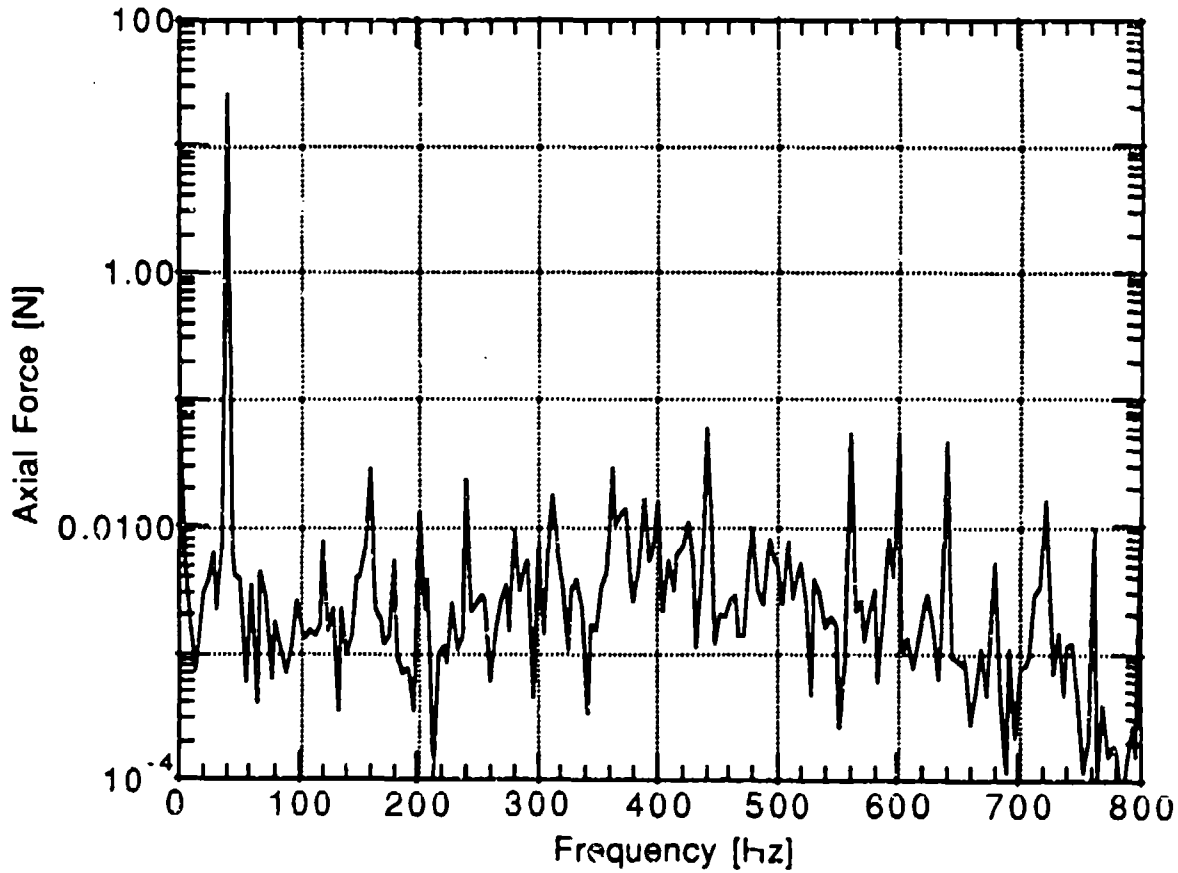


Figure 8. Spectrum of reaction force for BAe 80K compressor, with control system active to 520Hz. Note that this is not a counterbalanced cryocooler, and so the 40Hz drive frequency is not affected.

REFERENCES

- 1) "Performance Specification for an 80K, Long Life, Low Vibration Cryocooler for Space Applications", NASA Contract #NAS5-31785, Attachment B, p7-3 (1991)
- 2) R. Boyle, E. James, P. Miller, V. Arillo, L. Sparr, & S. Castles, "Structural and Thermal Interface Characteristics of Stirling Cycle Cryocoolers for Space Applications", *Advances in Cryogenic Engineering*, Vol 37, pp1063-1068, 1991
- 3) R. Ross, D. Johnson, & V. Kotsubo, "Vibration Characterization and Control of Miniature Stirling-Cycle Cryocoolers for Space Application", *Advances in Cryogenic Engineering*, Vol 37, pp1019-1028, 1991

REFERENCES (Cont'd)

- 4) E. James, R. Fink, R. Boyle, L. Sparr, R. Cory, F. Connors, V. Arillo, "NASA GSFC Test Program Results", to be published in the proceedings of the 7th International Cryocooler Conference, 1992
- 5) LabVIEW™ National Instruments Corp., Austin TX
- 6) B. Johnson, M. Gaffney, "Description of Active Vibration Control on the JPL Cryocooler Vibration Testbed", Report R30-91, SatCon Technology Corp., Cambridge, MA

DEMONSTRATION OF ACTIVE VIBRATION REDUCTION ON A
STIRLING-CYCLE CRYOCOOLER TESTBED

Bruce G. Johnson (Presenter)
Mechtronics, Colorado Springs, CO

David B. Eisenhaure, Frederick J. Flynn,
Monique S. Gaffney, and Richard L. Hockney
SatCon Technology Corporation
12 Emily Street
Cambridge, MA 02139

Dean L. Johnson and Ronald G. Ross, Jr.
Jet Propulsion Laboratory
4800 Oak Grove
Pasadena, CA 91109

INTRODUCTION

SatCon Technology Corporation has demonstrated excellent vibration reduction performance using active control on the Jet Propulsion Laboratory Stirling-cycle cryocooler testbed. This paper addresses the use of classical narrow-band feedback control to meet the cryocooler vibration specifications using one cryocooler in a self-cancellation configuration. Similar vibration reduction performance was obtained using a cryocooler back-to-back configuration by actively controlling a reaction mass actuator that was used to mimic the second cooler. In addition to the classical feedback approach, SatCon is executing other narrow-band control approaches to compare stability, performance, and implementation issues.

BACKGROUND

JPL has an extensive research program supporting the development of near-term long-life space Stirling-cycle cryocoolers (ref.1). They have identified low vibration as one of the key technical challenges for these coolers. The dominant source of these vibrations are the cryocooler compressors, which are essentially linear motors with reaction masses, the pistons, attached. The compressors are driven at a single frequency, typically between 40 and 60 Hz for this class of coolers. Because of nonlinearities in the motor drive electronics, the compressor linear motor, the piston support flexures, and the gas dynamics, the resulting force contains significant signal levels at the fundamental drive frequency harmonics, in addition to force at the drive or fundamental frequency. In addition, these narrow-band forces can coincide with internal structural resonances, amplifying the vibratory forces that are produced.

The baseline approach to controlling these vibratory forces is to mechanically place the compressors in a back-to-back configuration and drive the compressor motors with out-of-phase currents. In this manner the forces produced by the compressors can be used to cancel each other. Simple open loop control of back-to-back cryocooler compressors, however, has not been sufficient to reduce residual vibrations to desired level of under 0.2 Newton at any frequency. Better performance can be gained by manually adjusting the relative phase and amplitude of the drive signals to the two compressors. By using phase-locked signal generators, this approach was successfully demonstrated at JPL. In this approach, the relative amplitude and phase of the drive signals was iteratively changed in an attempt to minimize the force at single frequencies. Using this human-in-the-loop active control approach, the net force produced at the fundamental can be significantly reduced.

SatCon Technology was tasked to "automate" this approach, with an electronic based implementation, to obtain the results that had been achieved by manual

tuning the drive amplitudes and phases (ref. 2). The goal was to reduce the force harmonics using active control.

NARROW-BAND CONTROL

As mentioned earlier, the harmonic force structure that is produced by the cryocooler when driven with a single frequency is caused by various nonlinearities in the motor and associated mechanical systems. In general, therefore, the net force produced by the cryocooler is a nonlinear function of the drive voltage time-history. When driven by a single frequency sinusoid, however, the net force is produced only at the fundamental drive frequency and its harmonics. Because of the essentially time-invariant nature of the cryocooler, the amplitudes of these harmonics remain nearly stationary. The cryocooler, therefore, can be accurately treated in steady state as mapping the fixed-frequency input voltage amplitude into a number of harmonic force amplitudes and phases. Alternatively, the cryocooler can be modelled as a linear voltage to force system corrupted by additive harmonic forces. This view of the cryocooler is shown in Figure 1, where $G(s)$ is the cryocooler voltage to force "plant". The harmonic forces are modelled as additive output disturbances to the plant.

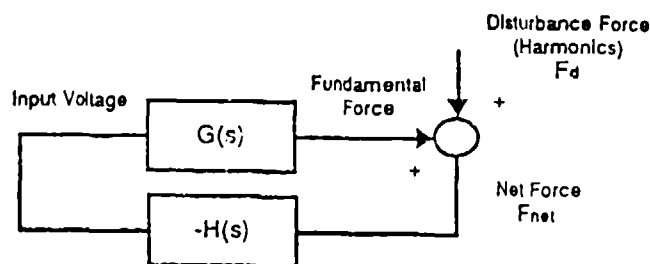


Figure 1 Classical feedback approach block diagram

When viewed in this manner, the cryocooler vibration control problem fits neatly into the paradigm of "narrow-band disturbance control", where the disturbances are periodic in nature. Numerous approaches exist to the narrow-band disturbance control problem, including classical feedback and adaptive feedforward. The performance of these algorithms can be made similar (ref.3), at least for the relatively simple problem of controlling only the axial force. The implementation of these control algorithms, however, can differ significantly. This paper addresses the harmonic vibration problem using the "classical" feedback approach.

In the classical feedback approach, the compensator gain $H(s)$ is made infinite at disturbance frequency ω_d and small elsewhere. Typically this is implemented with a second-order filter, an undamped oscillator. The filter transfer function shown in Figure 1 is given by

$$H(s) = k \frac{s}{\left(\frac{s}{\omega_d}\right)^2 + 1} = \frac{H_{num}(s)}{\left(\frac{s}{\omega_d}\right)^2 + 1} \quad (1)$$

where k is the compensator gain and ω_d is the disturbance frequency. Because the feedback gain is infinite at the disturbance frequency, the net force will be driven to zero, if the system is stable.

For a general plant all we need know to design the compensator and analyze its stability properties is the maximum gain of the plant G_{max} and the phase of the plant at the disturbance frequency $\angle G(j\omega_d)$. At frequencies away from the disturbance frequency, we can guarantee stability if the loop gain is kept below 0 db independent of the plant phase, that is we "gain stabilize" the plant at these frequencies. If the loop gain is less than one (0 db) it can never encircle the minus one point on the Nyquist plot, which is the stability condition for this system. At frequencies near the disturbance frequency, the loop gain becomes infinite and the best stability robustness will be achieved if the loop gain changes

from +90 to -90 degrees. The undamped poles in the compensator will contribute a change in loop phase of -180 degrees to the loop gain at the disturbance frequency. Therefore at the disturbance frequency we want the plant phase and the numerator portion of the compensator to contribute +90 degrees of phase. Restated, the best stability will be obtained if

$$\angle G(j\omega_d) + \angle H_{num}(j\omega_d) = +90^\circ \quad (2)$$

RESULTS

Because of the lack of a second cryocooler, the active vibration control demonstration discussed herein involves actively controlling one cryocooler to cancel its own higher harmonic forces. Figure 2 is a block diagram of the test setup. The main components of the control loop include the BAe cryocooler, the force dynamometer, the control computer, and the Hafler amplifier. The BAe cryocooler amplifier is driven with a constant amplitude, constant frequency "fundamental" signal, which is the output on D/A channel 1 of the 16 bit board. This signal is generated by the Texas Instruments TMS320C30 floating point DSP that is used as the control computer. The amplitude of this signal can be adjusted using the Hafler amplifier, which changes the stroke of the BAe compressor. The output on D/A channel 0 is the harmonic compensation from the control computer. For the self-canceling approach, the two channel outputs are summed using a Tektronix differential amplifier. The resulting signal is sent to the left channel of the Hafler amplifier to drive the BAe cryocooler.

For this configuration, the narrow-band feedback compensation consists of a notch at the fundamental 40 Hz, and five undamped oscillators at the higher harmonics of 80, 120, 160, 180, and 220 Hz. Because the cooler is running alone, the 40 Hz fundamental force is not canceled. The notch at 40 Hz ensures that the harmonic compensation from channel 0 does not contribute any 40 Hz signal to the

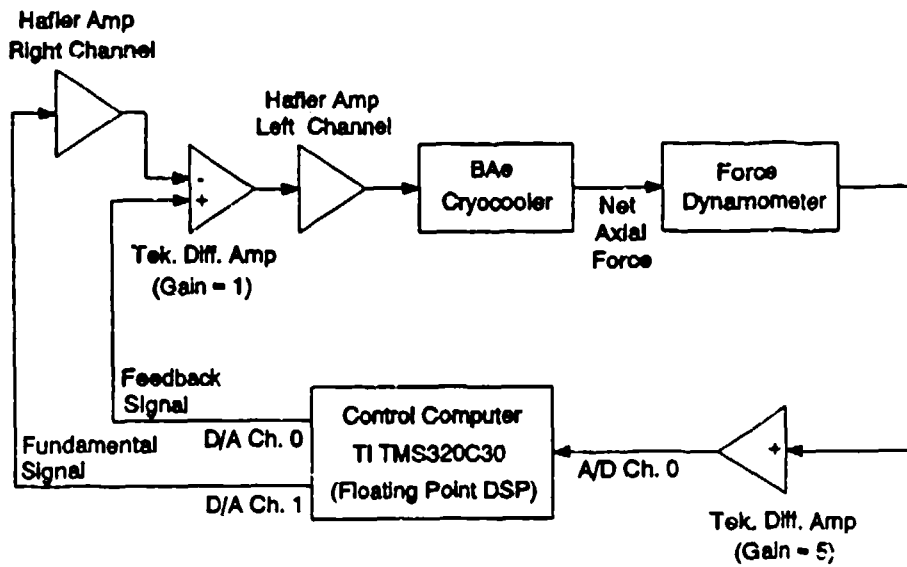


Figure 2 Block diagram of JPL active controller using self-cancellation

fundamental signal from channel 1. Hence, channel 1 drives the cryocooler at the fundamental and channel 0 compensates for the higher harmonics.

The self-cancellation approach had excellent vibration reduction performance. The resulting plot of the axial force spectra comparing open-loop and actively controlled systems is illustrated in Figure 3. In both cases, the cryocooler compressor stroke was the same, producing approximately 35 N of peak force at the fundamental frequency. As shown, the forces at the target higher harmonics were driven into the noise floor of the force dynamometer. These results confirmed the technical feasibility of actively controlling the cryocooler to reduce the harmonic vibrations.

GENERAL PURPOSE ELECTRONICS

Development of a general purpose electronics rack to implement vibration control is currently underway. The rack is configured for control of two compressors and two displacers. This general purpose electronics rack will provide three distinct

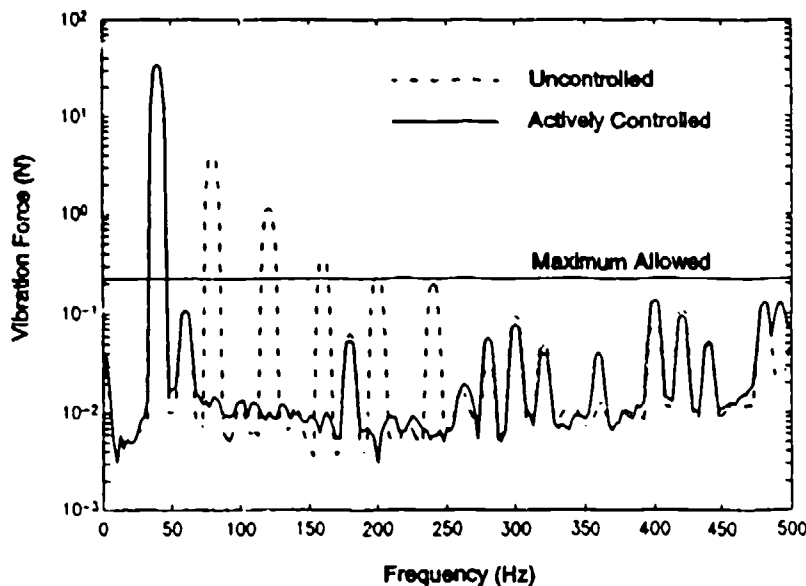


Figure 3 Axial vibration force spectra using self-cancellation configuration:
Five harmonics canceled

modes of vibration control. These modes are manual mode, an active analog closed loop control and a DSP control mode.

Under manual control mode the user has control of phase, amplitude and offset through front panel adjustments. Each of these adjustments operates independently upon the cooler or displacer connected to its drive output. Front panel display of AC and DC stroke, current and voltage is available as well as relative phase between either the two compressors or the compressor and its displacer.

The active analog closed loop provides position feedback control of phase, amplitude and offset through use of a LVDT. Each of these loops are combined to provide control with the desired phase, amplitude and offset adjustable through the front panel controls.

DSP mode provides a narrow band controller using a digital signal processor as described above but uses the power amplifiers of the rack to drive the compressors and displacers.

ACKNOWLEDGEMENT

The research in this paper was prepared under JPL Contracts No. 959057 and 959278. The authors wish to thank Vince Kotsubo and Simon Collins for their technical insights.

REFERENCES

1. Ross Jr., R.G., Johnson, D.L., Sugimura, R.S., "Characterization of Miniature Stirling-Cycle Cryocooler for Space Application", Proceedings of the 6th International Cryocooler Conference, Plymouth, Massachusetts, October 25, 1990
2. Johnson, B.G., Gaffney, M.S., "Demonstration of Active Vibration Control on the JPL Cryocooler Vibration Testbed", SatCon Final Report, R30-91, August 1991
3. Sievers, L.A., von Flotow, A.H., "Comparison and Extensions of Control Methods for Narrowband Disturbance Rejection", Active Noise and Vibration Control -- 1990, Proceeding of the ASME Winter Annual Meeting, NCA-Vol8, American Society of Mechanical Engineers, New York, pp 11-22.

THURSDAY SESSION

EVOLUTION OF THE 10 K PERIODIC SORPTION REFRIGERATOR CONCEPT

Alfred L. Johnson
Design Engineering Subdivision
Vehicle and Control Systems Division
The Aerospace Corporation
El Segundo, CA 90245

Jack A. Jones
Jet Propulsion Laboratory
California Institute of Technology
4800 Oak Grove Drive
Pasadena, CA 91109

BACKGROUND

A spacecraft borne infrared surveillance system capable of detecting cool objects against an Earth, near-Earth, or space background requires that the sensor be cryogenically cooled. If the surveillance system is intended to observe long wave infrared signals current technology dictates that the sensor subsystem be composed of a detector cooled to below 12K, mounted within a 30K-40K cavity, illuminated via an optical train maintained at less than 80K, and shielded from extraneous thermal radiation sources with cold, low emittance baffling. The operational characteristics of the cryogenic refrigerator necessary to provide this thermal environment will depend on the satellite orbit, the sensor aperture size, and surveillance system mission. For geosynchronous applications, large aperture continuously operating sensors are required.

From the 1960's through the 1980's, the development of long life, high reliability spacecraft cryogenic refrigerators concentrated on continuous duty, three stage, homogeneous cycle technology. This approach resulted in relatively heavy, high input power hardware. Of the four major efforts funded during this period, the Philips magnetic bearing Stirling [1], the AiResearch foil bearing Turbo-Brayton [2], the A.D.Little gas dynamic bearing "R-cubed" Ericsson [3], and the HAC Vuilleumier [4], only the Philips and the HAC refrigerators were successfully demonstrated.

In the last 10 years, several small one and two stage cryogenic refrigerator development programs have been funded. Figure 1 classifies these mechanical cryogenic refrigerator developments by contractor, thermodynamic cycle, and type of moving elements. Designs based on the flexure bearing supported moving coil linear motor drive Stirling cycle configuration have proven to be the most successful, confirming the 1982 prediction [5].

Much of the surveillance capability provided by a small number of large elaborate surveillance satellites deployed in geosynchronous constellations could be satisfied by a large number of small simple surveillance satellites deployed in near-Earth constellations. Due to the reduced distance between a near-Earth satellite and its target, the sensor aperture area could be reduced, resulting in lower cooling loads. Continuous 10 K cooling (12K detector) would be unnecessary for the vast majority of the near-Earth surveillance missions. For any given sensor, providing the required cryogenic environment for a few tens of minutes per orbit, for a few orbits per day would generally suffice. This alternate cryogenic refrigerator design requirements paradigm resulted in the invention of the 10 K periodic sorption refrigerator concept described in this paper.

INITIAL DESIGN

Table I outlines the initial cryogenic cooling problem statement. The basic concept was structured around a dormant vehicle that would be activated only in time of imminent need. In considering the rapid thermal conditioning required for such response, the potential for thermal distortion of the optical train due to the transient cool-down suggests that it would be prudent to maintain the optical elements at operational temperature at all times. Since near earth platforms require that the sensor telescope be capable of rapid positioning, the telescope could be stowed in an orientation that minimized internal heating due to insolation and earth thermal loading. Such an operational procedure keeps the standby cryogenic cooling design requirement at less than 1 watt (60K-80K). This need can be readily met with cryogenic refrigerator technology based on the flexure supported moving coil linear drive split Stirling cycle technology[6,7,8].

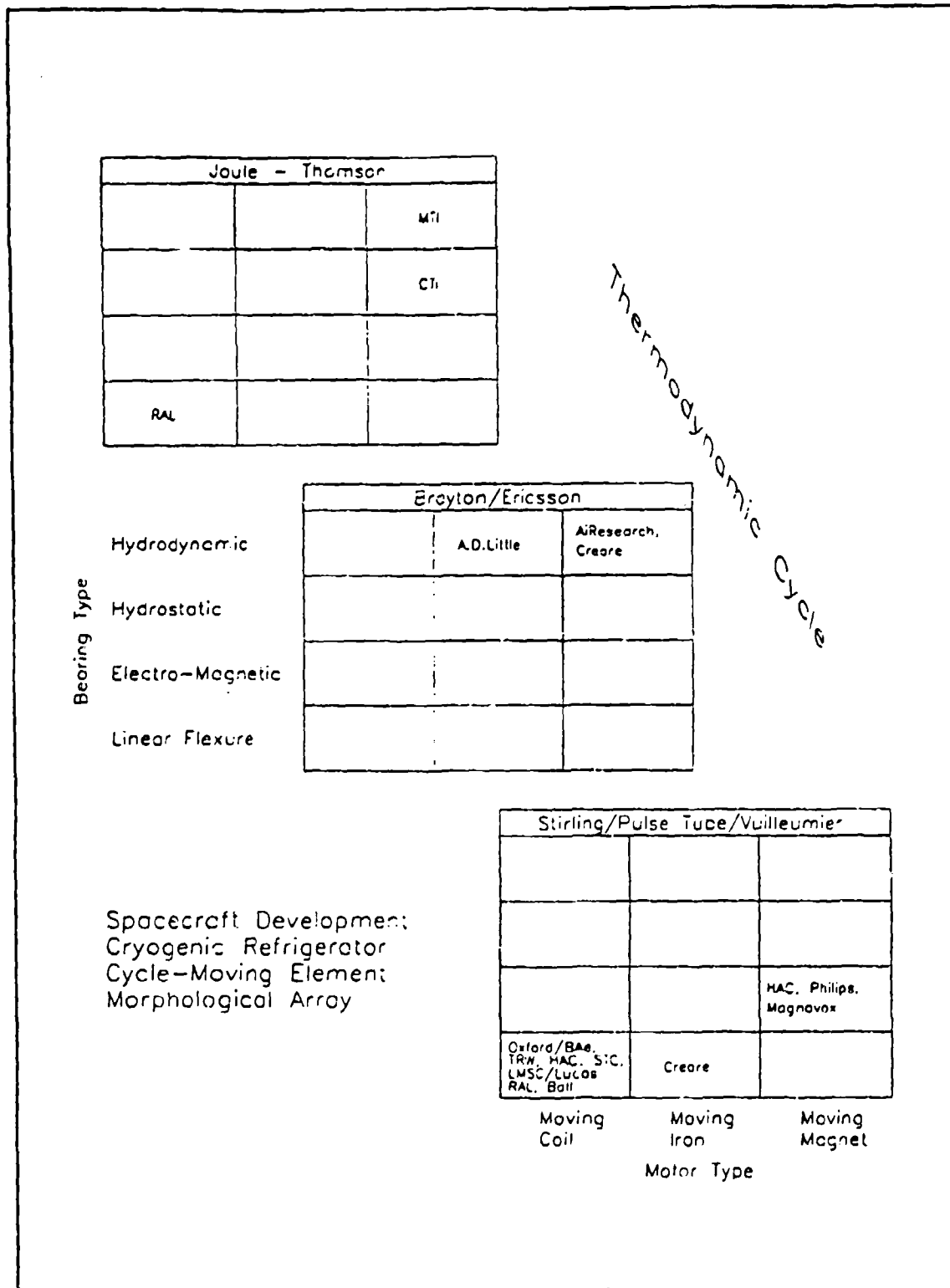


Figure 1 - Morphological Array - Mechanical Cryogenic Refrigerators

Basic Design Requirements

Design a cryogenic cooling system for a periodically activated Long Wavelength Infrared sensor;
Assume a 20 centimeter aperture telescope;
10 year orbital life, 95% reliability;
15 minute operation, several times during orbital life;
Rapid response from dormant mode required;
Use light weight, low risk technology

Derived Design Requirements

Scale cooling requirements from SIRE sensor telescope design;

Scaled sensor operating thermal design:

Optics/Baffles - 4 watts,

Optics - 80K maximum,

Baffles - 150K Maximum;

Focal Plane Cavity - 1 watt @ 30K, 40K maximum;

Detector - 0.1 watt @ 12K.

Assume that the 15 minute operation is required 6 times in 10 years, and that 120 seconds are allowed to reach operating conditions from dormant mode;
Due to the rapid response requirement, maintain the optics, sensor cavity at ~65K during the dormant mode;

Minimizes potential for thermally induced optical distortion,

Reduces transient cool-down heat load on 30K and 12K items;

Assume that telescope can be stowed in a low parasitic heat load orientation during the dormant mode;

Estimate the parasitic heat load @ 60K-80K at less than 1 watt;

Use flexure bearing supported linear drive Stirling cycle cryogenic refrigerator to provide continuous cryogenic cooling;

Use thermal mass sensible heat, or Oxygen-Oxide sorption latent heat, or triple point Nitrogen heat of fusion cryogenic thermal storage unit for operational heat load;

Use stored high pressure gas J-T for 25K and 5K* cooling

The cryogenic cooling system temperatures must be less than the sensor temperatures to allow for heat transfer.

* 5K rather than 10K due to Helium having a 5.25K critical temperature.

Table I - Limited Life Expendable Cryogenic System Design Requirements

To provide the high heat load 60K to 80K cryogenic cooling environment that would be required during the occasional short duration operational mode, thermal capacitance in the form of high specific heat sensible cooling, regenerable heat of evaporation liquid Oxygen cooling, or regenerable heat of fusion Nitrogen triple point cooling could be utilized. Reconditioning of the thermal storage unit would increase the design heat load requirement for the continuously operating 60K cryogenic refrigerator, however, by not more than 100%, a value easily met by the chosen technology.

In conducting this research, it was determined that the occasional short duration 30K and 12K environments could be most easily provided by incorporating a multiplicity of expendable Hydrogen and Helium high pressure, ambient temperature bottles with related one-shot solenoid valves and shared Joule-Thomson cryocoolers. The 60K-80K thermal capacitance provided the required upper temperature heat sink for both the Hydrogen and Helium J-T systems. The 25K Hydrogen produced by the Hydrogen J-T system provided the inversion temperature heat sink for the Helium J-T system. The ability of the J-T cryocoolers to provide the required cooling within the allotted cool-down time had been previously demonstrated by Longworth and Steyert [9].

An intrinsic advantage of maintaining the dormant sensor at 60K to 80K is the low enthalpy difference of the cavity and sensor materials when cycled between storage and operating temperatures. Thus the transient cooling required to bring the sensor from its dormant mode to its operational mode is low. Potential problems associated with differential thermal expansion resulting from the transient cool-down are also greatly mitigated. Figure 2 illustrates these features by presenting a plot of temperature versus thermo-physical properties for typical materials.

Based on the above reasoning, the cryogenic thermal control system shown in Figure 3 was designed. The system operation is outlined in Table II.

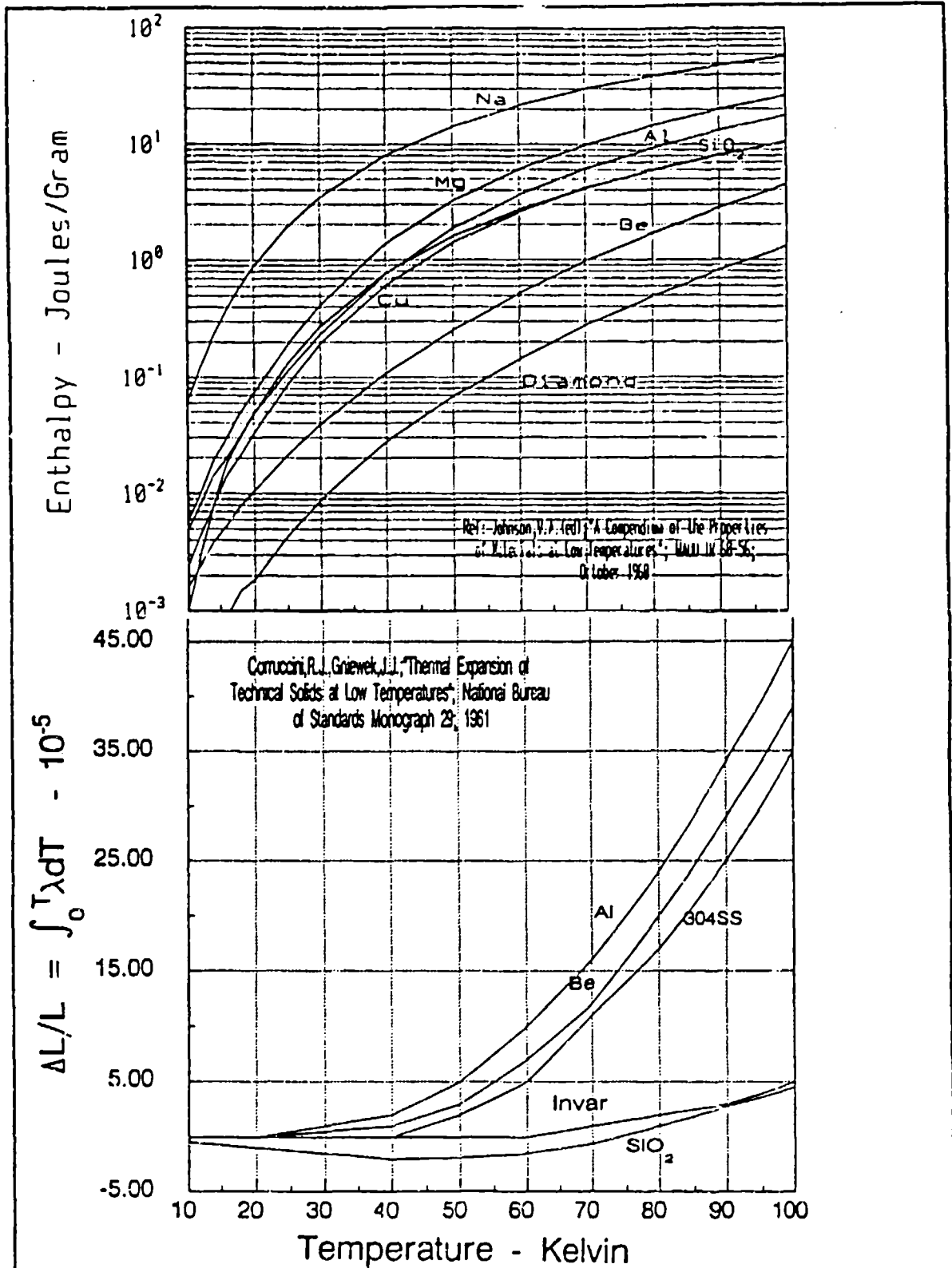


Figure 2 - Selected Cryogenic Properties for Typical Sensor Materials

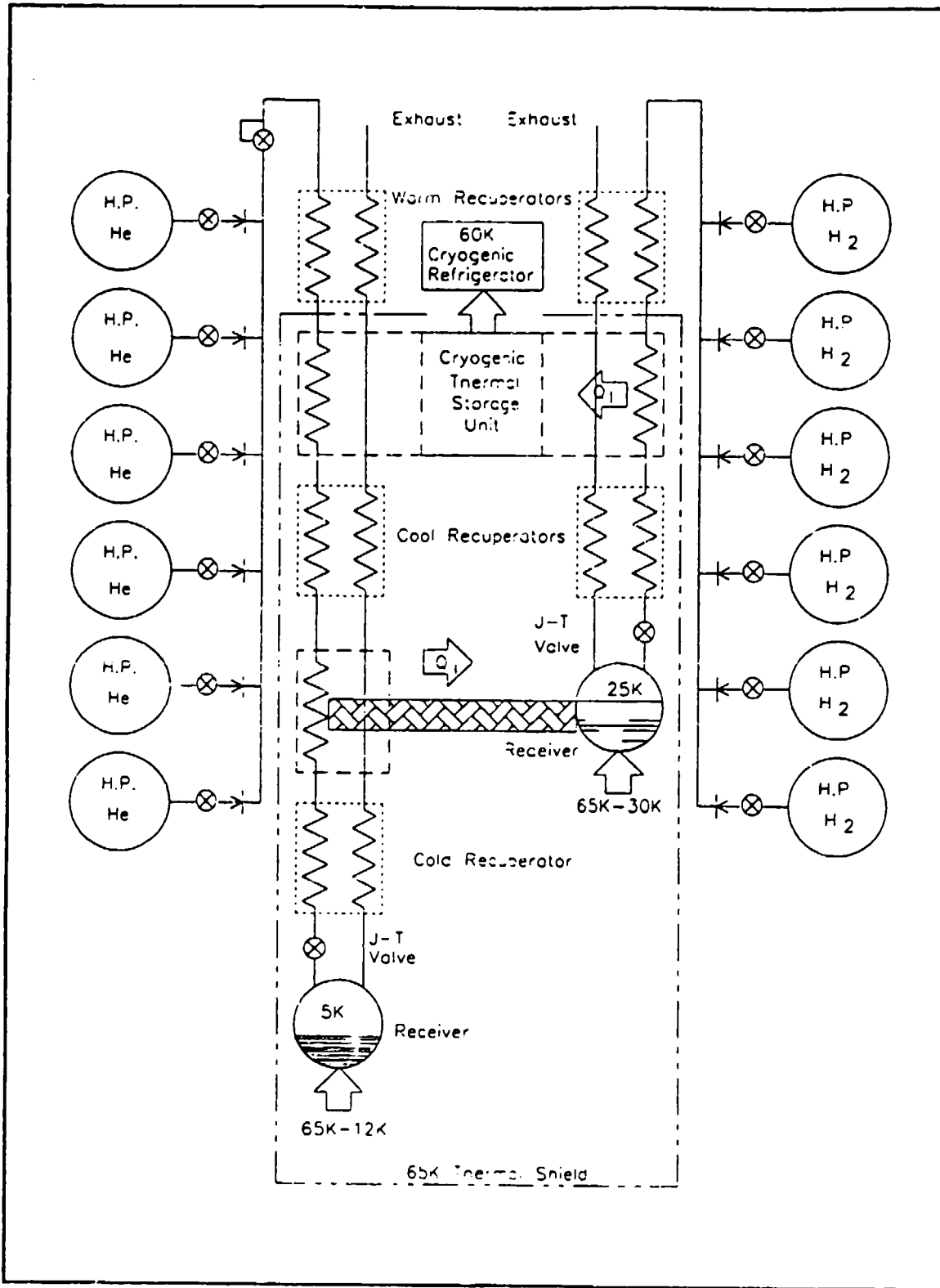


Figure 3 - Limited Life Expendable Cryogenic System Schematic

Standby Mode:

The telescope is stowed, thus minimizing the parasitic heat leak. The 60K cryogenic refrigerator maintains the precooled cryogenic thermal storage unit and the telescope internal environment at ~65K.

Cool-down Mode:

Fire the squib valve on one of the charged high pressure Hydrogen bottles. The gas will blow-down through the Hydrogen J-T system. The Hydrogen is cooled below its inversion temperature by the cryogenic thermal storage heat sink. After about 60 seconds, the Hydrogen gas bottle is depleted, and the desired quantity of liquid Hydrogen has accumulated in the 30K heat sink wick. The squib valve on one of the charged high pressure Helium bottles is fired about 90 seconds into the cool-down phase. By this time, the liquid Hydrogen will have cooled down to about 25K. The pressure regulated discharging Helium gas is precooled by the cryogenic thermal storage heat sink, then cooled below its inversion temperature by the 25K liquid Hydrogen heat sink. Flow through the low temperature recuperator and expansion across the J-T valve cools and liquifies the Helium down to below 5K.

Operational Mode:

After the 120 second transient cool-down, sufficient liquid Hydrogen remains in the "25K" cryogen receiver to maintain its temperature well below 25K for at least 15 minutes. Similarly sufficient liquid Helium* have been produced to keep the "5K" cryogen receiver well below 5K for at least 15 minutes. The high heat load imposed on the baffles and the optical system is absorbed by the cryogenic thermal storage unit. If the 60K cryogenic refrigerator mechanical vibration causes too much jitter, it can be shut down during the operational phase.

Recovery Mode:

After use, the telescope is returned to its stowed position. The 60K cryogenic refrigerator removes the parasitic heat leak plus the heat absorbed by the cryogenic thermal storage unit. This segment of the process can take several hours to several tens of hours, depending on the capacity of the 60K cryogenic refrigerator.

* Since the critical temperature of Helium is 5.25K, it is necessary to for the detector sink temperature to be <5K to assure the liquid Helium state.

Table II - Limited Life Expendable Cryogenic System Operation

FIRST REVISION

After consideration of the operational mission limitations imposed on an orbital surveillance system constrained to a few cool-down cycles, the revised problem statement summarized in Table III was generated. The long wave infrared detector could still only be used during a few extreme need occasions, but a mid-wave infrared detector could be used on a daily basis if it proved advantageous. In essence, the orbital resource would have a dual use.

This new requirement could be satisfied by either incorporating a continuous 30K cryogenic refrigeration capability, or by utilizing a periodic, regenerable 30K subsystem. Both technologies had been demonstrated through the proof of concept stage, a two stage Stirling cycle cryogenic refrigerator (continuous) by Bradshaw [10] at Rutherford Appleton Laboratories (RAL) based on the Oxford/British Aerospace Corporation technology, and a single stage Hydrogen J-T cryocooler (quasi-periodic) by Jones et al [11] at JPL based on Hydrogen-Hydride sorption cycle techniques. Figure 4 depicts the Hydrogen-hydride sorption cycle thermal schematic. Although the RAL 30K Stirling cycle cryogenic refrigerator utilizes two stages to obtain the 30K heat sink, the operating temperature of the first stage is too high and the available cooling capacity too low to satisfy the 60K design requirements. Thus it was necessary to retain the 60K single stage Stirling cycle cryogenic refrigerator for either approach. With this constraint, a weight/power trade study clearly favored the periodic sorption concept. Extrapolation of the performance prediction to an optimized two stage Stirling cycle unit designed to provide both the first and second stage temperatures and cooling capacities reduced the effective spacecraft weight penalty, but not sufficiently to reverse the selection.

The periodic Hydrogen-Hydride sorption cryocooler designed to replace the expendable Hydrogen J-T system, thus satisfying the requirements of Table III, is shown in Figure 5. The system differs considerably from that shown in Figure 4. The periodic system requires only one metal hydride bed. A high pressure gas accumulator (bottle) is used to supply the high flow rate Hydrogen to the J-T unit. This reduces the peak power demand on the spacecraft power system batteries that a rapid desorption bed (2 minutes) would impose.

Basic Design Requirements

Design a cryogenic cooling system for a periodically activated LWIR *and* MWIR sensor array;
 Assume a 20 centimeter aperture telescope;
 10 year orbital life, 95% reliability;
 30 minute LWIR operation, several times during orbital life;
 30 minute MWIR operation daily;
 Rapid response from dormant mode required;
 Use light weight, low cost, low risk technology

Derived Design Requirements

Scale cooling requirements from SIRE sensor telescope design;
 Scaled sensor operating thermal design:
 Optics/Baffles - 4 watts *ave.*, 8 watts *peak*,
 Optics - 80K maximum;
 Baffles - 150K maximum;
 MWIR detector + LWIR Focal Plane Cavity - 1 watt @ 30K,
 40 K maximum.,
 LWIR Detector - 0.1 watt @ 12K
 Assume that the 30 minute LWIR operation is required 6 times in 10 years,
 and that 120 seconds are allowed to reach operating conditions from dormant
 mode;
 Due to the rapid response requirement, maintain the optics, sensor cavity at
 ~65K during the dormant mode;
 Minimizes potential for thermally induced optical distortion,
 Reduces transient cool-down heat load on 30K and 12K items;
 Assume that telescope can be stowed in a low parasitic heat load orientation
 during the dormant mode;
 Estimate the parasitic heat load @ 60K-80K at less than 1 watt *during*
 dormancy;
 Use flexure bearing supported linear drive Stirling cycle cryogenic refrigerator
 to provide continuous cryogenic cooling;
 Use thermal mass sensible heat, or Oxygen-Oxide sorption latent heat, or
 triple point Nitrogen heat of fusion cryogenic thermal storage unit for
 operational heat load;
 Use *regenerable Hydrogen - Hydride sorption J-T for 25K cooling*;
 Use stored high pressure *Helium J-T for 5K cooling*
 The cryogenic cooling system temperatures must be less than the sensor
 temperatures to allow for heat transfer.

Italic text indicates changes from previous design requirements.

Table III - Extended Life Cryogenic System Design Requirements

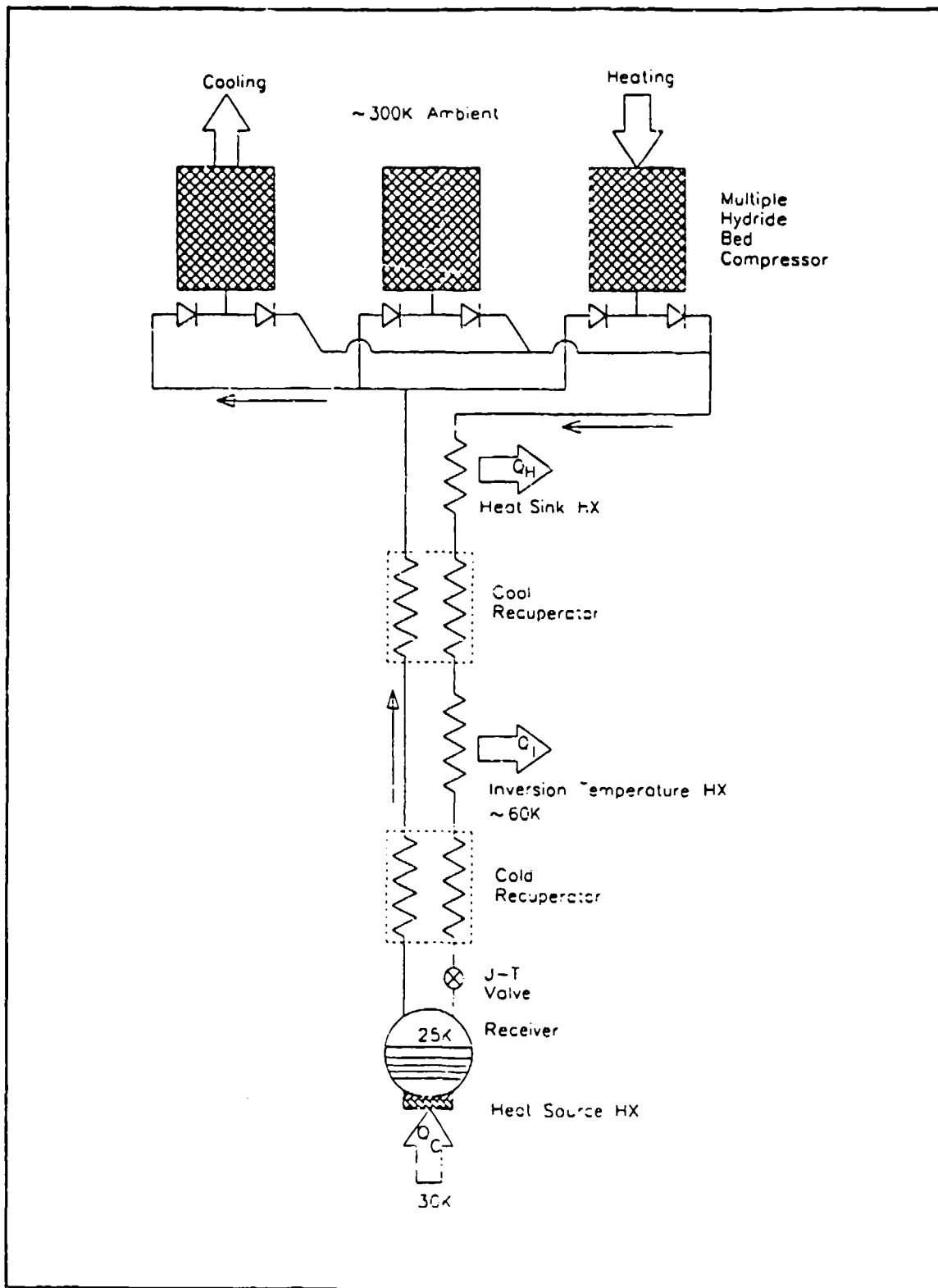


Figure 4 - Hydrogen-Hydride Cryogenic Refrigerator (ref. 11)

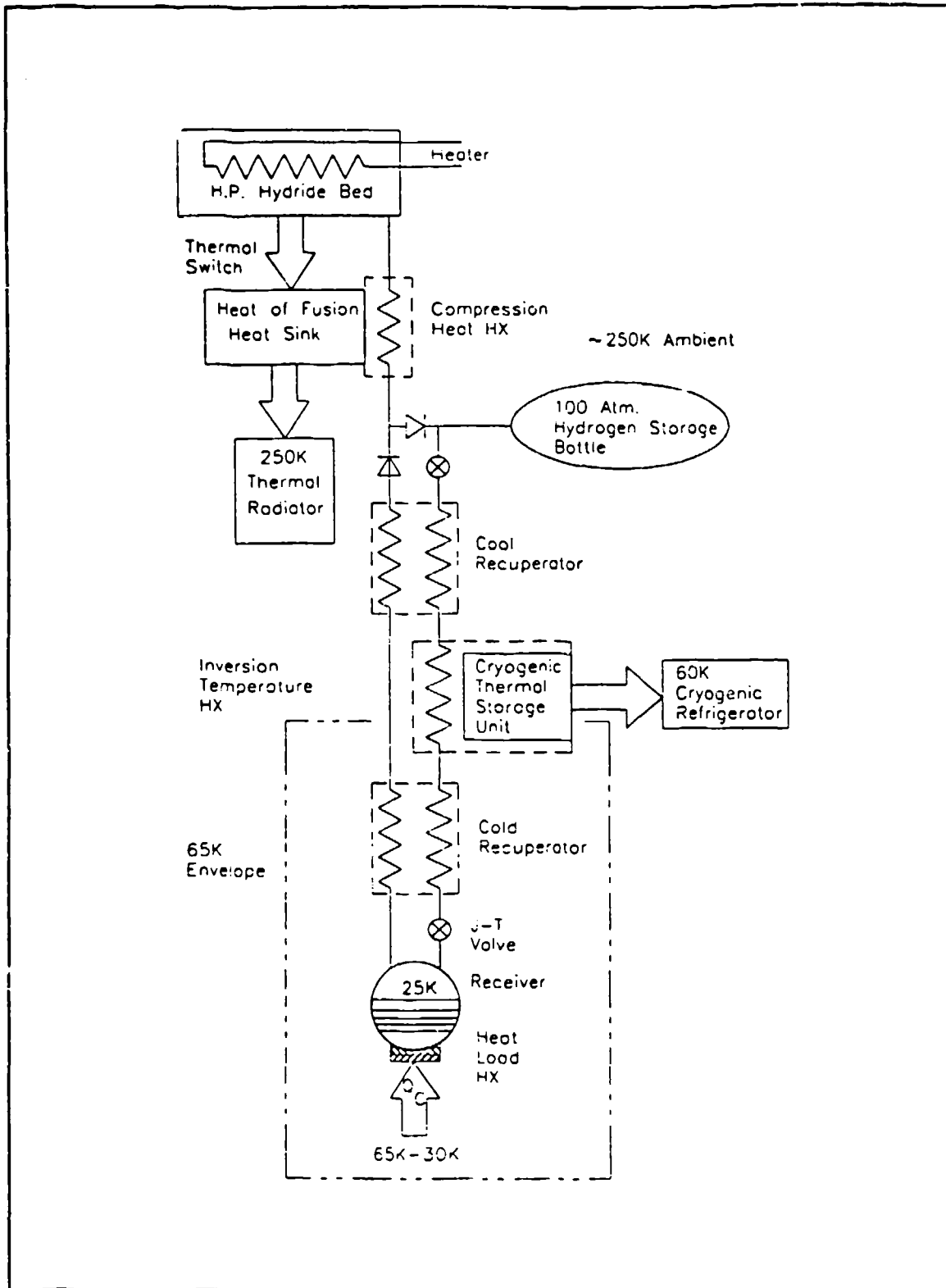


Figure 5 - Periodic Hydrogen-Hydride 25K Cryocooler Schematic

To minimize the size of the sorption bed thermal radiator, a high temperature heat of fusion heat thermal storage unit [12] is incorporated between the sorption bed and the thermal radiator. This allows the thermal radiator to be sized based on the average thermal dissipation rather than on the peak thermal dissipation. To provide the necessary thermal disconnect between the thermal storage unit and the sorption bed during desorption, a gas gap thermal switch [13] has been added. The resultant periodic 30K sorption cryogenic refrigeration system is thus based on a collection of previously demonstrated technologies. The subsystem operation is summarized in Table IV.

FINAL REVISION

The design process continued through several iterations until the problem statement summarized in Table V finally evolved. To meet the design requirements of this final design, the limited cycle expendable Helium J-T system must be replaced. A method for continuously producing a 10K heat sink using Hydrogen sorption technology had been previously proposed by Jones [14], expanding upon a suggestion by Johnson. Jones subsequently patented an improved version of this concept, a schematic of which is shown in Figure 6 [15]. The low pressure recuperator could prove to be very difficult to physically realize due to its very low operating pressure, ~ 1 Torr. As an alternative configuration which circumvents the low pressure recuperator implementation problem, the cycle shown in Figure 7 has been suggested. This alternative configuration will have a lower overall thermodynamic cycle efficiency due to the irreversibility associated with the venting Hydrogen during the freezing/subliming segment of the cycle, however, there will be a lower parasitic heat leak due to the elimination of the low pressure recuperator. For either configuration, the continuous mode operation is obtained by consecutive operation of a pair of periodic units. From consideration of the Figure 7 schematic, it is apparent that by eliminating the thermal switches and entire fluid circuit on the right hand half of the diagram, and adding a check valve and a high pressure Hydrogen gas accumulator, it is possible to create a periodic 10K refrigerator. The periodic cycle configuration can also be synthesized as an extension of the cycle configuration previously shown in Figure 5 (which is actually how the concept evolved).

Standby Mode:

The discharged Hydrogen-Hydride bed is maintained at a relatively cool temperature by thermal interaction with the heat of fusion heat sink via the closed thermal switch. The bed heater is off. The Hydrogen storage bottle is fully charged with 100 Atmosphere Hydrogen at ambient temperature (~280K). The solenoid activation valve is closed. The cryogenic thermal storage unit is "fully charged" (at its lowest enthalpy condition). The cold recuperator, J-T valve, and the receiver are in thermal equilibrium with the surrounding 65K heat shield.

Cool-down Mode:

The Hydrogen bottle solenoid is activated, allowing the gas to blow-down through the Hydrogen J-T system. The Hydrogen gas is cooled below its inversion temperature by the cold recuperator and the cryogenic thermal storage heat sink. The cool Hydrogen is liquified by the cold recuperator and the J-T expansion. The venting low pressure Hydrogen is heated through the recuperators and then absorbed in the metal hydride bed. The hydride bed is thermally coupled to the heat of fusion heat sink via the thermal switch thus maintaining its temperature and thereby its low suction pressure. After about 60 seconds, the Hydrogen gas bottle pressure has dropped to ~ 50 Atmospheres), and the desired quantity of liquid Hydrogen will have accumulated in the 25K receiver. The solenoid valve is closed.

Operational Mode:

After the 120 second transient cool-down, sufficient liquid Hydrogen remains in the 25K cryogen receiver to provide the required cryogenic cooling while maintaining its temperature at 25K for at least 30 minutes.

Recovery Mode:

The thermal switch is opened, the bed heaters energized, the bed temperature increased, and the Hydrogen-Hydride equilibrium pressure thereby increased thus recharging the high pressure Hydrogen bottle. The hot gas is cooled by the heat of fusion heat sink prior to entering the storage tank. When the bottle is fully charged (~100 Atmospheres), the heater is turned off, the bed allowed to cool, then the thermal switch is closed and the bed further cooled to its low temperature standby condition. The 60K cryogenic refrigerator reconditions the cryogenic thermal storage unit. This segment of the process can take several hours, depending on the bed heating rate and capacity of the 60K cryogenic refrigerator.

Table IV - Periodic Hydrogen - Hydride 25K Cryocooler Operation

Basic Design Requirements

Design a cryogenic cooling system for a periodically activated LWIR and MWIR sensor array;
 Assume a 20 centimeter aperture telescope;
 10 year orbital life, 95% reliability;
 30 minute LWIR operation *daily*
 30 minute MWIR operation daily;
 Rapid response from dormant mode required;
 Use light weight, low cost, low risk technology

Derived Design Requirements

Scale cooling requirements from SIRE sensor telescope design;
 Scaled sensor operating thermal design:
 Optics/Baffles - 4 watts ave., 8 watts peak,
 Optics - 80K maximum;
 Baffles - 150K maximum;
 MWIR detector + LWIR Focal Plane Cavity - 1 watt @ 30K - 40 K maximum.,
 LWIR Detector - 0.1 watt @ 12K
 Assume that 120 seconds are allowed to reach operating conditions from dormant mode;
 Due to the rapid response requirement, maintain the optics, sensor cavity at ~65K during the dormant mode;
 Minimizes potential for thermally induced optical distortion,
 Reduces transient cool-down heat load on 30K and 12K items;
 Assume that telescope can be stowed in a low parasitic heat load orientation during the dormant mode;
 Estimate the parasitic heat load @ 60K-80K at less than 1 watt during dormancy;
 Use flexure bearing supported linear drive Stirling cycle cryogenic refrigerator to provide continuous cryogenic cooling;
 Use thermal mass sensible heat, or Oxygen-Oxide sorption latent heat, or triple point Nitrogen heat of fusion cryogenic thermal storage unit for operational heat load;
 Use regenerable Hydrogen - Hydride sorption J-T for 10K and 25K cooling;
 The cryogenic cooling system temperatures must be less than the sensor temperatures to allow for heat transfer.

Italic text indicates changes from previous design requirements.

Table V - Periodic Cryogenic Refrigerator Design Requirements

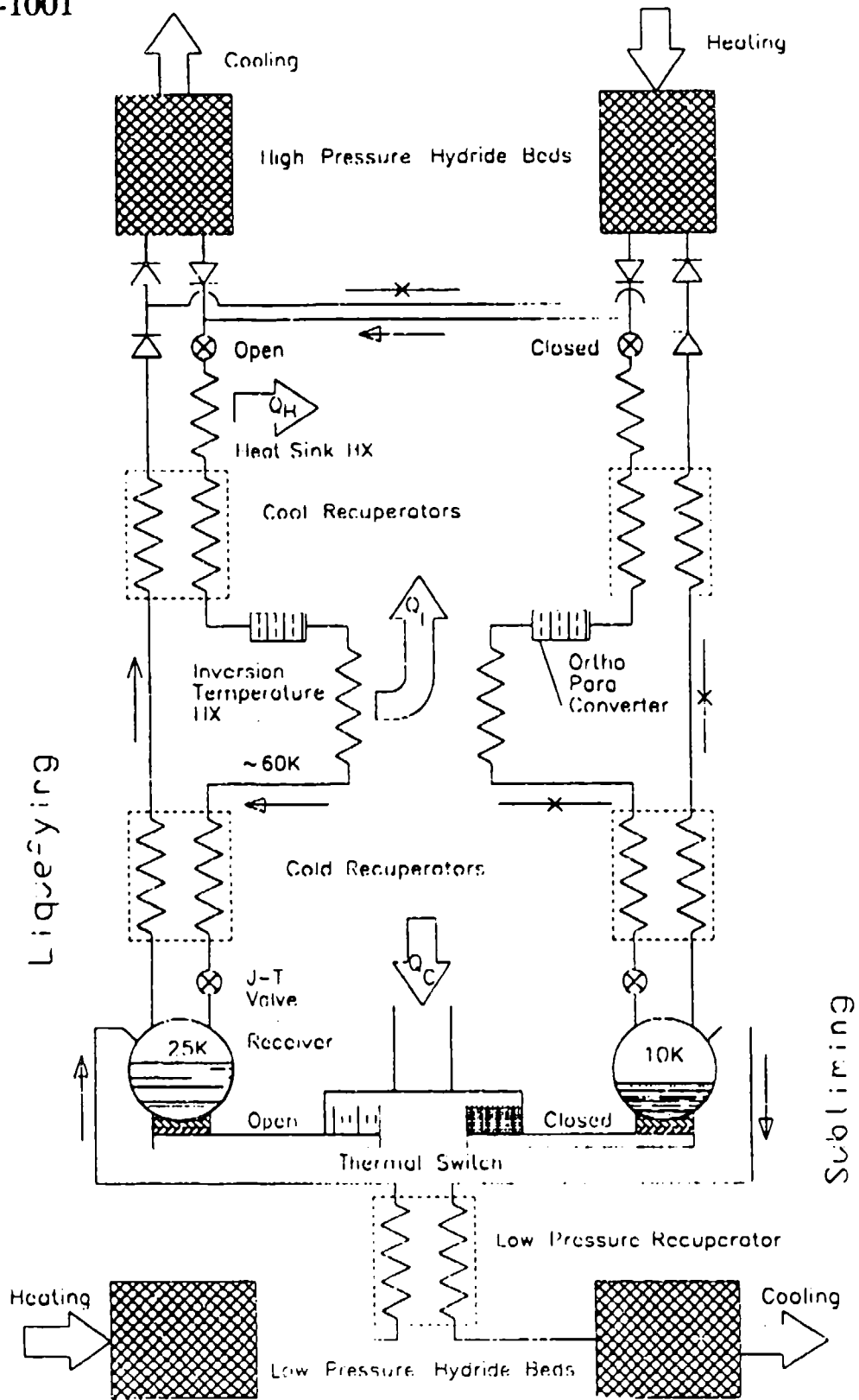


Figure 6

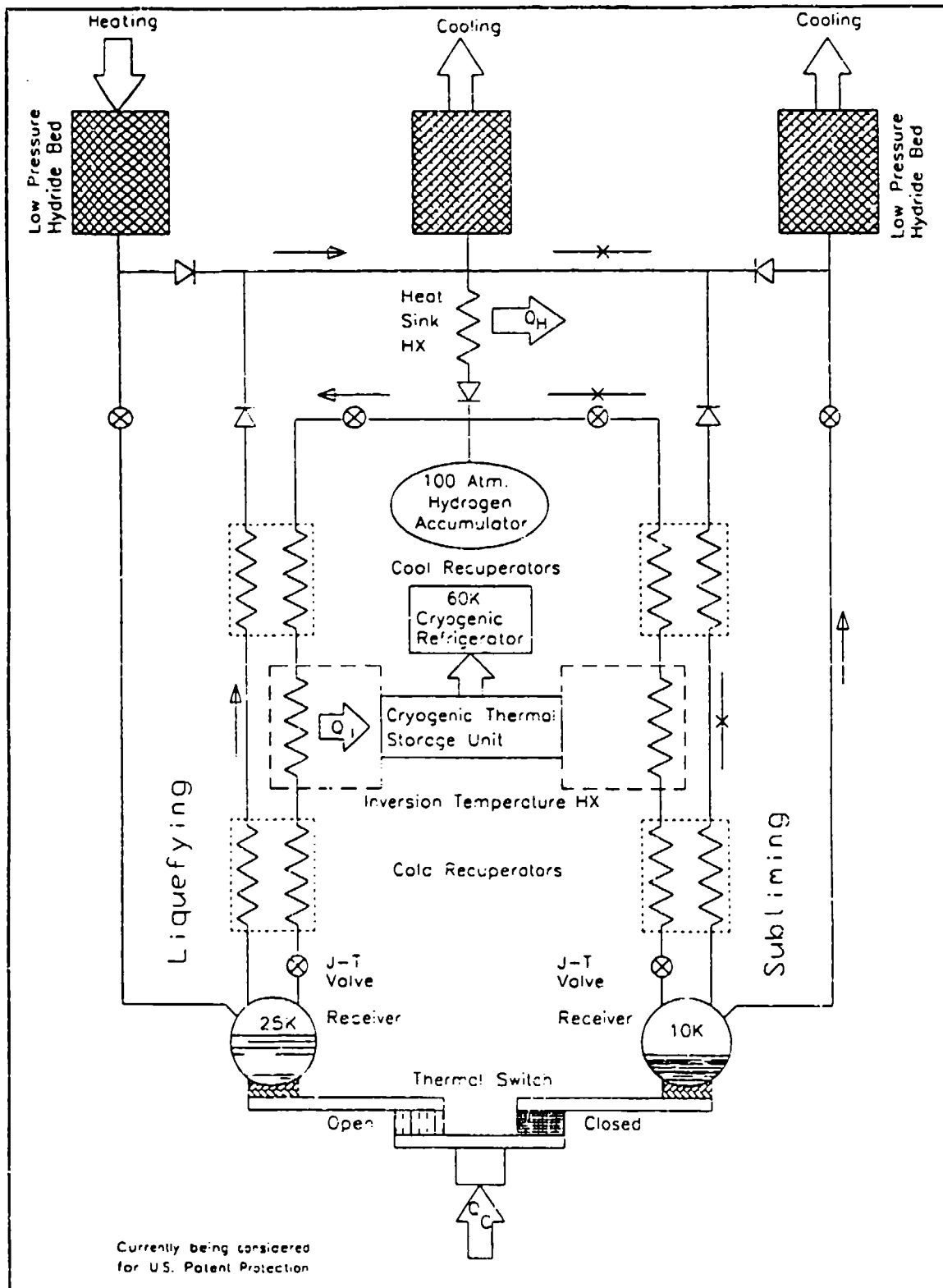


Figure 7 - Alternate Continuous 10K Sorption Cryogenic Refrigerator

Based on the foregoing, the periodic 10K cryogenic refrigerator shown in Figure 8 was synthesized. The cycle is an obvious extension of the 25K periodic Hydrogen sorption cryogenic refrigerator previously described. The 10K capability is obtained by adding a low pressure (~ 1 Torr.) Hydride sorption bed that provides the low pressure Hydrogen sink required to freeze, and subsequently sublimate, the liquid Hydrogen produced by the J-T expansion of the bottled gas into the high pressure (~8 Atms.) Hydride sorption bed. Proof of principle experimental demonstration of the critical liquid/solid sublimation Hydrogen J-T subsystem operating in a quick cool-down mode has been demonstrated by Longworth, et al[16], albeit using mechanical compressors. Table VI summarizes the periodic Hydrogen - hydride 10K cryocooler subsystem operation.

The subsystems shown in Figures 5 and 8 can be integrated as is shown in Figure 9. The periodic operation of the integrated system is a combination of the processes described in Tables IV and VI. As is shown in subsequent papers, the total concept has been successfully implemented in proof of principal experimental demonstration hardware [17].

TOTAL EFFECTIVE VEHICLE PENALTY - PERIODIC VERSUS CONTINUOUS

For the periodic system design depicted in Figure 9, the estimated weight is 35 kilograms, and the estimated average power consumption is 120 watts. Using a weight-power factor of 0.25 kilograms per watt of power consumed, which is typical for current spacecraft systems, the total effective vehicle penalty for the periodic cryogenic refrigerator approach is approximately 65 kilograms. Several alternative continuous three stage cryogenic refrigerator concepts were considered, pulse tube, Stirling, cascaded Joule-Thomson, hybrid two stage Stirling with third stage mechanical compression J-T, and hybrid two stage Stirling with third stage Hydrogen-hydride sorption. Based on an assumed cooling requirement of 4 watts @ 60K plus 1 watt @ 30K plus 0.1 watt @ 10K, the estimated total effective vehicle penalty ranged from 220 kilograms for the three stage Stirling to 360 kilograms for the cascaded J-T system. For this particular application, there is a significant advantage in using the periodic cryogenic refrigerator.

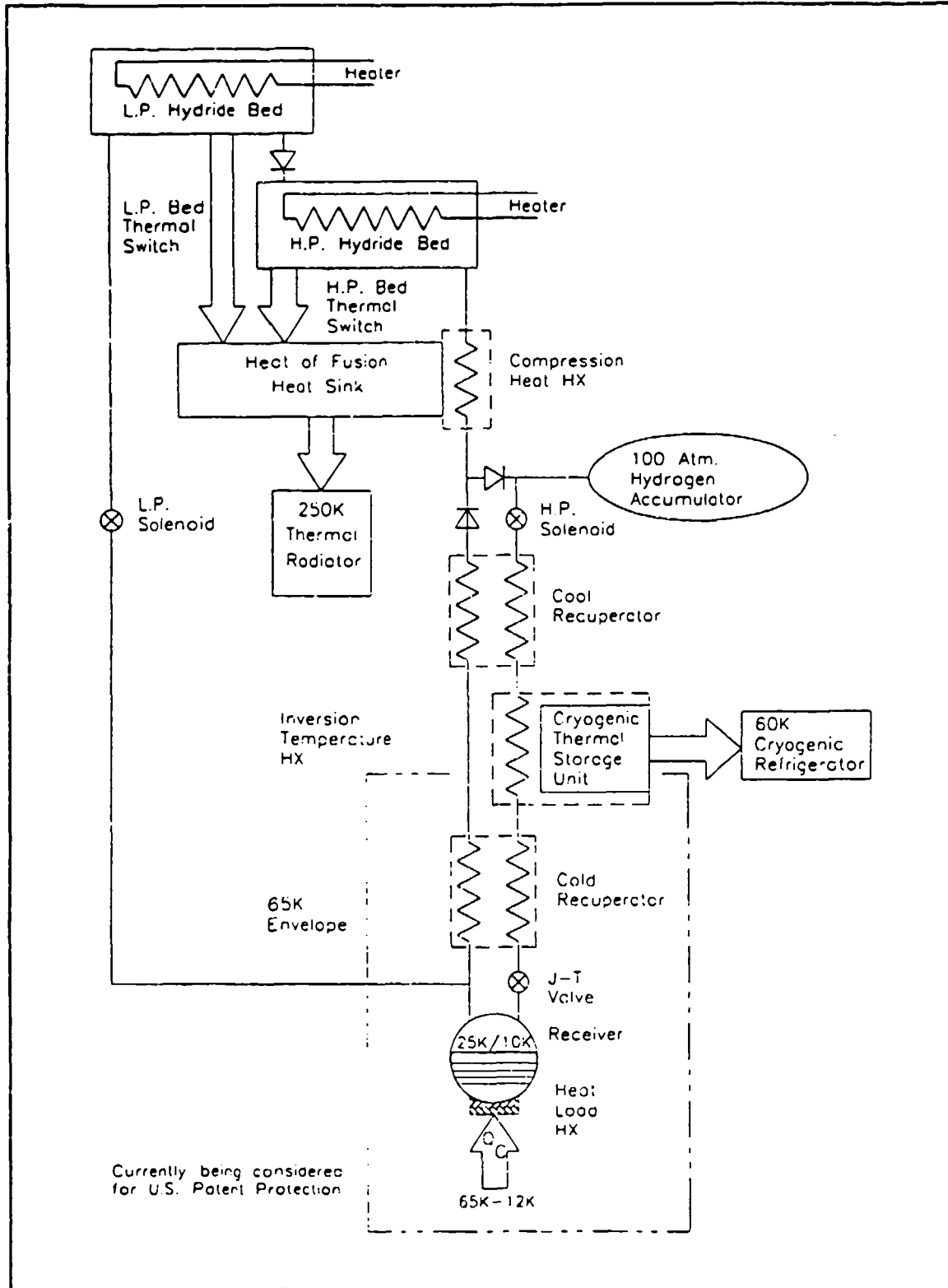


Figure 8 - Periodic Hydrogen - Hydride 10K Cryocooler Schematic

Standby Mode:

The discharged Hydride beds are maintained at a cool temperature by the heat of fusion heat sink via closed thermal switches. The bed heaters are off. The Hydrogen storage bottle is fully charged with 100 Atmosphere Hydrogen at ambient temperature (~280K). The solenoid valves are closed. The cryogenic thermal storage unit is at its lowest enthalpy condition. The cold recuperator, J-T valve, and the receiver are in thermal equilibrium with the surrounding 65K heat shield.

Cool-down Mode:

The high pressure solenoid is activated, discharging gas through the J-T system. The Hydrogen is cooled below its inversion temperature by the cold recuperator and the cryogenic thermal storage heat sink. It is liquified by the J-T expansion after passing through the cold recuperator. The returning recuperated low pressure Hydrogen is absorbed in the high pressure hydride bed. The H.P. hydride bed is thermally coupled to the heat of fusion heat sink via the thermal switch, thus maintaining its low suction pressure. After about 60 seconds, the gas bottle pressure will drop to ~ 50 Atmospheres. The desired quantity of liquid Hydrogen will have accumulated in the receiver. The H.P. solenoid valve is closed and the low pressure solenoid valve is opened. The Hydrogen will be absorbed in the L.P. hydride bed, lowering the equilibrium pressure over the liquid, thereby lowering its temperature. Within 60 seconds, the gas pressure will reach ~ 2 torr. The Hydrogen in the receiver will be frozen.

Operational Mode:

After the 120 second transient cool-down, sufficient solid Hydrogen remains in the receiver to provide the required cryogenic cooling while maintaining its temperature at ~10K for at least 30 minutes.

Recovery Mode:

The L.P. solenoid valve is closed, the L.P. bed thermal switch is opened, the L.P. bed heater energized, the L.P. bed temperature increased, and the Hydrogen thereby transferred into the H.P. bed. When the L.P. bed is fully discharged, the L.P. heater is turned off, the L.P. bed allowed to cool, the L.P. bed thermal switch is closed, and the L.P. bed further cooled to its low temperature standby condition. The rest of the system is then recharged as previously described.

Table VI - Periodic Hydrogen - Hydride 10K Cryocooler Operation

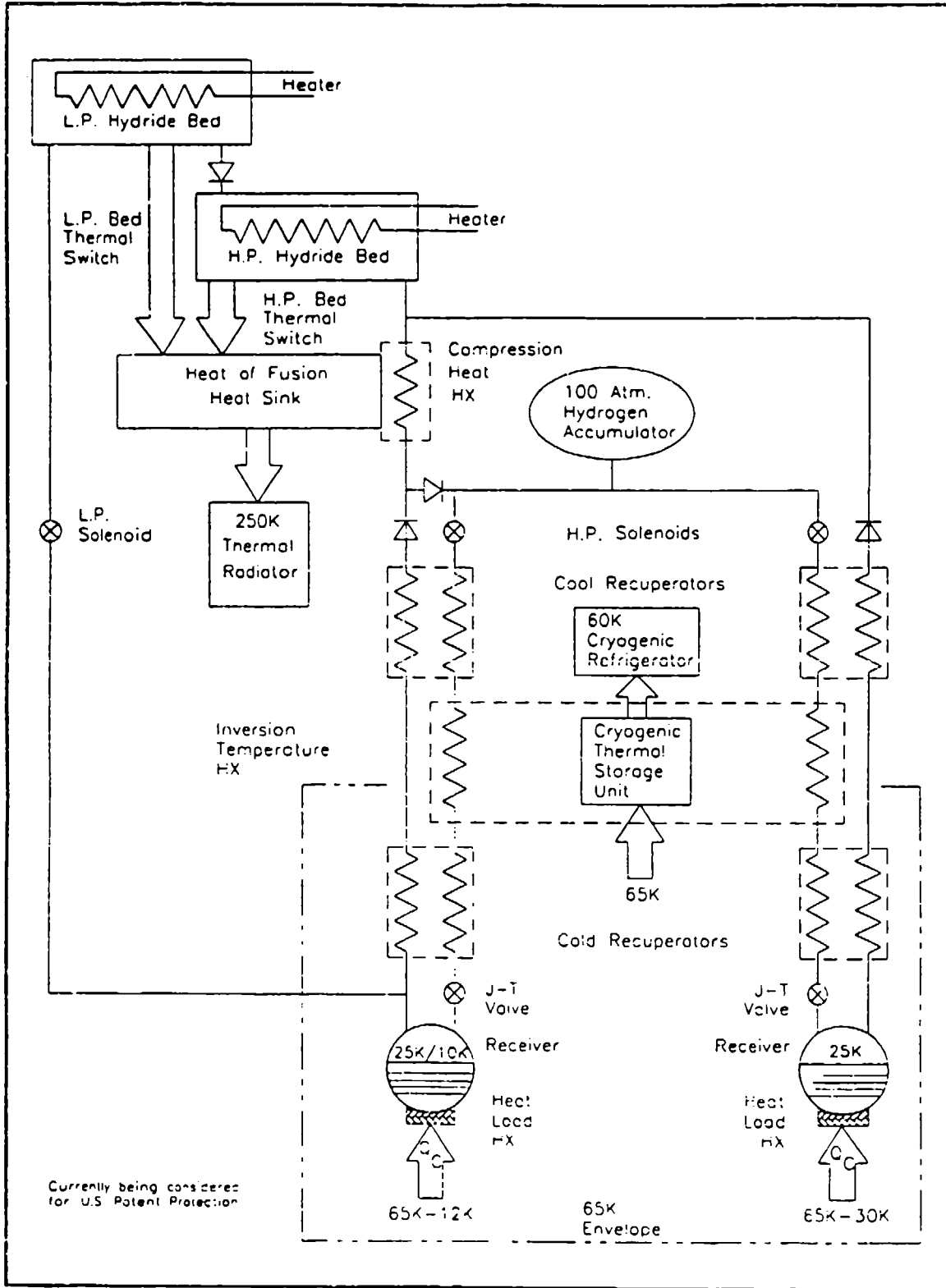


Figure 9 - Three Stage Periodic 60K/25K/10K Cryogenic Refrigerator

References

- [1] Stolfi, F.R., Daniels, A.; "Parametric Testing of a Linearly Driven Stirling Cryogenic Refrigerator"; Proceedings of the Third Cryocooler Conference; NBS; Boulder, CO, 17-19 September 1984
- [2] Wapato, P.G., et al; "Prototype Flight Cryocooler Design and Component Demonstration"; AFSTC-TR-87-14; Final Report; December 1988
- [3] Breckenridge, R.W., et al; "Prototype Flight Cryocooler Design and Component Demonstration"; AFSTC-TR-88-01; Final Report; July 1988
- [4] Vourgourakis, E.J., Sherman, N.I.; "Component Development for a Five-Year Vuilleumier (VM) Cryocooler"; AFFDL-TR-79-3092; Part XV-Final Report; December 1987
- [5] Johnson, A.L.; "Spacecraft-Borne Long Life Cryogenic Refrigeration -- Status and Trends"; Proceedings of the Second Biennial Conference on Refrigeration for Cryogenic Sensors and Electronic Systems; NASA GSFC; Greenbelt, MD, 7-8 December 1982
- [6] Werrett, S.T., et al; "Development of a Small Stirling Cycle Cooler for Spacecraft Applications"; RAL-85-087; October 1985
- [7] Lewis, C.A.; "Long Life Stirling Cycle Coolers for Application in the 60-110K Range: Vibration Characteristics and Thermal Switch Development"; 19th Intersociety Conference on Environmental Systems; 891496; San Diego, CA; 24-26 July 1989
- [8] Russo, S.C.; "Stirling Cycle 65K Standard Spacecraft Cryocooler Development"; Proceedings of the Fourth Interagency Meeting on Cryocoolers; Plymouth, MA; 24 October 1990; (Published by the David Taylor Research Center)
- [9] Longworth, R.C., Steyert, W.A.; "Fast Cooldown J-T Refrigerators for IR Detectors"; Proceedings of the Second Interagency Meeting on Cryocoolers; Easton, MD; 24 September 1986; (Published by the David Taylor Naval Ship R&D Center);
- [10] Bradshaw, T.W.; "First Results on a Prototype Two Stage Miniature Stirling Cycle Cooler for Spacecraft Applications"; Proceedings of the Fourth International Cryocooler Conference; Easton, MD; 25-26 September 1986
- [11] Jones, J.A., Golben, P.M.; "Design Life Testing and Future Designs of Cryogenic Hydride Refrigeration Systems"; Cryogenics; Volume 25; April 1985
- [12] Knowles, T.R., Webb, G.W.; "Metal/Phase-Change Material Composite Heatsinks"; AFWAL-TR-88-3069; WPAFB, Ohio; October 1988

- [13] Chan, C.K., Ross, R.G. Jr.; "Design and Application of Gas Gap Heat Switches - Final Report of Phase II"; JPL Publication 90-38; 15 March 1990
- [14] Jones, J.A.; "Hydride Absorption Refrigerator System for Ten Kelvin and Below"; Proceedings of the Third Cryocooler Conference; NBS Special Publication 698; NBS, Boulder, CO; 17-18 September 1984
- [15] Jones, J.A.; "Ten Degree Kelvin Hydride Refrigerator"; U.S. Patent 4,641,499; 10 February 1987
- [16] Longworth, R.C., Steyert, W.A., Pittenger, R.L., Lax, R.; "J-T Cryostat with Solid Cryogen Storage for Short Missions"; Proceedings of the Second Interagency Meeting on Cryocoolers; Easton, MD; 24 September 1986; (Published by the David Taylor Naval Ship R&D Center);
- [17] Bard, S., Wade, L., Rodriguez, J., Wu, J.J.; "Development of a Periodic 10K Sorption Cryocooler"; Proceedings of the 7th International Cryocooler Conference; Santa Fe, NM; 17-19 November 1992

Acknowledgements:

A portion of the research described in this paper was carried out by the Jet Propulsion Laboratory, California Institute of Technology, under a contract with the National Aeronautics and Space Administration.

A portion of the research described in this paper was carried out by the Aerospace Corporation, under a contract with the United States Air Force.

DEVELOPMENT OF A PERIODIC 10 K SORPTION CRYOCOOLER

Steven Bard, Toshito Fujita, Larry Wade, Jose Rodriguez, and J.J. Wu
Jet Propulsion Laboratory
California Institute of Technology
4800 Oak Grove Drive
Pasadena, CA 91109

ABSTRACT

10 K sorption cryocooler technology is ideal for spacecraft sensor cooling applications that require periodic quick-cooldown, negligible vibration, low average power consumption, and long-life (5 to 10 years). The basic feasibility of a periodic 10 K hydrogen/ hydride sorption cryocooler was proven in laboratory experiments in 1991 that demonstrated the ability to cooldown in under 2 minutes and maintain an I²R simulated detector heat load of 150 mW below 10 K for over 30 minutes. This paper summarizes past experimental results, presents an overview of the present development status, and describes plans to further advance the technology maturity level and mitigate the risks of utilizing periodic 10 K sorption cryocoolers for future spacecraft sensor cooling applications. To create the technology base needed to understand and demonstrate performance and reliability, the development program includes comprehensive component-level characterization and reliability physics investigations and tests, a near-term spaceflight technology demonstration, and flight-like engineering model and protoflight system development and life testing.

INTRODUCTION

One of the concepts for the Brilliant Eyes (BE) surveillance satellite system includes a very long-wavelength infrared (VLWIR) detector focal plane that needs to be periodically operated at near 10 K. A periodic 10 K sorption cooler concept was conceived by Dr. A. Johnson and Mr. J. Jones to meet the VLWIR cooling requirements [1,2]. Because sorption cooling provides low-vibration, long-life, and repeated quick cooldown capability, and the intermittent operation results in low average power consumption, sorption cooler technology provides an ideal method to produce periodic operation of cryogenic infrared sensors for future astronomy, earth-observation, and surveillance satellite systems such as BE.

The concept has been investigated analytically, and the proof-of-principle of a 10 K stage has been experimentally demonstrated in laboratory experiments [3]. A comprehensive technology development program is underway to advance the maturity level and mitigate the risks of utilizing this novel technology for spaceflight systems such as BE. This paper presents an overview and summarizes the status of the various elements of the development program, including the proof-of-principle (PoP) experiments, the BETSCE spaceflight

technology demonstration experiment, component-level characterization and reliability physics investigations, and engineering model and protoflight development by industry.

PERIODIC SORPTION CRYOCOOLER CONCEPT

Figure 1 describes the periodic sorption cryocooler system. The basic principle is based on alternately heating and cooling beds of metal hydride powders to circulate hydrogen in a closed cycle and periodically cool the detector cold head assembly to 10 K on command [1-3].

For the 60 K upper stage, a Stirling cryocooler such as an SDIO Standard Spacecraft Cryocooler (SSC), provides a continuous standby environment of about 60 K by cooling a thermal storage device (TSD). The TSD simply consists of a solid block of material with high specific heat at 60 to 70 K, such as aluminum. The sensible heating of the TSD buffers the mechanical cryocooler from the large power surge that occurs during the quick-cooldown operation. As hydrogen gas circulates past the TSD during cooldown, the TSD temperature rises by 5 to 10 K.

Cooldown to 10 K occurs in two separate steps. First, a solenoid valve is opened to release high pressure hydrogen at about 10 MPA (1500 psia) from the storage tank. The hydrogen flows through a Joule-Thomson refrigeration loop where it is cooled and partially liquified. The liquid is collected in a wick contained in the cryogen reservoir. The hydrogen vapor is absorbed by a hydride sorbent bed that is capable of absorbing at suitable vapor pressures corresponding to the desired liquification temperature (between 24 and 30 K).

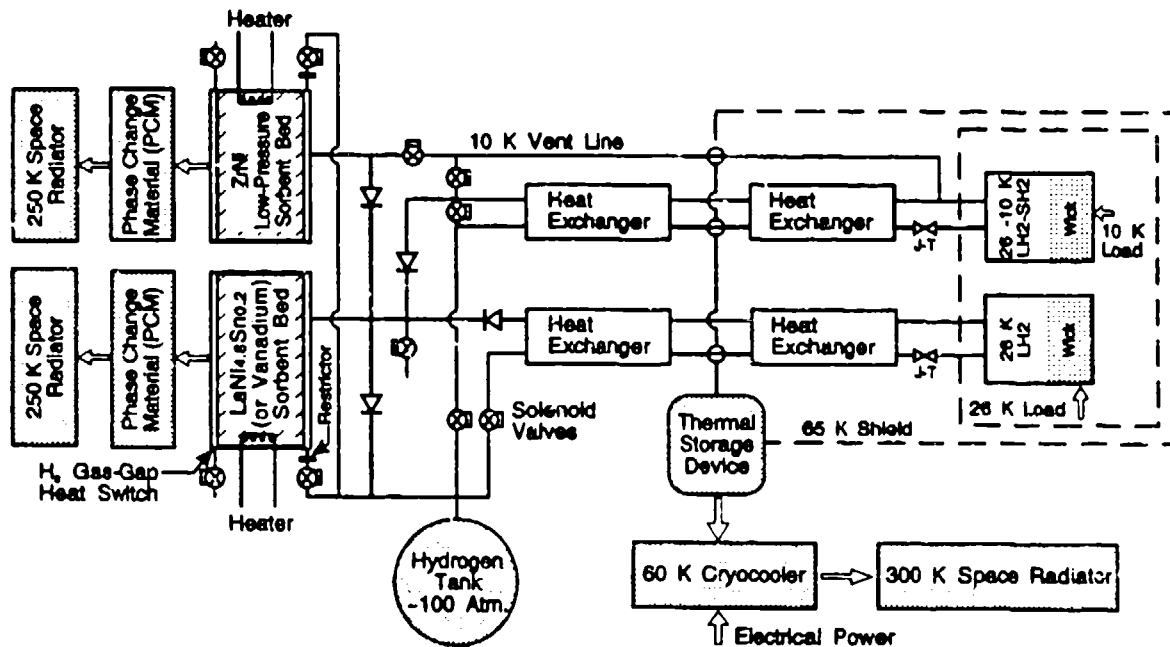


Figure 1. Periodic 10 K sorption cryocooler concept for Brilliant Eyes (based on original concept of A. Johnson and J. Jones [1,2]).

The second cooldown step begins after a sufficient quantity of liquid hydrogen is collected (about 0.5 to 2 g). Then, the J-T flow is stopped by closing the solenoid valve. Next, solid H₂ at ≤ 11 K is produced by vacuum pumping the cold head reservoir to below about 2.6×10^{-4} MPa (2 torr) with a low-pressure sorbent bed. Under simulated infrared sensor heat load and continued vacuum pumping, the solid H₂ sublimates and is adsorbed by the low-pressure sorbent bed while providing cooling below 11 K for the desired period. Then to recharge the system, hydrogen is returned to the storage tank by sequentially heating the sorbent beds.

Various operational scenarios are being considered by BE. Table I summarizes key performance specifications and parameter ranges under consideration. The 10 K cooler system design details will vary somewhat, but the basic technology is adaptable to accommodate the different scenarios. Note also that the BE periodic 10 K cooler shown in Figure 1 also includes a separate ≤ 30 K stage to cool the VLWIR focal plane cavity.

TECHNOLOGY DEVELOPMENT PROGRAM OVERVIEW

Figure 2 presents a technology development road map that shows the evolution from the original periodic sorption cooler concept and the PoP experiments, through BE cooler utilization. Table II presents a summary description of the program elements. Each of the program elements are described in more detail below.

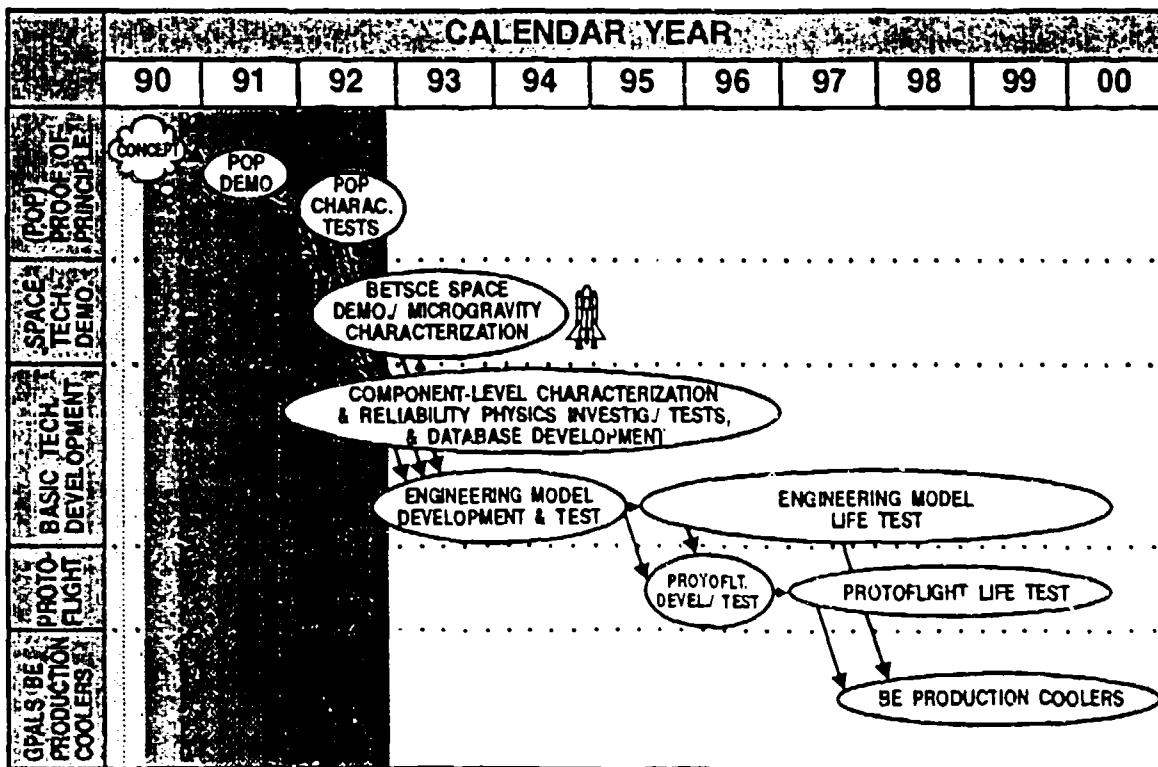


Figure 2. BE 10 K sorption cryocooler technology development program elements.

Table I. Periodic 10 K Sorption Cooler Design Specifications

	Nominal	Study Range		Comments
		Minimum	Maximum	
Detector Temperature	≤ 11	n/a	n/a	
Detector Temperature Stability	+/- 0.1	n/a	n/a	
Detector Power Dissipation	0.100	0.075	0.200	Not including parasitics
Focal Plane Cavity Temperature	40	30	40	Parasitics
Cavity Heat Load	0.5	0.25	1.5	TSD can heat up during operation
Upper Stage Standby Temperature	60-70	60	80	To be calculated
Upper Stage Heat Load	TBD	TBD	TBD	
Cooldown Time To ≤ 11 K From Upper Stage Temp.	≤ 2.0	1.5	3.0	
Cooling Duration During Operation at ≤ 11 K	15	5	30	
Wait Period Between Consecutive Cooldowns	90	5	240	No recharge between cooldowns
Consecutive Cooldowns Before Recharge	3	n/a	n/a	Cooldowns + Operations + Recharge
Total Cycle Time	24	1	48	
Heat Rejection Temperature	250	230	300	
Focal Plane Weight (Beryllium)	600	250	1000	
Power Supply	28 +/- 4	n/a	n/a	
Service Life (Ground Storage)	2	n/a	n/a	
Service Life (Orbital Lifetime)	10	n/a	n/a	
Ground Storage Temperature	250-350	n/a	n/a	
Performance Goals:				
Total Input Power Requirement	≤ 200			
Total Cooler System Weight	≤ 50			
Weight/Power Penalty Factor	0.25			Kilograms per Watt Input Power
Total Vehicle Effective Weight	≤ 100			

Table II. BE 10 K Sorption Cryocooler Technology Development Program Elements

Program Element	Basic Objective
Proof-of-Principle	Demonstrate that ≤ 2 minute cooldown to ≤ 11 K can be achieved & sustained by basic sorption cryocooler concept
BETSCE	Industry spaceflight technology demonstration, and space/microgravity performance characterization & database development
Basic Technology Development	
a) Component-Level Characterization & Reliability Physics Investigations	Component-level testing to provide required design database for BETSCE & engineering model efforts
b) Engineering Model Development	Industry-developed flight-like engineering model targeted to BE performance goals (size, mass & power), interfaces, & constraints; Includes performance characterization testing & life testing
Protoflight	Industry-developed protoflight cooler to be flight qualified; Contains flight-packaged electronics and flight-like interfaces to the BE spacecraft, IR sensor, & upper stage mechanical cooler; Includes performance characterization & life testing
GPALS BE Production Coolers	Industry-developed coolers for integration into BE satellites

Proof-of-Principle (PoP)

The PoP element accomplished a successful ground based experimental demonstration showing that cooldown in under 2 minutes to temperatures ≤ 11 K could be achieved and sustained by J-T refrigeration and the freezing of liquid hydrogen using a low-pressure sorption compressor. Tests conducted with the cold head in an adverse gravity orientation (i.e. upside down) demonstrated no change in liquid retention capability, as the capillary forces in the wick were strong enough to overcome gravitational forces. Thus, the cold head should work in a microgravity environment. This program element provided the foundation for undertaking the subsequent elements. Figures 3 and 4, respectively, show the PoP test apparatus and test data that demonstrated the ability of the cooler to cooldown in under 2 minutes from 79 K and maintain a simulated detector heat load of 150 mW for over 30 minutes [3].

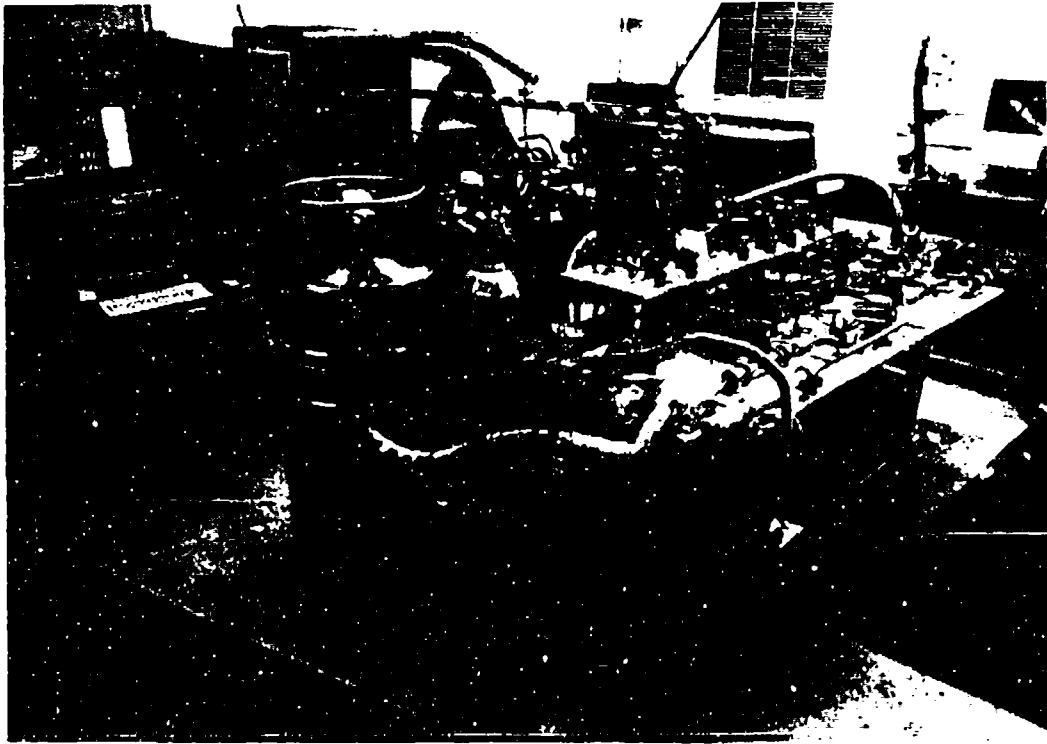


Figure 3. 10 K Proof-of-principle (PoP) apparatus.

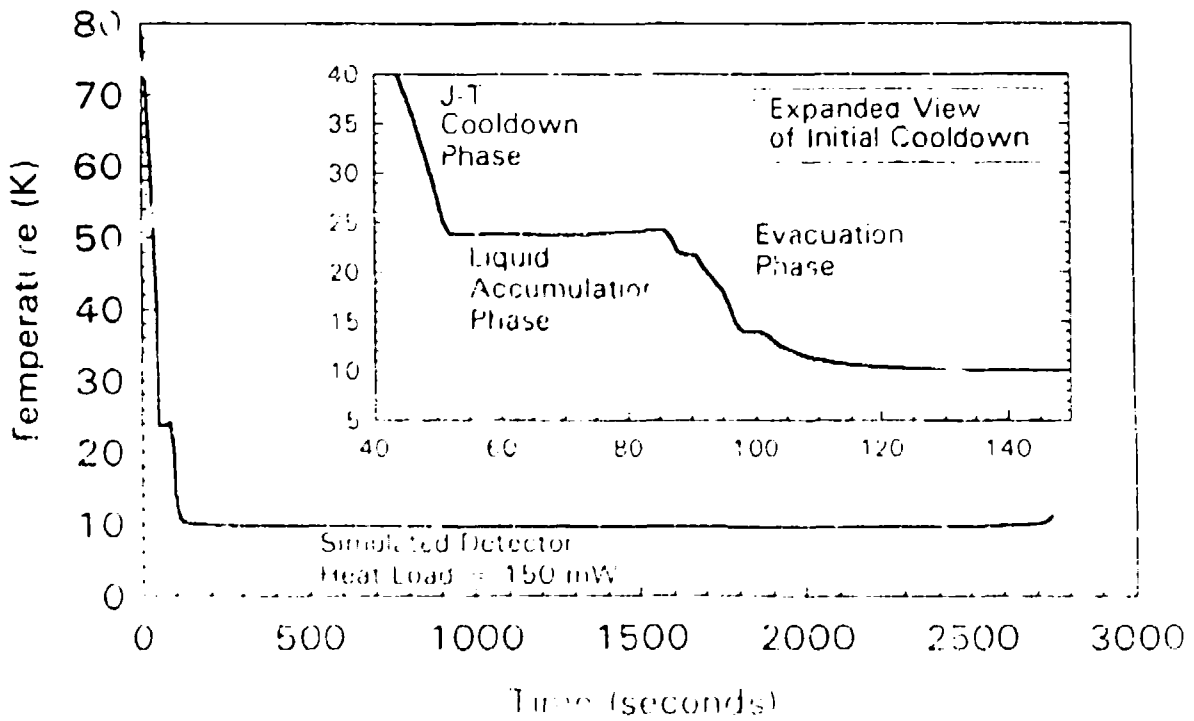


Figure 4. 10 K proof-of-principle experiment.

BETSCE

The Brilliant Eyes Ten-Kelvin Sorption Cryocooler Experiment (BETSCE) is scheduled for launch in 1994 as one element of the Shuttle Pallet Satellite (SPAS III) payload of experiments. BETSCE is a Shuttle side-wall mounted experiment that is focused on: (1) demonstrating sorption cryocooler technology in a microgravity space environment, (2) advancing the enabling technologies and integration techniques by developing an automated, space flightworthy instrument, and (3) characterizing spaceflight performance to develop the needed flight database to aid the future cooler development effort. The BETSCE effort is described in detail in Ref. 4.

10 K Basic Technology Development

The Basic Technology Development effort involves: (1) Comprehensive component-level characterization and reliability physics investigations and tests to develop the needed performance and reliability database, and (2) flight-like engineering model development by industry, targeted to BE cooling requirements, mission constraints, and spacecraft designs and interfaces. The engineering model will undergo comprehensive characterization testing followed by life testing. These program sub-elements are described below.

Component-Level Characterization and Reliability Physics Investigations

This aspect of the 10 K basic technology development activity is directed at providing the basic technology base required to design and manufacture high reliability 10 K sorption cryocooler stages. The investigations provide the database to aid the design efforts for BETSCE, the engineering model and the protoflight cooler development activities. In turn, the design efforts for both BETSCE and the engineering model will help to sharply focus on issues that need to be addressed by the component-level characterization and reliability physics investigations. A key initial focus is on issues associated with the candidate hydride materials, including lanthanum-nickel-tin hydride ($\text{LaNi}_4\text{Sn}_2\text{H}_2$) for the upper sorption stage and zirconium-nickel (ZrNiH_2) hydride for the low-pressure sorption stage. Vanadium hydride (VH_2) is also planned to be studied for the upper sorption stage in the future. Ultra-pure hydrogen gas supply equipment that provides gas containing under 50 parts per billion contaminants, a large capacity (2 m^3) high-purity glove box for limiting contaminants during equipment assembly and hydride handling, and class 1000 laminar flow benches are in place in JPL's sorption cooler development laboratory to support this effort. Specific hydride studies planned and underway include the following:

- Studies are being performed for JPL by T. Flanagan and D. Clewley at the University of Vermont to characterize chemical composition, isotherms, and kinetics. They are also conducting long-term storage tests at various elevated temperatures to determine disproportionation mechanisms. In addition phase purity, lattice parameters and metallurgical composition of various hydride materials are being experimentally determined at JPL and the California Institute of Technology.

- A detailed understanding of manufacturing processes is required to insure that the required hydride purity levels are repeatedly achieved, and batch-to-batch variations need to be controlled in order to produce the large quantity of reliable coolers needed by the BE program. Studies are currently underway to determine the effects of purity, manufacturing techniques, and annealing processes on isotherm plateau slope, hysteresis and equilibrium pressure. Assisting JPL and the University of Vermont is Hydrogen Consultants Inc. (HCI), who is under contract to produce $\text{LaNi}_{4.8}\text{Si}_{110.2}$ hydride. In addition, HCI is producing five other stoichiometries so that the variance in isotherm plateau pressure with tin content can be determined. Also assisting in this effort is Ergenics, Inc., who has provided ZrNi hydride.
- Apparatuses have been constructed and tests are underway to characterize kinetics and absorption capabilities of fast absorption beds containing phase change material (PCM) heat sinks. See Figure 5. Energy Sciences Laboratory Inc. (ESLI) has performed materials compatibility and cycling stability tests for n-hexadecane and n-octadecane PCM materials. In addition, they are constructing prototype copper fin and carbon fiber heat exchange structures for containing PCM's and enhancing their heat transfer.
- Thermal/pressure cycling apparatuses are being constructed and tests are planned to characterize long-term stability and degradation of candidate hydride materials. See Figure 6. These tests accurately duplicate the anticipated BE cooler's time, temperature, hydrogen concentration and pressure profiles throughout the cycle. The tested hydrides are characterized metallurgically and with x-ray diffraction upon delivery. Initial isotherms are taken upon activation and x-ray diffraction studies are then repeated. Later, as hydride material cycling continues, isotherms and x-ray diffraction studies will be conducted on samples periodically. The evolution in the crystallography data gives information about accumulated lattice strain and changes in unit cell size and other properties related to hydride long-term stability.
- Near-term tests are planned to investigate hydride compaction with candidate compressor geometries to understand the potential for inducing stresses in the hydride container when the hydride expands during the absorption process.
- Preliminary hydride migration tests have been conducted by vibrating canisters filled with pre-cycled vanadium hydride contained by sintered filters of various filtration ratings from 0.5 micron to 60 microns. See Figure 7. Post-test microscopic examination indicated that no particles penetrated filters as large as 20 microns. Because the filter rating typically used for hydride compressors is 2 microns, these tests were highly encouraging in providing a preliminary indication that hydride particles will not migrate through containment filters when subjected to launch vibration. Furthermore, because flow through the filter continually reverses throughout the sorption cycle, and no evidence of degradation of any valve or system performance due to sorbent migration has ever been noted in other sorption cryocooler systems [5-7], migration is not considered to be a serious issue. Nevertheless, long-term migration through filters will be studied using the cycling apparatuses described previously.

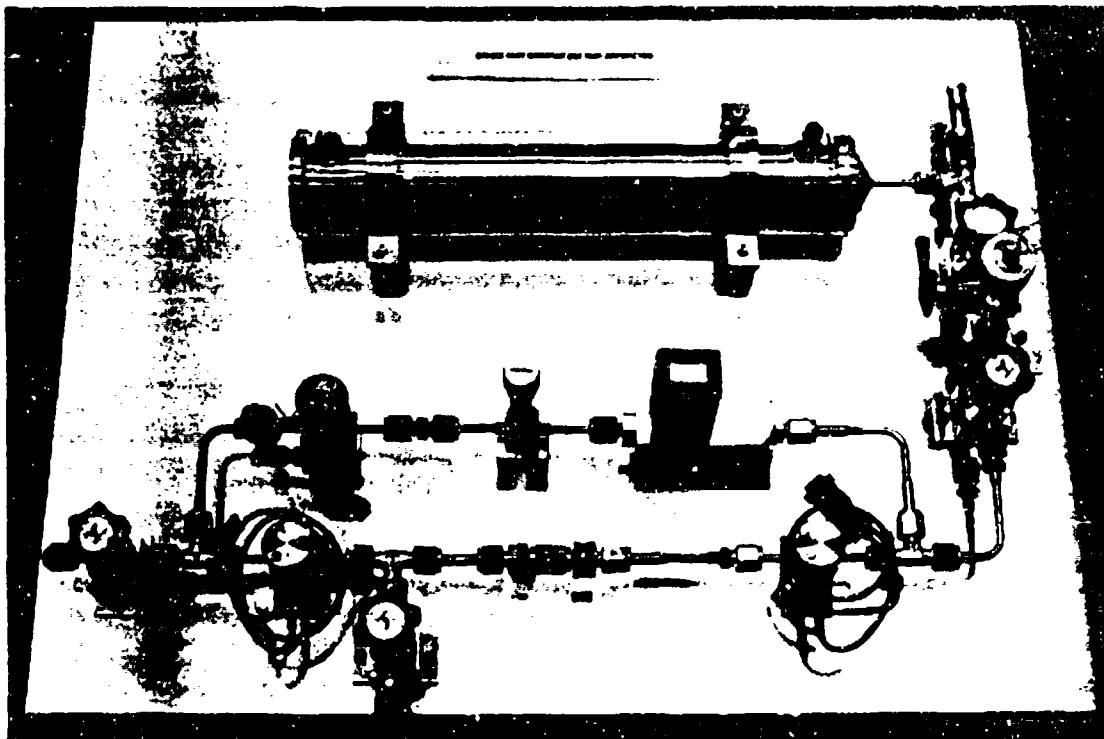


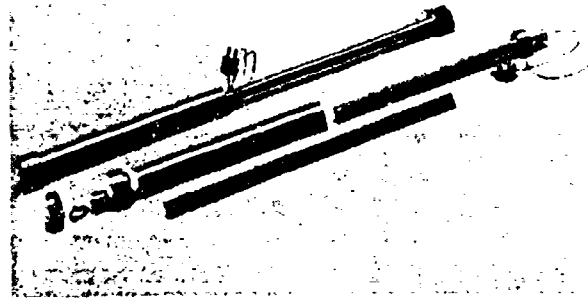
Figure 5. Fast absorber sorbent bed prototype.

- Future studies will be aimed at gaining a detailed understanding of the tolerance of hydride materials to contaminants. Characterization tests will be conducted after precise impurity levels of various species are intentionally introduced. The ability of the hydrides to recover from contamination by prolonged vacuum pumping will also be evaluated. For example, the ZrNi hydride in the PoP system was inadvertently exposed to ambient air due to a valve leak, but recovered its full absorption and kinetic capability after vacuum pumping [3].

In addition to the hydride materials, other issues to be studied include high-strength pressure vessel container materials, electrical heaters, valves, phase change materials, and candidate cryostat TSD materials.

Although 316L stainless steel is highly compatible with hydrogen and is being used in the BETSCE instrument [4], alternative higher-strength materials would provide weight and efficiency advantages for BE. A286 and Incoloy 903 are candidate high-strength hydrogen compatible materials that are planned to be subjected to long-term temperature/ pressure cycling tests with hydrogen, using a similar apparatus to that used previously for Inconel alloy containers designed for oxygen sorption cryocoolers [7].

Long-term electrical heater tests originally conducted for oxygen sorption cryocooler reliability studies are still continuing, after over 10 years of equivalent life has been demonstrated under more severe temperature cycling limits than ever expected for most sorption systems [7]. A set of five heaters has been continuously cycled every 3 minutes

LaNi_{4.4}Sn_{0.2} RELIABILITY TEST CELL

ZrNi RELIABILITY TEST CELL

Figure 6. Long-term stability of hydride materials is being evaluated by hydrogen pressure/temperature cycling tests.

between 21°C and 500°C for over 2 years since June 1990. A similar set of five heaters has been continuously exposed to a constant temperature of 700°C for this same period. All ten heaters are still operational. The major difference for a hydride compressor heater is that the inconel sheath in the present test heaters would be replaced by a hydrogen compatible material such as 316L, A286 or Incoloy 903.

A valve seat decompression experiment has been conducted to evaluate the effect of fast decompression of candidate valve seat materials. Preliminary results indicate that this should not be a problem under the 10 K sorption cooler design conditions. However, tests are to be conducted with actual candidate valves. Valve reliability tests under long-term cycling and hydrogen exposure also are to be conducted.

Candidate phase change materials (PCM's) for the sorbent beds include the family of normal paraffins. The precise PCM selected depends on system design parameters such as heat rejection temperature. Long-term stability, degradation due to contamination, and materials compatibility issues are to be studied in detail to insure 10 year life.

The baseline TSD material is aluminum, which has a specific heat of 212.2 J/kg-K at 60 K. Other candidate materials with high specific heats include sodium, lithium, and magnesium. Use of these materials may result in an overall system mass savings because they have lower low-temperature specific heats than aluminum. However, some of these materials may be more complex to utilize in the cryostat because they may need to be contained. If system-level trade-offs indicate the potential advantages of alternate TSD materials, the materials will be characterized and any long-term degradation issues will be investigated experimentally.

A computer model has been developed as a system design tool [8]. This model incorporates J-T thermodynamics, transient cooldown effects, evaporative cooling and freezing processes, sorption bed characteristics, and transient sorbent heating/ desorption processes. By

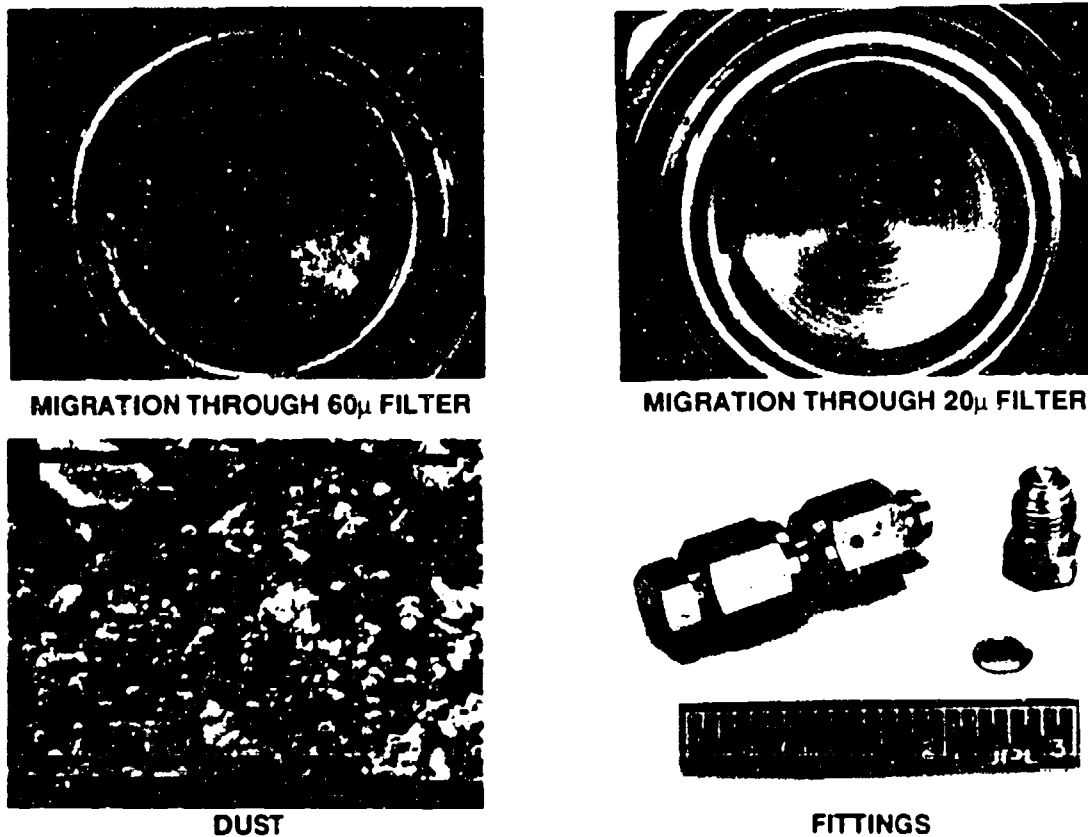


Figure 7. Hydride filter migration test. No evidence of vibration-induced particle migration was evident with microscopic examination of ≤ 20 micron filters.

inputting desired performance characteristics such as cooldown time, cooling duration, cold head heat load, and known parameters such as heat sink temperatures and detector assembly mass, the model outputs the required characteristics of key components such as sorbent bed sizes, thermal storage device mass, mechanical cooler cooling load, and radiator sizes. Varying key parameters such as storage bottle size and pressure enables system optimization studies to be performed. This model was an invaluable design tool used for developing the BETSCE instrument [4]. As the database evolves from the component-level characterization and reliability physics tests, this model will be updated.

A system performance simulation model is also being developed to enable transient performance predictions. This model will also be updated as the experimental database evolves

Engineering Model Development

To provide the necessary precursor to eventual flight BE coolers, a flight-like engineering model is scheduled to be contracted to industry in early 1993. The engineering model will be targeted directly to the BE cooling requirements, mission constraints, satellite design,

interfaces. The engineering model effort will include design trade-off studies that will examine the entire study range shown in Table I. The selected design performance range will be a result of negotiation between the BE system developers and the 10 K cooler development team. Close cooperation between the BE system developers and the 10 K cooler development team is needed to insure that the engineering model design is faithful to BE needs. Following comprehensive performance characterization testing, the engineering model will undergo continuous life testing.

Protoflight Cryocooler Development

The protoflight cooler development follows directly from the engineering model. The protoflight cooler will contain flight-packaged electronics and flight-like interfaces to the 60 K mechanical cooler upper stage, the 10 K sensor, and the BE spacecraft. The protoflight cooler will undergo characterization testing, flight qualification testing and life testing. Although engineering model characterization and life test data will enable refinement and validation of analytical models leading to some limited additional optimization of the protoflight cooler design, the basic protoflight cooler design is expected to be very similar to the engineering model. Thus it is crucial that an acceptable and stable set of performance specification ranges and interface guidelines be defined early based on negotiations between the BE system developers and the 10 K cooler development team.

BE Production Cryocoolers

The final program element involves production of flight cryocooler units for integration into the BE satellites. Note that at least 17 months and 34 months of life test data are expected to be obtained on the protoflight and engineering model coolers, respectively, by the start of production cooler manufacture in early 1998.

SUMMARY

A comprehensive technology development program is well underway to mitigate the risks of utilizing 10 K sorption cooler technology in future periodic 10 K cooling applications such as BE. Program elements include component-level investigations and tests, flight-like engineering model and protoflight cooler development and life test, and an early spaceflight technology demonstration of the critical technologies (BETSCE). The technology developed under this program provides an ideal method to produce periodic operation down to 10 K of cryogenic infrared sensors for future astronomy, earth-observing and surveillance satellites.

ACKNOWLEDGEMENTS

The work described in this paper was carried out by the Jet Propulsion Laboratory (JPL), California Institute of Technology under contract with the National Aeronautics and Space Administration. The work was sponsored by the Brilliant Eyes program office, Strategic Defense Initiative Organization (SDIO), USAF Space and Missiles Systems Center (SMC). The authors wish to thank the entire 10 K cooler development team for their invaluable

contributions to this effort. The technical advice and guidance provided by Dr. Robert Bowman of Aerojet Electronic Systems in the hydride characterization effort, and editing of the manuscript by Dr. Donald Rapp of JPL is greatly appreciated.

REFERENCES

1. Johnson, A. L. and Jones, J. A., "Periodic 10 K Sorption Cooling," USA Patent Pending, 1992.
2. Johnson, A. L. and Jones, J. A., "Evolution of the 10 K Periodic Sorption Refrigerator Concept," 7th International Cryocoolers Conference, Santa Fe, NM, November 17-19, 1992.
3. Wu, J.-J., Bard, S., and Longworth, R., "10 K Sorption Cryocooler Proof-of-Principle Experiment," in preparation, 1993.
4. Bard, S., Cowgill, P., Wu, J.J., Rodriguez, J., Wade, L., Gehrlein, M., and Von Der Ohe, W., "10 K Sorption Cryocooler Flight Experiment (BETSCE)," 7th International Cryocoolers Conference, Santa Fe, NM, November 17-19, 1992.
5. Jones, J. A. and Golben, P. M., "Design, Life Testing and Future Designs of Cryogenic Sorption Refrigeration Systems," Cryogenics, Vol. 25, April 1985.
6. Karperos, K., "Operating Characteristics of a Hydrogen Sorption Refrigerator Part I: Experimental Design and Results," Proc. Fourth International Cryocoolers Conference, Easton, MD, September 25-26, 1986.
7. Mon, G., Wen, L. C., Wu, J. J., Bard, S., and Garnica, A., "Reliability and Life of Sorbent Materials for Sorption Cryocoolers," Proc. 6th International Cryocoolers Conference, DTRC-91/002, January 1991.
8. Rodriguez, J., Wu, J.-J., Wade, L. and Bard, S., "System Design Model for a Periodic 10 K Sorption Cryocooler," in preparation, 1993.

EVALUATION OF A PROTOTYPE HYDRIDE COMPRESSOR
FOR PERIODIC HYDROGEN SORPTION CRYOCOOLERS

R. C. BOWMAN, JR., B. D. FREEMAN, AND D. LABOR
AEROJET ELECTRONIC SYSTEMS DIVISION
AZUSA, CA 91702

F. E. LYNCH AND R. W. MARMARO
HYDROGEN CONSULTANTS INC.
LITTLETON, CO 80125

L. A. WADE
JET PROPULSION LABORATORY
CALIFORNIA INSTITUTE OF TECHNOLOGY
PASADENA, CA 91109

ABSTRACT

A metal hydride sorbent bed, which promotes rapid hydrogen distribution along with efficient heat transfer, has been fabricated and tested. The compressor consists of six reaction tubes containing a total of 1.4 Kg of the alloy $\text{LaNi}_{4.27}\text{Sn}_{0.24}$ to give storage and compression of hydrogen. The measured reversible capacity of this bed exceeds 15.5 gms of H_2 when the bed is cycled between room temperature and 200°C. Thermocouples imbedded within the hydride powder of each reaction tube detected rapid, large temperature rises as the bed absorbed hydrogen. Measurements of these temperatures along with the hydrogen pressure changes have been analyzed to assess the reaction properties of the sorbent alloy and the bed design. This sorbent bed validated the analytic models used to design a very high performance sorption compressor for the Brilliant Eyes Ten-Kelvin Sorption Cryocooler Experiment (BETSCE) project. The measured properties for this bed also relate to the performance that can be achieved when similar hydride compressors are used in fast cool-down cryocoolers to produce liquid hydrogen for either a 25K cooler or as the first stage in a 10K solid hydrogen cooler.

INTRODUCTION

The production of liquid hydrogen via Joule-Thomson (JT) expansion valves connected to metal hydride compressors has been demonstrated [1-3]. Jones [4] has described a hydride sorption refrigeration system that could achieve 10K operating temperatures through the solidification and sublimation of liquid hydrogen. Recent experiments [5] conducted at the Jet Propulsion Laboratory (JPL) have confirmed that temperatures down to 9.2K can be reached with an appropriate combination of a metal hydride sorbent and reactor bed design. Johnson and Jones [6] have developed concepts for 10K periodic sorption refrigerators that utilized separate hydride sorbent beds staged to produce liquid hydrogen ($T < 30\text{K}$) and then pump on the accumulated liquid to form solid hydrogen ($T \approx 10\text{K}$). Due to the very different absorption pressure requirements of 1-10 atm for liquid hydrogen and 0.002 atm for solid hydrogen, a minimum of two metal hydride sorbents are staged for practical closed-cycle operation of these proposed cryocoolers.

The proof-of-principle demonstration of solid hydrogen below 10K was done at JPL [5] using a ZrNi hydride bed to pump on a 24K liquid H_2 reservoir. The present breadboard compressor was used to demonstrate that the reaction kinetics and hydrogen capacity of $\text{LaNi}_{4.8}\text{Sn}_{0.2}$ are sufficient to permit rapid formation of liquid H_2 . To achieve periodic cooldowns [6] of 2 minutes or less, the design and construction of the sorbent bed must provide high hydrogen mass flow rates within the metal hydride powder bed as well as efficient dissipation of the heat produced by the hydrogen absorption process. The present paper describes a prototype reactor bed containing the alloy $\text{LaNi}_{4.27}\text{Sn}_{0.24}$ as the sorbent material and reports results obtained during laboratory tests.

Although the first hydride refrigerators [1, 2] incorporated LaNi_5 as the sorbent, this metal-hydrogen system is highly prone towards extensive degradation during thermal cycling [7]. However, very recent work [8] has shown that partial substitution of tin (Sn) for nickel produces an alloy that is extremely resistant to changes in either its reversible hydrogen storage capacity or absorption/desorption isotherms. Consequently, the $\text{LaNi}_{5-y}\text{Sn}_y$ alloy is an excellent candidate for long life refrigerator compressors.

DESCRIPTION OF HYDRIDE COMPRESSOR

A breadboard hydride compressor bed configured for enhanced hydrogen flow and heat transfer during the hydrogen absorption and desorption processes was fabricated at Hydrogen Consultants, Inc. Schematic illustrations of this unit are given in Fig. 1. The compressor consists of six tubes connected through a common plate manifold to a single exit line and valve. Each tube is divided into fifteen sections by aluminum filter supports as shown at the bottom of Fig. 1. A stainless steel sheathed type K (chromel-alumel) thermocouple penetrates each tube through the endcap next to the gas-connection and passes axially through seven filter tube supports to the center of the eighth segment of alloy powder. The thermocouples are located radially opposite from the porous filter tubes such that approximately equal amounts of hydride surround them. The orientations of the thermocouples are shown in the center of Fig. 1 and were silver soldered into the endcaps at the indicated positions. All other joints and connections for this compressor were made by welding.

The compressor was loaded with a $\text{LaNi}_{4.27}\text{Sn}_{0.24}$ alloy that had been annealed under argon for 90 hours at 950°C in chunks and subsequently ball milled into a coarse powder. The total amount of $\text{LaNi}_{4.27}\text{Sn}_{0.24}$ alloy loaded into the 6-tube compressor was 1440 grams. Using the 25°C absorption/desorption isotherms measured for this alloy and shown in Fig. 2., the minimum reversible hydrogen storage capacity was predicted to exceed 15.0 grams. Initial activation consisted of a vacuum bakeout at 482°C until outgassing was negligible. After the unit was cooled to room temperature and helium leak checked with rate below 3×10^{-9} scc/s, it was exposed to ultrapure hydrogen which was readily absorbed.

An overview diagram of the system assembled at Aerojet to activate, charge, and test metal hydride sorbent beds is shown in Figure 3. The hydrogen manifold and reference volumes were constructed entirely of electropolished 316L stainless steel. All connections and joints utilize metal-to-metal face seals of either the VCR or Conflat type. Furthermore, high-quality diaphragm or bellows valves were used throughout the system. Pressure transducers and all system volumes were carefully calibrated prior to start of experiments on the $\text{LaNi}_{4.27}\text{Sn}_{0.24}$ compressor. A Mac/Quadra computer provided data acquisition and processing. System operation and data monitoring was via a Labview 2.2 software package from National Instruments.

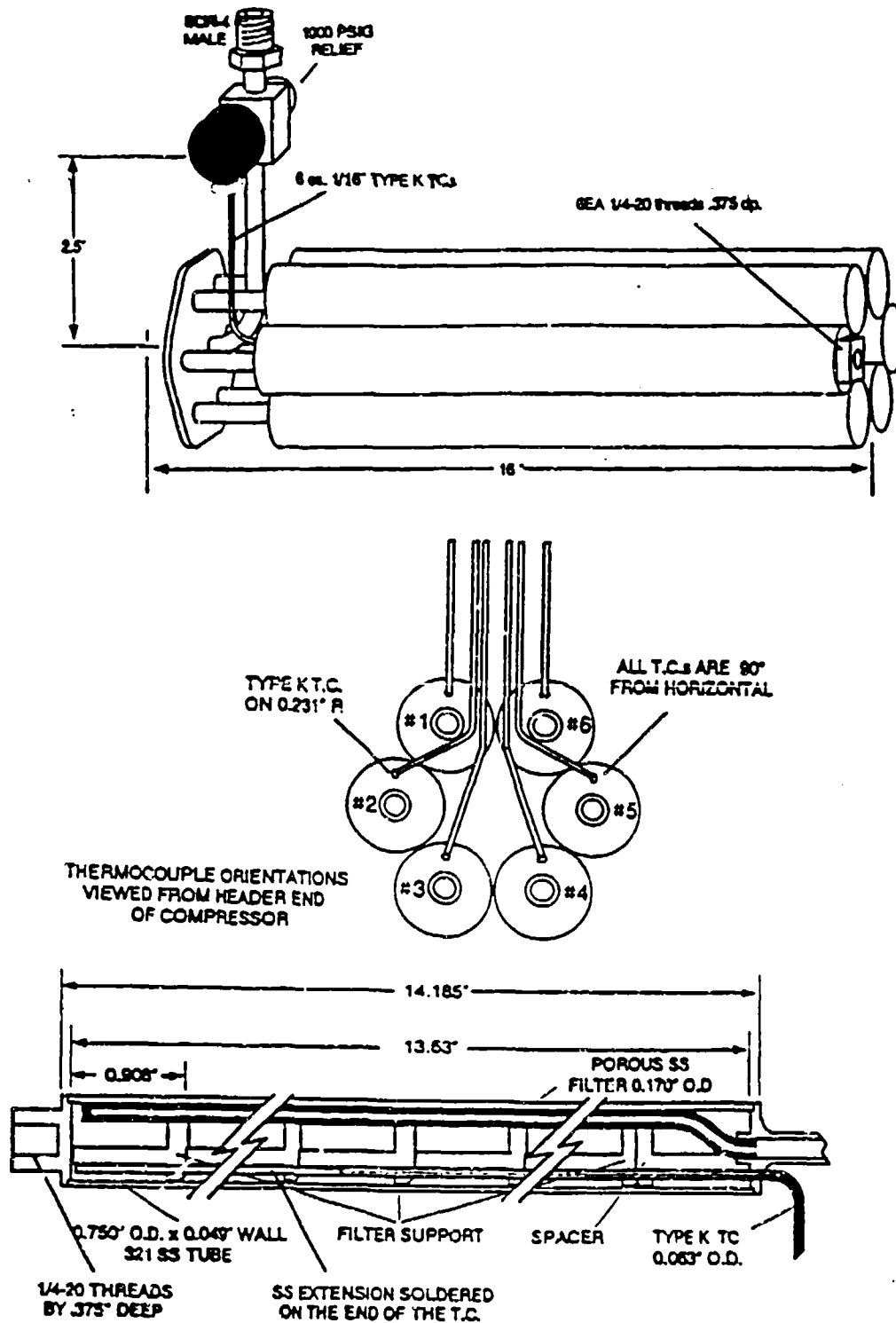


Fig. 1. Schematic diagrams of prototype hydride compressor consisting of six tubes each filled with $\text{LaNi}_{4.27}\text{Sn}_{0.24}$ powder and separated into 15 segments having a sheathed grounded-junction chromel-alumel thermocouple (TC) in the center of the eight segment. All dimensions are given in inches.

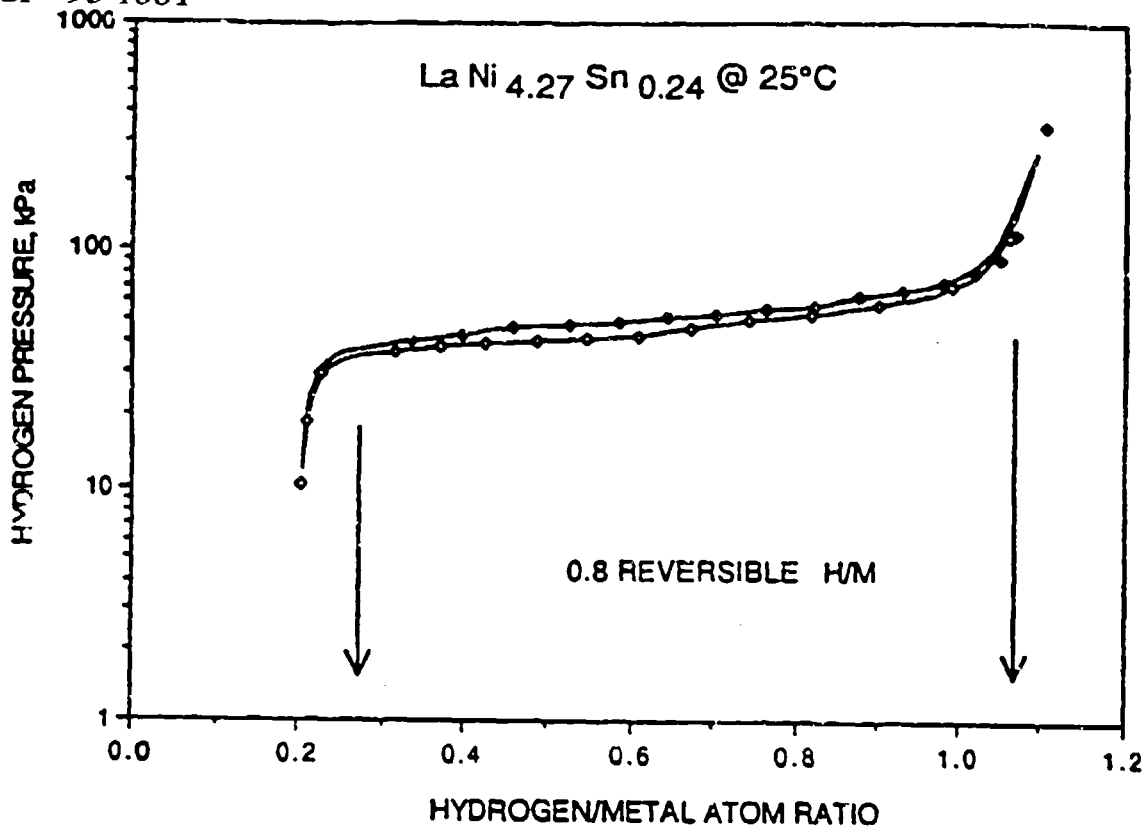


Fig. 2. Hydrogen absorption and desorption isotherms for $\text{LaNi}_{4.27}\text{Sn}_{0.24}$ measured at 25°C. The alloy had been annealed at 950°C for 90 hours before ballmilling into a powder.

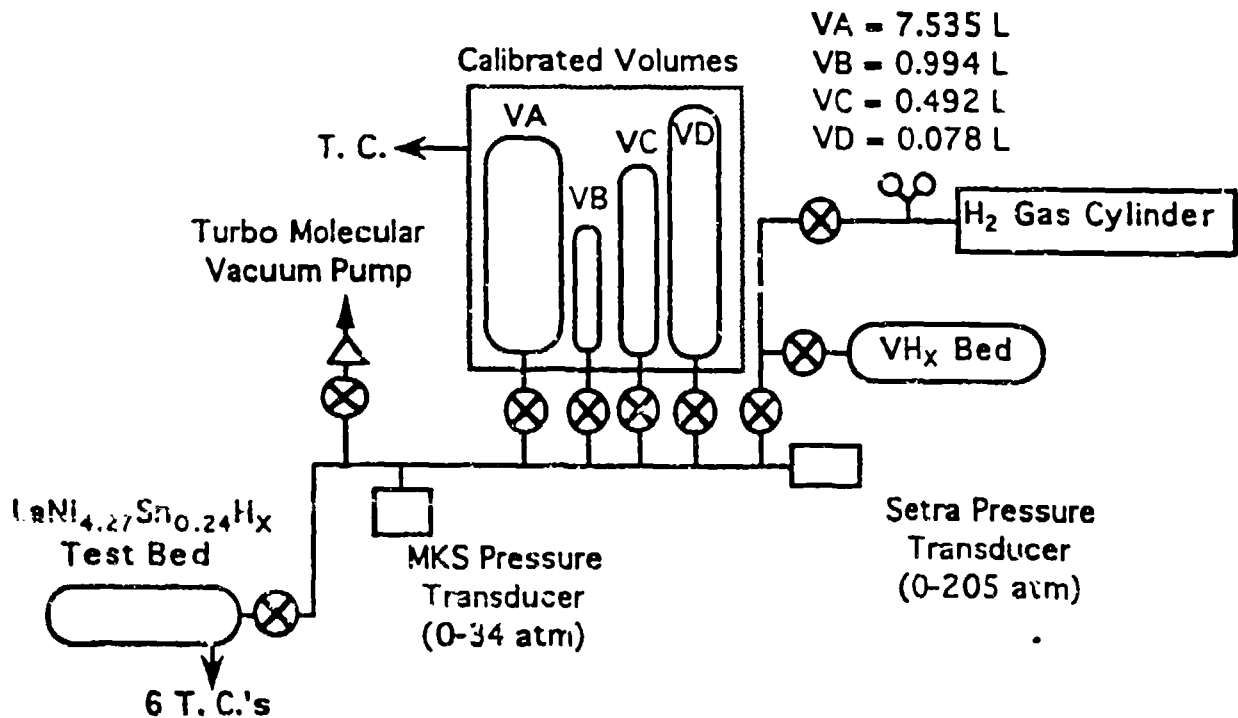


Fig. 3. Schematic Diagram of the test station used to evaluate the $\text{LaNi}_{4.27}\text{Sn}_{0.24}$ compressor bed during hydrogen absorption and desorption experiments.

RESULTS AND DISCUSSION

The breadboard $\text{LaNi}_{4.27}\text{Sn}_{0.24}\text{H}_x$ compressor shown schematically in Figure 1 was fabricated, initially activated, and charged with approximately 17.5 grams of hydrogen at Hydrogen Consultants Inc. Upon arrival at Aerojet, the compressor was attached to the hydrogen analysis station as shown in Figure 3. After hydrogen was pumped out of the compressor through the turbomolecular pump, it was heated for several hours at 200°C until vacuum at the pump was about 5×10^{-5} torr and measurements with a residual gas analyzer indicated removal of impurity species. Volumetric measurements with ultrapure helium gas was used to determine that the free internal volume of the $\text{LaNi}_{4.27}\text{Sn}_{0.24}$ filled compressor was 0.258 liters. After a second heating to 200°C under dynamic vacuum of the turbomolecular pump and cooling back to room temperature, the compressor immediately absorbed hydrogen. Thermocouple TC#3 (see Figure 1) behaved erratically during these initial tests, which indicated damage, and has been disregarded for all remaining work. All other thermocouples behaved normally. Starting with initial H_2 pressure of 33.6 atm, the reactor absorbed 19.19 gms of hydrogen, which corresponds to the composition $\text{LaNi}_{4.27}\text{Sn}_{0.24}\text{H}_{5.53}$. When it was heated to 200°C with the valves open to all the reference volumes, the compressor desorbed 15.5 gms of hydrogen at a final pressure of 29 atm, which is taken as the reversible storage capacity.

The first series of tests on the $\text{LaNi}_{4.27}\text{Sn}_{0.24}\text{H}_x$ compressor were conducted with the bed in static air. Representative internal bed temperature and pressure data from one of these tests is presented in Figure 4. As is most clearly shown in Figure 4b, the alloy rapidly absorbs hydrogen to produce a composition of $\text{LaNi}_{4.27}\text{Sn}_{0.24}\text{H}_{2.47}$ within 7.5 sec after opening the valve to the compressor. However, the temperature inside the bed rises to nearly 130°C in this time interval and complete absorption to $x=5.29$ requires over three hours as the hydride powder slowly cools back towards room temperature. This experiment illustrates the critical importance of dissipating the heat of reaction if rapid and complete absorption is to be achieved.

A second set of absorption experiments were performed with the $\text{LaNi}_{4.27}\text{Sn}_{0.24}\text{H}_x$ compressor completely immersed under water in a controlled circulating bath at various temperatures between 5°C and 45°C . A typical test for hydrogen absorption at 20°C bath temperature is summarized in Figure 5. A peak temperature of 128°C was reached within the

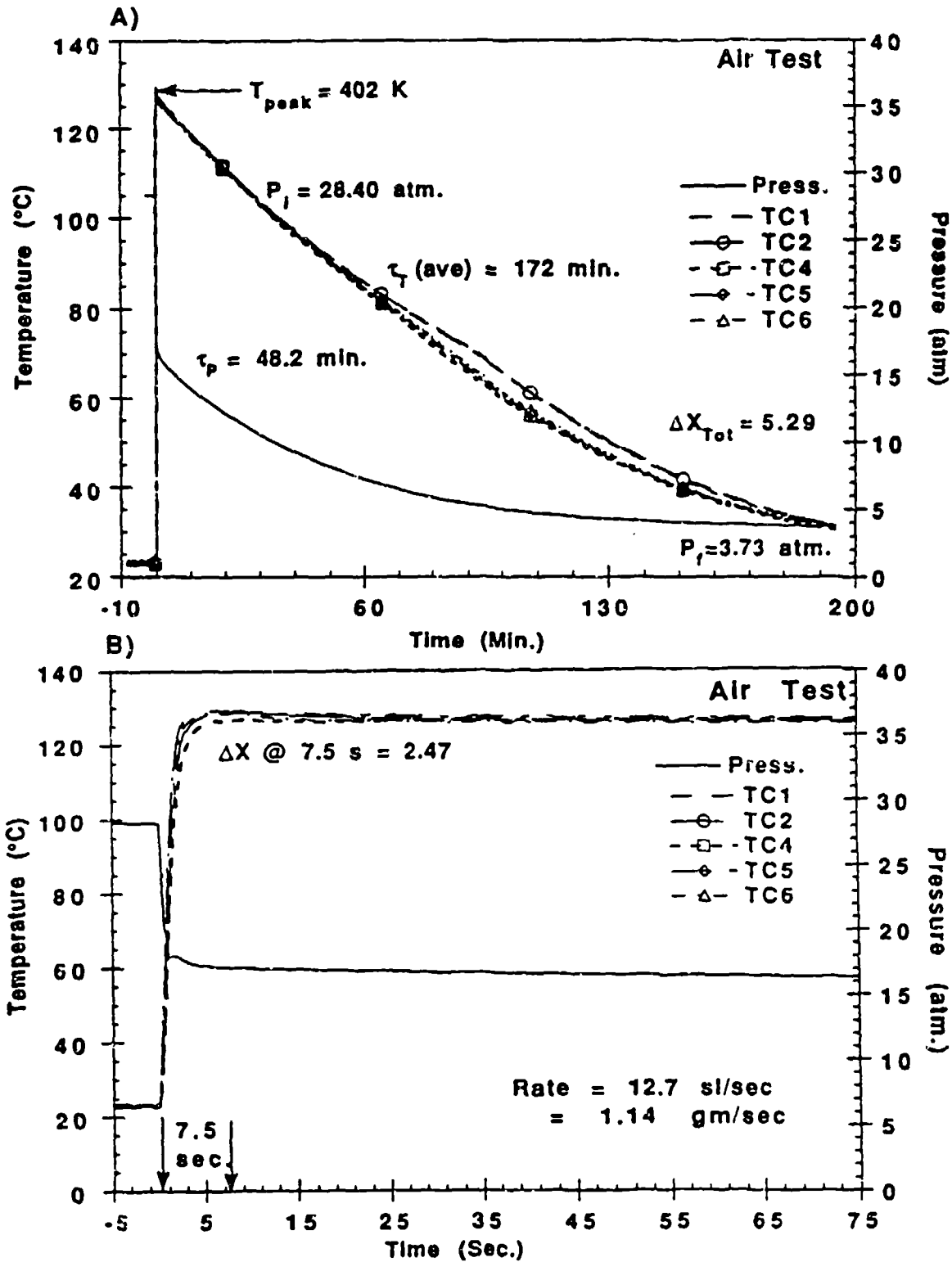


Fig. 4. (a) Representative test results obtained when the $\text{LaNi}_{4.27}\text{Sn}_{0.24}\text{H}_x$ compressor was in ambient air during hydrogen absorption. The thermocouples (TC) are located in the powder beds as indicated in Fig. 1. (b) Expanded scale plots of the initial reaction parameters.

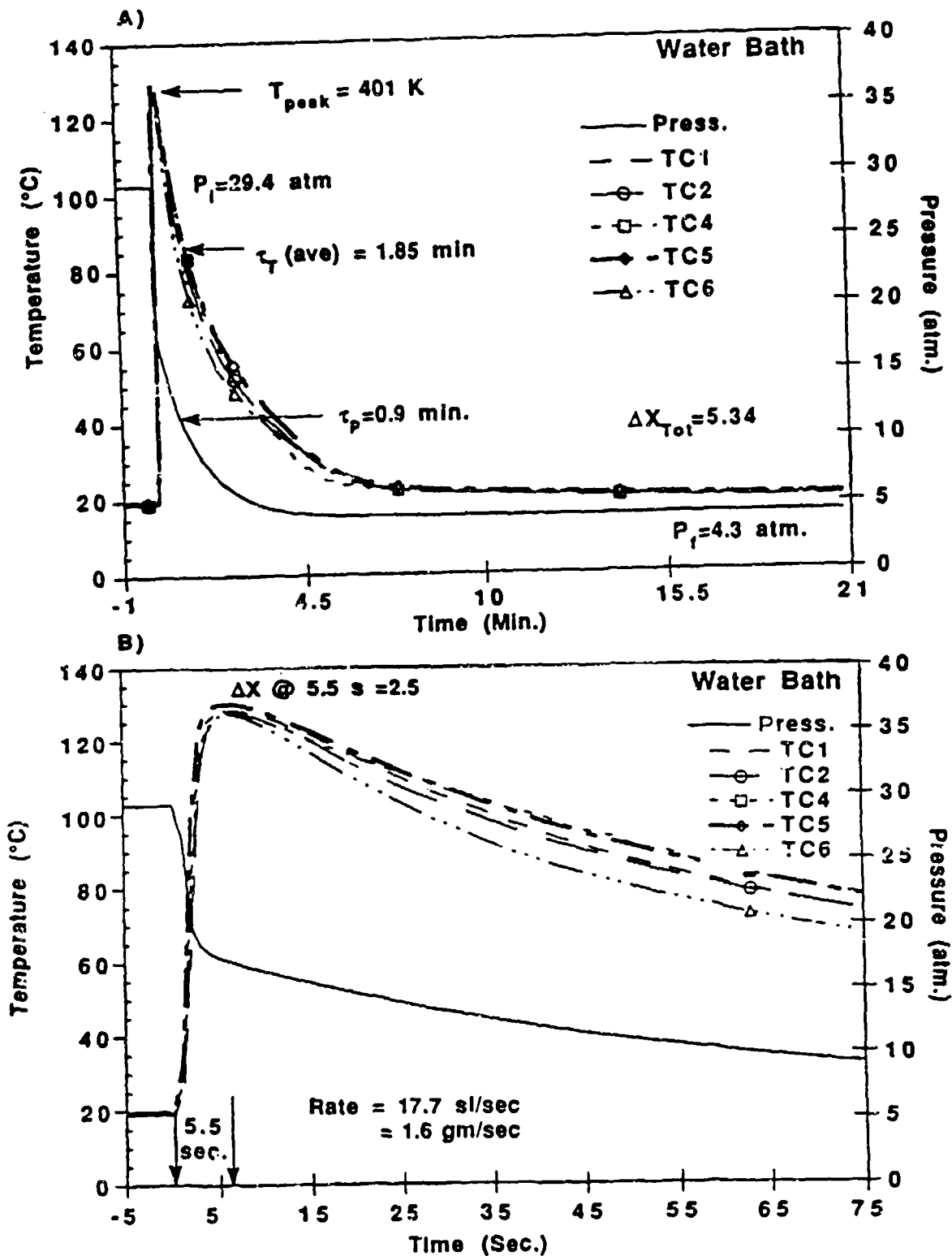


Fig. 5. (a) Representative data obtained during hydrogen absorption when the $\text{LaNi}_{4.27}\text{Sn}_{0.24}\text{H}_x$ compressor was contained in water bath that was regulated at 20°C . The temperatures were measured in the centers of the tubes by thermocouples (TC). (b) Expanded scale plots of initial reaction parameters.

bed about 5 sec after admitting hydrogen. Absorption was essentially complete in 10 min. The time constants of the thermocouples (for a $1/e$ decay from the peak temperature) in Figure 5a are almost 100 times shorter than the parameters shown in Figure 4a. The much larger thermal capacity of the water bath as compared to ambient air is primarily responsible for the more efficient removal of the heat of reaction from the hydride bed during absorption. Of course, circulation of water around the tubes also greatly enhances thermal transfer across the tubewall to give faster cooling rates. These results confirm that $\text{LaNi}_{5-y}\text{Sn}_y$ alloys are viable candidate hydrogen sorbents for rapid-cooldown periodic cryocoolers [6].

The influences of the water bath temperatures and initial hydrogen pressure on the measured pressure and thermocouple time constants are summarized in Figures 6 and 7, respectively. Increasing the bath temperature slows hydrogen absorption (i.e., lengthens the time constants in Figure 6) due to a reduced driving force as the equilibrium plateau pressure [8] rises with temperature. Figure 7 shows the expected behavior of slightly faster hydrogen absorption rates when the initial pressure is increased. While raising the bath temperature leads to a decrease in the quantity of hydrogen absorbed (as shown in Figure 6), a greater initial hydrogen pressure provides more hydrogen for reaction in the fixed volume test station to produce the larger hydrogen absorption indicated in Figure 7.

Figure 8 shows a portion of an experiment that was used to calculate the effective bed conductivity (K_{eff}) from the indicated internal temperatures of the $\text{LaNi}_{4.27}\text{Sn}_{0.24}$ bed and the exterior bath temperature. The bath temperature was monitored by a thermocouple in contact with the exterior wall of the compressor, which is assumed to represent the exterior wall temperature of the compressor during the test. From test data, we analyzed two distinct regions. The first was the initial burst reaction due to the high initial pressure in the manifold volumes. During this initial fast reaction the bed would heat up to some maximum temperature for a short time and then start to cool. As indicated in Figure 8 the bed and bath isothermal regions (near the maximum temperature) are noted in Figure 8. When the compressor bed started to cool, it was isolated from the manifold volumes as the temperature and pressure within the bed was monitored. In Figure 8 this corresponds to the time after the valve was closed (i.e., time > 8.6 sec.).

During the time when both the bath (or compressor wall) and the $\text{LaNi}_{4.27}\text{Sn}_{0.24}$ powder are isothermal can be assumed the bed approximates thermal steady state

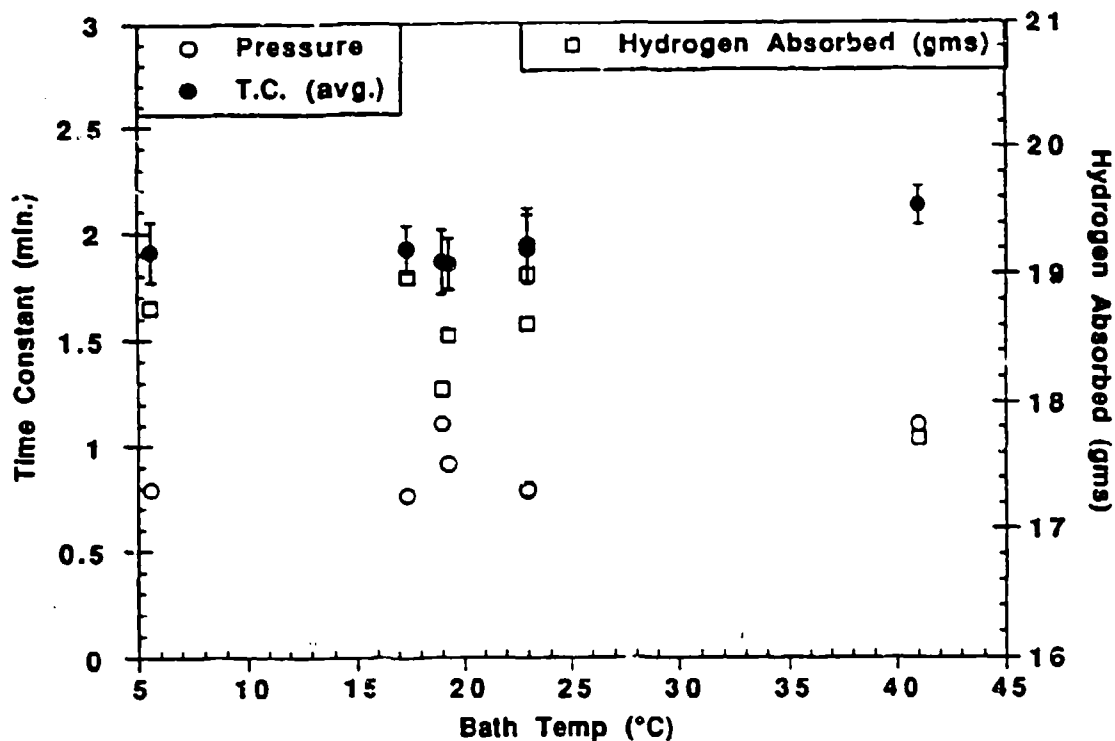


Fig. 6. Empirical time constants for average bed temperature (T.C.) and pressure changes during hydrogen absorption when the compressor was in water bath and regulated at different temperatures. The total quantity of hydrogen absorbed is also shown.

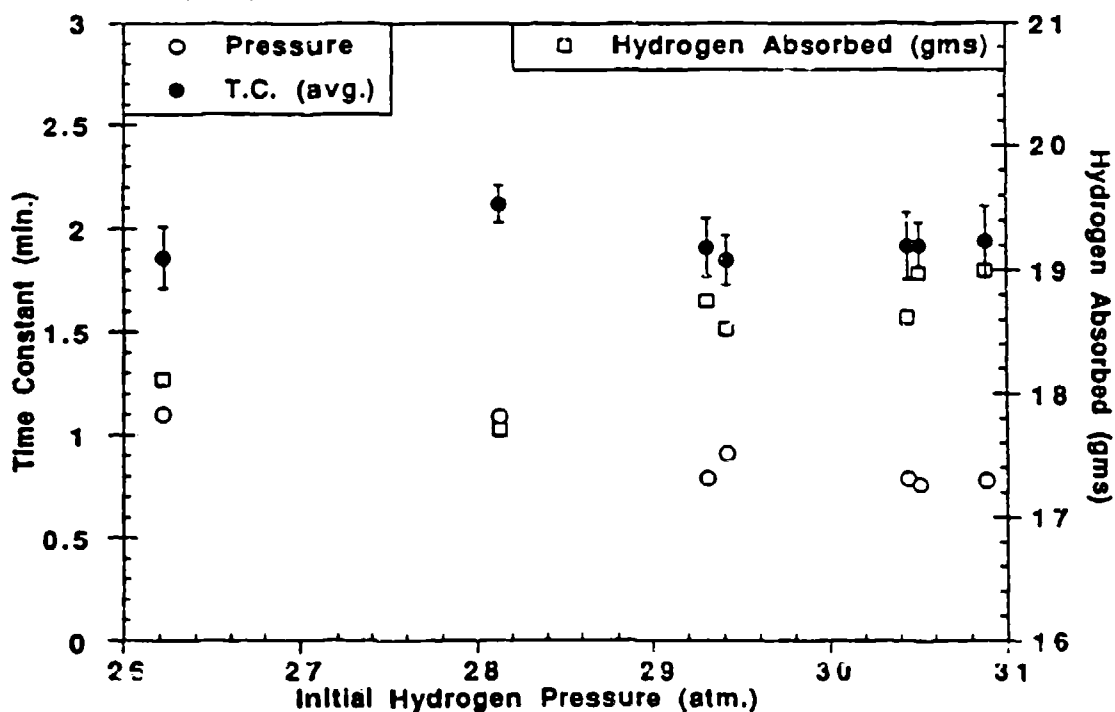


Fig. 7. Effect of initial H₂ pressure on total hydrogen absorbed by LaNi_{4.27}Sn_{0.24} compressor and the time constants for average bed temperature (T.C.) and hydrogen absorbed when compressor was in water bath during the experiments.

conditions. Under these conditions the energy generated from the absorption reaction will be equal to the energy conducted to the water bath via thermal conduction which can be written as [9].

$$UA\Delta T = Q = m_{H_2}\Delta H_{abs} \quad (1)$$

Where A is the area of the wall normal to the heat flow at rate Q, ΔT is temperature difference between the bed and bath, U is overall heat transfer coefficient calculated from

$$UA = 1/\Sigma R_t \quad (2)$$

using R_t for the individual thermal resistances of the system, m_{H_2} is the mass of $LaNi_{4.27}Sn_{0.24}H_x$ hydrogen absorbed per second, and ΔH_{abs} is the heat of absorption [8] assumed for $LaNi_{4.27}Sn_{0.24}H_x$.

In Figure 8 it can be seen that the compressor was nearly isothermal at 120°C for 6.25 seconds, with the bath/wall being isothermal for the last four seconds. During that 4.0 seconds, 0.56 grams of hydrogen were absorbed by the bed while releasing 2.26 kWatts of energy. The resulting heat generated is conducted from the hydride bed radially through the tube and into the water bath. For a cylinder, the thermal resistance for radial conduction is given by the equation [9]

$$R_{t,cond} = \ln(r_2/r_1)/2\pi L K_{eff} \quad (3)$$

where the radii used for the inside (r_1) and outside (r_2) of the external tube wall are 0.326" and 0.375", respectively, and tube length L is taken from Figure 1. The inside radius used for the hydride powder was the radius of the average mass point which coincided with the placement of the thermocouples. When equations 2 and 3 are substituted into equation (1), the effective thermal conductivity K_{eff} can be obtained.

For the temperature differences shown in Figure 8, this analysis yielded an effective bed conductivity of 1.0 ± 0.1 W/mK. This value lies within the range of 0.5-1.8 W/mK found by others [10] for hydride powders in reactor vessels that do not enhance hydride powder thermal conduction. When additional analyses were performed on other independent absorption experiments with the $LaNi_{4.27}Sn_{0.24}$ bed, the derived K_{eff} values were between 0.8 ± 0.05 W/mK and 1.5 ± 0.1 W/mK. These variations can arise from failure of the bed to meet the steady state assumptions [9] as well as nonideal component geometry and insufficient monitoring of the tube wall and bath temperatures. Consequently, the present experiments give $K_{eff} = 1.1 \pm 0.4$ W/mK for $LaNi_{4.27}Sn_{0.24}H_x$ powder.

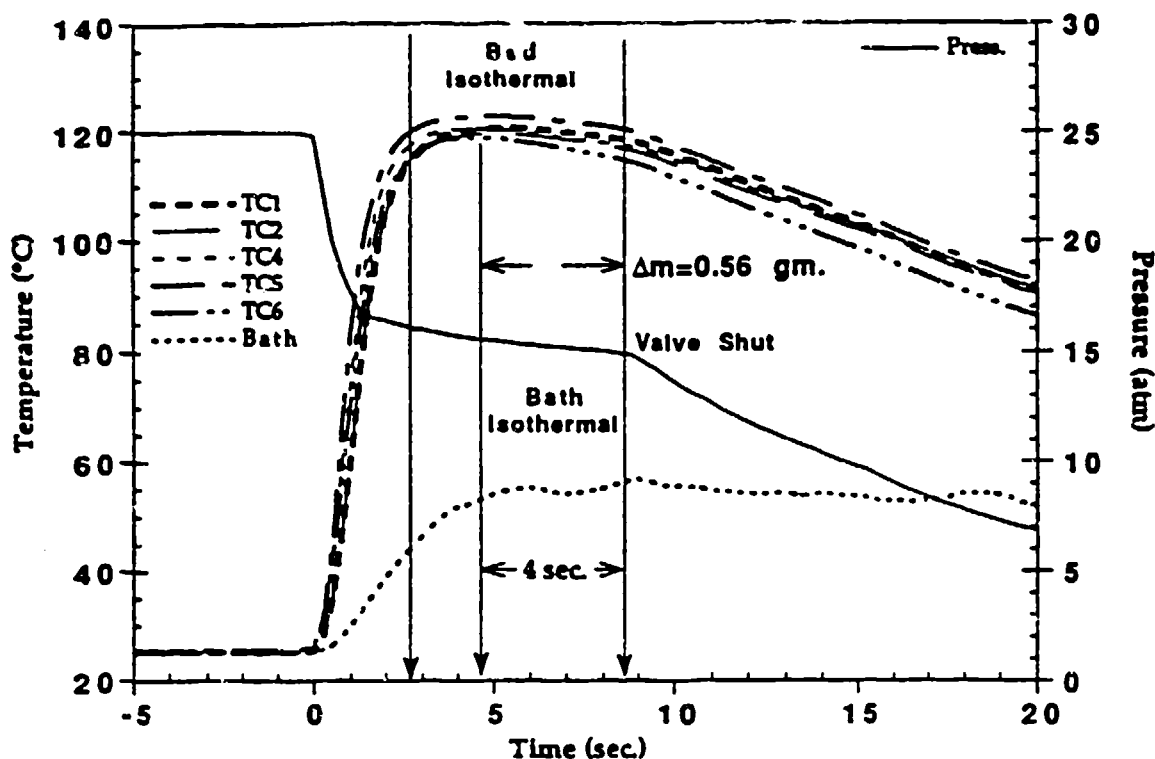


Fig. 8. Summary of pressure and temperature changes during hydrogen absorption experiment to determine effective thermal conductance. See text for details and discussion.

SUMMARY AND CONCLUSIONS

A breadboard hydride compressor was built and tested to assess the performance potential of a $\text{LaNi}_{5-y}\text{Sn}_y$ alloy for fast cooldown periodic 25K cryocooler systems [6]. Initial observations have successfully demonstrated the requisite rapid hydrogen absorption at suitable pressures to generate liquid hydrogen. The importance of sorbent bed heat transfer and capacity to dissipate the energy released by the hydrogen absorption process was clearly indicated by the present test results. An advanced compressor design which addresses these criteria is currently being developed at JPL and Aerojet as part of the BETSCE program.

ACKNOWLEDGMENTS

This work was performed for the Jet Propulsion Laboratory, California Institute of Technology, under contract with by the National Aeronautics and Space Administration (NASA). The work was sponsored by the Brilliant Eyes program office, Strategic Defense Initiative Organization (SDIO), USAF Space and Missiles Systems Center (SMC). The authors wish to thank M.D. Canon for his generous support and assistance and E.A. Liu for her contributions to these studies.

REFERENCES

1. H.H. van Mal and A. Mijnheer, Proc. ICEC 4 (Science and Technology Press, Guildford, UK, 1972) p. 122.
2. J.A. Jones and P.M. Golben, *Cryogenics* 25, 212 (1985).
3. T. Kumano, B. Tada, Y. Tsuchida, Y. Kuraoka, T. Ishige, and H. Baba, *Z. Phys. Chem. NF* 164, 1509 (1989).
4. J.A. Jones, U.S. Patent 4,641,499, Issued Feb. 10, 1987.
5. J. Wu, S. Bard, and R. Longworth, to be presented at this conference.
6. A. Johnson and J. Jones, to be presented at this conference.
7. H.-J. Ahn and J.-Y. Lee, *Int. J. Hydrogen Energy* 16, 93 (1991).
8. S.W. Lambert, D. Chandra, W.N. Cathey, F.E. Lynch, and R.C. Bowman, Jr., *J. Alloys and Compounds* 187, 113 (1992).
9. F.P. Incropera and D.P. DeWitt, Fundamentals of Heat and Mass Transfer (Wiley, New York, 1985).
10. E. Suissa, I. Jacob, and Z. Hadari, *J. Less-Common Metals* 104, 287 (1984).

ASSESSMENT OF A HYDROGEN JOULE-THOMSON
EXPANDER AND VANADIUM HYDRIDE SORPTION
BEDS FOR 20K CRYOCOOLERS

E. L. Ryba, B. D. Freeman, and R. C. Bowman, Jr.
Aerojet Electronic Systems Division
Azusa, CA 91702

R. E. Spjut, E. A. Liu, P. Budic, and C. Okado
Department of Engineering
Harvey Mudd College
Claremont, CA 91711

ABSTRACT

The ability of vanadium metal to absorb large quantities of hydrogen makes it a promising candidate to produce temperatures below 30K by connecting a vanadium hydride compressor to a Joule-Thomson (J-T) expander. The hydrogen absorption and desorption characteristics of a prototype compressor that uses vanadium as the sorbent have been measured under various conditions. These experiments confirm that vanadium sorption beds can meet the requirements for cryogenic refrigerators. A J-T expander for the blowdown production of liquid hydrogen has been built and tested. When the expander is precooled to 85K, temperatures down to 22K were achieved within 60 s at a hydrogen flowrate of 35 slpm. A vanadium hydride compressor with a reversible storage capacity of 10 grams hydrogen has been coupled to the J-T expander and produced temperatures below 30K.

INTRODUCTION

Cooling requirements for spaceborne surveillance systems have become increasingly demanding. Cooling systems must exhibit long life (i.e., 5 to 10 years), low input power, small volume and mass, and multistage cooling from 5 to 200K. While many surveillance systems require constant refrigeration over the lifetime of the system, some proposed applications require cooling to operational temperatures only on a periodic basis. Possible system operation would provide periodic temperatures at 10-25K for a duration of at least 20 minutes. This periodic operation would need to be repeatable at least once in every 24 hour period. Between these burst cooling periods, the system would be maintained in a standby mode at 65K by either Stirling cycle mechanical [1] or sorption [2] refrigeration methods. A 65K heat sink provides the necessary precooling for H₂ to achieve quick cooldown to 10-25K. A single bed hydride compressor and J-T expander would be very suitable to produce 25K while a second low pressure hydride is required [3] to reach 10K.

We have performed initial proof-of-principle testing of a breadboard liquid hydrogen blowdown sorption system. The specific details of the components and test results are described in the present paper. Although previous hydrogen sorption cryocoolers used LaNi₅ or its substituted alloys as the sorbent [3, 4], recent analyses by Bowman, et al. [5, 6] indicated that vanadium hydride (VH_x) should be an attractive candidate for 25K cryocoolers. Therefore, another objective of the present work was to assess its behavior during laboratory experiments.

DESIGN

System Overview

The blowdown sorption refrigeration system is composed of two major components: a Joule-Thomson (J-T) expander cryostat and a vanadium hydride compressor element (Figure 1.). Hydrogen gas is supplied to the system from a high pressure cylinder. The high pressure hydrogen passes through a liquid nitrogen bath where it is precooled to 85K. After passing through the cryostat heat exchanger, the H₂ gas is expanded before exiting the cryostat. The hydrogen can then be vented from the system or absorbed into the vanadium hydride compressor element. During blowdown experiments the vanadium hydride compressor operates purely as a hydrogen getter, absorbing effluent hydrogen from the cryostat. Between blowdown experiments the vanadium hydride compressor must be heated to desorb hydrogen through the vacuum pump. In a closed system this gas would produce the high pressure gas that is currently supplied by the hydrogen cylinder in Figure 1.

Vanadium Hydride Bed

A schematic drawing of the prototype hydride bed used for the present experiments is presented in Figure 2. This cylindrical vessel was fabricated from electropolished 316L stainless steel with a 4.45 cm internal diameter and 19.0 cm length. An internal helical coil of 0.635 cm o.d. 316L stainless steel tubing permits circulation of a thermal control fluid (i.e.,

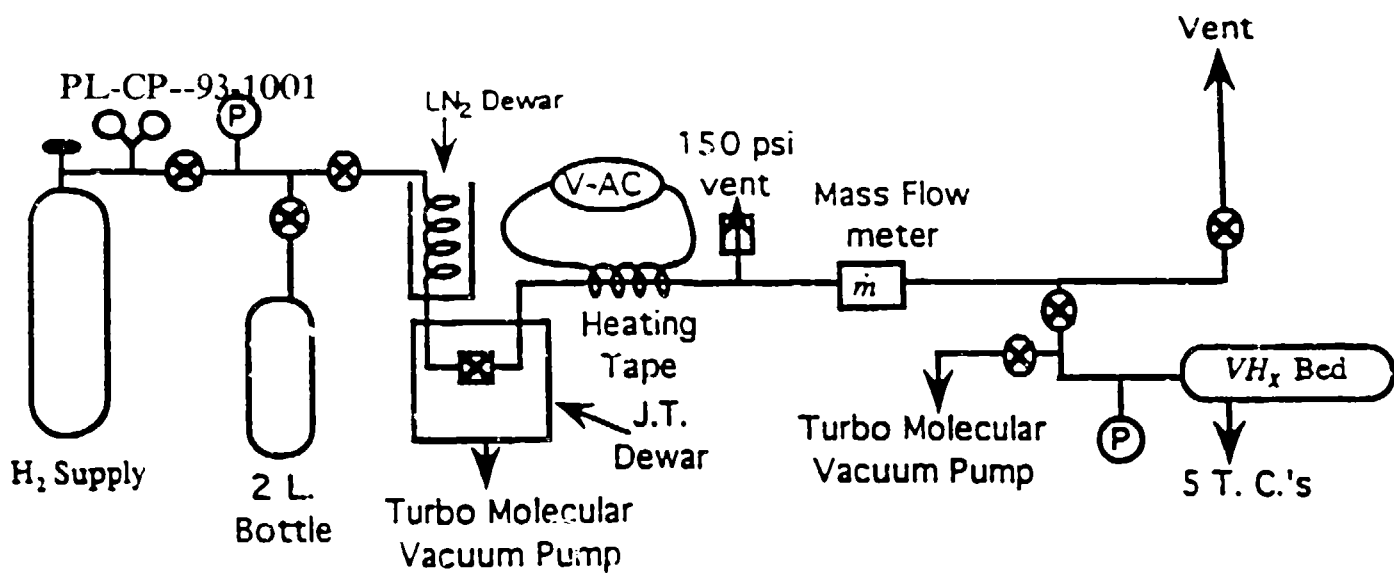


Fig. 1. Blowdown system schematic which shows high pressure H₂ supply, J-T expander dewar, vanadium hydride bed and connecting lines and valves.

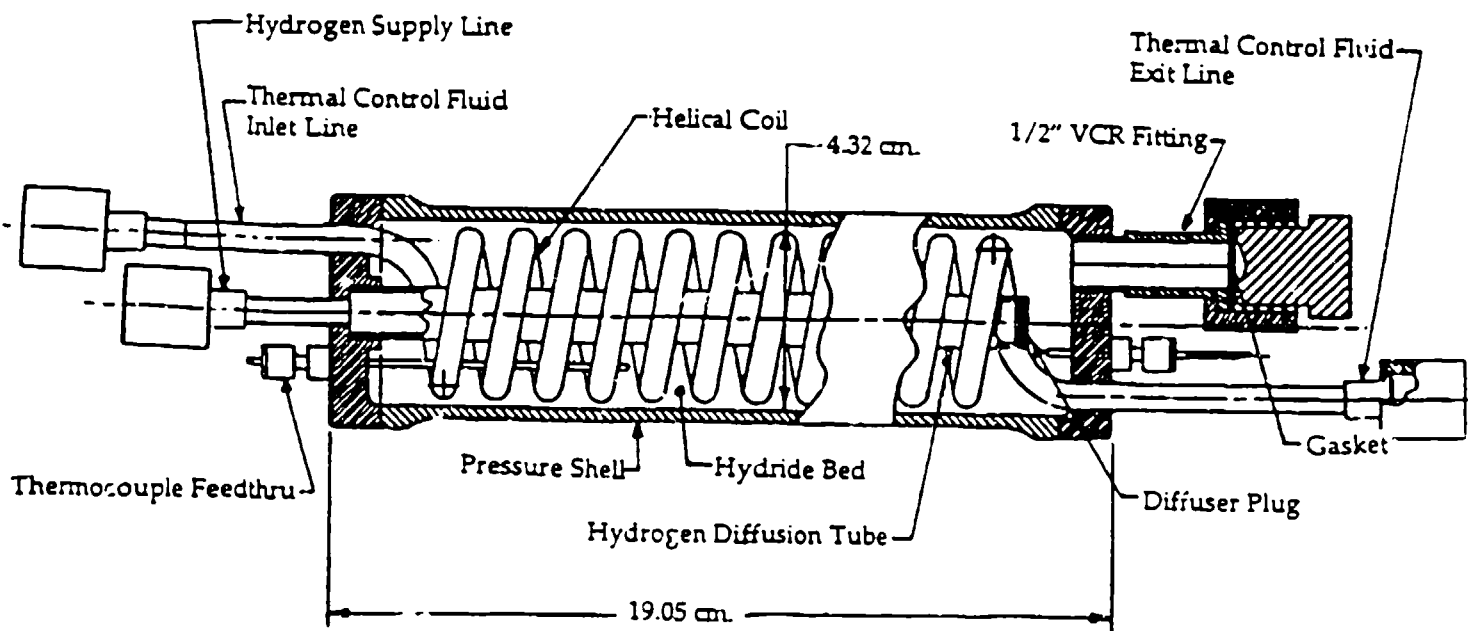


Fig. 2. Valex vanadium hydride compressor element. 316L stainless case, heat exchanger coil, sintered stainless filter and thermocouples.

heated or cooled water) through the hydride powder bed. A 1.27 cm diameter porous 316L SS tube of nominal 2 micron pore size is centered in the vessel and is welded to the 0.635 cm o.d. hydrogen supply line that terminates with at a VCR-fitting. The sintered porous tube provides more direct access of hydrogen to the metal powder along the entire length of the storage bed while containing the activated vanadium powder. A fill tube and 1.27 cm diameter VCR-connection plug, which is located on the opposite end from the hydrogen gas inlet line, allows the bed to be reused with different sorbent materials. Stainless steel sheathed grounded-junction chromel-alumel thermocouples were inserted into the bed from both ends. These thermocouples were sealed by metal compression fittings and were verified tight by helium mass spectrometer leak testing methods for both vacuum and high pressure conditions. The thermocouples monitor temperature at five locations throughout the bed during the absorption and desorption of hydrogen.

The bed used for the hydrogen blowdown experiments was loaded with 633 gms of vanadium metal powder with particle sizes that passed between 20 and 100 mesh sieve screens. The metal had been purchased from Teledyne Wah Chang with an analyzed purity of 99.5% vanadium. After sealing the bed and determining its free volume using helium gas, the vanadium was activated by heating the bed to above 400°C under dynamic vacuum using a turbomolecular pump until the pressure was below 10^{-3} Pa. After cooling to room temperature, the vanadium powder reacted readily with hydrogen gas. After several hydrogen absorption-desorption cycles, the

final composition was $VH_{1.63}$ at an H_2 pressure of 1.6 MPa. This value is consistent with the isotherms measured by Luo, et al. [7] for vanadium powder of similar purity. The reversible storage capacity across the β - γ phase plateau [7] for VH_x corresponds to about 10 grams of hydrogen for this bed as confirmed by our direct measurements.

Joule-Thomson Expander Cryostat

Cooling to below 30K is achieved by the Joule-Thomson expansion of high pressure hydrogen gas through a cryostat built at Aerojet. The entire cryostat device consists of the J-T expander, a liquid reservoir and a counterflow heat exchanger (Figure 3). Temperature sensors mounted to various cryostat components allow the temperature to be recorded and a small resistance heater provides heat input which simulates a potential load. The J-T expander is a metering valve which has been heavily modified to allow it to function below 30K. The original micrometer adjustment control has been extended away from the body of the valve with a 17 cm long extension shaft. This allows the o-ring seals to be located at ambient temperature and still permits precision flow control by the metering valve. The inlet and outlet fittings of the valve have been removed in an effort to reduce the valve's thermal mass. The valve body casting has also been reduced in certain areas. The liquid reservoir is located immediately after the J-T expander. It accumulates liquid hydrogen formed by the expansion process. The internal volume of the reservoir is 20 cm³. The lower half of the reservoir is

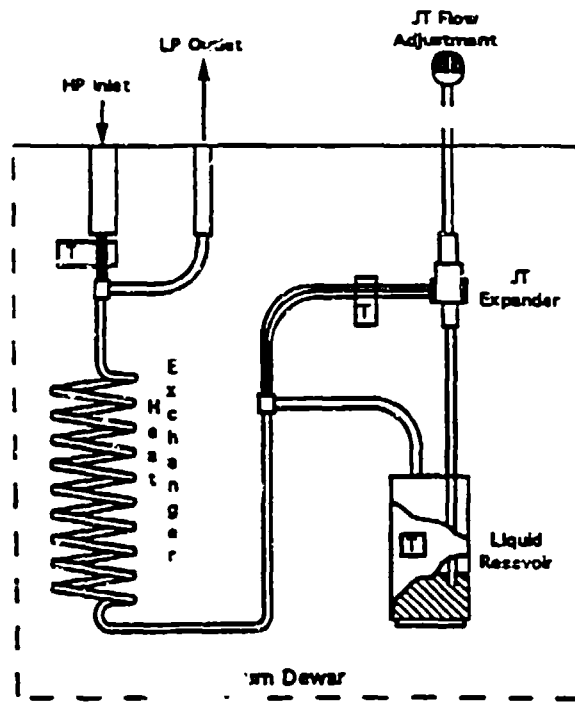


Fig. 3. Joule-Thomson expansion cryostat, consists of J-T expansion valve, counterflow heat exchanger, liquid reservoir and temperature sensors.

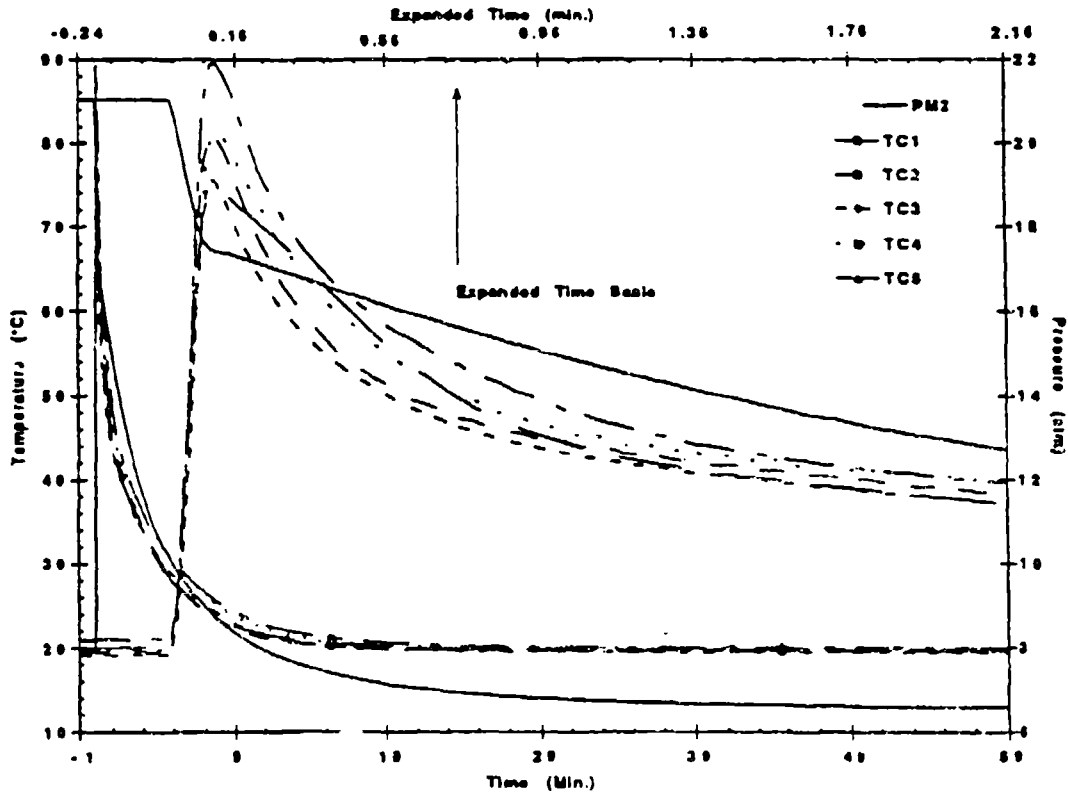


Fig. 4. Thermal response of vanadium filled Valex compressor. Includes expanded time scale to show rapid transient response.

filled with 10% density copper foam. The inlet tube protrudes through the upper half of the copper foam. The exit tube from the reservoir is flush with the top of the reservoir. The copper foam is intended to reduce turbulence in the liquid hydrogen so that it is not blown directly back into the heat exchanger. The counterflow heat exchange contains three capillary tubes inserted into a single 3.18 mm diameter tube. The capillary tubes have a diameter of 1.07 mm. The heat exchanger is approximately 275 cm long.

SYSTEM DESCRIPTION

Hydrogen gas for all experiments is supplied from cylinders of 99.9995% pure hydrogen. Inlet pressure is regulated to approximately 9.6 MPa. Immediately prior to entry into the cryostat the hydrogen is cooled to 85-90K by passing the tubing through a liquid nitrogen bath. After expansion the hydrogen exits the cryostat vacuum dewar at a temperature less than 80K. It is warmed to ambient by an AC resistance heater coiled around the exit tubing. Flow rates are monitored by a Unit Instrument model 2100 flowmeter on the low pressure gas leaving the cryostat. After exiting the cryostat the hydrogen gas can be either absorbed by the vanadium hydride or vented from the system.

The vanadium hydride bed is mounted to a manifold containing several calibrated reference volumes that allow accurate measurement of the amount of hydrogen that is absorbed or desorbed by the VH_x bed. During the absorption of hydrogen the

critical characteristics are the temperature and pressure response of the hydride bed. As mentioned earlier, thermocouples monitor the bed's temperature and a pressure transducer monitors the equilibrium pressure. In order for the blowdown system to work properly it is necessary for the hydride bed to absorb hydrogen at a rate sufficient to maintain a pressure below 1MPa at the J-T expander. The equilibrium pressure of the VH_x system [7] is primarily controlled by the temperature of the hydride bed. Since the absorption of hydrogen is an exothermic process with a measured [7] enthalpy of 19.1 kJ/mol H across the β - γ plateau region, the released heat must be removed from the bed for the reaction to proceed. Temperature control of the bed is provided by flowing chilled water through the internal heat exchange tubing as well as by immersing the entire bed in a refrigerated water bath.

COMPONENT TESTS

Extensive performance testing of both the cryostat and the hydride bed were performed prior to conducting the blowdown tests. It was necessary to determine their individual operating characteristics prior to "system" level tests. All "system" level tests would be initiated at a starting temperature of approximately 65K. This simulates the expected standby baseline temperature for potential spacecraft applications. Cooling the cryostat so that the inlet to the heat exchanger was ~85K and the cold tip was ~65K required in excess of 1000 standard liters hydrogen. But from this "initial" state only comparatively small

amounts of hydrogen needed to be used to achieve cold tip temperatures below 30K. The following table summarizes the flowrate (M_H) versus time response of the cryostat and the total amount of hydrogen consumed from the "initial" 85K starting point.

TABLE 1. Relationship of hydrogen flowrate (M_H) to J-T cooldown time and hydrogen consumption.

M_H (SLPM)	Cool Down Time (sec)	H ₂ Consumed (SL)
12	~470	96
13	~305	65
15	~240	60
18	~165	49
30	~ 70	35

As can be seen from Table 1, the higher the hydrogen flowrate the faster the cool-down and the less hydrogen consumed. However, at the same time the hydride bed must be able to absorb the hydrogen without experiencing an excessive increase in pressure due to rises in the bed temperature.

Figure 4 displays the time/temperature/pressure response of the vanadium hydride bed when allowed to react with hydrogen from the starting composition of $VH_{0.59}$ to reach $VH_{1.44}$ at a final pressure of 0.66 MPa. The temperature and pressure responses are displayed on two different time scales. Data

collected during the first two minutes of the absorption reaction is displayed on the expanded time scale. Variations in thermocouple responses are due to non-uniform reactions within the hydride bed. Several additional tests were conducted with cooling of the hydride bed provided only from the heat exchanger coil internal to the bed. Water at 20 °C was the cooling fluid. Also, in each of these tests the hydride bed was exposed to a fixed quantity of hydrogen gas at ~2 MPa. No effort was made to throttle the hydrogen flow into the hydride bed. The behavior was always similar to Figure 4 where the hydride bed experiences a nearly instantaneous increase in temperature and the pressure of the hydrogen reservoir drops rapidly upon initiation of the reaction. The absorption reaction is essentially completed within the first 10 minutes which is followed by a gradual reduction of the hydrogen pressure to about 0.7 MPa once the hydride bed's temperature has reached ~20°C.

SYSTEM PERFORMANCE TESTING

Four series of tests were conducted to identify most effective operating characteristics of the blowdown system. It was quickly discovered that the cooling provided by flowing 5°C water through the internal heat exchanger was not capable of providing sufficient cooling to allow the hydride bed to absorb hydrogen at flow rates necessary to achieve cooldown. With the additional cooling provided by immersing the hydride bed in a refrigerated water bath at 5°C it was then possible to perform tests which were capable of absorbing hydrogen at rates necessary to achieve the desired cooldown at the J-T expander cold tip.

The temperature/pressure response of the hydride bed as well as the temperature/flowrate response of the cryostat are shown in Figure 5 and Figure 6, respectively. During the test it was necessary for the hydrogen flowrate through the J-T expander to be manually adjusted. Initially, a high flowrate (~20 SLPM) is maintained until the cryostat achieves its baseline temperatures of approximately 85K at the heat exchanger inlet and 65K at the cold tip. During this period the hydrogen is vented out of the system. When the baseline temperatures are achieved, hydrogen flow is diverted into the hydride bed by closing and opening two manual valves. During the cooldown phase of the J-T expander a constant hydrogen flowrate is maintained. Flow is reduced when the temperature is sufficiently low to produce liquid hydrogen. This change also allows the hydride bed to be more effectively cooled from a peak temperature of 28°C to between 14 and 21°C. As the pressure over the hydride bed begins to rise due to a sloping absorption isotherm [7] and the J-T expander has produced some quantity of liquid hydrogen in the reservoir, the hydrogen flow through the J-T expander is stopped by fully closing the metering valve. At this time the only hydrogen flow to the hydride bed is from the boil-off of the liquid reservoir. The cold tip temperature typically drops slightly at this point due to the reduction in pressure when the metering valve is closed. The cold tip temperature remains relatively stable until the hydrogen has completely boiled off or the hydride bed becomes saturated and its pressure increases more rapidly [7]. Under these conditions it has been possible to obtain temperatures of ~27K at the cold tip. Cooldown of the cold tip is achieved in about four minutes with a

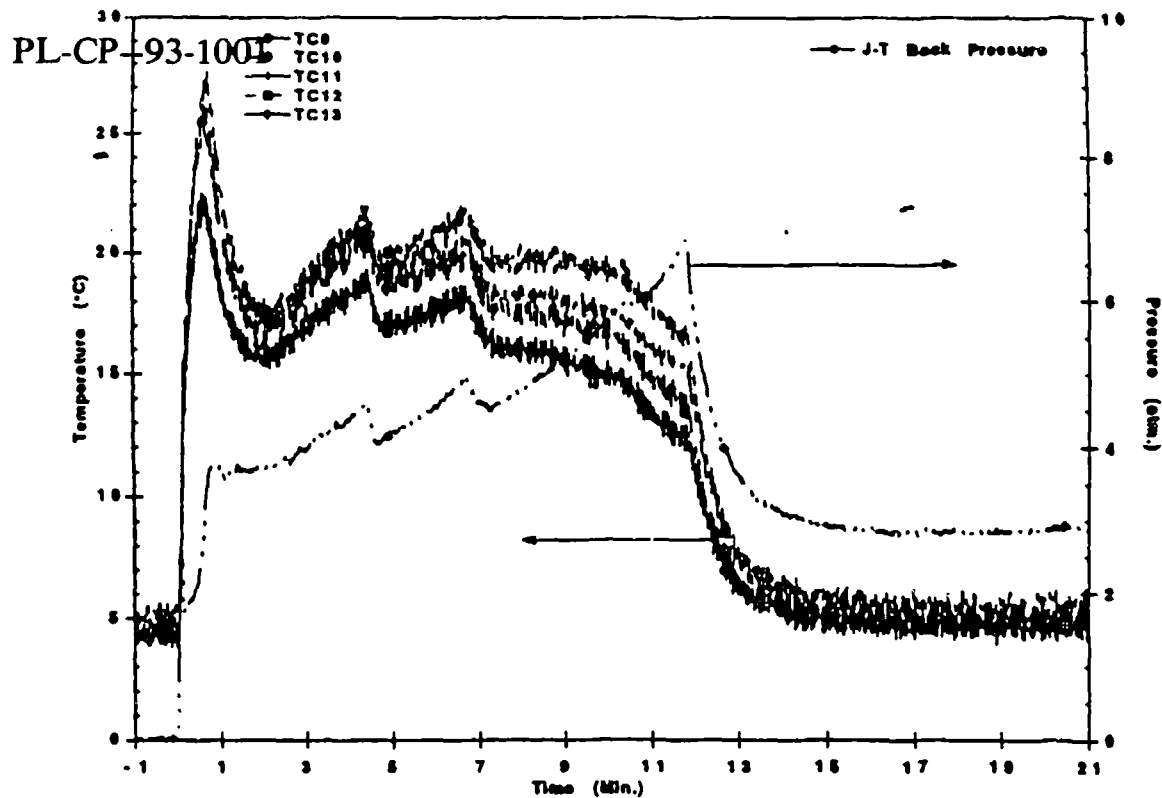


Fig. 5. Thermal response of Valex compressor as a function of H_2 flowrate during an actual blowdown experiment.

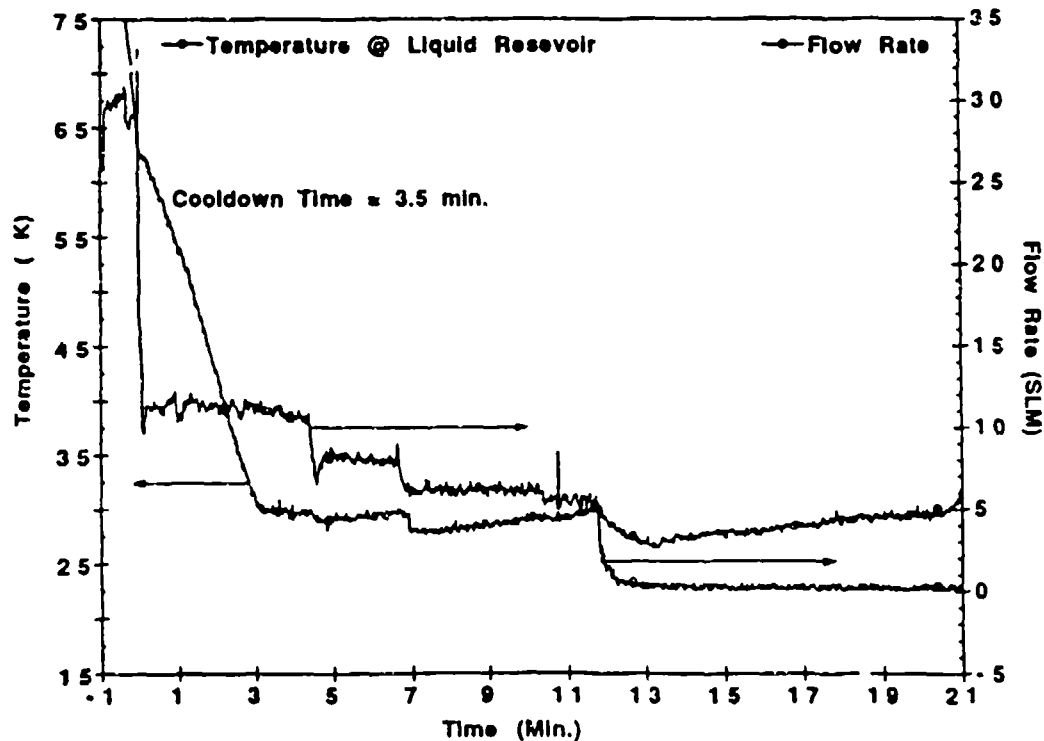


Fig. 6. Cold tip temperature during blowdown experiment. Data initiated at 65K. Shows flow changes as different cold tip conditions occur.

hydrogen flow rate of approximately 12 SLPM. The current configuration is very sensitive to hydrogen flow rate. If the flowrate is below 12 SLPM, the J-T expander will not cool to below 30K. If the flowrate is slightly above 12 SLPM, the hydride bed cannot absorb the hydrogen fast enough to maintain a sufficiently low pressure to allow the formation of liquid hydrogen below 30K.

THERMAL CYCLING OF A VH_x BED

In addition to the periodic 25K cryocooler systems, VH_x beds should also be viable candidates [5, 6] for continuous cryocooler applications that involve four or more beds undergoing heating-cooling cycles with nominal one hour cycle times [3,4]. Consequently, a second vessel identical to Figure 2 was filled with a thoroughly mixed combination of 356 grams V and 448 grams Cu powders. Copper serves as a potential enhancement for heat conduction as well as thermal ballast. After an activation treatment similar to that described previously for the bed containing only vanadium, a stoichiometry of $VH_{1.69}$ was reached in this bed.

A separate and previously described [8] test station was employed to characterize the VH_x /Cu sorbent bed during a series of thermal cycling experiments. Hot (i.e., temperatures between 70 and 90°C) and cold (i.e., 10°C) water was alternatively pumped through the inner stainless steel tube of the bed. Representative data collected during a test with a 3.0 l/min water flowrate are presented in Figure 7. After heating until the pressure exceeded 5.0 MPa, the valve connecting the VH_x /Cu bed to

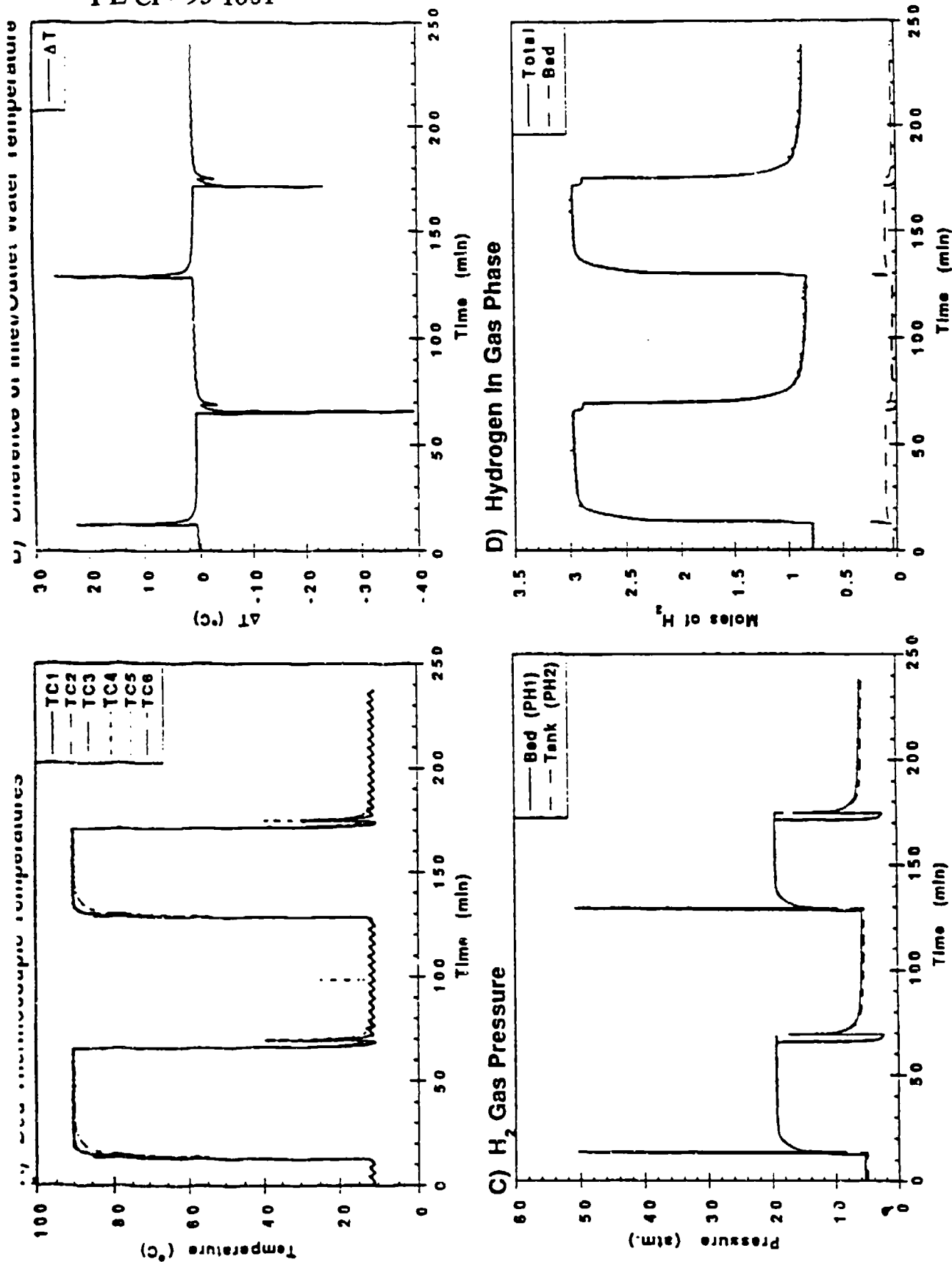


Fig. 7. Characteristic response during thermal cycling of an experimental vanadium/copper sorbent bed reacting with hydrogen.

a 3.0 liter reference volume was opened to permit desorption. When desorption was complete and the bed was at a uniform high temperature (i.e., 90°C), the valve was closed and the bed was quickly cooled by flowing 10°C water through the tube. Hydrogen was absorbed from the volume when the valve was again opened. These tests were repeated for various combinations of hydrogen pressure, water flow rate, and hot water temperature. The time constants for hydrogen absorption varied between 4.0 and 7.0 min while the desorption constants ranged between 6.0 and 8.2 min. These values are 2 to 3 times longer than those observed from another VH_x bed with an entirely different design [8] that circulates the water around seven 1.91 cm diameter tubes. Furthermore, the VH_x/Cu bed examined in the current tests exhibited variations in thermocouple response times that indicate non-uniform reactions within the bed. This behavior is due to the low effective thermal conductivity of metal hydride powder. The quantity of hydrogen absorbed or desorbed varied with the applied pressure and temperature difference between the hot and cold water baths. The maximum reversible storage capacity corresponds to a Δx of 0.70 for the cycles between 10 and 90°C. These temperature cycling experiments demonstrate that VH_x is also a competitive hydrogen sorbent for continuous sorption cryocoolers operating around 25K.

SUMMARY AND FUTURE PLANS

A prototype J-T expander and VH_x sorbent beds have been built and tested to assess the potential of VH_x for fast cooldown production of liquid hydrogen. Initial experiments have

demonstrated their feasibility. However, the design of the container must be modified to enhance removal of heat generated during hydrogen absorption. Furthermore, the VH_x beds probably need cooling below 0°C if the J-T cold tip is to go below 25K.

Additional tests are planned to perform further hydrogen blowdown experiments but using different hydride materials. In particular, hydrides with lower equilibrium pressures at the refrigerated bath temperature should allow the J-T expander to achieve lower temperatures. $\text{LaNi}_{4.8}\text{Sn}_{0.2}$ which has a ~ 0.05 MPa plateau pressure [9] at 20°C , will be the next hydride material to be tested in combination with the current J-T expander. The boiling point of liquid hydrogen at this pressure is less than 20K. However, due to the pressure drop in the heat exchanger tubing and other lines and valves we expect the minimum temperature to be 20-21K for an adequately cooled $\text{LaNi}_{4.8}\text{Sn}_{0.2}$ sorbent bed.

ACKNOWLEDGMENTS

The authors wish to thank Tom Cotter, Dallas Labor, Dan Crevier, Scott Banachowski, David Stepp, James Heaps-Nelson, and Teh-Tien Su for their contributions to these studies.

REFERENCES

1. W. D. Stacy, *Cryogenics* 32, 138 (1992) and B. G. Jones and S. R. Scull, *Cryogenics* 32, 850 (1992).
2. S. Bard, J. A. Jones, R. W. Hughes, D. M. Moore, N. Sherman, P. Sywulka, L. Wade, and R. C. Bowman, Jr., in *Proc. 4th Inter. Meeting Cryocoolers*, Plymouth, MA, Oct. 1990, p. 99.
3. J. A. Jones and P. M. Golben, *Cryogenics* 25, 212 (1985).
4. T. Kumano, B. Tada, Y. Tsuchida, Y. Kuraoka, T. Ishige, and H. Baba, *Z. Phys. Chem. N. F.* 164, 1509 (1989).
5. R. C. Bowman, Jr., B. D. Freeman, and J. R. Phillips, *Advances in Cryogenic Eng.* 37B, 973 (1992).
6. R. C. Bowman, Jr., B. D. Freeman, and J. R. Phillips, *Cryogenics* 32, 127 (1992).
7. W. Luo, J. D. Clewley, and T. B. Flanagan, *J. Chem. Phys.* 93, 6710 (1990).
8. R. C. Bowman, Jr., B. D. Freeman, E. L. Ryba, R. E. Spjut, E. A. Liu, J. M. Penso, and F. E. Lynch, *Z. Phys. Chem. N. F.* (In Press).
9. S. W. Lambert, D. Chandra, W. N. Cathey, F. E. Lynch, and R. C. Bowman, Jr., *J. Alloys Compounds* 187, 113 (1992).

DESIGN OF A METAL HYDRIDE SORPTION CRYOCOOLER SYSTEM

HAL J. STRUMPF
ROBERT H. NORMANALLIED-SIGNAL AEROSPACE COMPANY
AIResearch LOS ANGELES DIVISION
TORRANCE, CA 90509INTRODUCTION

A study is being performed by the AiResearch Los Angeles Division of Allied-Signal Aerospace Company for the analysis and design of a metal hydride sorption cryocooler system to cool a focal plane array. The work is being performed for Hughes Aircraft Company. Cryocoolers were studied at 30 K and 10 K. Both systems provide intermittent cooling at these levels. The work emphasized the key component in the cryocooler system, the metal hydride sorption bed assembly. This component acts as a thermal compressor to recycle the hydrogen used to produce the refrigeration. The present paper concentrates on the 10 K system.

The refrigeration is effected by sublimating solid hydrogen at 10 K. The solid hydrogen is contained in a porous wick that interfaces with the heat load. The solid hydrogen is produced in a batch process by cooling, solidifying, and subcooling liquid hydrogen formed at 30 K by a Joule-Thomson (J-T) expansion. Precooling for the J-T expansion is provided by a Stirling cycle standard spacecraft cryocooler (SSC).

METAL HYDRIDE SORPTION CRYOCOOLERS

Certain metals react with hydrogen to form a metal-hydrogen compound called a metal hydride. Such reactions are often fully reversible, i.e.:



where M is the reacting metal.

At a given temperature, the forward reaction (hydrogen absorption) and the reverse reaction (hydrogen desorption) occur at a relatively constant pressure over a wide range of compositions. This pressure, called the plateau pressure, may be

different for the absorbing and desorbing isotherms due to hysteresis effects. The absorption reaction is usually exothermic while the desorption reaction is usually endothermic.

These properties make metal hydrides useful for hydrogen storage and retrieval. Hydrogen can be stored by absorbing at constant pressure if the heat of reaction is removed. To retrieve hydrogen, the metal hydride can be desorbed at constant pressure by heating. The temperature level maintained in the metal hydride determines the equilibrium hydrogen pressure.

These storage and retrieval characteristics can be utilized in cryogenic systems that produce cooling by the expansion and phase change of hydrogen. The spent hydrogen can be absorbed by metal hydride beds at a low pressure and relatively low temperature. To recover the hydrogen, the beds can be desorbed at a high pressure and relatively high temperature. This hydrogen "thermal compression" acts to refill the high-pressure hydrogen source used to feed the refrigeration system.

POROUS METAL HYDRIDE COMPACTS

AiResearch is proposing the use of porous metal hydride (PMH) compacts for the metal hydride sorption bed. The PMH compacts consist of a porous, three-dimensional, inert metallic matrix incorporating metal hydride particles. PMH compacts offer a stable form of metal hydride that will not comminute (degrade to a fine powder) with repeated cycling. This feature is especially important in a space microgravity environment. The use of PMH compacts is viewed as a risk-reduction approach for the sorption bed that will increase the probability of success and provide a robust hydride bed design.

Description of the Porous Metal Hydride Compact

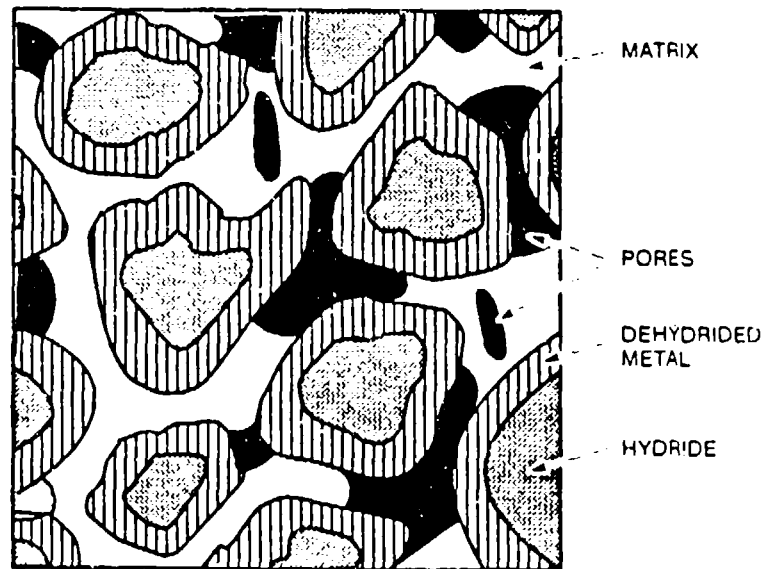
Porous metal hydrides^(1 to 3) are metal composites (or compacts) made from the compaction of a thermally conductive metal powder with a fully hydrided (and therefore swollen) metal hydride powder. The high compaction pressure causes the inert metal powder to flow plastically; this binds the metal hydride together to form the compact. The inert metal does not form an alloy with the metal hydride. Subsequently, the hydrogen is desorbed from the compact, resulting in shrinkage of the dehydriding

metal particles and the formation of a porous structure within the compact. The microstructure of a partially desorbed PMH compact is illustrated in Figure 1. The cross-hatched, white, and dark areas represent the metal hydride, conductive metal, and pores, respectively. The conductive metal, which forms a continuous matrix through the compact, is nonporous and does not absorb hydrogen. Dehydrated metal is shown with vertical lines.

Advantages of PMH Compacts Over Metal Hydride Powders

PMH compacts offer a number of advantages over metal hydride powders in hydrogen heat pumps and heat storage devices, including:

- (a) An increase in thermal conductivity (10 to 50 times greater than powder)⁽⁵⁾
- (b) A stable structure with a constant porosity that will not comminute with repeated cycling
- (c) Easier engineering (configuration design)
- (d) Avoidance of potential plugging, agglomeration, and handling problems associated with metal hydride powders in a microgravity environment. Depending on geometry, agglomeration (self-compression) could degrade



IG-08649

Figure 1. Schematic of Microstructure of Porous Metal Hydride⁽⁴⁾

mass transfer and/or create structural failures due to swelling upon hydrogen absorption.

The increased thermal conductivity of the compact results from the continuous metallic matrix that forms between the metal hydride particles. The metal matrix effectively provides a path for transfer of the heat of reaction to and from the metal hydride particle. In metal hydride powders, no such conductive path exists, and these powder beds inherently have lower heat and mass transfer characteristics than PMH compacts.^(5, 6) The low thermal conductivity of powder beds has been shown to be responsible for the slow heat transfer response of heat pumps containing the powdered metal hydride.⁽⁵⁾ In contrast, the increased heat transfer characteristics of PMH compacts may improve the overall thermal response of the heat pump. As discussed below, the poor thermal conductivity of powdered metal hydrides is a key factor in comminution and agglomeration, which may be exacerbated in the microgravity environment of space.

Powders are poor thermal conductors. Due to the high heats of reaction associated with metal hydrides, high localized surface temperatures may result from their poor heat transfer properties. This will invariably result in sintering and agglomeration. Experience indicates that the size of hydride particles will be reduced due to the comminution common to these systems, and the strength of the sintered agglomerates is expected to increase as the metal particle size decreases. The expansion of the metal hydride mass from hydrogen absorption, coupled with high-strength sintered agglomerates, could result in structural containment failures. The use of PMH compacts should eliminate this potential problem.

The PMH compacts may be easier to engineer into a suitable configuration than metal hydride powder systems. Comminution of the hydride powders decreases both the heat and mass transfer characteristics of a hydrogen heat pump over time.⁽⁶⁾ In addition, the hydride powder must be enclosed or encapsulated to prevent the fine powder from escaping the system. Fine powders can plug their porous containers, requiring larger pressure drops to remove the hydrogen. In the PMH compact, the compact remains integral and stable with time. Very little deterioration of the compact occurs after many cycles, and the porosity of the compact remains constant from cycle to cycle.⁽⁷⁾ Since the porosity of the compact remains constant, the pressure drop across the compact does not vary from cycle to cycle as may be the case in the

powder systems. The PMH compacts also exhibit a faster and more constant thermal response over time.

The PMH compacts inherently provide for compartmentalization of the metal hydride material. AiResearch development of other systems undergoing large reversible volume changes in microgravity, such as the heat-of-fusion thermal storage containment canisters for the Space Station Freedom solar receiver, has indicated the desirability of compartmentalization.⁽⁸⁾ Compartmentalization limits potential agglomeration and migration effects, which could cause structural damage to the material container.

The PMH compacts have the potential for very long life and numerous cycles. Lanthanum pentanickel/aluminum compacts have been successfully tested at over 22,000 cycles, with very little disintegration or cracking.⁽⁹⁾

CRYOCOOLER DESIGN REQUIREMENTS

The cryocooler is required to produce an intermittent 0.15-w cooling load at 10 K. The required duty cycle is 15 min on, 75 min off for a maximum of three consecutive cycles. Following these three 90-min cycles, the remainder of a 24-hr day is available for recovery. A continuous 2-w load at 65 K is provided by an SSC Stirling refrigerator (not studied in the present effort). Cooldown time from 65 K to 10 K is 2 min. The equivalent space sink temperature is taken as 285 K.

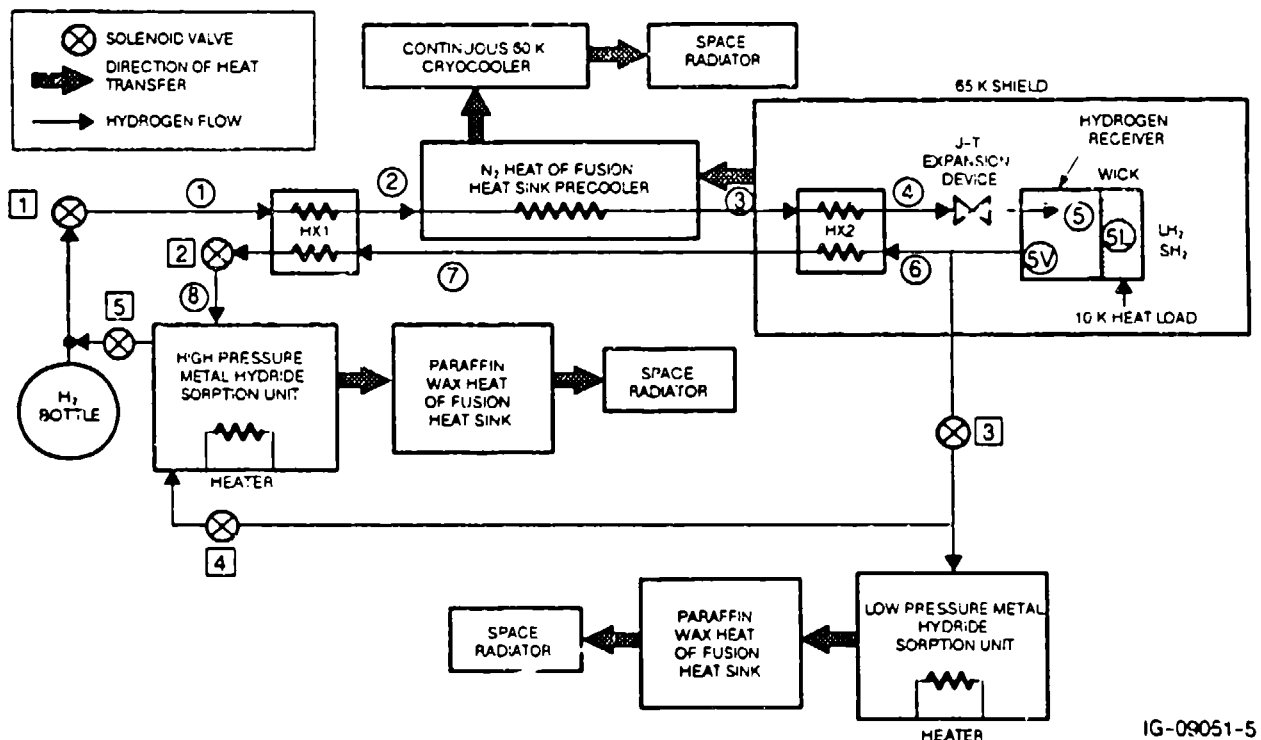
SYSTEM ARCHITECTURE AND OPERATION

The intermittent cooling is accomplished using a three-stage cryocooler. The first stage is a continuous SSC operating at 60 K. The SSC also provides the required 65 K load. The SSC is connected to a nitrogen heat of fusion heat sink, operating at the nitrogen triple point, 63.1 K. The heat sink acts as a precooler for the second stage, an intermittent J-T expander that produces liquid hydrogen at 30 K. This liquefaction occurs only during a portion of the 2-min cooldown period (90 sec). The liquid hydrogen is collected in a porous wick that interfaces with the heat load. The produced hydrogen vapor is absorbed by a high-pressure metal hydride sorption bed. The third-stage cooling is effected by hydrogen sublimation at 10 K. During the remainder of the 2-min cooldown period (30 sec), the liquid hydrogen produced by the second stage is

cooled, solidified, and subcooled to 10 K by exposure to low pressure provided by a low-pressure metal hydride sorption bed. Sublimation continues at 10 K for the 15-min load period. Paraffin wax heat of fusion heat sinks are required for both the high-pressure and low-pressure metal hydride beds, to absorb the released heat of reaction and ensure constant temperature operation of the sorption beds.

To reuse the system, hydrogen from the second and third stages is recycled using thermal compression effected by bed heating and hydrogen desorption. The compression occurs in two stages. First, hydrogen from the low-pressure bed is transferred to the high-pressure bed, then the high-pressure bed hydrogen is transferred to the hydrogen storage bottle.

The system operation can be followed with the aid of the system schematic (Figure 2), with the five solenoid valves indicated as boxed numbers. The circled numbers are the system statepoints. Note that HX2, the J-T expansion device, and the hydrogen receiver/wick are maintained inside a 65 K temperature shield at all times.



IG-09051-5

Figure 2. Cryocooler Schematic

To initiate cooldown to 10 K, valves 1 and 2 are opened. Valves 3, 4, and 5 are closed. High-pressure hydrogen from the storage bottle is precooled by the heat exchangers and the nitrogen heat of fusion device and expanded in the J-T device. The expansion results in a partial liquefaction of the hydrogen in the receiver. The liquid is collected in the porous wick. The vapor flows back through the heat exchangers (cooling the incoming flow) and is absorbed in the high-pressure metal hydride sorption unit. Temperature control of the sorption unit results in a sorption bed pressure of 120 psia. This is the equilibrium pressure of hydrogen at 30 K, which is thus the liquid temperature in the wick. This process continues for 90 sec. The J-T expander is sized such that the required quantity of liquid will be collected in the wick during this period.

At this point, valves 1 and 2 are closed, and valve 3 is opened. This subjects the collected hydrogen to a downstream pressure of 1.5 torr, achieved by controlling the temperature of the low-pressure metal hydride sorption unit. With this low downstream pressure, hydrogen will evaporate from the collected liquid in the wick. The evaporated hydrogen is absorbed in the low-pressure bed. The evaporation process cools the collected liquid. As the process continues, the hydrogen triple point is reached (13.8 K) and the hydrogen is solidified. Cooling of the solid hydrogen is effected by sublimation until 10 K is attained. The hydrogen vapor pressure at this temperature is 1.9 torr, comfortably above the 1.5 torr bed pressure. This cooldown process continues for 30 sec.

At this point, 2 min have elapsed and the 10 K heat load can now be handled. The heat load is dissipated by continued sublimation of hydrogen, with absorption in the low-pressure bed. The cooling period is 15 min. After this cooling period, no hydrogen desorption is effected during the remainder of the 90-min orbit. The sorption beds and hydrogen bottle are sized such that three orbits, each with a 2-min cooldown and a 15-min cooling period at 10 K, can be handled.

At the end of the third orbit, recovery can begin. A total of 19.5 hr is available for recovery. Valves 1, 2, 3, and 5 are closed while valve 4 is opened. The low-pressure bed is heated to a temperature appropriate for desorption at 120 psia. The hydrogen desorbed from the low-pressure bed is absorbed by the high-pressure bed. This process continues for approximately 4 hr.

Valve 4 is now closed and valve 5 is opened. The high-pressure bed is heated to a temperature appropriate for desorption at the initial hydrogen bottle pressure of approximately 800 psia. The hydrogen is transferred to the storage bottle over a 10-hr

period. At the end of this time, essentially all the hydrogen in the system (except for small quantities remaining in the beds and lines) has been returned to the storage bottle. Valve 5 is closed.

During the remainder of the recovery period, the beds are cooled to operating temperatures by heat rejection to space. The nitrogen heat of fusion pre-cooler, and the paraffin wax heat of fusion heat sinks associated with the sorption beds, are regenerated (frozen) during the recovery period. At the end of the recovery period, the system is ready for another 24-hr cycle.

CRYOGENIC SYSTEM PERFORMANCE

A preliminary performance analysis was conducted to predict system operation during the liquefaction, solidification, and steady-state cooling periods. Cryogenic system transient and steady-state computer programs were used to aid in the prediction.

Steady-State Cooling

The sublimation rate at 10 K required to provide 0.15 w of cooling is 0.0025 lb/hr (based on a latent heat of sublimation of 204.9 Btu/lb). Since the system operates for three 15-min periods, the total required sublimation is (0.0025 lb/hr) (0.75 hr) = 0.00188 lb.

Solidification

Each solidification process occurs over a 30-sec period. During this time, hydrogen in the wick is evaporated and sublimed to provide the cooling to lower the temperature of the remaining hydrogen from 30 to 10 K. The equilibrium vapor pressure is lowered from 119.3 psia to 1.94 torr. The process can be analyzed by using the same principles that apply to a cryogenic tank venting vapor. Details of the analysis are presented elsewhere⁽¹⁰⁾.

The calculated pressure decay in the receiver as a function of the mass removed is plotted in Figure 3. Here the mass removed is expressed as a fraction of the initial mass that was evaporated and sublimed to reach the final state (solid and vapor at 10.0 K). Expressed this way, the path is independent of receiver volume or initial mass.

As indicated, 44.56 percent of the initial mass of liquid hydrogen at 30 K is lost in the process of evacuating to solid/vapor at 10 K.

Based on the total required hydrogen sublimation of 0.00188 lb, the total required liquefaction is $0.00188 \text{ lb} / (1 - 0.4456) = 0.00338 \text{ lb}$.

A simplified flow rate model was adopted to estimate the flow rate variation during the evacuation process. It was assumed that the evacuation line restriction will be dominated by flow through a valve (valve 3 in Figure 2) with a flow coefficient, C_v , defined as the number of gallons per minute of room temperature water that will flow through the valve with a pressure drop of 1 psi. The same flow coefficient is used with appropriate formulas for flow of gases. Details are presented elsewhere⁽¹⁰⁾.

The desired C_v resulted in a mass change of $0.00338 - 0.00188 = 0.0015 \text{ lb}$ (determined by integrating the flow rate over the three identical 30-sec evacuation periods). The calculated C_v is 0.0057, equivalent to an orifice size of 0.014 to 0.018 in. The results are plotted in Figure 4, which shows both flow rate and pressure over the 30-sec evacuation period.

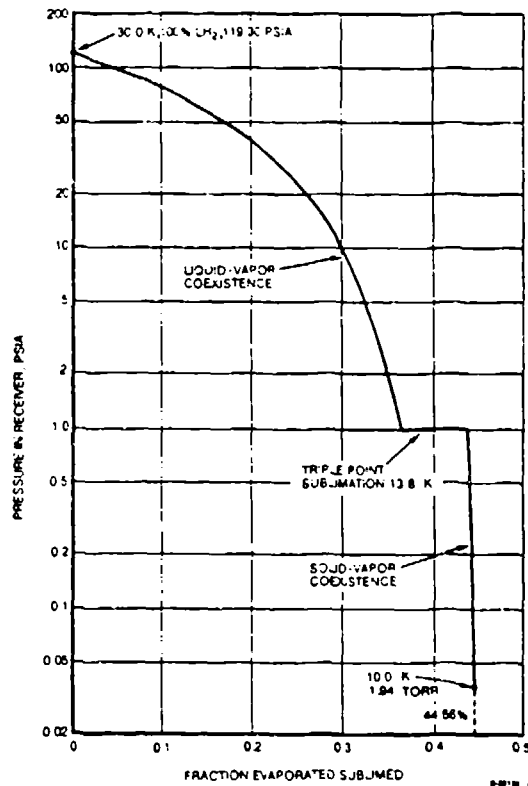


Figure 3. Pressure Decay in Receiver During Evacuation

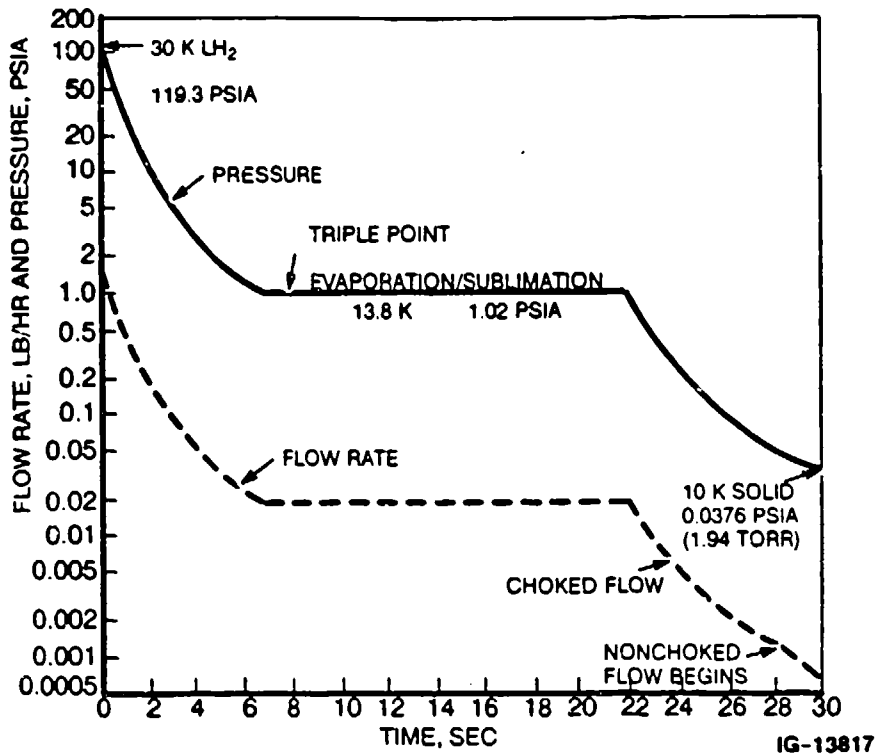


Figure 4. Evacuation Flow Rate and Receiver Pressure Time Dependence

It is interesting to note when comparing Figure 3 with Figure 4, that at the triple point, over 51 percent of the time is associated with removing only about 16 percent of the mass. This is a direct function of the significantly lower flow rate at that pressure.

Typical system statepoints during the 90-sec liquefaction period are presented in Table 1; statepoint locations are the circled numbers in Figure 2. System conditions change during the cooling period as the hydrogen supply tank pressure varies. Table 1 represents conditions for a tank pressure of 600 psia. Typical tank pressure variation is from 800 to 400 psia. The statepoints are based on effectiveness values of 0.99 for both HX1 and HX2. These high effectiveness values are attainable since the heat exchanger capacity rate ratios are considerably different from unity; 0.82 for HX1 and 0.62 for HX2. The produced liquid fraction is 0.1332.

The total hydrogen required to be expanded is $0.00338 \text{ lb}/0.1332 = 0.0254 \text{ lb}$. Since this expansion occurs over three 90-sec periods, the average flow rate is $(0.0254 \text{ lb})/[(3)(90 \text{ sec})] = 0.3387 \text{ lb/hr}$.

Statepoint	P, psia	T, K	H, Btu/lb
1	600.00	300.00	1814.16
2	600.00	108.34	499.98
3	600.00	65.00	233.44
4	600.00	43.43	60.27
5	119.30	30.00	60.27
5L	119.30	30.00	-48.04
6 (5V)	119.30	30.00	76.91
7	119.30	64.65	276.69
8	119.30	297.65	1792.80

METAL HYDRIDE MATERIAL SELECTION

Low-Pressure Bed

The metal hydride material selected for the low-pressure bed is zirconium nickel. This metal exhibits a reversible hydriding reaction between hydrides of nominal composition $ZrNiH$ and $ZrNiH_3$. The $ZrNiH$ composition represents the solubility limit.

The actual hydrogen capacity can be determined from available $ZrNi$ -hydrogen pressure-composition isotherms. The capacity is the difference between the maximum composition at the absorbing pressure (1.5 torr) and temperature and the minimum composition at the desorbing pressure (120 psia) and temperature.

The only available isotherms at pressures as high as 120 psia are those of Luo,⁽¹¹⁾ which indicate a composition of $ZrNiH_{0.84}$ at the approximate desorbing temperature of 660°F (622 K). At the absorbing pressure, Luo's data indicate a composition of $ZrNiH_{2.41}$. Other data sources indicate attainable absorbing compositions of $ZrNiH_{2.80}$ ⁽¹²⁾ and $ZrNiH_{2.86}$ ⁽¹³⁾. These data are at an absorbing temperature of 224°F (380 K). The arithmetic average of the available data yields a range of $ZrNiH_{0.84}$ to $ZrNiH_{2.69}$, for a net hydrogen capacity of 1.85 gm-atom hydrogen per gm-mole $ZrNi$.

The heat of reaction is taken as 35,000 joule/gm-atom hydrogen = 14,900 Btu/lb hydrogen.⁽¹¹⁾

High-Pressure Bed

The baseline material was selected from a group of vanadium-titanium-iron alloys. Vanadium and vanadium alloys absorb significantly more hydrogen by weight and volume than competing materials such as lanthanum pentanickel. Vanadium forms a body-centered cubic (bcc) lattice and can react with hydrogen to form a dihydride. There is an α -phase at low loadings of hydrogen representing the solid solution of hydrogen in the metal, followed by the formation of the β -phase representing the monohydride. Once the β -phase is completed, another solid solution phase is formed, representing the formation of the dihydride (γ -phase).

The β -phase (monohydride) formation occurs at very low pressure. In practice, once hydrided, the monohydride phase hydrogen can never be recovered, and a practical system would cycle between the monohydride and dihydride phases.

Extensive work has been done at Allied-Signal on systems based on bcc-hydride-forming alloys.⁽¹⁴⁻¹⁶⁾ This work led to the discovery that these alloys exhibit rapid rates of hydride formation at room temperature without prior activation.⁽¹⁵⁾ This is accomplished by the addition of a minor amount of a metal whose radius is at least 5 percent smaller than the major component metal. The effect was found not to be restricted to binary alloys. The bcc alloys of V-Ti prepared by high-temperature quenching exhibit rapid hydriding with the addition of a third element.⁽¹⁷⁾ Third elements identified as appropriate were Fe, Mn, Co, Cr, and Ni.

The properties of the metal hydrides were found to be closely tied to the lattice parameter. For the V-Ti alloy, adding increasing amounts of Fe yields a shrinkage of the lattice parameter, decreasing both reaction enthalpy change (ΔH) and entropy change (ΔS). This results in pressure-composition isotherms having varying plateau pressures as the Fe content is changed.

For the absorbing pressure of 119.3 psia, the alloy $(V_{0.9}Ti_{0.1})_{0.98}Fe_{0.02}$ exhibits an isotherm at about 194°F, a reasonable operating temperature. The desorbing temperature at 800 psia is 330°F.

Detailed isotherms for the selected alloy, measured previously at Allied-Signal, are shown in Figure 5. Figure 6 shows the van't Hoff plot of the selected alloy. Van't Hoff plots estimate the enthalpies and entropies of reaction by plotting the log of the average plateau pressure (P_{H_2}) as a function of reciprocal temperature using the van't Hoff relationship:

$$\ln P_{H_2} = \frac{\Delta H}{RT} - \frac{\Delta S}{R} \quad (2)$$

where R is the gas constant, and T is the absolute temperature.

The actual hydrogen capacity of the selected alloy is the difference between the maximum composition at the absorbing pressure and temperature, and the minimum composition at the desorbing pressure and temperature. This net capacity is approximately 0.85 gm-atom hydrogen per gm-mol metal. The heat of reaction is 10,240 Btu/lb hydrogen.

PMH COMPACT FORMULATION

Low-Pressure Bed

The ZrNi compacts contain 35 percent aluminum by volume (16.4 percent aluminum by weight). The porosity is approximately 25 percent. The resulting PMH compact density is 271.3 lb/cu ft.

The compacts are in the shape of flat cylinders—0.125 in. dia by 0.025 in. thick. The compacts are configured into a packed bed. For the compact geometry, a reasonable bed void fraction is 50 percent.

High-Pressure Bed

The compacts contain 35 percent aluminum by volume (20.1 percent aluminum by weight). The porosity for this loading is approximately 25 percent. The resulting PMH compact density is 222 lb/cu ft.

The compacts are in the shape of cylinders—0.0625 in. dia by 0.0625 in. thick. The compacts are configured into a packed bed. For the compact geometry, a reasonable bed void fraction is 40 percent.

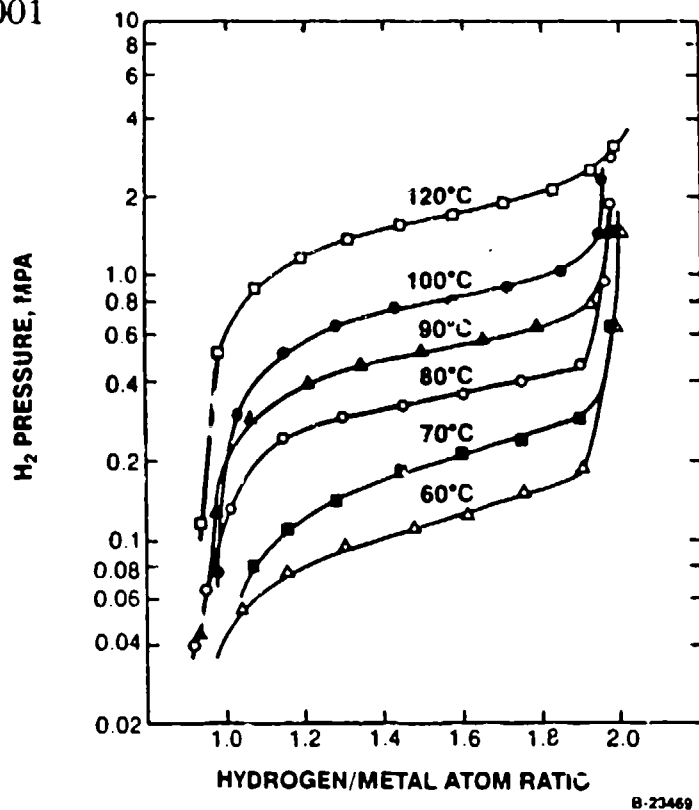


Figure 5. Pressure-Composition Isotherms for the $\gamma \leftrightarrow \beta$ Transition in the $(V_{0.9}Ti_{0.1})_{0.98}Fe_{0.02}$ -Hydrogen System⁽¹⁸⁾

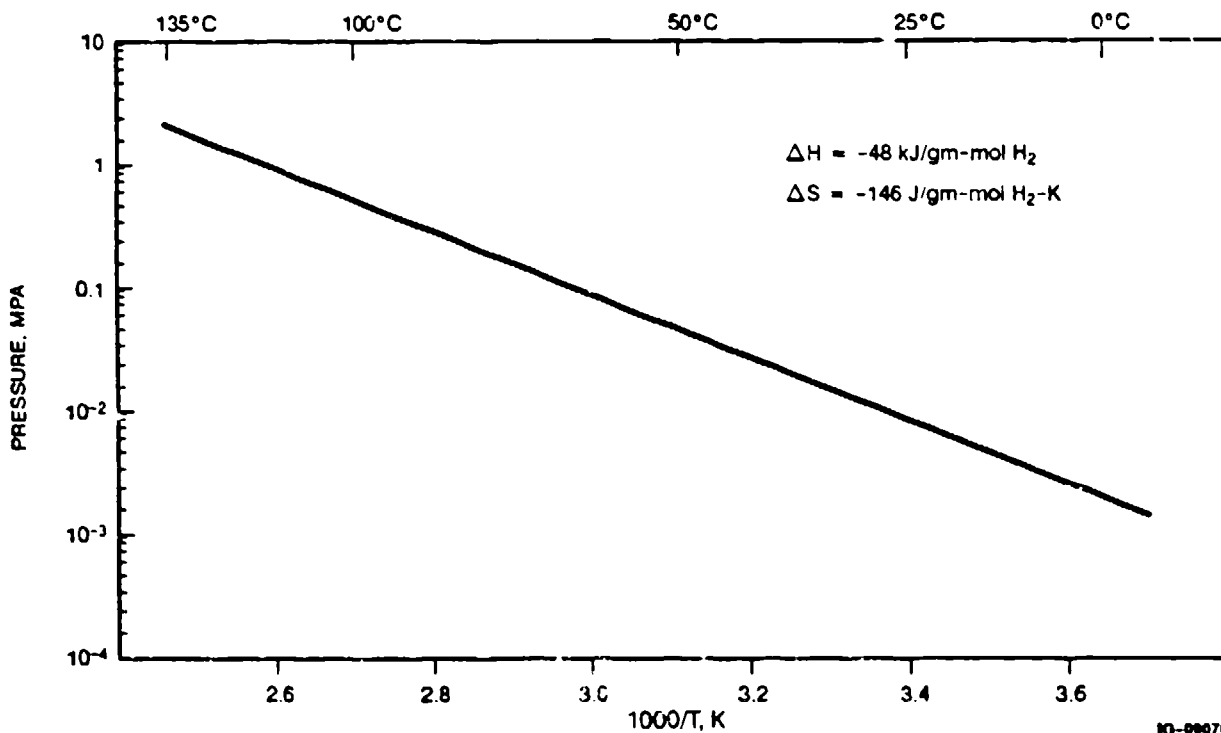


Figure 6. Van't Hoff Plot for the $(V_{0.9}Ti_{0.1})_{0.98}Fe_{0.02}$ -Hydrogen System⁽¹⁶⁾

PHASE CHANGE MATERIAL

A heat-of-fusion phase change material (PCM) is utilized as part of the metal hydride bed assembly. The PCM absorbs the heat of reaction during hydrogen absorption while maintaining a constant temperature. The PCM is regenerated (frozen) during the recovery period.

The selected PCM for both beds is n-docosane ($n\text{-C}_{22}\text{H}_{46}$), a normal paraffin wax with a congruent melting temperature of 111.2°F. Other relevant properties are latent heat of fusion = 107 Btu/lb, solid density = 47.6 lb/cu ft, and solid thermal conductivity = 0.0865 Btu/hr-ft-°F.

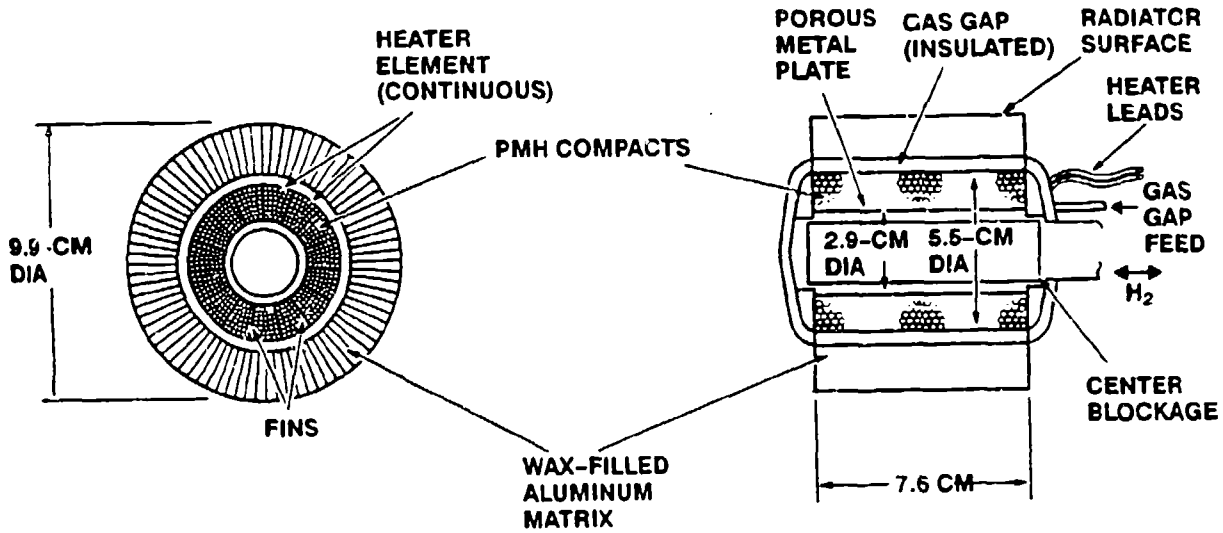
METAL HYDRIDE BED ASSEMBLY

The two bed assemblies are similar in functional configuration, i.e., an integral assembly comprising a PMH compact bed, a gas gap thermal switch, a thermal storage unit (TSU), and a space radiator.

The high-pressure bed is much larger than the low-pressure bed even though there is no required load corresponding to the 120-psia bed pressure (30 K). This is because the high-pressure bed must absorb the hydrogen vapor produced during the J-T liquefaction. The liquid fraction is only 0.1332.

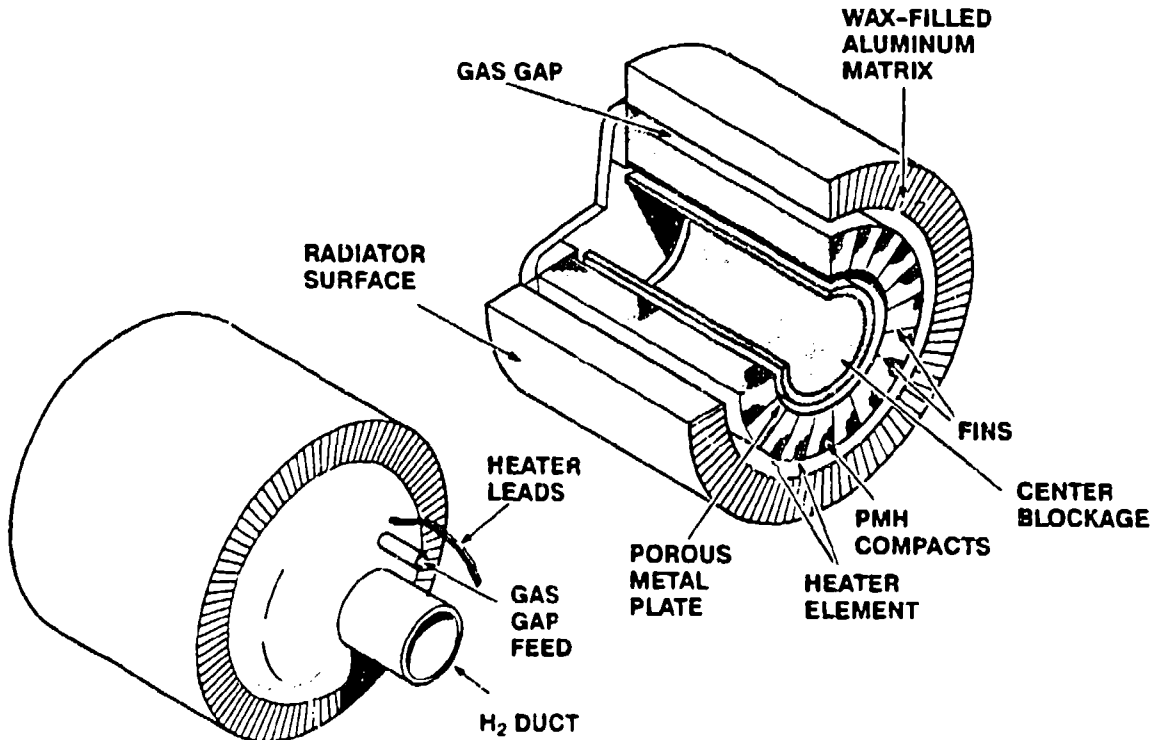
Low-Pressure Bed Assembly

The low-pressure bed assembly is shown in Figures 7 and 8. Hydrogen flows into or out of the PMH bed via a 1.1-in. (2.9-cm) dia duct with walls fabricated from a porous stainless-steel plate. The duct has a center blockage to reduce wasted volume. The porous plate mesh should be fine enough to contain any metal hydride particles broken off the PMH compacts. This arrangement allows for flow in the radial direction, thus minimizing pressure drop. The PMH compacts reside in an annular region between the porous plate and an outer stainless-steel tube that contains the hydrogen pressure [at 2.2-in. (5.5-cm) dia]. Approximately 12,300 PMH compacts are required. Axial stainless-steel fins attached to the porous plate aid in heat transfer. Fifteen fins are used, each 0.5 in. high and 0.006 in. thick. A continuous heater element is wound within the fin passages. This element provides the heat for hydrogen desorption.



IG-11342-A

Figure 7. Low-Pressure Metal Hydride Bed Assembly



IG-11342-1

Figure 8. Low-Pressure Metal Hydride Bed Isometric

The metal hydride bed is surrounded by an annular gas gap of 0.180 in. The gap is filled with 30 layers of aluminum multilayer insulation (MLI). The gas gap functions as a thermal switch, offering a conductive path when filled with helium and acting as an insulator when evacuated.

Outside the gas gap is the TSU, consisting of an aluminum structure containing the PCM. The structure is composed of inner and outer tubes with axial fins in the annular region. Eighty fins are used, each 0.627 in. high and 0.01 in. thick. The PCM is contained and compartmentalized within the fin passages. The outer surface of the TSU acts as the radiator. The total metal hydride bed assembly weight is 2.0 lb.

High-Pressure Bed Assembly

The high-pressure bed assembly is shown in Figures 9 and 10. Approximately 76,700 PMH compacts are required. There are 32 fins in the metal hydride bed, each 0.25 in. high and 0.016 in. thick. The gas gap is 0.018 in. high, and contains three layers of MLI. The TSU comprises 99 fins, each 0.602 in. high and 0.01 in. thick. The total metal hydride bed assembly weight is 8.0 lb.

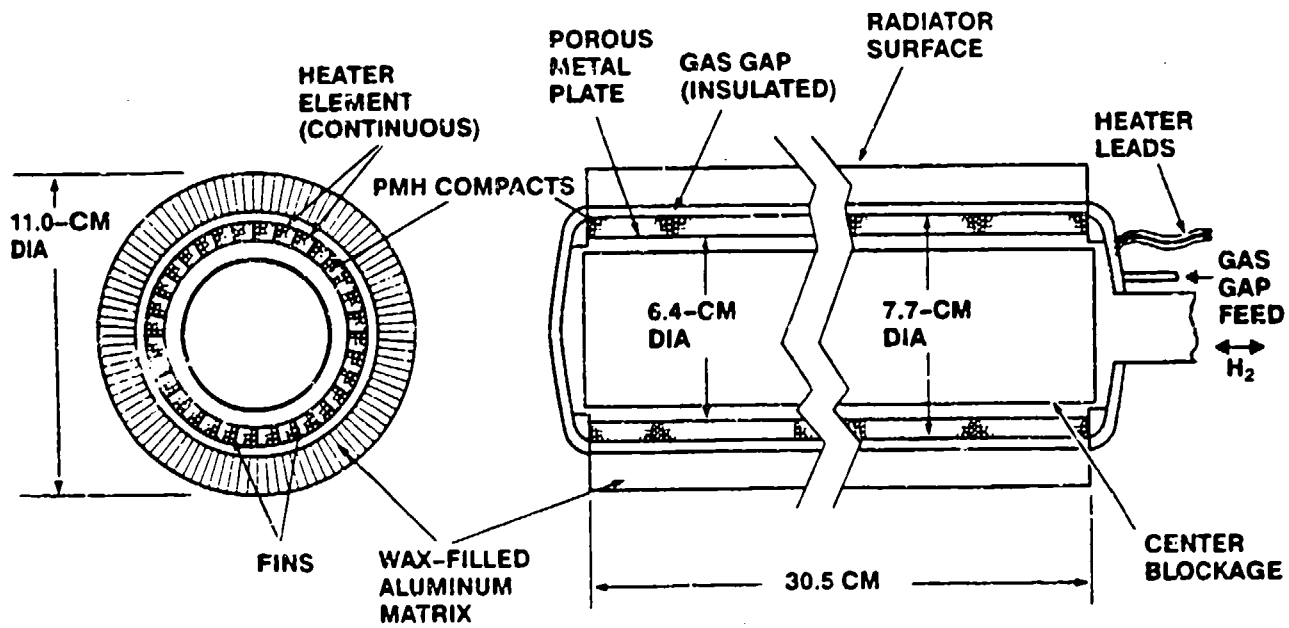
PRESSURE DROP

Low-Pressure Bed Assembly

Perhaps the key consideration concerning the viability of the PMH compacts for the low-pressure metal hydride bed is the adequacy of the individual compact permeability to hydrogen. Although the total mass flow rate is quite low (0.0025 lb/hr), the low hydrogen density at the bed operating pressure of 1.5 torr results in a moderately high volumetric flow rate.

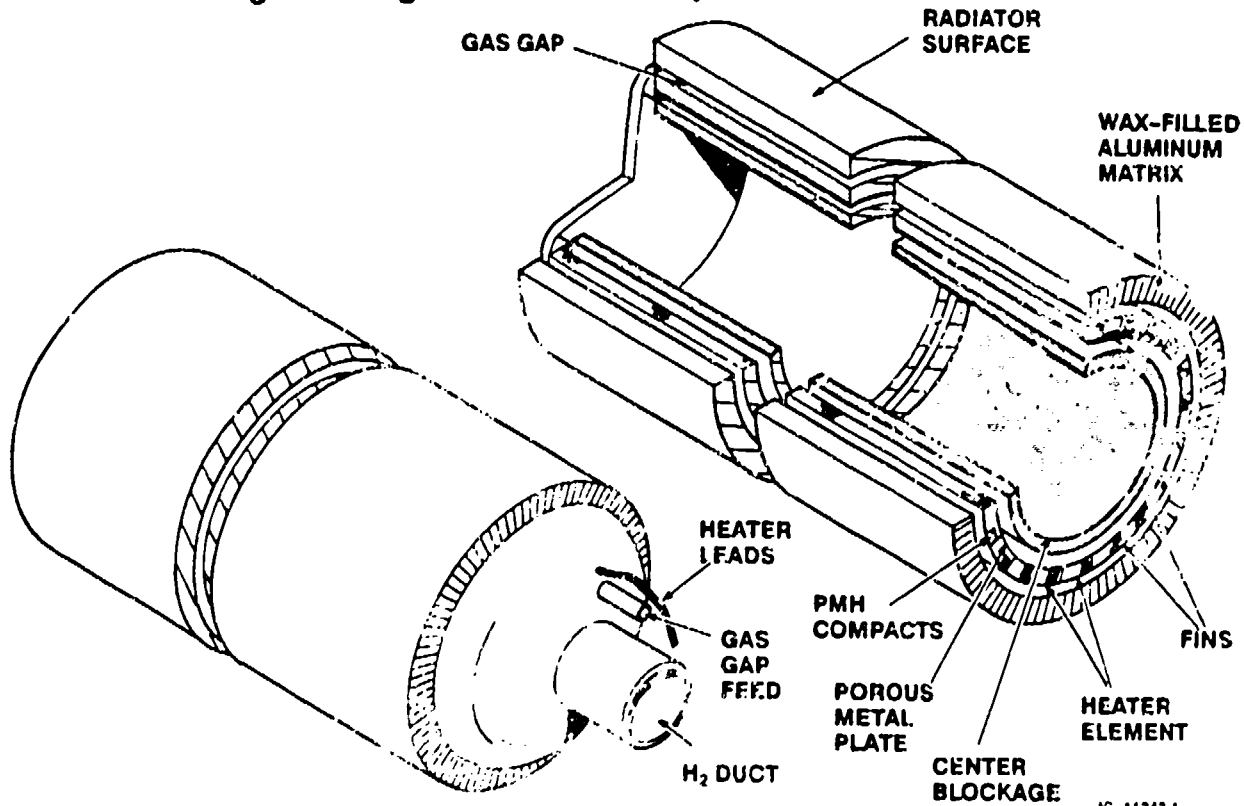
The permeability of LaNi_5 PMH compacts has been measured. However, these measurements were taken at ambient pressures, resulting in a continuum or viscous flow regime. At 1.5 torr, the flow can be shown to be primarily in the rarefied gas or molecular flow regime. No PMH compact permeability data exist for this flow regime. In lieu of data, a predictive approach was taken.

The approach, which is discussed in detail elsewhere⁽¹⁾, predicts the molecular flow permeability from the measured viscous flow permeability and a calculated



IG-11343-A

Figure 9. High-Pressure Metal Hydride Bed Assembly



IG-11343-1

Figure 10. High-Pressure Metal Hydride Bed Isometric

molecular-to-viscous flow conductance ratio⁽²⁰⁾. The calculated permeability is 4.108×10^{-12} sq ft.

Based on this permeability, the maximum pressure drop through the PMH compacts (at the end of the absorbing period) is approximately 0.3 torr. The reaction penetration depth is 0.006 in. into the 0.025-in.-thick compacts, resulting in some unused metal hydride available for reserve. The bed design accounts for this unused region.

In addition to the PMH compact pressure drop, there will be a pressure drop associated with flowing hydrogen in the bed formed by the compacts. This pressure drop is approximately 0.03 torr.⁽¹⁹⁾

High-Pressure Bed Assembly

Because of the high operating pressure (119.3 psia), the pressure drop in the PMH compact bed is quite small.

THERMAL STORAGE

The thermal storage units were sized to handle the entire heat loads for the three consecutive cooling periods. For the low-pressure bed, the heat storage requirement is: $(14,900 \text{ Btu/lb}) (0.00338 \text{ lb}) = 50.4 \text{ Btu}$. The PCM requirement is $50.4 \text{ Btu}/107 \text{ Btu/lb} = 0.47 \text{ lb}$. For the high-pressure bed, the heat storage requirement is: $(10,240 \text{ Btu/lb}) (0.2938 \text{ lb/hr}) (3) (90 \text{ sec}) = 225.6 \text{ Btu}$. The PCM requirement is $225.6 \text{ Btu}/107 \text{ Btu/lb} = 2.11 \text{ lb}$.

RECOVERY

Bed heatup, desorption, and cooling occur during the 19.5-hr recovery period; heat rejection to space occurs during the entire cycle. Since no recovery is required between the three cycles, the cooling loads can be taken consecutively to provide up to 45 min of continuous cooling at 10 K. The recovery occurs in two stages: first, hydrogen is desorbed from the low-pressure bed to the high-pressure bed and second, hydrogen is desorbed from the high-pressure bed to the storage vessel.

Low-Pressure Bed Recovery1. Bed Heatup

During bed heatup, the bed is heated from its operating temperature (around 206°F) to its desorbing temperature (660°F). The gas gap thermal switch is evacuated; the average heat loss through the MLI is 1.5 w. The bed mass is approximately 1.0 lb. At an average heat capacity of 0.1 Btu/lb-°F, the bed thermal capacitance is 0.1 Btu/°F. The energy required for bed heatup is thus: $(0.1 \text{ Btu/°F}) (660^\circ - 206^\circ \text{F}) = 45.4 \text{ Btu} = 13.3 \text{ w-hr}$.

2. Bed Desorption

Desorption occurs with the gas gap evacuated. The total energy requirement is $50.4 \text{ Btu} = 14.8 \text{ w-hr}$.

3. Heater Power

For an assumed time of 4 hr to effect the bed heatup and desorption, the heat leak is $(1.5 \text{ w}) (4 \text{ hr}) = 6.0 \text{ w-hr}$ and the required heater energy is: $13.3 + 14.8 + 6.0 = 34.1 \text{ w-hr}$. The heater power is $34.1 \text{ w-hr}/4 \text{ hr} = 8.5 \text{ w}$.

4. PCM Regeneration

The PCM is regenerated continuously, since the radiator always rejects heat to space. Thus, the time available for PCM regeneration and bed cooldown is 24 hr, with the proviso that the cooldown cannot begin prior to completion of bed desorption. To regenerate the PCM, the heat absorbed by the PCM plus the heater heat leak through the MLI must be rejected to space $(14.8 + 6.0 = 20.8 \text{ w-hr} = 71.0 \text{ Btu})$.

The radiator heat rejection rate, based on a radiating temperature equal to the PCM melting temperature, a space heat sink temperature of 285 K, and a thermal emissivity of 0.85, is approximately 54 Btu/hr-sq ft. For the radiator area of 0.254 sq ft, the heat rejection rate would be 13.7 Btu/hr. The PCM will thus be regenerated in $71.0 \text{ Btu}/13.7 \text{ Btu/hr} = 5.2 \text{ hr}$.

5. Bed Cooldown

Bed cooldown can begin after bed desorption. The available time is $19.5 - 4 = 15.5 \text{ hr}$. The required heat rejection is 45.4 Btu. The required rate is $45.4 \text{ Btu}/15.5 \text{ hr} =$

2.9 Btu/hr. This is below the radiator heat rejection rate. Bed cooldown occurs with the gas gap filled with helium.

High-Pressure Bed Recovery

After absorbing the hydrogen from the low-pressure bed, the high-pressure bed has 15.5 hr remaining for recovery.

1. Bed Heatup

During bed heatup, the bed is heated from its operating temperature (194°F) to its desorbing temperature (330°F). The gas gap is evacuated; the average heat loss through the MLI is 16.3 w. The bed mass is approximately 4.0 lb. At an average heat capacity of 0.1 Btu/lb-°F, the bed thermal capacitance is 0.4 Btu/°F. The energy required for bed heatup is thus: $(0.4 \text{ Btu/°F}) (330^\circ - 194^\circ \text{F}) = 54.4 \text{ Btu} = 15.9 \text{ w-hr}$.

2. Bed Desorption

Desorption occurs with the gas gap evacuated. The total energy requirement is: $(10,240 \text{ Btu/lb}) (0.3387 \text{ lb/hr}) (3) (90 \text{ sec}) = 260.1 \text{ Btu} = 76.2 \text{ w-hr}$.

3. Heater Power

For an assumed time of 10 hr to effect the bed heatup and desorption, the heat leak is $(16.3 \text{ w}) (10 \text{ hr}) = 163 \text{ w-hr}$ and the required heater energy is: $15.9 + 76.2 + 163 = 255.1 \text{ w-hr}$. The heater power is $255.1 \text{ w-hr}/10 \text{ hr} = 25.5 \text{ w}$. This is larger than the heater power required for the low-pressure bed. The power is supplied sequentially for each bed.

4. PCM Regeneration

The heat rejection requirement is $76.2 + 163 = 239.2 \text{ w-hr} = 816.4 \text{ Btu}$. For the radiator area of 1.136 sq ft, the heat rejection rate would be 61.3 Btu/hr. The PCM will thus be regenerated in $816.4 \text{ Btu}/61.3 \text{ Btu/hr} = 13.3 \text{ hr}$.

5. Bed Cooldown

Bed cooldown can begin after bed desorption. The available time is $15.5 - 10 = 5.5 \text{ hr}$. The required heat rejection is 54.4 Btu. The required rate is $54.4 \text{ Btu}/5.5 \text{ hr} = 9.9 \text{ Btu/hr}$. This is below the radiator heat rejection rate.

SUMMARY

Analysis and preliminary design have been conducted for a focal plane array cryocooler. Cryocoolers were studied at 30 K and 10 K. Both systems provide intermittent cooling at these levels. The work effort emphasized the key component in the cryocooler system, the metal hydride sorption bed assembly. This component acts as a thermal compressor to recycle the hydrogen used to produce the refrigeration. The present paper concentrated on the 10 K system.

The sorption beds utilize porous metal hydride compacts. These compacts consist of a porous, three-dimensional, inert metallic matrix incorporating metal hydride particles. The compacts offer a stable form of metal hydride that will not comminute with repeated cycling. This feature is especially important in a space microgravity environment.

In addition to the porous metal hydride compacts, the bed assemblies comprise a gas gap thermal switch, a thermal storage unit using a phase change wax, and an integral space radiator. There are two bed assemblies required for the 10 K cryocooler—a low-pressure bed assembly weighing 2.0 lb and a high-pressure bed assembly weighing 8.0 lb.

The peak electrical power requirement is 25.5 w. This power is exclusive of the SSC requirements.

NOMENCLATURE

J-T	Joule-Thomson
MLI	Multilayer insulation
P	Pressure
PCM	Phase change material
PMH	Porous metal hydride
R	Gas constant
SSC	Standard spacecraft cryocooler
T	Temperature
TSU	Thermal storage unit
ΔH	Enthalpy change
ΔS	Entropy change

ACKNOWLEDGMENT

The authors would like to acknowledge the significant contributions made to the study effort by Beth Klucher and Larry Wismer.

REFERENCES

- (1) Ron, M., D. Gruen, M. Mendelsohn, and I. Sheft, *J. Less-Common Metals*, V. 74, p. 445, 1980.
- (2) Ron, M., D. Gruen, M. Mendelsohn, and I. Sheft, U.S. Patent 4,292,265, 1981.
- (3) Ron, M., U.S. Patent 4,507,263, 1985.
- (4) Ron, M., *Proc. 11th IECEC*, p. 954, 1976.
- (5) Ron, M., E. Bershadsky, and Y. Josephy, "The Thermal Conductivity of PMH Compacts," International Symposium on Metal Hydrogen Systems, Banff, Alberta, 1990.
- (6) Ron, M. and Y. Josephy, "Development Problems on Metal Hydride Reaction Beds," International Symposium on Metal Hydrogen Systems, Banff, Alberta, 1990.
- (7) Bershadsky, E., Y. Josephy, and M. Ron, *J. Less-Common Metals*, V. 153, p. 65, 1989.
- (8) Strumpf, H. J. and M. G. Coombs, *J. Eng. Gas Turbines and Power*, V. 110, pp. 295-300, 1988.
- (9) Bershadsky, E., Y. Josephy, and M. Ron, *Z. Phys. Chem. Neue Folge*, V. 164, p. 1373, 1989.
- (10) Strumpf, Hal J., *Brilliant Eyes Metal Hydride Sorption Cryocooler Study*, AiResearch Document 92-65352, July 1992.
- (11) Luo, W., et al, *J. Less-Common Metals*, V. 162, pp. 251-266, 1990.
- (12) Libowitz, G. G., H. F. Hayes, and T. R. Gibb, *J. Phys. Chem.*, V. 62, pp. 76-79, 1958.
- (13) Kost, M. E., et al, *Russian J. Inorg Chem.*, V. 25, pp. 471-473, 1980.
- (14) Maeland, A. J., G. G. Libowitz, and G. Rak, U.S. Patent 4,425,318 January 10, 1984.
- (15) Lynch, J. F., A. J. Maeland, and G. G. Libowitz, *Zeit. Phys. Chem. Neue Folge.*, V. 145, p. 51, 1985.
- (16) Libowitz, G. G., and A. J. Maeland, *J. Less-Common Metals*, V. 131, p. 275, 1987.
- (17) Maeland, A. J., G. G. Libowitz, J. F. Lynch, and G. Rak, *J. Less-Common Metals*, V. 104, p. 133, 1984.
- (18) Libowitz, G. G., A. J. Maeland, and J. F. Lynch, *Advanced Hydrogen Storage: Modified Vanadium Hydrides*, Brookhaven National Laboratory Report BNL 37866, August 1985.
- (19) Strumpf, Hal. J, *Porous Metal Hydride Compact Study*, AiResearch Document 91-64840, November 1991.
- (20) Guthrie, A. and R. K. Wakerling, *Vacuum Equipment and Techniques*, McGraw-Hill Book Co., Inc., New York, 1949.